The Generation, Segregation and Mobilisation of Granitic Melt in the Continental Crust

THE UNIVERSITY *of* LIVERPOOL

Matthew David Jackson

A dissertation submitted in accordance with the requirements of the University of
Liverpool for the degree of Doctor of Philosophy

September 1997

Abstract

The Generation, Segregation and Mobilisation of Granitic Melt in the Continental Crust

An understanding of the origin and evolution of granitic rocks is fundamental to a wider understanding of the origin and evolution of the continental crust. Many granites originate by partial melting of lower crustal rocks, but our understanding of the physical processes which lead to a granitic melt fraction in the lower crust segregating from its protolith, mobilising to form a magma, and ascending to the emplacment level in the upper crust are poorly understood. The process of melt segregation is particularly poorly understood; moreover, the evidence presents a paradox: granitic melt fractions correspond to only small degrees of partial melting of their source rocks, and appear to segregate from partially molten rocks in which the contiguity of the solid matrix is maintained (i.e. melt fractions are *less* than the Critical Melt Fraction (CMF)), yet magma mobilisation occurs only if the contiguity of the solid matrix breaks down (i.e. melt fractions are *greater* than the CMF). Previous models of melt generation and segregation in the crust have failed to resolve this paradox.

A new, *quantitative* physical model is presented of phase change and phase transport in a multicomponent material which is heated from below. Solid-liquid phase change leads to the formation of a mushy, mixed phase region adjacent to the heat source; the liquid phase is buoyant and interconnected along grain edges, and the solid phase may viscously deform in response to liquid phase transport. This model represents the most general description of partial melting in the crust following underplating or asthenospheric upwelling. The 1-D results indicate that the spatial distribution of the liquid volume fraction (porosity) within the mixed phase region depends upon the relative transport rates of heat and liquid, and is governed by the magnitude of a dimensionless parameter termed the *effective thermal diffusivity* (κ_{eff}). Both the position of the solidus isotherm (which defines the 'top' of the mixed phase region) and the buoyant liquid migrate upwards away from the heat source, and in systems characterised by a wide range of values for κ_{eff}, the liquid phase migrates more quickly than the solidus isotherm and accumulates below it, which results in the formation of a *porosity wave*, the amplitude of which increases with time until it exceeds the CMF and a mobile slurry forms. Because the liquid in the slurry has thermodynamically equilibrated with the solid phase at low temperatures near the top of the mixed phase region, its composition corresponds to only a *small* degree of melting of the solid phase.

This general model is applied to the partial melting of fertile source rocks in the lower crust, and the results indicate that granitic (*sensu-lato*) melt, the composition of which corresponds to only a small degree of partial melting (<CMF) of the source rock, may segregate and form a mobile magma; moreover, the solid matrix of the source rock is not disrupted during segregation except in the localised region of magma mobilisation. Thus is the paradox resolved. However, the results are sensitive to the values of the dimensional variables which govern the magnitude of the dimensionless parameter κ_{eff}; in particular, the viscosities of the melt and partially molten rock matrix, the grain size and the permeability constant. These variables are poorly constrained for crustal rocks; the limited experimental and theoretical data available is used to estimate suitable values. Magma mobilisation is likely in partial melt zones characterised by values of the variables in the mid-range of those estimated, or in partial melt zones where, for example, a large grain size is countered by small matrix viscosities. For a basaltic protolith, mobilisation is predicted within ~15,000 yrs. to ~10 M.y., and the composition of the mobilised melt ranges from granodioritic - trondjhemitic. Until the values of the governing variables are better constrained, it must suffice that the model predicts the segregation and mobilisation of granitic (*sensu-lato*) melt within geologically reasonable timescales, and in agreement with the geological and geochemical evidence.

A quantitative description of heat transport in the underlying heat source is included in the model, and the results indicate that, in partial melt zones characterised by a wide range of values for κ_{eff}, basaltic underplating provides sufficient heat to generate mobile granitic magma in the overlying source rock; for example, underplate thicknesses of 700m - 10km are required to generate mobile granitic magma in a basaltic protolith. The granitic magma is likely to migrate laterally through the source region and ascend to the emplacement level through a localised zone of dykes. If the dykes can extract melt from high porosity zones *before* magma mobilisation, then different melt compositions may be extracted from the same protolith, and the order of extraction is in agreement with the order of intrusion of many granitic plutons and suites.

Faust: Then to the moment could I say:
Linger you now, you are so fair!
Now records of my earthly day
No flights of aeons can impair -
Foreknowledge comes, and fills me with such bliss,
I take my joy, my highest moment this.

Mephistopheles: A foolish word, bygone.
How so then, gone?
Gone, to sheer Nothing, past with null made one!
What matters creative endless toil,
When, at a snatch, oblivion ends the coil?

Acknowledgements

First and foremost, I would like to thank my supervisors, Michael Atherton and Mike Cheadle, for providing their expertise and time so generously, for their unstinting enthusiasm and encouragement, and for teaching me about granites (Mike A.) and basalts (Mike C.) both in Liverpool and in the field. Thanks are also due to Nick Petford for his role in initiating the project, and for 'looking after' me in the States. I would also like to thank all the members of staff at Liverpool with whom I have had numerous illuminating and informative discussions; in particular, Rob Hunter, John Wheeler, Steve Flint and Steve Reddy, and also Graham Potts and his 'compacting sand' conundrum. Fawzy Naggar is thanked for his boundless patience and support during the lean times. The Natural Environment Research Council are gratefully acknowledged for funding.

My time in Liverpool would not have been so enjoyable without the help and support which I received throughout my research from my fellow postgraduate students. Firstly, I would like to thank the 'old guard' (who have now gone on to bigger and better (?) things), for introducing me to Liverpool and the mysterious ways of scientific research; in particular, Dougal (to whom the colour scheme in figure 6.1 is dedicated); Mark C., Gary H., Stevie J, and Tim R. Secondly, I would like to thank the 'new guard' for help and support towards the end of my research; in particular, Pat T. for maintaining the office in the style to which we were both accustomed and for reading even the most boring of my chapters, and Mike E. for bizarre 'scientific' conversations and for being even more stressed than I. Thanks also to all my friends who have picked me up when I've been down, and reminded me that there is life outside of a dissertation: Lizzy, Julie, Deborah, Emma P., Dougal, Mark C., Gary H., John 'dodgy fringe' Aitken, mad Louise, Sam E., Mark R., Sophie B., Kath S., Lena, Pete S. and Marcus (?!).......I love you all! If I've missed anybody out, then I'm sorry and I'll acknowledge you in the next dissertation I write. Extra special thanks to Emma P. for keeping me sane and for still being here, to Lizzy for being understanding about the 'Welsh Deadline', and to Dougal for making it all the way back for my viva.

I would not have survived a further four years as a student without the support, both moral and financial, of my mother and father, and I can't thank them enough. The next meal is on me!

I would like to thank my examiners, Mike Bickle (University of Cambridge) and Hugh Davis (University of Liverpool) for their constructive criticism and comments.

Finally, I would like to thank the Stella Artois Brewery and my bank manager, whose reluctant but close co-operation over the years has ensured many memorable nights and several unmemorable mornings.

Table of Contents

Chapter 1

Chapter 2

Chapter 3

Chapter 6

Chapter 7

Appendix A

Appendix B

Chapter 1: Introduction.

"We recognise such a close connection between the composition of the continental crust, especially the upper crust, and granitoid rocks, that to explain one may take us a long way to explaining the other." **(Clarke, 1992, p. 8).**

An understanding of the processes which lead to the formation of granitic[1] bodies is fundamental to a wider understanding of the origin and evolution of the continental crust. Granitic plutonism is intimately linked with the generation of continental crust. Throughout Earth history, from the trondhjemite-tonalite-granodiorite batholiths which characterise the earliest Archaean continental crust to the common Phanerozoic composite batholiths, granites are, and have been, the most abundant plutonic rocks in the upper crust (Clarke, 1992). The geochemical differentiation of the continental crust into a felsic upper and mafic lower crust observed today has evolved as a result of granitic magmatism through time (Fyfe, 1973; Leake, 1990; Vielzuf *et al.*, 1990).

During the first half of this century, the debate on the formation of granitic rocks was centred on whether they were metasomatic or magmatic in origin (Bowen, 1948; Read, 1948, 1949). Following the publication of papers by Bowen and Tuttle (1950) and Tuttle and Bowen (1958), most geologists today would agree that the debate was won by the "magmatists", whilst acknowledging that metasomatic granitisation can explain the formation of some granites (Atherton, 1993). The recognition that most granitic bodies are magmatic in origin generated a host of new questions concerning the physical and chemical processes which are responsible for their formation, many of which remain unanswered.

The intrusive nature of most granites is evidence that they crystallised from magma which was mobile and which had migrated from its site of origin. This observation leads to the sub-division of the formation of a granitic body into three separate, but interrelated processes (e.g. Miller *et al.*, 1988; Atherton, 1993; Brown, 1994):

i) granitic melt production at depth (the *source*)
ii) magma[2] migration through the crust (the *ascent*)
iii) magma intrusion, cooling, and crystallisation (the *emplacement*)

---

[1] unless otherwise specified, 'granite' and 'granitic' *sensu lato* are used in preference to 'granitoid' to describe granites, granodiorites, tonalites, and trondhjemites.

[2] throughout this dissertation, *melt* refers to crystal free liquid, *magma* refers to melt plus suspended crystals, whilst *mush* refers to a continuous, interconnected solid matrix containing interstitial liquid.

Geochemical evidence indicates that many granites are produced, migrate, and are emplaced entirely within the continental crust (figure 1.1). Granitic melt is produced at depth by partial melting of crustal rocks, and then migrates upwards through the crust to higher structural levels where it is intruded and cools to form a pluton (e.g. Chappell, 1984; D'Lemos *et al.*, 1992; Atherton and Petford, 1993; Brown, 1994). However, although *geochemical* evidence confirms that many high level granitic bodies originated as partial melts within the crust, the *physical* processes which lead to a partial melt in the lower crust eventually forming a pluton in the upper crust are poorly understood. Source, ascent, and emplacement processes have each been studied in isolation, but no convincing unified physical model has yet been proposed.

Our understanding of source region processes is particularly poor, because the lower crustal zones in which partial melting occurs to produce *large* quantities of granitic melt are rarely exposed, and as yet, no convincing, quantitative models of source region processes have been developed. Yet source region processes are important because they exert a fundamental control on the composition of the magma which reaches the emplacement level (Bergantz and Dawes, 1994; Brown, 1994); for example, chemical heterogeneities within and between genetically related granitic bodies can be inherited from the source region (e.g. Tepper *et al.*, 1993; Petford *et al.*, 1996). To understand how this petrological diversity is produced, a better understanding of the physical processes which operate in the source region is required. How is partial melting initiated? How efficiently can the granitic melt fraction separate from the unmelted protolith? By what physical mechanism does this separation occur? Can the separation process generate petrological diversity? How long must partial melting be sustained to produce batholithic quantities of granite? Can partial melting be sustained for this length of time?

The objective of this dissertation is to develop a new, *quantitative* physical model of a crustal granite source region, with the aim of answering, or at least constraining the answer to, some of these key questions concerning granite petrogenesis. It is important to place this new work in the context of a changing outlook on the rheology of granitic magmas. The traditional view is that they are crystal laden and behave as non-Newtonian fluids with high viscosities ($\sim 10^{15}$ - 10^{19} Pa s) (e.g. Ramberg, 1970; Bateman, 1984; Kukowski and Neugebauer, 1990). But recent studies have challenged this orthodoxy, arguing that hot, granitic magmas which contain volatiles and bear a relatively low fraction of crystals, behave as Newtonian fluids with much lower viscosities ($\sim 10^{4}$ - 10^{7} Pa s) (Kerr and Lister, 1991; Petford *et al.*, 1993; Petford, 1995; Wolf and Wyllie, 1991, 1995). A dramatic reduction in the proposed viscosity of granitic magmas implies an increase in the *rate* of fluid-dynamical processes associated with granitic magmatism. Is granitic magmatism dominated by slow processes, hindered by high magma viscosity, or by rapid processes, facilitated by low magma viscosity?

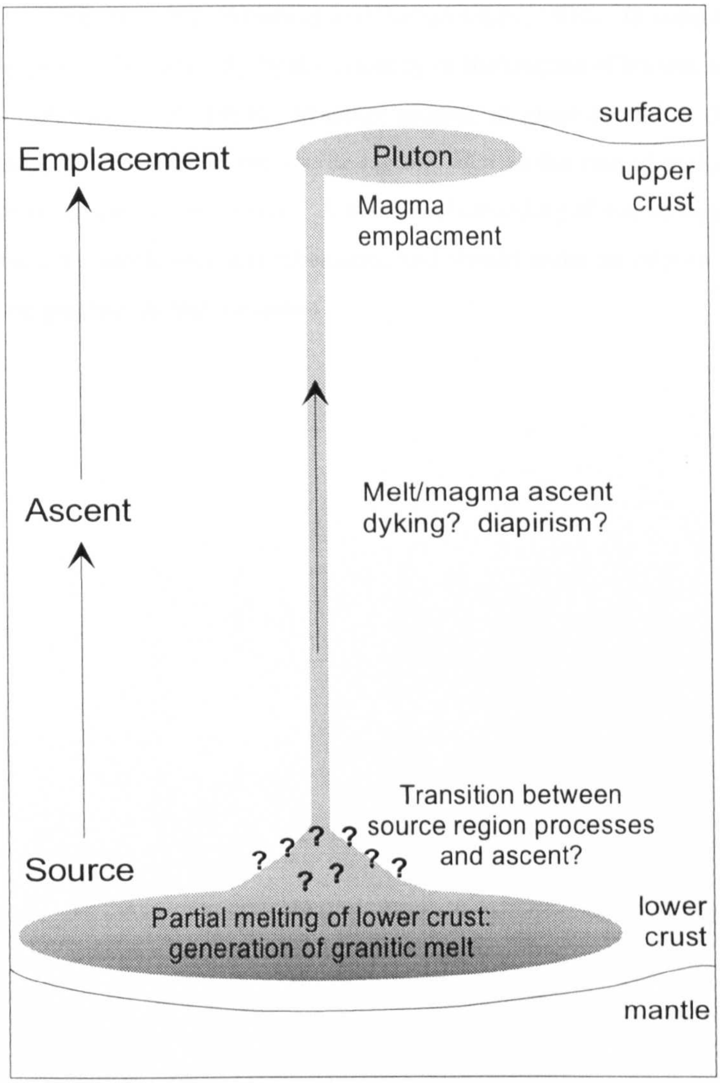

Figure 1.1. Schematic of the processes leading to the formation of an intracrustal granitic body

The contrast between old and new doctrines is most clearly manifested in the debate between those who believe that granitic magmas ascend as diapiric bodies, and those who believe that granitic magmas ascend through dykes, faults, or fractures in a manner analogous to that of basaltic magmas. Diapirism is the "upwelling of relatively mobile rock material through, or into, overlying rocks" (van den Eeckout *et al.*, 1986), and is a slow process limited by the high viscosity of the surrounding crust ($\sim 10^{15}$ - 10^{25} Pa s) (e.g. Marsh, 1982; Weinberg and Podladchikov, 1994). In contrast, magma ascent via dykes is a rapid process limited only by the viscosity of the magma (Clemens and Mawer, 1992; Petford *et al.*, 1993; Petford *et al.*, 1994). Whether granitic magmas ascend as diapirs or through dykes may be dictated by processes in the source region, such as the rate of melting, the degree of melting, and the ability of the melt to migrate. A better understanding of source region processes may therefore help constrain possible ascent mechanisms, and should make an important contribution to the current debate on granitic magma dynamics.

Chapter 2: Melt generation and mobilisation in the continental crust.

"Despite the undoubted involvement of the mantle, there is now good isotopic and other evidence that usually the continental crust is at least an important contributor to the material which constitutes most granite batholiths." **(Leake, 1990, p. 580)**

2.1 Introduction

The aim of this chapter is to briefly review the processes which lead to the production of anatectic granitic melt, which is mobile and so is able to migrate upwards through the crust from its source region in the mid- to lower crust, to the emplacement level in the upper crust. The first step must be the generation of granitic melt by partial melting; the importance of *dehydration* melting reactions, and the role of basaltic intra/underplating in this process will be highlighted. The granitic melt must then become mobilised; the importance of melt *segregation* in this process will be emphasised. Melt segregation is defined as "the separation of the melt fraction from its restite" (Sawyer, 1994). Unless melt segregation is completely effective, the mobilised melt will contain at least a small proportion of solid, restitic material. Following the definitions of melt and magma presented in chapter 1, the mobilised melt will be termed magma, although it is accepted that, depending upon the efficacy of the segregation process, the magma may contain a negligibly small proportion of restite.

2.2 Melt generation

To partially melt a rock, either a flux such as water must be added, the rock must decompress adiabatically, or heat must be supplied (e.g. Wilson, 1989). Crustal rocks which can produce partial melts of granitic composition are termed *fertile* (Brown, 1994; Vielzuf *et al.*, 1990), and include many common compositions ranging from meta-sediments to hydrated basalt (e.g. Vielzuf and Holloway, 1988; Rushmer, 1991). Regions which have already been partially melted and differentiated cannot produce further granitic melt, and are termed *sterile* (Brown, 1994).

2.2.1 Flux melting

Flux melting may occur when a volatile rich fluid is introduced to the protolith which depresses its solidus temperature. It has been invoked as the cause of granitic melt generation in some cases. For example, small volumes of granitic melt in the mid- to upper crust are believed to be generated by flux melting of sediments following the introduction of water (e.g. Strong and Hanmer, 1981; Wickham, 1987a). However, granitic melt produced by melting in the presence of excess water is cool and water-saturated; consequently, even if the melt becomes mobilised as a magma, the magma is effectively immobile because on ascent and decompression the water exsolves, and the magma rapidly crosses its solidus and crystallises. *Mobile* granitic magmas are water-undersaturated, and must originally form by dehydration melting in a water-undersaturated or water-absent environment (e.g. Tuttle and Bowen, 1958; Clemens 1984; Clemens and Vielzuf, 1987; Whitney, 1988; Tepper *et al.*, 1993, Brown, 1994). Numerous melting experiments have demonstrated that melts of granitic composition are produced by dehydration melting of common crustal rock types (e.g. Wyllie, 1977; LeBreton and Thompson, 1988; Vielzuf and Holloway, 1988; Beard and Lofgren, 1991; Patiño Douce and Johnston, 1991; Rapp *et al.* 1991; Rushmer, 1991; Wolf and Wyllie, 1994; Rapp and Watson, 1995); moreover, high pressure melting experiments under water-saturated conditions, used to model melting in the mid- to lower crust, have produced melt compositions unlike those of most silicic rocks (Beard and Lofgren 1989, 1991).

2.2.2 Pressure release melting

Pressure release melting may occur when rocks adiabatically decompress by rapidly migrating upwards without cooling. Although adiabatic decompression melting of upwelling mantle rocks is a primary source of basaltic magmatism (Wilson, 1989), decompression melting in the crust would require extremely rapid rates of uplift, and has been suggested as a potential mechanism for the generation of granitic melt only in conjunction with crustal heating (e.g. Thompson, 1982, 1990; Brown, 1983, 1994; Jones and Brown, 1990).

2.2.3 Melting due to crustal heating

In general, to generate *significant* amounts of mobile granitic melt, heat must be supplied to the mid- to lower crust (e.g. Clemens and Vielzuf, 1987; Huppert and Sparks, 1988; Clemens, 1990; Brown, 1994; Bergantz and Dawes, 1994). This is especially true of dehydration melting, which occurs at higher temperatures than water-saturated melting. The available heat sources for crustal melting are heat transferred from the mantle, and internal heat production within the crust due to radioactive decay. Heat must be transferred from the mantle to the crust by some form of advection, because the lower crust is not normally partially molten during steady state conductive heat transfer.

2.2.3.1 Intra/ underplating

Heat may be advected from the mantle into the crust via the intrusion of mantle derived basalt (Huppert and Sparks, 1988; Bergantz and Dawes, 1994). The interaction of mantle derived basalt with the crust has been described as magmatic intra/underplating, although the term underplating has also been used to describe a variety of other lower crustal processes. I follow Bergantz and Dawes (1994) in using the terms intra- and underplating to describe only the accumulation of mantle derived basalt in the mid- to lower crust. The importance of underplating as a mechanism for crustal growth has been confirmed by both geophysical and geochemical evidence (e.g. Drummond and Collins, 1986; Klemperer *et al.*, 1986; Feeley and Grunder, 1991; Nelson, 1991; Rudnick, 1992; Tepper *et al.* 1993; Atherton and Petford, 1993; Petford and Atherton, 1996; Petford *et al.*, 1996); moreover, some exposures of exhumed deep crust, such as the Ivrea-Verbano zone in northern Italy, provide direct evidence of underplating (Voschage *et al.*, 1990; Zingg, 1990; Handy and Zingg, 1991). Numerous quantitative models have demonstrated that underplating may supply sufficient heat to generate significant quantities of granitic partial melt from fertile crustal rocks (Hodge, 1974; Huppert and Sparks, 1988; Bergantz, 1989; Fountain *et al.*, 1989; Bergantz and Dawes, 1994).

Underplating is an important mechanism in granitic magmatism, because it can act both as a heat source to drive melting, and as a *material* source of granitic partial melt. Repeated underplating leads to the production of a young, mafic lower crust, which may be partially re-melted by subsequent underplating (Bergantz and Dawes, 1994). Newly underplated basalt concomitant with crustal thickening has been invoked as the source rock of the Cordillera Blanca batholith in the Peruvian part of the Andes (Atherton and Petford, 1993; Petford and Atherton, 1996; Petford *et al.*, 1996), a proposal supported by the results of experimental work which has demonstrated that granitic melt can be produced during the dehydration melting of hydrated basalt (e.g. Beard and Lofgren, 1989, 1991; Rushmer, 1991; Wolf and Wyllie, 1994; Rapp and Watson, 1995).

2.2.3.2 Asthenospheric upwelling

Heat may be advected to the base of the crust if hot, buoyantly upwelling asthenosphere replaces colder mantle lithosphere. Several workers have proposed that cooling mantle lithosphere can become gravitationally unstable, detach from the overlying crust, and fall away, to be replaced by asthenospheric material; a process described as delamination (e.g. Bird, 1979; Kay and Mahlburg-Kay, 1991; Nelson, 1991). Alternatively, during crustal thickening, cold mantle lithosphere may be pushed downwards into the convecting asthenosphere, with the same result (Houseman *et al.*, 1981). In continent-continent collision zones, buoyancy forces may result in the subducting plate undergoing rifting and eventually complete break-off, allowing asthenospheric material to rise and fill the gap (Davies and von Blanckenburg, 1995). In all cases, hot asthenospheric material is brought into close proximity with the lower crust, leading to rapid heating of the crust which may be accompanied by intraplating of basalt derived from the upwelling asthenosphere (Kay and Mahlburg-Kay, 1991; Nelson, 1991). Granitic melt may be produced if the lower crust is fertile (e.g. Houseman *et al.*, 1981), although no quantitative models of granitic melt production as a result of this process have been developed. In support of these models, Seber *et al.* (1996) have presented recent geophysical evidence which, in conjunction with observed surface volcanism and high surface heat flow, is consistent with asthenospheric upwelling in the western Mediterranean. They note that melting of the lower crust would be expected.

The viability of delamination due to gravitational instability of the mantle lithosphere alone has been questioned by Ellis (1992). He argues that compositional differences between depleted mantle lithosphere and asthenosphere, neglected in earlier physical models of delamination, cause even cold mantle lithosphere to remain less dense than the underlying asthenosphere. However, he accepts that detachment of the mantle lithosphere may occur if the lithosphere is forced downwards into the asthenosphere as a result of crustal shortening or subduction, and that asthenospheric upwelling will follow detachment.

2.2.3.3 Crustal thickening/thinning

Heat may be advected with the crust during crustal thickening or thinning. Several workers have developed quantitative models of the thermal regime in crust which is thickened by collision or overthrusting, or thinned by extension, with specific reference to crustal anatexis and the production of granitic melt (England and Thompson, 1984; Zen, 1988, 1995; Patiño Douce *et al.*, 1990). These models are not applicable to crust which is actively being, or has recently undergone, intra/underplating or delamination, because in developing them it is assumed that the only available heat sources are conductive transfer to the base of the crust from the upper mantle, and radioactive decay within the crust. Generally, the results suggest that temperatures high enough to cause dehydration melting of fertile crustal rocks may be achieved by crustal thickening or thinning; in particular, Patiño Douce *et al.* (1990) suggest that dehydration melting of fertile meta-sediments is possible in the mid-crust, and predict the formation of significant quantities of granitic melt. In contrast, England and Thompson (1984), and Zen (1988), predict small degrees of dehydration melting restricted to the deep crust. Crustal thickening/thinning is unlikely to generate significant quantities of melt from a basic igneous protolith, because of the high solidus temperatures of basic igneous rocks (Patiño Douce *et al.*, 1990).

2.2.4 Summary

Large volumes of mobile granitic melt are generated in the crust by dehydration melting of fertile rock under fluid-absent or fluid-undersaturated conditions. Intra/underplating of mantle derived basaltic magma can provide sufficient heat to generate significant quantities of granitic melt, and may also act as a material source of melt. Asthenospheric upwelling may cause partial melting, but no quantitative models of the volume or composition of melt produced have yet been developed; crustal thickening/thinning may cause partial melting, but models predict that only small volumes of melt will be produced unless a suitable meta-sedimentary protolith is available in the mid crust. Intra/underplating is likely to be the most significant heat source for the generation of granitic melts, especially from basic igneous protoliths in deep crustal environments.

2.3 Magma mobilisation

2.3.1 Magma mobilisation and the Critical Melt Fraction

When a rock partially melts, the unmelted solid fraction maintains a continuous, interconnected crystalline matrix until the melt volume fraction reaches a certain value, usually termed the Critical Melt Fraction (CMF) (Arzi, 1978; van der Molen and Paterson, 1979). A solid matrix containing interstitial fluid is termed a *mush*. When the melt fraction reaches the CMF, the solid matrix disaggregates, resulting in the formation of a mobile magma. The concept of the CMF was developed as a result of investigations into the rheological behaviour of partially molten rocks, and is strictly defined as the melt fraction at which the flow behaviour of a partially molten rock changes between "flow as a granular mass [*low melt fraction*] and flow as a dense suspension [*high melt fraction*]" (van der Molen and Paterson, 1979, p.300). It is related to the concept of contiguity, which is a measure of solid grain-grain contact and originated in the metallurgical literature. The contiguity of a mush depends upon the liquid volume fraction, the microscopic distribution of liquid throughout the mush, and the solid grain size distribution, and is used in metallurgy to estimate the liquid volume fraction at which a mush will disaggregate. However, the value of the CMF for a particular geological mush may depend not only upon grain contiguity, but also factors such as the rate of externally imposed deformation. Experimentally and theoretically derived estimates of the CMF for a variety of common lower crustal rock types range from 0.2-0.70 (e.g. Arzi, 1978; van der Molen and Paterson, 1979; Marsh, 1981; Cheadle, 1989; Lejeune and Richet, 1995; Philpotts and Carroll, 1996).

2.3.2 The importance of melt segregation

To form a mobile *granitic* magma, a granitic partial melt fraction *must* be able to segregate to some extent from its restite. Several workers have proposed that melt segregation occurs *after* magma mobilisation; a process termed *restite unmixing*. They argue that partial melting of the protolith proceeds until the melt fraction exceeds the CMF, in which case both melt and restite become mobilised *en masse* and migrate upwards through the crust. The bulk composition of the buoyantly ascending magma is initially unchanged from that of the original protolith, but partial or complete segregation of the melt from the restite during ascent results in the formation of a granitic magma (e.g. White and Chappell, 1977, 1990; Chappell, 1984; Chappell *et al.*, 1987). However, abundant laboratory and field evidence indicates that granitic partial melt must usually segregate in the source region *before* magma mobilisation, from partially molten rock in which the solid fraction maintains an interconnected matrix (Wickham, 1987b; Brown, 1994; Sawyer, 1994). For example, experimental work on the melting relations of fertile lower crustal rocks, ranging in composition from meta-sedimentary to basaltic, suggests that partial melts of granitic composition represent *small* degrees of partial melting, which are less than the CMF (table 2.1). Moreover, many exposed lower

Reference	Protolith	Melt compositions obtained	Degree of melting required
Beard and Lofgren, 1991.	Basaltic and Andesitic Greenstones and Amphibolites.	Trondhjemitic - tonalitic - granodioritic.	10-40% (0.1-0.4).
Rapp and Watson, 1995.	Metabasalt.	High K_2O granitic. Trondhjemitic. Tonalitic-Granodioritic.	~5% (0.05). ~5-10% (0.05-0.1). 20-40% (0.2-0.4).
Vielzuf and Holloway, 1988.	Meta-pelite.	"S-Type granitic."	~40% (0.4).
Rushmer, 1991.	Amphibolite.	Tonalitic.	~30% (0.3).

Table 2.1. A summary of the results of melting experiments on naturally occuring rock types. In all cases melting occurs under fluid absent or fluid undersaturated conditions. "Degree of melting required" refers to the modal quantity of glass recorded after rapidly cooling the partially melted rock; expressed as a percentage and as a fraction.

crustal granulite terrains, such as the Ivrea-Verbano zone, exhibit geochemical and mineralogical characteristics which suggest they are residues left after the *in-situ* extraction of a granitic partial melt fraction (e.g. Fyfe, 1973; Clifford *et al.*, 1981; Clemens, 1989, 1990; Pin, 1990; Vielzuf *et al.*, 1990; Rudnick, 1992). Of these, some retain mesoscopic layering structures which indicate that the solid matrix was not disrupted during segregation of the melt (Clemens, 1989).

The evidence that granitic melt segregation and mobilisation occurs *in the source region* is consistent with the evidence that granitic magmatism has led to the differentiation of the continental crust into a felsic upper crust and a restitic, mafic lower crust (Christensen and Mooney, 1995). Indeed, without an efficient mechanism of granitic melt segregation and mobilisation at lower crustal levels, which has operated consistently throughout Earth history, it is difficult to envisage how such differentiation could have come about.

2.3.3 Minimum requirements for melt segregation

Melt may segregate from a partially molten rock matrix only if the matrix is permeable, and a pressure gradient is present to drive melt migration relative to the matrix. The permeability of a partially molten rock depends upon the microscopic distribution of the melt, which in turn depends upon the pore space morphology, and has been investigated both theoretically and experimentally. Theoretical studies have successfully determined the pore space morphology in an equigranular, monomineralic mush of isotropic grains, which has attained thermodynamic and textural equilibrium (Beere, 1975; von Bargen and Waff, 1986; Cheadle, 1989). In this ideal mush, the pore space morphology is governed only by the liquid-solid and solid-solid interfacial energies, and liquid interconnectivity is governed by the magnitude of the dihedral angle, which is defined as 'the angle formed between the two walls of a pore at a solid-solid-fluid junction' (Smith, 1948, 1964; Bulau *et al.*, 1979). For dihedral angles between 0° and 60°, the liquid is interconnected along grain edges even for very small liquid fractions (<0.01), so the mush is permeable (von Bargen and Waff, 1986; Cheadle, 1989). Partial melting experiments on fine grained powder compacts of silicate rocks have revealed equilibrium melt distributions in agreement with those predicted by theory (e.g. Waff and Bulau, 1979; Jurewicz and Watson, 1984, 1985; von Bargen and Waff, 1988; Laporte, 1994); moreover, measured values of the dihedral angle range between 30° and 60° (Cheadle, 1989, and references therein), a result which has been used as evidence that a partially molten rock matrix is likely to be permeable if local equilibrium is maintained during melting and melt segregation. However, the crystalline anisotropy of the grains in partially molten rocks, and the polymineralic nature of the matrix, may play a more important role than the magnitude of the dihedral angle in dictating equilibrium melt interconnectivity (Waff and Faul, 1992). Moreover, even if local equilibrium is not achieved, the melt may still be interconnected. In an experimental study of a partially molten amphibolite, Wolf and Wyllie (1991) found that, despite the failure to achieve an equilibrium melt distribution, melt interconnectivity along grain edges was achieved for melt fractions of <0.02 and above. They suggested that the melt distribution was dictated predominantly by the morphologies and distribution of hornblende and plagioclase crystals.

Although the majority of models of melt segregation in the continental crust have assumed that the partially molten rock matrix is permeable at the grain edge scale, the origin of the pressure gradient invoked to drive melt segregation has differed. Models based on theoretical studies of melt segregation in the mantle have assumed that the pressure gradient is due to the buoyancy of the melt; models based on field studies of exposed crustal terrains have assumed that the pressure gradient results from the deformation of an anisotropic protolith (Brown, 1994).

2.3.4 Previous models of melt segregation in the continental crust

The paradox that models of melt segregation must resolve, is that the available evidence suggests that granitic melts correspond to small degrees of melting, and are extracted from partially molten rocks in which the solid fraction maintains an interconnected matrix (i.e. melt fractions are *less* than the CMF), yet a mobile magma is produced only if the connectivity of the matrix breaks down (i.e. melt fractions are *greater* than the CMF). How then does a small, granitic partial melt fraction become mobilised? The existing models of melt segregation in the continental crust will be reviewed, and their failure to resolve this paradox highlighted.

2.3.4.1 Buoyancy driven melt segregation

Several workers have presented the equations governing conservation of heat, mass, and momentum, which are required to quantitatively describe buoyancy driven melt segregation from a permeable rock matrix (McKenzie, 1984; Scott and Stevenson, 1984, 1986). The equations are a macroscopic continuum approximation of the system, valid for lengthscales which are much larger than the characteristic spacing of the liquid channels, and smaller than any characteristic variation in porosity (Speigelman, 1993). They are a special case of the general equations governing liquid migration through a permeable mush, which are well established in the engineering and metallurgical literature (e.g. Hills *et al.*, 1983; Bennon and Incropera, 1987a, 1987b; Beckerman and Viskanta, 1988). However, models developed in the engineering and metallurgy literature are not directly applicable to geological systems, because they assume the matrix is rigid. A partially molten rock matrix is not rigid, because melt enhanced diffusional creep processes provide a mechanism for changing the morphology of the solid matrix, so that on a macroscopic scale the matrix may viscously deform in response to melt transport (e.g. Pharr and Ashby, 1983; Cooper and Kohlstedt, 1984, 1986; Hollister and Crawford, 1986; Karato *et al.*, 1986; Dell'Angelo *et al.*, 1987, Dell'Angelo and Tullis, 1988; Wheeler, 1992; Kohlstedt and Chopra, 1994). Melt migration along grain edges, accompanied by matrix deformation, is often termed *compaction*. As melt migrates out of a region, the solid matrix viscously deforms and *compacts* to occupy the space previously occupied by melt; conversely, if melt migrates into a region the matrix *dilates* to accommodate it.

The equations of McKenzie (1984), and Scott and Stevenson (1984, 1986), have been used to develop numerous quantitative models of melt segregation in the mantle (e.g. Scott and Stevenson, 1986; Ribe and Smooke, 1987: Spiegelman and McKenzie, 1987; Wiggins and Spiegelman, 1995); in contrast, only a simplified model examined by McKenzie (1984), and Richter and McKenzie (1984), has been applied to the crust. They investigated a subset of the equations governing compaction, which describe the behaviour of a deformable, porous, permeable mush of thickness *h*, with initially uniform liquid volume fraction ϕ (the porosity), when placed on an impermeable surface. Liquid and matrix are individually conserved; hence, as Richter and McKenzie (1984) point out, this is not, strictly speaking, a model of *melt* segregation. The buoyant liquid migrates upwards through the permeable matrix, and is expelled from the top, whilst the matrix compacts within a boundary layer at the base (figure 2.1). The fundamental time and length scales of this process are the compaction length δ:

$$\delta = \left(\frac{\left(\xi_s + \frac{4}{3}\mu_s\right)K}{\mu_l} \right)^{1/2} \tag{2.1}$$

and the characteristic compaction time required to reduce the amount of liquid in the deformable mush by a factor e:

$$t_h = \frac{h\mu_l\phi}{K(1-\phi)^2(\rho_s-\rho_l)g} \tag{2.2}$$

(see table 2.2 for a list of the terms used). The compaction length is obtained by solving the governing equations analytically, and describes the initial thickness of the compacting layer (McKenzie 1984, 1985, 1987; Richter and McKenzie, 1984). The characteristic compaction time, valid when $h \gg \delta$, is a simplification of an analytic expression which agrees well with numerical results (Richter and McKenzie, 1984). These equations have been used to assess the viability of buoyancy driven compaction as a segregation mechanism in the crust (Wickham, 1987b; Wolf and Wyllie, 1991, 1994; Petford, 1995). The common approach has been to equate the initial liquid volume fraction ϕ, with the melt content of the source region; for a melt of granitic composition, $\phi \sim 0.05 - 0.4$ (table 2.1). The compaction length (δ) is then used to estimate the maximum thickness of a partial melt zone from which melt is likely to segregate by compaction, whilst the characteristic compaction time (t_h) is used to estimate the time required for melt to segregate from a partial melt zone of thickness *h*. Figure 2.2 shows the compaction length as a function of initial liquid fraction for a typical granitic melt-restite system. For liquid viscosities $>10^4$ Pa s, the compaction length has a maximum value of ~220m, which is at least an order of magnitude smaller than a partial melt zone capable of generating batholithic quantities of granitic magma. Figure 2.3 shows the characteristic compaction time as function of initial liquid fraction. For liquid viscosities $>10^4$ Pa s, the estimated

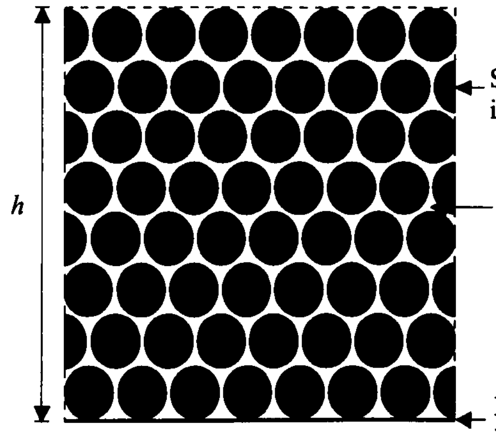

Solid matrix grains, interconnected in three dimensions.

Buoyant liquid phase, interconnected along grain edges in three dimensions.

Impermeable surface at base of layer.

Figure 2.1(a). Initial distribution of solid and liquid phases at time t=0.

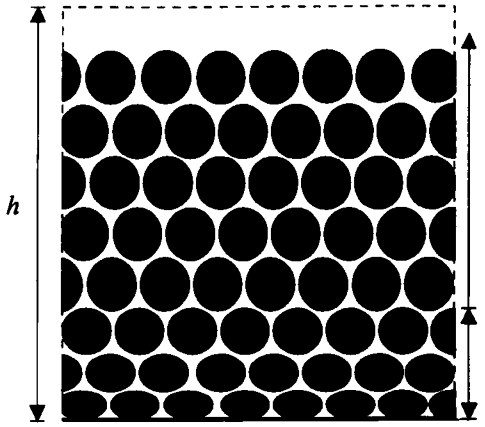

Liquid is expelled from the top of the compacting material.

Buoyant liquid migrates upwards through the permeable matrix.

The solid matrix compacts above the impermeable base within a boundary layer of thickness δ.

Figure 2.1(b). Distribution of solid and liquid phases at small times (t<<1).

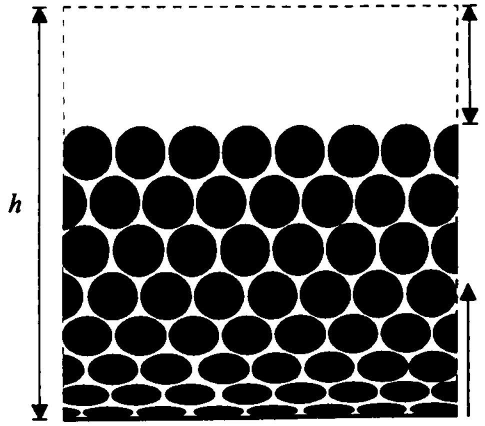

Layer of 'segregated' liquid above compacting layer.

Compacting boundary layer at base increases in thickness as liquid migrates upwards.

Figure 2.1(c). Distribution of solid and liquid phases at large times (t>1).

Figure 2.1. The evolution through time of a layer of porous, permeable, deformable material of thickness *h*, when placed on an impermable surface. Liquid and solid are individually conserved; the liquid phase is buoyant relative to the solid. After Richter and McKenzie (1984).

Symbol	Description	Units
t	Time.	s
h	Layer thickness.	m
δ	Compaction length: the thickness of the compacting boundary layer soon after the onset of compaction ($t << 1$).	m
K	Initial (uniform) permeability of material before onset of compaction ($t = 0$).	m^2
ξ_s	Bulk viscosity of the deformable solid matrix.	Pa s
μ_s	Shear viscosity of the deformable solid matrix.	Pa s
μ_l	Shear viscosity of the liquid.	Pa s
t_h	Characteristic compaction time: the time required to reduce the total liquid content of the layer from $h\phi$ to $h\phi/e$.	s
ϕ	Initial (uniform) liquid content of material before the onset of compaction ($t = 0$), expressed as a liquid volume fraction.	dimensionless
$\rho_s - \rho_l$	Density contrast between melt and matrix.	kg m^{-3}
g	Acceleration due to gravity.	ms^{-2}

Table 2.2. Nomenclature for the buoyancy driven compaction model (after McKenzie, 1984, 1985; Richter and McKenzie, 1984).

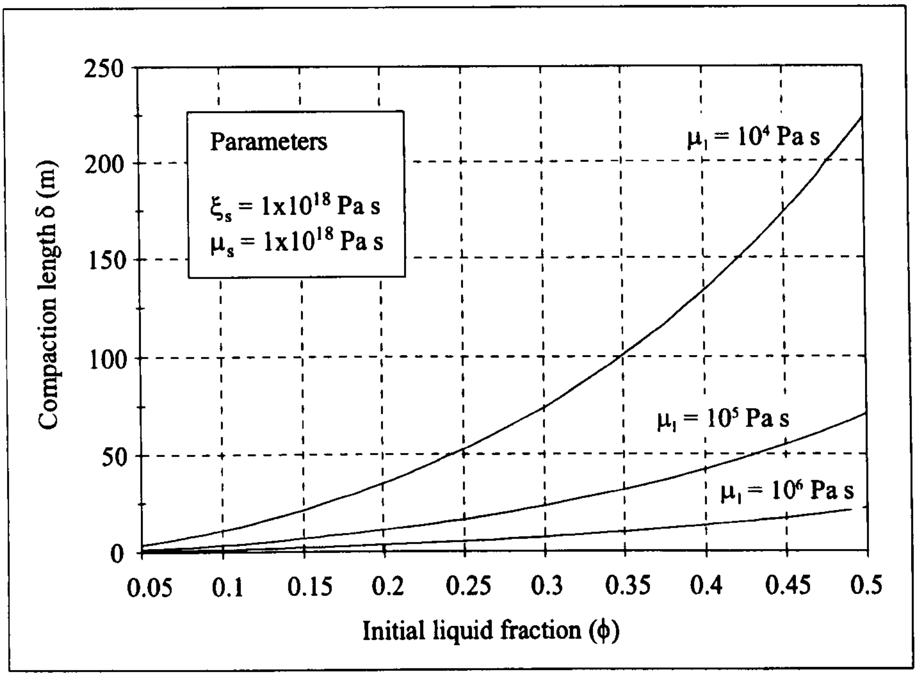

Figure 2.2 Compaction length versus initial liquid fraction, calculated using parameters suitable for a granitic melt-restite layer (Wickham, 1987b; Petford, 1995). The compaction length is short compared to the size of a melt zone in the crust. Permeability was calculated using the Blake-Cozeny-Carman relation given in McKenzie (1984), using a grain size (diameter) of 1mm.

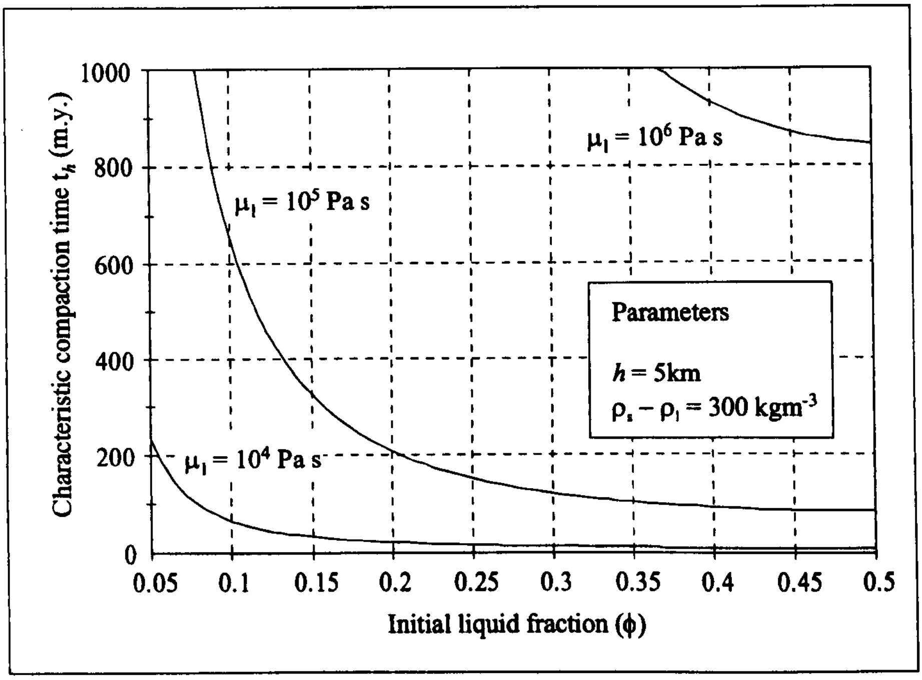

Figure 2.3. Characteristic compaction time versus initial liquid fraction, calculated using parameters suitable for a granitic melt-restite layer (Wickham, 1987b; Petford, 1995). Segregation times are high, except for low melt viscosities. Permeability was calculated using the Blake-Kozeny-Carman relation given in McKenzie (1984), using a grain size (diameter) of 1mm.

time for segregation is >10 m.y., and ranges up to >>1000 m.y. for liquid viscosities >10^6 Pa s. In contrast, quantitative models of crustal melting, as a result of both intra/underplating and crustal thickening/thinning (§2.2.3), predict that the maximum duration of a crustal melting event is <20-30 m.y. From this evidence, both Wickham (1987b) and Petford (1995) conclude that, for typical granitic melt viscosities ($\mu \sim 10^4$-10^7 Pa s), the melt will freeze before it can segregate from the source rock, and that, except for high degrees of partial melting, buoyancy driven compaction alone is not a viable segregation mechanism in the crust except over short (cm-m) lengthscales. The conclusions of Wolf and Wyllie (1991, 1994) are generally in agreement, although they suggest that segregation by compaction may occur for particularly low melt viscosities (<10^4 Pa s).

Several workers have proposed that buoyancy driven melt segregation may operate efficiently in the crust if a pervasive network of interconnected fractures is present in the partially molten protolith (Clemens and Mawer, 1992; Petford, 1995). A fracture network provides a high permeability network through which melt may rapidly migrate; melt is assumed to flow along grain edges only into the nearest fracture. This is a potential segregation mechanism originally suggested by Sleep (1988) for melt segregation in the mantle beneath mid-ocean ridges. However, he did not present a complete quantitative description of a fractured partial melt zone, and his approach cannot be directly applied to the crust, because the deviatoric stress field beneath a mid-ocean ridge differs from that in the crust. As yet, only qualitative or semi-quantitative models of melt migration through a fracture network have been presented for crustal melt zones. The detailed dynamics of melt flow along grain edges, fracture nucleation and growth, and melt flow through fractures, and the interplay of pressure gradients as the system evolves through time, have not been explicitly considered. Moreover, the formation a magma which can migrate away from the source region, and the composition of the magma, have also not been explicitly considered. Buoyancy driven melt segregation through fractures may be an effective mechanism in the continental crust, but the evidence as yet is inconclusive.

2.3.4.2 Migmatites and deformation enhanced melt segregation

An alternative approach to the problem of granitic melt segregation is based on the study of migmatites. Read (1957) was amongst the first to propose that high grade migmatite terrains represent the "birth zones of granite", and migmatites have the advantage of being exposed for field study. Several workers (e.g. Sawyer, 1991, 1994; Brown, 1994; Brown *et al.*, 1995) have proposed models of melt segregation based on studies of migmatites, which invoke deformation rather than buoyancy as the dominant driving force for melt migration. Melt is assumed to flow along grain edges, collecting in dilatant sites such as shear bands, tension gashes, and boudins. However, several workers have suggested that studies of migmatites do not lead to a greater understanding of the processes which lead to the formation of a mobile granitic magma, because migmatites represent '*failed*' granites. They argue that migmatites are produced when the granitic melt remains trapped in the source region as leucosome, rather than escaping to higher crustal levels (e.g. White and Chappell, 1990; Clemens and Mawer, 1992).

2.3.4 Summary

When a rock partially melts, the solid fraction maintains an interconnected crystalline matrix until the melt volume fraction reaches the Critical Melt Fraction (CMF), which denotes the melt fraction at which the solid matrix disaggregates, and a mobile magma forms. In order to form a *granitic* magma, a granitic partial melt fraction *must* segregate to some extent from its restite; field and experimental evidence indicates that granitic melt must usually segregate in the source region *before* magma mobilisation, from partially molten rock in which the solid fraction maintains an interconnected matrix. Models of granitic melt segregation and mobilisation must therefore resolve the paradox that segregation appears to occur at melt fractions which are less than the CMF, yet mobilisation can occur only at melt fractions which are greater than the CMF. How does a small, granitic partial melt fraction form a mobile magma? Previous models of melt segregation in the continental crust have failed to resolve the paradox; moreover, they have failed to answer the questions posed in Chapter 1.

2.4 The need for a quantitative, coupled model of melt generation and segregation in the continental crust

Most previous models of melt generation and segregation in the continental crust have treated them as separate processes. Models of melt generation consider the thermal conditions required to produce granitic melt, and calculate the static volumes of melt produced if no melt migration occurs (e.g. Clemens and Vielzuf, 1987; Bergantz, 1989; Patiño Douce *et al.*, 1990). Conversely, models of melt segregation assume a pre-existing melt distribution, and then model how this melt migrates or becomes mobilised (e.g. Richter and McKenzie, 1984; McKenzie, 1985). Often the chosen melt distributions are unrealistic. For instance, use of equations (2.1) and (2.2) to evaluate compaction in the crust assumes the entire source region is melted uniformly and simultaneously, with no movement of melt during melting, yet thermal modelling indicates that melt distributions will not be uniform (e.g. Yoder, 1990; Bergantz and Dawes 1994). Melt generation and segregation in the continental crust are complementary, coupled processes which occur simultaneously, and a new physical model is required which is capable of describing them *quantitatively* as such. Moreover, the model must be able to produce results which answer, or at least constrain the answers to, the questions posed in chapter 1.

Chapter 3: A general continuum model for the transport of heat, mass, and momentum in a deformable, multicomponent mush undergoing solid-liquid phase change.

"*A central question is, how easily can liquid separate out from crystal mush?*" **(Pitcher, 1993, p. 104)**

3.1 Introduction

Most silicate rock types are complex, non-eutectic, multicomponent substances which undergo solid-liquid phase[1] change over a temperature and pressure range, leading to the formation of a mixed phase region, such as a partial melt zone, in which both solid and liquid phases coexist. If the phases are mobile, then during phase change they may migrate relative to one another, resulting in their partial or complete separation; this occurs when melt segregates from a melting rock, or crystals separate from a solidifying magma. These coupled, multicomponent, phase change and phase transport processes are of fundamental importance in the Earth sciences, because they are responsible for the origin and chemical diversity of all the igneous rocks.

Interest in binary and multicomponent phase change processes spans a range of scientific and engineering disciplines outside of the Earth sciences, including metallurgy and materials science, and has motivated the development of an increasing number of quantitative transport models (e.g. Loper and Roberts, 1978; Hills *et al.*, 1983; Bennon and Incropera, 1987a, 1987b; Beckerman and Viskanta, 1988; Hills and Roberts, 1988). Most of these concern binary phase change systems such as metallic alloys, and have been applied to solidification processes such as casting and welding (e.g. Clyne, 1982; Viskanta, 1988). In contrast, few quantitative coupled models of phase transport during multicomponent melting have been developed. Those which are available in the engineering literature cannot be directly applied to geological systems, because of differences in the initial and boundary conditions of the mixed phase region (Bergantz, 1992), and because they assume that the solid matrix forms a *rigid* mush. In a partially molten rock, the solid matrix does not form a rigid mush; liquid enhanced creep processes provide a mechanism for changing the morphology of the solid matrix at the microscopic scale, which means that the solid matrix may viscously deform in response to the migration of liquid at the macroscopic scale (e.g. Pharr and Ashby, 1983; Cooper and

---

[1] In this context, *phase* refers to the solid or liquid (melt), rather than to solid phases. Solid phases are referred to as *components*.

Kohlstedt, 1984, 1986; Hollister and Crawford, 1986; Karato *et al.*, 1986; Dell'Angelo *et al.*, 1987, Dell'Angelo and Tullis, 1988; Wheeler, 1992; Kohlstedt and Chopra, 1994; see also §2.3.4.1).

Previous quantitative models of liquid transport through a melting, *deformable* mush have decoupled the phase change and phase transport processes. Either a simple initial distribution of liquid is imposed, and the subsequent migration of the liquid is modelled in the absence of phase change, or a simple rate of phase change is imposed, which is not coupled to the local thermodynamic conditions (§2.4). However, whilst this may be a valid approach for modelling melting and melt segregation in the mantle (e.g. Scott and Stevenson, 1986; Ribe and Smooke, 1987: Spiegelman and McKenzie, 1987; Sparks and Parmentier, 1991; Wiggins and Spiegelman, 1995), it is not valid for models of melting and melt segregation in the crust, because melting and melt segregation are *complementary* processes which occur simultaneously (§2.4).

The aim of this chapter is to develop a new, quantitative, coupled physical model of phase change and phase transport in a deformable mush, which may be applied to the problem of melt segregation from a melting rock in the continental crust. Melting of the rock will be assumed to be due to heating from below, following the emplacement of hot, mantle derived magma; in the crust, this may be as a result of either basaltic intra/underplating, asthenospheric upwelling, or a combination of these processes (§2.2). Heating of the rock and cooling of the magma are conjugate processes which should, and subsequently will, be modelled simultaneously (Bergantz, 1992; see chapter 5); however, in this chapter cooling of the magma will be neglected, so as not to obscure the processes which occur in the partially molten rock. Only the mathematical and physical details of the model will be considered; a discussion of the choice of geologically relevant parameters is deferred until the model is applied to specific geological systems in chapters 4 and 5.

The partially molten rock is described in general terms as a viscously deformable, multicomponent mush which is being heated from below. The liquid[2] phase is assumed to be both interconnected along grain edges, and compositionally and thermally buoyant, leading to relative phase migration (§2.3.3). The system is complex because compositional gradients exist in both phases, and the phases may interact and exchange components during phase transport (Lowell and Bergantz, 1987). A continuum approach is adopted, because continuum formulations are well suited for modelling the transition between solid and liquid phases over a temperature and pressure interval, with associated latent heat evolution and coupled transport processes (Bennon and Incropera, 1987a). Although motivated by a geological problem, the formulation presented in this chapter may be applied to any melting, multicomponent mush in which fluid migration coupled with solid deformation is an important process, and which satisfies the assumptions made in deriving the governing equations.

---

[2] As befits a general model, the term liquid rather than melt will be used throughout this chapter, except when a specifically geological context is implied.

3.2 Model Formulation

Consider a homogenous, isotropic, multicomponent material which is initially at its solidus temperature T_{sol}, and which is semi-infinite in the positive z (vertical) direction. At t = 0 the temperature of the z = 0 plane is instantaneously increased to a temperature T_b which is greater than the solidus of the overlying material, and is subsequently maintained at this temperature for all time (figure 3.1). Solid-liquid phase change in the material leads to the formation of a mushy mixed phase region adjacent to the z=0 plane. The liquid phase produced is buoyant and interconnected along grain edges; the solid phase can viscously deform in response to liquid phase transport. Liquid and solid phases are assumed always to be in local thermodynamic equilibrium.

3.2.1 Governing equations

The equations governing conservation of mass, energy, and momentum in the mixed phase region are presented in Cartesian coordinates throughout, with z positive upwards.

Assuming there are no void spaces or other phases present in the mixed phase region, the statement of conservation of mass of the liquid and solid phases may be expressed in terms of the liquid volume fraction (porosity) ϕ as (Loper and Roberts, 1978; Hills *et al.*, 1983; McKenzie, 1984; Bennon and Incropera, 1987a; Beckerman and Viskanta, 1988; Hills and Roberts, 1988)

$$\frac{\partial}{\partial t}(\rho_l \phi) + \nabla.(\rho_l \phi \mathbf{v}_l) = \Gamma_l \tag{3.1}$$

$$\frac{\partial}{\partial t}(\rho_s(1-\phi)) + \nabla.(\rho_s(1-\phi)\mathbf{v}_s) = -\Gamma_l \tag{3.2}$$

(see table 3.1 for the nomenclature).

Neglecting kinetic energy, the rate at which surface stresses do work on the solid and liquid, the work done by body forces, and assuming there is no internal heat production, and given that the mixed phase region is assumed to be in local thermodynamic equilibrium, the statement of conservation of energy in the mixed phase region may be expressed as (McKenzie, 1984; Bennon and Incropera, 1987a)

$$\nabla.(k_m \nabla.T) = L\Gamma_l + \left[(1-\phi)\rho_s c_p^s + \phi \rho_l c_p^l\right]\frac{\partial T}{\partial t} + (1-\phi)\rho_s c_p^s \mathbf{v}_s.\nabla T + \phi \rho_l c_p^l \mathbf{v}_l.\nabla T \tag{3.3}$$

with

$$k_m = (1-\phi)k_s + \phi k_l \tag{3.4}$$

Derivation of the statement of conservation of linear momentum in the mixed phase region requires specific consideration of its structure and rheology. Assuming that the pressures in the solid and

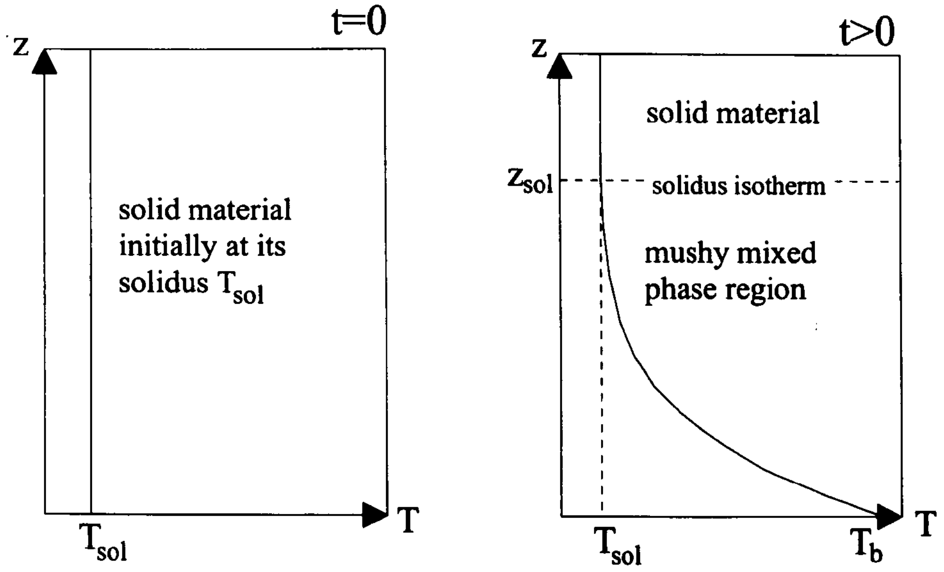

Figure 3.1. The development of a mushy mixed phase region due to heating from below. At t=0, the temperature at z=0 is increased from T_{sol} to T_b, and maintained at the new temperature T_b for all time.

Symbol	Description	Units
a	solid phase grain radius	m
b	constant in permeability relationship	None
c_p	specific heat capacity	J kg^{-1} K^{-1}
c_{eff}	effective specific heat capacity	J kg^{-1} K^{-1}
c_p^l	specific heat capacity of liquid phase	J kg^{-1} K^{-1}
c_p^s	specific heat capacity of solid phase	J kg^{-1} K^{-1}
C	dimensionless compaction rate	None
D_i	normalised difference between the ith isotherms	None
g	acceleration due to gravity	m s^{-2}
$\mathbf{I}$	interphase force per unit volume	N m^{-3}
k	thermal conductivity	W K^{-1} m^{-1}
k_l	thermal conductivity of liquid phase	W K^{-1} m^{-1}
k_s	thermal conductivity of solid phase	W K^{-1} m^{-1}
k_m	thermal conductivity of mixture	W K^{-1} m^{-1}
k	permeability	m^{-2}
K	characteristic permeability	m^{-2}
$\hat{k}$	unit vector in the vertical	None
L	latent heat	J kg^{-1}
n	exponent in permeability relation	None
P	pressure	Pa
Ste	Stefan number	None
t	time	s
T	temperature	K
T_b	temperature at $z = 0$	K
T_{sol}	solidus temperature	K
T_{liq}	liquidus temperature	K
$\mathbf{v}_l$	liquid phase velocity vector	m s^{-1}
$\mathbf{v}_s$	solid phase velocity vector	m s^{-1}
$\mathbf{v}_m$	mixture velocity vector	m s^{-1}
w_l	vertical component of liquid phase velocity	m s^{-1}
w_s	vertical component of solid phase velocity	m s^{-1}
w_m	vertical component of mixture velocity	m s^{-1}
z	vertical Cartesian coordinate	m
z_{sol}	position of solidus isotherm	m
z_0	position of dimensionless solidus isotherm ($\theta = 0$)	None
δ	characteristic lengthscale (McKenzie's compaction length)	m
ϕ	liquid volume fraction (porosity)	None
φ	dimensionless temperature at $z = 0$	None
Γ_l	rate of production of liquid phase	kg m^{-3} s^{-1}
κ_{eff}	dimensionless effective thermal diffusivity	None
μ_l	liquid shear viscosity	Pa s
μ_s	solid matrix shear viscosity	Pa s
ν_l	equilibrium liquid volume fraction	None
ν_b^l	equilibrium liquid volume fraction at $z = 0$	None
θ	dimensionless temperature	None
ρ	density	kg m^{-3}
ρ_l	density of liquid phase	kg m^{-3}
ρ_s	density of solid phase	kg m^{-3}
ρ_m	density of mixture	kg m^{-3}
σ_l	stress tensor in the liquid phase	Pa
σ_s	stress tensor in the solid phase	Pa
ω	characteristic velocity scale	m s^{-1}
τ	characteristic timescale	s
ξ_s	solid matrix bulk viscosity	Pa s

Table 3.1. Nomenclature for chapter 3.

liquid phases are equal, that both phases may be treated as Newtonian fluids which are incompressible at the microscale, that the rate of change of momentum in each can be neglected, that the Reynolds number of each is small compared to unity, and that the body force acting upon each phase is due only to gravity, then conservation of linear momentum in the liquid and solid may be expressed as (Bennon and Incropera, 1987a)

$$\nabla.(\phi\sigma_l)-\rho_l\phi g\hat{k}-\mathbf{I}=0 \tag{3.5}$$

$$\nabla.((1-\phi)\sigma_s)-\rho_s(1-\phi)g\hat{k}+\mathbf{I}=0 \tag{3.6}$$

Note that the interphase force per unit volume (**I**) acting upon the solid is equal and opposite to that acting upon the liquid, and so satisfies Newton's third law (Prescott *et al.*, 1991). The interphase force per unit volume may be expressed as

$$\mathbf{I}=C(\mathbf{v}_l-\mathbf{v}_s)-P\nabla\phi \tag{3.7}$$

where the value of C depends upon the distribution of phases within the mixed phase region (McKenzie, 1984). Substituting equation (3.7), and the standard equation for the stress tensor within an incompressible fluid (Landau and Lifshitz, 1987) into equation (3.5), and simplifying, yields

$$\mathbf{v}_l-\mathbf{v}_s=-\frac{\phi}{C}\nabla(P+\rho_l gz) \tag{3.8}$$

If $\mathbf{v}_s = 0$ then equation (3.8) corresponds to D'Arcy's law with

$$C=\mu_l\phi^2/k \tag{3.9}$$

The deformable solid matrix will expel the liquid phase if subjected to isostatic compression, and may be treated at the macroscopic scale as a viscous, compressible fluid (McKenzie, 1984; Scott and Stevenson, 1986). Substituting equations (3.7), (3.9), and the standard equation for the stress tensor within a compressible fluid (Landau and Lifshitz, 1987) into equation (3.6), and simplifying assuming that the bulk and shear viscosities of the matrix are constant, yields

$$\nabla(P+\rho_l gz)=\left(\xi_s+\tfrac{1}{3}\mu_s\right)\nabla(\nabla.\mathbf{v}_s)+\mu_s\nabla^2\mathbf{v}_s-(1-\phi)(\rho_s-\rho_l)g\hat{k} \tag{3.10}$$

Summation of equations (3.8) and (3.10), having substituted for C in equation (3.8) using equation (3.9), yields the statement of conservation of linear momentum in the mixed phase region, valid if the liquid volume fraction does not exceed the CMF (McKenzie, 1984)

$$\left(\xi_s+\tfrac{1}{3}\mu_s\right)\nabla(\nabla.\mathbf{v}_s)=\frac{-\mu_l\phi}{k}(\mathbf{v}_l-\mathbf{v}_s)-\mu_s\nabla^2\mathbf{v}_s+(1-\phi)(\rho_s-\rho_l)g\hat{k} \tag{3.11}$$

Practical use of this expression requires that the permeability of the solid matrix be specified. Generally, for an isotropic matrix, permeability may be related to porosity by an equation of the form

$$k=\mathrm{b}\mathrm{a}^2 f(\phi) \tag{3.12}$$

where b is a constant, and a is the radius of the solid grains (Bear, 1972). The form of $f(\phi)$ and value of b depend upon the microscopic distribution of the liquid phase. Several expressions for $f(\phi)$ have been proposed (e.g. Bear, 1972; Scott and Stevenson, 1986); a simple, commonly used form, based on the Blake-Kozeny-Carman equation, yields the permeability-porosity expression

$$k = \mathrm{b}\mathrm{a}^2\phi^{\mathrm{n}} \tag{3.13}$$

where n varies between 2 and 3 (Scott and Stevenson, 1986).

3.2.2 Phase compositions and the rate of phase change

To close the system of conservation equations, the rate of phase change and the composition of each phase must be specified. The rate of phase change is dictated by the rate at which the phases experience changing thermodynamic conditions; in this system, a phase may experience changing thermodynamic conditions both because the conditions throughout the mixed phase region are changing temporally, and because the phases are migrating through conditions which vary spatially. Migration may occur because the mixture itself is mobile, and because the phases migrate relative to the mixture. Consequently, the net rate of change of thermodynamic conditions experienced by the phases at any point is given by

$$\dot{f}(\mathrm{P},\mathrm{T}) = \frac{\partial}{\partial t}\left(f(\mathrm{P},\mathrm{T})\right) + \left(\mathbf{v}_l + \mathbf{v}_s - \mathbf{v}_m\right).\nabla\left(f(\mathrm{P},\mathrm{T})\right) \tag{3.14}$$

where $\mathbf{v}_m$ is the mass averaged mixture velocity

$$\mathbf{v}_m = \rho_l\phi\mathbf{v}_l/\rho_m + \rho_s(1-\phi)\mathbf{v}_s/\rho_m \tag{3.15}$$

and the mixture density is given by

$$\rho_m = \phi\rho_l + (1-\phi)\rho_s \tag{3.16}$$

If a system is in local thermodynamic equilibrium, phase change may be related to the thermodynamic conditions by a suitable equilibrium phase diagram or phase distribution curve (Hills *et al.*, 1983; Bennon and Incropera, 1987a, 1987b; Hills and Roberts, 1988; Bergantz, 1992). Phase distribution curves give the volume fraction and composition of each phase present at given thermodynamic conditions; they have been derived for several commonly occurring silicate rock types (e.g. Rutter and Wyllie, 1988; Vielzuf and Holloway, 1988; Patiño Douce and Johnston, 1991; Rushmer, 1991; Beard and Lofgren, 1991; Rapp and Watson, 1995). Once the equilibrium liquid volume fraction ν_l is known as a function of the thermodynamic conditions, equation (3.14) may be rewritten in terms of $\rho_l\nu_l$, and the rate of solid-liquid phase change is given by

$$\Gamma_l = \dot{f}(\mathrm{P},\mathrm{T}) = \frac{\partial}{\partial t}\left(\rho_l\nu_l\right) + \left(\mathbf{v}_l + \mathbf{v}_s - \mathbf{v}_m\right).\nabla\left(\rho_l\nu_l\right) \tag{3.17}$$

The second term on the right hand side of equation (3.17) demonstrates that relative phase transport coupled with local thermodynamic equilibration leads to component exchange between solid and liquid phases. A full continuum description of a multicomponent system would strictly require an explicit statement of conservation of mass for each component, but for most geological materials this would lead to a prohibitive increase in the complexity of the formulation due to the large number of components present (Bergantz, 1992). In the system discussed here, phase compositions are fixed by the requirement of local thermodynamic equilibrium, and may be deduced at given thermodynamic conditions using empirical data derived from equilibrium melting experiments. Consequently, an explicit description of mass conservation for each component is not given. This approach is no less rigorous than one in which macroscopic continuum equations for each component are explicitly stated, because in the absence of an atomic level description of the system, component exchange must in any case be deduced from empirical data (Hills *et al.*, 1983; Bennon and Incropera, 1987a, 1987b; Hills and Roberts, 1988).

3.2.3 A one-dimensional Boussinesq model of the mixed phase region

Equations (3.1), (3.2), (3.3), (3.11), (3.13) and (3.17) together with the necessary empirical data represent a complete description of the system, but the task of solving them in their current form would be considerable. At this stage, in order to identify the generic features of the system, a simplified one dimensional (1-D) subset of the governing equations will be considered, and the solutions investigated numerically. An understanding of the essential physics may then lead to the solution of more complex formulations.

Expressed only in terms of vertical velocity components, the governing equations become

$$\frac{\partial}{\partial t}(\rho_l\phi)+\frac{\partial}{\partial z}(\rho_l\phi w_l)=\Gamma_l \tag{3.18}$$

$$\frac{\partial}{\partial t}(\rho_s(1-\phi))+\frac{\partial}{\partial z}(\rho_s(1-\phi)w_s)=-\Gamma_l \tag{3.19}$$

$$\frac{\partial}{\partial z}\left(k_m\frac{\partial T}{\partial z}\right)=L\Gamma_l+\left[(1-\phi)\rho_s c_p^s+\phi\rho_l c_p^l\right]\frac{\partial T}{\partial t}+(1-\phi)\rho_s c_p^s w_s\frac{\partial T}{\partial z}+\phi\rho_l c_p^l w_l\frac{\partial T}{\partial z} \tag{3.20}$$

$$\left(\xi_s+\tfrac{4}{3}\mu_s\right)\frac{\partial^2 w_s}{\partial z^2}=\frac{-\mu_l\phi}{k}(w_l-w_s)+(1-\phi)(\rho_s-\rho_l)g \tag{3.21}$$

$$\Gamma_l=\frac{\partial}{\partial t}(\rho_l\nu_l)+(w_l+w_s-w_m)\frac{\partial\rho_l\nu_l}{\partial z} \tag{3.22}$$

subject to the initial and boundary conditions

$$T(z,0)=T_{sol} \qquad \text{(3.23a),}$$

$$\phi(z,0)=\nu_l(z,0)=w_l(z,0)=w_s(z,0)=0 \qquad \text{(3.23b)}$$

$$T(0,t)=T_b \qquad T(z_{sol},t)=T_{sol} \qquad \text{(3.23c)}$$

$$\nu_l(0,t)=\nu_b^l \qquad \nu_l(z_{sol},t)=0 \qquad \text{(3.23d)}$$

$$w_l(0,t)=w_s(0,t)=w_l(z_{sol},t)=w_s(z_{sol},t)=0 \qquad \text{(3.23e)}$$

where ν_b^l denotes the equilibrium liquid volume fraction at $z = 0$, and z_{sol} denotes the time-dependant position of the solidus isotherm, which defines the 'top' of the mixed phase region (figure 3.1).

Applying the Boussinesq approximation, substituting equation (3.18) into equation (3.19), and integrating subject to the condition that $w_s = w_l = 0$ at $z = 0$ yields (McKenzie, 1984)

$$\phi w_l = -(1-\phi)w_s \tag{3.24}$$

Assuming that the thermodynamic properties of the solid and liquid are constant and identical, substituting equation (3.24) into equations (3.18)-(3.22), and simplifying yields

$$\rho\frac{\partial\phi}{\partial t} - \rho\frac{\partial}{\partial z}\left((1-\phi)w_s\right) = \Gamma_l \tag{3.25}$$

$$k\frac{\partial^2 T}{\partial z^2} = \rho c_p \frac{\partial T}{\partial t} + L\Gamma_l \tag{3.26}$$

$$\left(\xi_s + \tfrac{4}{3}\mu_s\right)\frac{\partial^2 w_s}{\partial z^2} = (1-\phi)(\rho_s - \rho_l)g + \frac{\mu_l w_s}{k} \tag{3.27}$$

$$\Gamma_l = \rho\frac{\partial v_l}{\partial t} + \rho(w_l + w_s)\frac{\partial v_l}{\partial z} \tag{3.28}$$

Note that in the heat conservation equation (3.26), the velocity terms which describe advective heat transport have now cancelled. Physically, this is because the upwards advection of hot liquid is exactly balanced by the downwards advection of cold solid; heat transport occurs only by conduction and latent heat exchange during phase change.

Phase change due to heating may be expressed as a function of temperature only (see §4.2.2), and for simplicity a linear variation of equilibrium liquid volume fraction with temperature will be used

$$v_l = \frac{T - T_{sol}}{T_{liq} - T_{sol}} \tag{3.29}$$

This is a reasonable approximation for a range of silicate rock types (Rutter and Wyllie, 1988; Vielzuf and Holloway, 1988; Patiño Douce and Johnston, 1991; Rushmer, 1991; Beard and Lofgren, 1991; Rapp and Watson, 1995; see also §4.2.2). In addition, latent heat will be assumed to be released linearly as phase change proceeds (Carslaw and Jaeger, 1986). A convenient scheme for non-dimensionalising temperature may be obtained from equation (3.29); by writing

$$T' = \frac{T - T_{sol}}{T_{liq} - T_{sol}} \tag{3.30}$$

the dimensionless temperature T' is numerically equivalent to the equilibrium liquid volume fraction v_l. In the interests of clarity, a new variable θ will be invoked which represents both these quantities; i.e. $\theta = T' = v_l$. Liquid volume fractions may be normalised by writing

$$\theta' = \theta/\varphi, \qquad \text{with } \varphi = \frac{T_b - T_{sol}}{T_{liq} - T_{sol}} \tag{3.31a}$$

$$\phi' = \phi/\varphi, \tag{3.31b}$$

where the scaling factor φ denotes both the equilibrium liquid volume fraction, and the dimensionless temperature, at z=0; i.e. $\varphi = T_b' = \nu_b^l$. Assuming a constant density contrast and liquid shear viscosity, the remaining variables may be non-dimensionalised by writing (McKenzie, 1984)

$$z' = z/\delta, \qquad \text{with } \delta = \left(\frac{(\xi_s + 4\mu_s/3)K}{\mu_l}\right)^{1/2} \tag{3.32}$$

$$t' = t/\tau, \qquad \text{with } \tau = \frac{1}{(1-\varphi)(\rho_s - \rho_l)g}\left(\frac{\mu_l(\xi_s + 4\mu_s/3)}{K}\right)^{1/2} \tag{3.33}$$

$$w' = w/\omega, \qquad \text{with } \omega = \frac{K(1-\varphi)(\rho_s - \rho_l)g}{\mu_l} \tag{3.34}$$

$$k' = k/K, \qquad \text{with } K = ba^2\varphi^n \tag{3.35}$$

where the characteristic lengthscale δ is the compaction length of McKenzie (1984, 1985). Substituting (3.29) into equation (3.28), substituting equation (3.28) into equations (3.25) and (3.26), substituting equation (3.13) into equation (3.27), substituting the scaled and dimensionless variables (3.31)-(3.35), simplifying, and dropping primes yields the dimensionless governing equations

$$\frac{\partial\phi}{\partial t} = \frac{1}{\varphi}\frac{\partial}{\partial z}\left((1-\varphi\phi)w_s\right) + \frac{\partial\theta}{\partial t} + (w_l + w_s)\frac{\partial\theta}{\partial z} \tag{3.36}$$

$$\frac{\partial\theta}{\partial t} = \kappa_{eff}\frac{\partial^2\theta}{\partial z^2} - Ste(w_l + w_s)\frac{\partial\theta}{\partial z} \tag{3.37}$$

$$\frac{\partial^2 w_s}{\partial z^2} = \frac{w_s}{\phi^n} + \frac{(1-\varphi\phi)}{(1-\varphi)} \tag{3.38}$$

$$\varphi\phi w_l = -(1-\varphi\phi)w_s \tag{3.39}$$

with

$$\kappa_{eff} = \frac{k\tau}{\rho c_{eff}\delta^2} \tag{3.40}$$

$$Ste = \frac{L}{c_{eff}(T_{liq} - T_{sol})} \tag{3.41}$$

$$c_{eff} = c_p + \frac{L}{T_{liq} - T_{sol}} \tag{3.42}$$

The liquid phase velocity w_l has not been eliminated using equation (3.39), because in this form, the effect of the net phase velocity ($w_l + w_s$) on the governing equations is clear. The initial and boundary conditions become

$$\theta(z,0) = \phi(z,0) = w_s(z,0) = w_l(z,0) = 0 \tag{3.43a}$$

$$\theta(0,t) = 1 \qquad \theta(z_0,t) = 0 \tag{3.43b}$$

$$w_s(0,t) = w_l(0,t) = w_s(z_0,t) = w_l(z_0,t) = 0. \tag{3.43c}$$

where z_0 denotes the position of the $\theta = 0$ isotherm.

As discussed by Bennon and Incropera (1987b), and Bergantz (1992), the results of binary and multicomponent phase change models are difficult to generalise, because of the large number of governing parameters and wide variety of naturally occurring equilibrium phase fraction distributions. Using suitable approximations, assuming a linear equilibrium liquid volume fraction distribution, and non-dimensionalising, the model description has been reduced to a system of four coupled equations in four unknowns, governed by four externally prescribed dimensionless parameters: κ_{eff}, Ste, n, and φ. The equations are amenable to solution using standard numerical techniques; in the next section the results are presented of numerical experiments designed to characterise, in terms of the externally prescribed dimensionless parameters, multicomponent phase change and phase transport in a deformable mush.

3.3 Results

Equations (3.36)-(3.39) were approximated using explicit finite difference schemes (Morton and Mayers, 1994), and solved numerically using FORTRAN codes (Press *et al.*, 1992) processed on a Sun SPARC 5 workstation. CPU times increased with increasing κ_{eff}, from several minutes to several tens of hours. Accuracy of the finite difference scheme for equation (3.37) was tested against a published analytic approximation to the solution of a diffusion-advection problem (Siemieniuch and Gladwell, 1978); accuracy of the scheme for equations (3.36) and (3.38) was tested against the published analytic solution for a solitary porosity wave with n=3, no phase change (Γ_l = 0), and in the limit of small background porosity (Barcilon and Richter, 1986). The implementation and testing of the finite difference schemes is described in Appendix A. All numerical experiments were performed using a value of n=3, to allow comparison with the analytic solution.

The numerical solutions were investigated for a variety of values of φ and Ste, over a fixed range of κ_{eff} between $\sim 10^{-8}$ and $\sim 10^{+8}$. This range is representative of most silicate rock phase change systems, and its size reflects the uncertainty in estimated values of the constant in the permeability relation (b), the liquid shear viscosity (μ_l), and the matrix bulk and shear viscosities (ξ_s and μ_s), all of which appear in the definition of κ_{eff} (equation (3.40)) (see §4.2.4.1 for a discussion of the magnitude of the uncertainty in the estimated values for these variables). Neither φ or Ste are independent of κ_{eff}; substituting equations (3.32) and (3.33) into equation (3.40) reveals that κ_{eff} varies with φ as

$$\kappa_{eff} \sim 1/(1-\varphi)\varphi^{9/2} \qquad (3.44)$$

while both Ste and κ_{eff} are governed by the values of the thermal parameters L, c_p, T_{liq} and T_{sol}. However, re-writing the expression for the Stefan number as

$$\mathrm{Ste} = \frac{L}{c_p\left(T_{liq} - T_{sol}\right) + L} \tag{3.45}$$

it is clear that it is constrained to lie between 0 and 1, whereas for a fixed value of Ste, κ_{eff} may still vary over effectively its entire range. Consequently, in all numerical experiments Ste is assumed to be independent of κ_{eff}.

3.3.1 Relative importance of conduction and pseudo-advection during heat transport

Models of heat transport within a mush often assume conduction is the dominant transport mechanism, implicitly assuming that phase transport has negligible effect on heat transport (e.g. Clyne, 1982; Viskanta, 1988; Bergantz, 1992). In the model presented here, phase transport affects heat transport due to the exchange of latent heat during local thermal equilibration, and is described in the energy conservation equation (3.37) by the second term on the right hand side, which is referred to as a 'pseudo-advection' term. Heat transport is governed externally by the dimensionless effective thermal diffusivity (κ_{eff}), and the Stefan number (Ste). The Stefan number represents the ratio of latent heat to effective specific heat during phase change; for Ste = 1 all heat is exchanged as latent heat, while for Ste = 0 all heat is absorbed as specific heat.

To assess the importance of phase transport on heat transport, the governing equations were solved with Ste = 1 (maximum pseudo-advection), and with Ste = 0 (conduction only). The difference between the resulting thermal profiles was measured as a function of κ_{eff} by recording the difference between the positions of selected isotherms, and normalising them to the conductive case

$$D_i = \frac{z_{i(\mathrm{Ste}=1)} - z_{i(\mathrm{Ste}=0)}}{z_{i(\mathrm{Ste}=0)}} \tag{3.46}$$

A value of $D_i = 0$ indicates that the isotherm positions are identical, and that heat transport is dominated by conduction, whilst a value of $D_i = 1$ indicates that they differ significantly and that heat transport is dominated by pseudo-advection. Figure 3.2 shows the normalised difference between the $z_{0.6}$, $z_{0.2}$, and z_0 isotherms after 30 time units, as a function of κ_{eff}, for three values of φ. In all cases, for large values of κ_{eff} heat transport is dominated by conduction. With decreasing κ_{eff}, pseudo-advection becomes increasingly important, and dominates for values of κ_{eff} in the range 10^{-7} - 10^{-2}. Conduction then becomes increasingly significant for small as well as large values of κ_{eff}. As φ decreases, the maximum in D_i occurs at larger values of κ_{eff}.

Lowell and Bergantz (1987) investigated heat transport in a deformable binary mushy zone heated from below, and concluded that in systems with large values of κ_{eff} (their 'dimensionless conduction lengthscale') and small values of Ste, heat transport is dominated by conduction, whilst in systems with small values of κ_{eff} and large values of Ste, heat transport is dominated by pseudo-advection

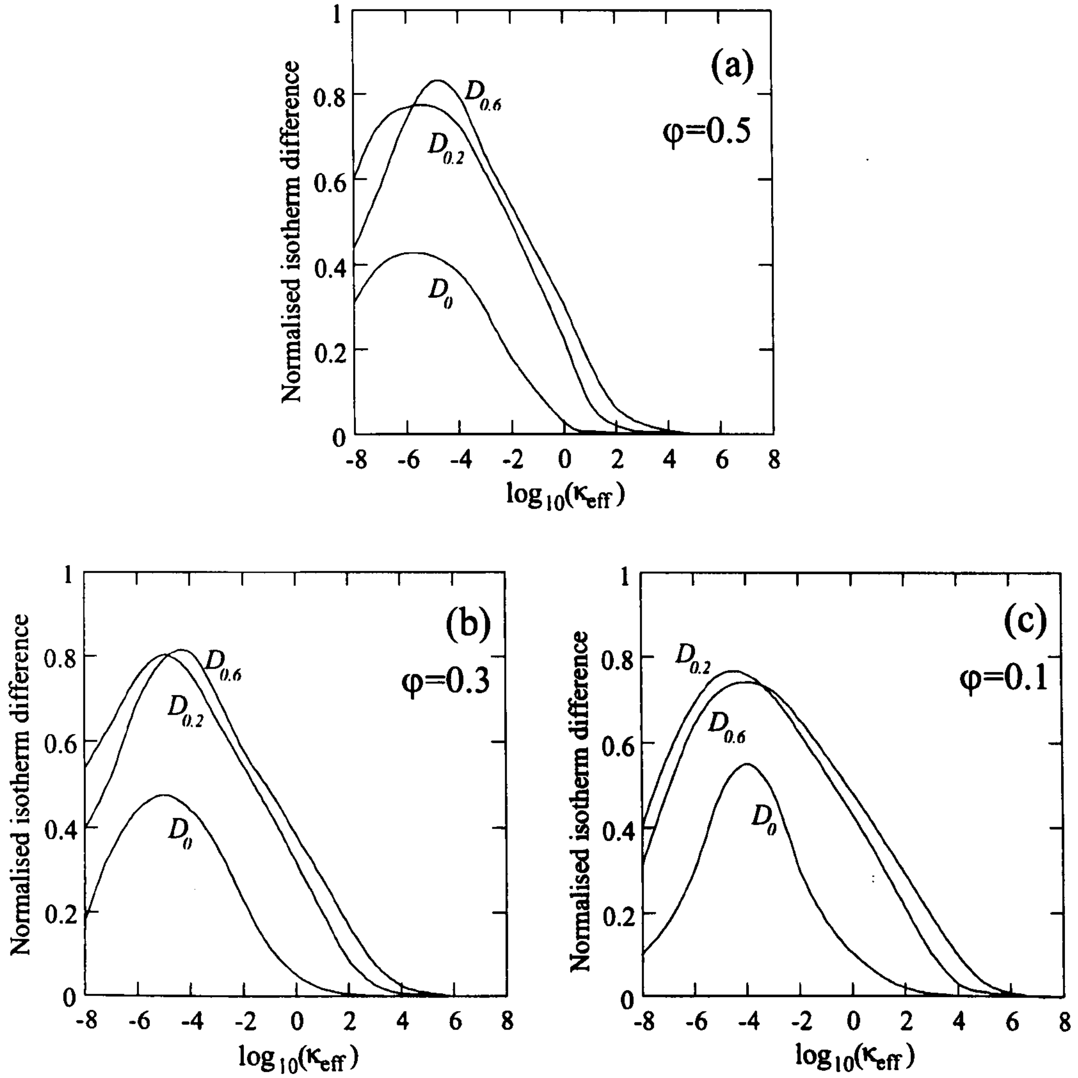

Figure 3.2. Normalised difference between the $z_{0.6}$, $z_{0.2}$, and z_0 isotherms for the Ste = 1 (maximum pseudo advection) and Ste = 0 (conduction only) cases, as a function of κ_{eff}, after 30 time units, with (a) $\varphi = 0.5$; (b) $\varphi = 0.3$; (c) $\varphi = 0.1$.

(their 'compaction dominated'). Their treatment neglects the effect of the net phase velocity (w_l+w_s) on the magnitude of the pseudo-advection term. As discussed in §3.2, the increasing significance of conduction in systems with *small* values of κ_{eff}, and the quantitative variation in the significance of pseudo-advection with decreasing φ, are both due to the effect of the net phase velocity.

3.3.2 Form of the liquid volume fraction (porosity) distributions

Figure 3.3(a-d) shows a representative selection of normalised spatial porosity (ϕ) and equilibrium liquid volume fraction (θ) distributions, for the case φ = 0.5, after 30 time units have elapsed. Note that the normalised equilibrium liquid volume fraction distribution denotes the predicted liquid volume fraction distribution in the *absence* of relative phase transport; it is also numerically equivalent to the normalised dimensionless temperature (§3.2.2).

In systems with large κ_{eff} ($\geq 10^5$), there is little difference between the porosity and the equilibrium liquid fraction distributions (figure 3.3(a)). In systems with κ_{eff} between $\sim 10^4$ and ~ 10, the upwardly migrating liquid develops a high amplitude 'porosity wave', and trailing porosity waves begin to develop behind the leading wave (figure 3.3(b)). In this range, as κ_{eff} decreases, the amplitude of the leading wave increases, and the position of the porosity maximum moves closer to z_0. In systems with κ_{eff} between ~ 10 and $\sim 10^{-3}$, the trailing waves are well developed, and display decreasing amplitude with depth (figure 3.3(c)). In this range, as κ_{eff} decreases, the amplitude of the leading wave decreases, the position of the porosity maximum moves closer to z_0, and the wave frequency increases. In systems with small κ_{eff} ($\leq 10^{-4}$), the porosity distribution breaks down into a series of small amplitude waves (figure 3(d)).

The spatial porosity distribution in a given system depends upon the relative rates of upward transport of liquid and heat, which for a particular value of φ is primarily governed by the magnitude of κ_{eff}. Using equations (3.37) and (3.39), the mass conservation equation (3.36) may be written in a form more open to physical interpretation

$$\frac{\partial \phi}{\partial t} = -C + \kappa_{eff}\frac{\partial^2 \theta}{\partial z^2} + (1 - \mathrm{Ste})(w_l + w_s)\frac{\partial \theta}{\partial z} \qquad (3.47)$$

with

$$C = \frac{\partial}{\partial z}(\phi w_l) \qquad (3.48)$$

The first term on the right hand side of equation (3.47), *C*, governs the compaction rate, and demonstrates that gradients in the liquid phase flux (ϕw_l) cause local changes in porosity. If the liquid phase flux at any point increases with height the compaction rate (*C*) is positive, the porosity locally decreases, and the deformable matrix *compacts* to occupy the space previously occupied by liquid. Conversely, if the liquid phase flux decreases with height the compaction rate is negative, the porosity

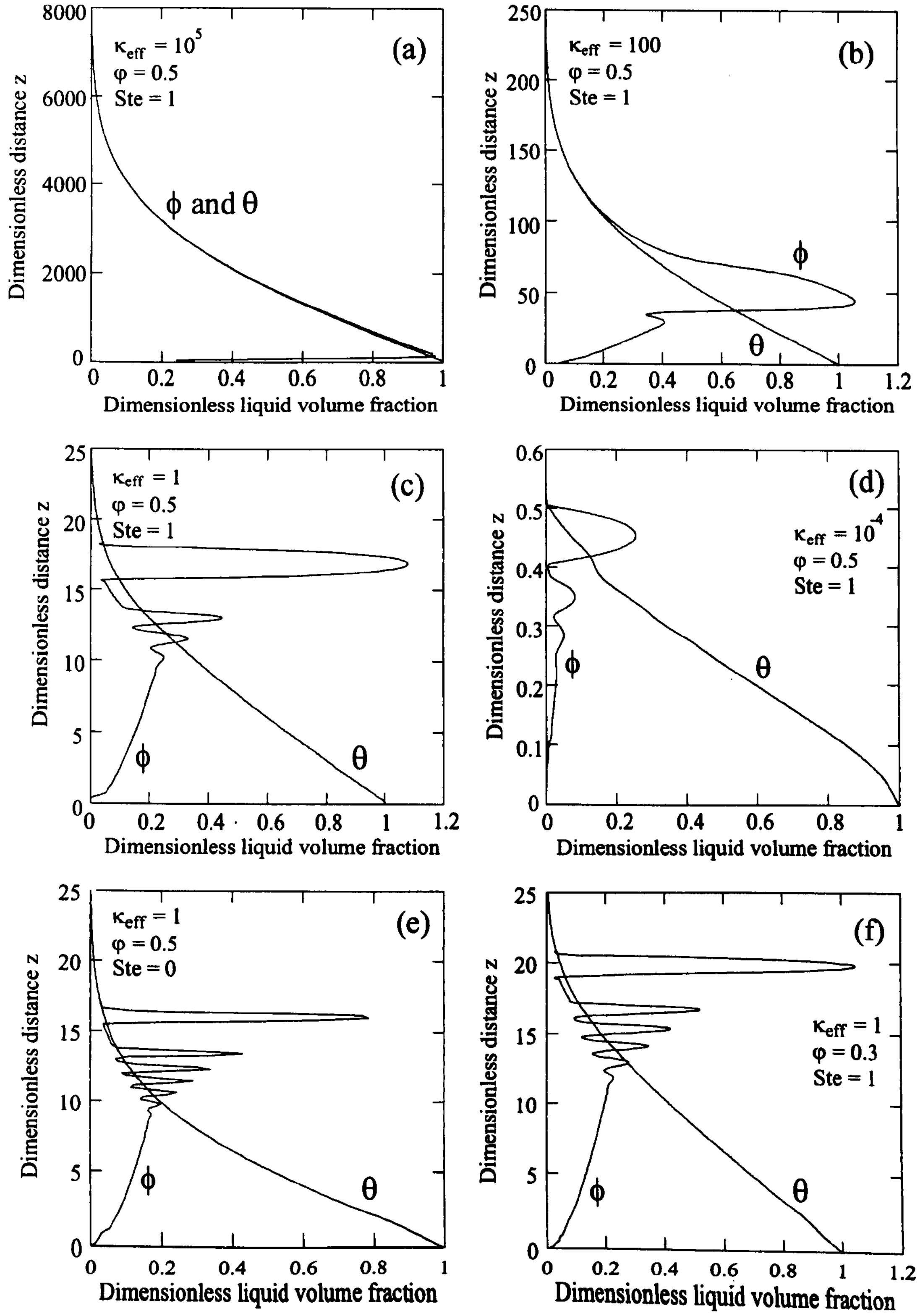

Figure 3.3. Normalised dimensionless spatial porosity and equilibrium liquid volume fractions, after 30 time units, with (a) $\kappa_{eff} = 10^5$, $\varphi = 0.5$, Ste = 1; (b) $\kappa_{eff} = 100$, $\varphi = 0.5$, Ste = 1; (c) $\kappa_{eff} = 1$, $\varphi = 0.5$, Ste = 1; (d) $\kappa_{eff} = 10^{-4}$, $\varphi = 0.5$, Ste = 1; (e) $\kappa_{eff} = 1$, $\varphi = 0.5$, Ste = 0; (f) $\kappa_{eff} = 1$, $\varphi = 0.3$, Ste = 1. Liquid volume fractions are normalised to the equilibrium liquid volume fraction at z = 0 (φ). Note that both the ordinate and abcsissa axis scales differ between plots.

locally increases, and the deformable matrix *dilates* to accommodate the accumulating liquid. The second and third terms are source terms which describe phase change due to conductive heat transport, and phase change due to pseudo-advective heat transport respectively.

For the case Ste = 1, the pseudo-advective source term is zero, so porosity change is governed by the relative magnitudes of the compaction and conduction terms only. For large κ_{eff}, the conductive heat transport term dominates the compaction term, and equation (3.47) may be approximated as

$$\frac{\partial \phi}{\partial t} \approx \frac{\partial \theta}{\partial t} \approx \kappa_{eff} \frac{\partial^2 \theta}{\partial z^2} \tag{3.49}$$

Consequently, there is little difference between the normalised spatial porosity and equilibrium liquid volume fraction distributions.

As κ_{eff} decreases, the rate of liquid phase transport increases relative to the rate of heat transport, until the liquid phase migrates upwards faster than the dimensionless solidus isotherm, z_0. At z_0 the porosity and hence permeability falls to zero, so upward migrating liquid must accumulate below it, resulting in the development of a porosity wave. In the region immediately below a porosity wave, the liquid phase flux increases with height, the compaction term is positive, so the porosity locally decreases. If the relative rate of liquid transport is sufficiently high that the compaction term in equation (3.47) dominates the conduction term, then trailing porosity waves develop, because compaction leads to a reduction in the permeability for which the creation of liquid by phase change cannot compensate. This acts as a local restriction to liquid transport, below which liquid accumulates and a new porosity wave develops. As the relative rate of liquid transport increases, so the local compaction rate below an incipient porosity wave increasingly outstrips the rate of phase change, leading to an increase in the wave frequency.

When κ_{eff} becomes very small, the conductive heat transport term in equation (3.47) becomes very small. Consequently, too little liquid is produced by phase change for a large amplitude porosity wave to develop. The generally low porosities and permeabilities inhibit phase transport, so phase velocities are low, the net phase velocity is small, and the pseudo-advective term in the energy conservation equation (3.37) is also small. Consequently, heat transport is dominated by conduction for small values of κ_{eff}, as observed in figure 3.2.

For the case Ste = 0, the pseudo-advective source term in equation (3.47) exerts maximum influence on the porosity distribution. Figure 3.3(e) illustrates the effect of this, and should be compared with figure 3.3(c); the most significant differences are that the amplitude of the leading porosity wave is reduced, and the wave frequency increased. Because $\partial\theta/\partial z$ is always negative, if $|w_l| > |w_s|$, the pseudo-advection term in equation (3.47) is negative, and so acts to reduce the porosity. Physically, this is because the rate at which liquid is migrating upwards (w_l) into cooler regions and freezing is greater than the rate at which solid is migrating downwards (w_s) into hotter regions and melting. Consequently, less liquid is produced by phase change, and porosity waves are more efficiently generated by compaction.

The effect of reducing φ is illustrated by figure 3.3(f), which again should be compared with figure 3.3(c). The amplitude of the leading porosity wave is similar in both cases, but the wave frequency is increased. This is because, over the range $0 < \varphi < 0.8$, κ_{eff} effectively varies with φ as

$$\kappa_{eff} \sim 1/\varphi^{9/2} \tag{3.50}$$

Consequently, reducing φ at constant κ_{eff} is *qualitatively* similar to reducing κ_{eff} at constant φ, because reducing φ causes the range of values of κ_{eff} available from varying the other constituent variables to be shifted upwards. The changes are *quantitatively* different because φ also appears independently in both the mass and momentum conservation equations (3.36 and 3.38).

Figure 3.4(a) shows dimensionless liquid and matrix velocities for a system with $\kappa_{eff} = 1$, Ste = 1, and $\varphi = 0.5$, after 30 time units, and should be compared with figure 3.3(c). Positive liquid velocities reflect the upwards migration of buoyant liquid; negative solid velocities reflect the downwards migration of matrix. Changes in velocity correlate with changes in porosity, because the permeability is governed by the local porosity. Figure 3.4(b) shows the dimensionless compaction rate (C) and matrix strain rate ($\partial w_s/\partial z$), for the same parameters, and should again be compared with figure 3.3(c). Negative compaction rates above local porosity maxima demonstrate that the porosity is increasing; conversely, positive compaction rates below local porosity maxima demonstrate that the porosity is decreasing. The association of negative and positive compaction rates with each porosity wave causes new waves to develop below existing waves, and existing waves to migrate upwards. The effect of this on the matrix is demonstrated by the matrix strain rate; negative compaction rates correlate with positive (dilating) strain rates, and vice-versa.

3.3.3 Increase in maximum porosity with time: formation of a slurry

If the amplitude of the porosity waves continually increases with time, then the local liquid volume fraction may eventually exceed the CMF, in which case the contiguity of the solid matrix grains will break down, and the rheological description of that part of the mixed phase region will change from mush to slurry[3] (Hills and Roberts 1988; Bergantz, 1992). The mush-slurry transition is important, because the liquid fraction of the slurry has effectively segregated from the mush. A slurry is mobile, and if a suitable route is made available, may migrate away from the mushy zone.

---

[3] 'Slurry' is a general term which describes a mixture of crystals suspended in liquid. In geological systems, a slurry is termed a magma. As befits a general model, the term slurry rather than magma will be used throughout this chapter, except when a specifically geological context is implied.

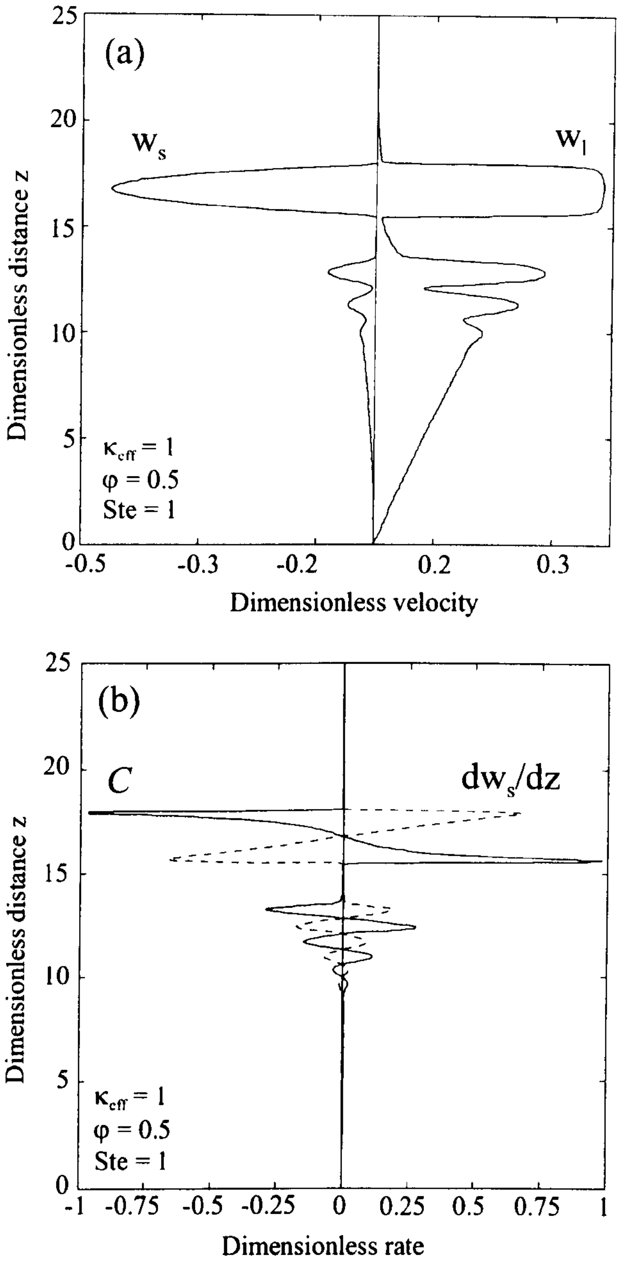

Figure 3.4. Results for the case $\kappa_{eff} = 1$, $\varphi = 0.5$, Ste = 1, after 30 time units. (a) dimensionless liquid and solid velocities; (b) dimensionless compaction rate (*C*) and matrix strain rate.

Figure 3.5 shows a representative selection of the maximum normalised porosity against time curves. In systems with large values of κ_{eff}, ($\geq 10^5$), the maximum porosity changes little with time (figure 3.5(a)). In systems with values of κ_{eff} between ~10^4 and ~10^{-3}, the rate of increase of maximum porosity is rapid with time (figure 3.5(b-c)); in systems with small values of κ_{eff}, ($\leq 10^{-4}$), the maximum porosity initially falls until the slope abruptly changes and the maximum porosity begins to increase, although the rate of increase is slow (figure 3.5(d)). The mush-slurry transition is possible only if the maximum normalised porosity eventually exceeds the normalised CMF, where the normalised CMF is given by CMF/φ. For the momentum conservation equation (3.38) to be valid, the normalised CMF must be greater than or equal to 1 (i.e. CMF/$\varphi \geq 1$); consequently, the *minimum* requirement for slurry formation is that the normalised porosity exceeds 1. Maximum normalised porosity against time curves obtained for the full range of values for κ_{eff}, indicate that slurry formation is possible in systems with κ_{eff} in the range $10^{-4} < \kappa_{eff} < 10^5$.

The model may be used to estimate the time required to *initiate* the mush-slurry transition, which is termed the *segregation time*, by recording the time required for the porosity at any point to reach the CMF. For most silicate rock types, the CMF lies in the range 0.3 - 0.65 (van der Molen and Paterson, 1979; Cheadle, 1989; Philpotts and Carroll, 1996; see also the discussion presented in §4.2.4.3). The segregation time depends upon the rate of increase of the maximum porosity, and the magnitude of the CMF. If the rate of increase of the maximum porosity is rapid and the CMF small, then the segregation time is small; if the rate of increase of the maximum porosity is slow and the CMF large, then the segregation time is large. Figure 3.6 shows an example of the dimensionless segregation time as function of κ_{eff}, for Ste = 1, with φ = CMF = 0.5 and φ = CMF = 0.3 (i.e. CMF/φ = 1). Taking φ = CMF is a convenient approximation to the situation in which the equilibrium liquid fraction at z=0 (φ) lies fractionally below the CMF, and results in the shortest segregation times for the chosen parameters. Segregation times for both the cases φ = CMF = 0.5 and φ = CMF = 0.3 are shortest in systems with κ_{eff} in the range $1 < \kappa_{eff} < 10^4$; the segregation time then increases in systems with both decreasing and increasing κ_{eff}. A maximum dimensionless time of 200 was imposed, to avoid excessive computational expense.

3.3.4 Prediction of phase compositions

Figure 3.7(a) shows the empirically derived liquid phase composition for a common lower crustal rock type, as a function of the normalised equilibrium liquid volume fraction (also termed the 'fraction of equilibrium melting'). As the normalised fraction of equilibrium melting increases from ~0.1 to ~0.8, the composition of the liquid phase changes from 'trondhjemitic' to 'tonalitic', and then to 'granodioritic'. These compositions are all 'granitic'(*sensu-lato*). Empirical data such as this may be combined with the results presented in §3.3.2, to deduce liquid phase compositions for a given

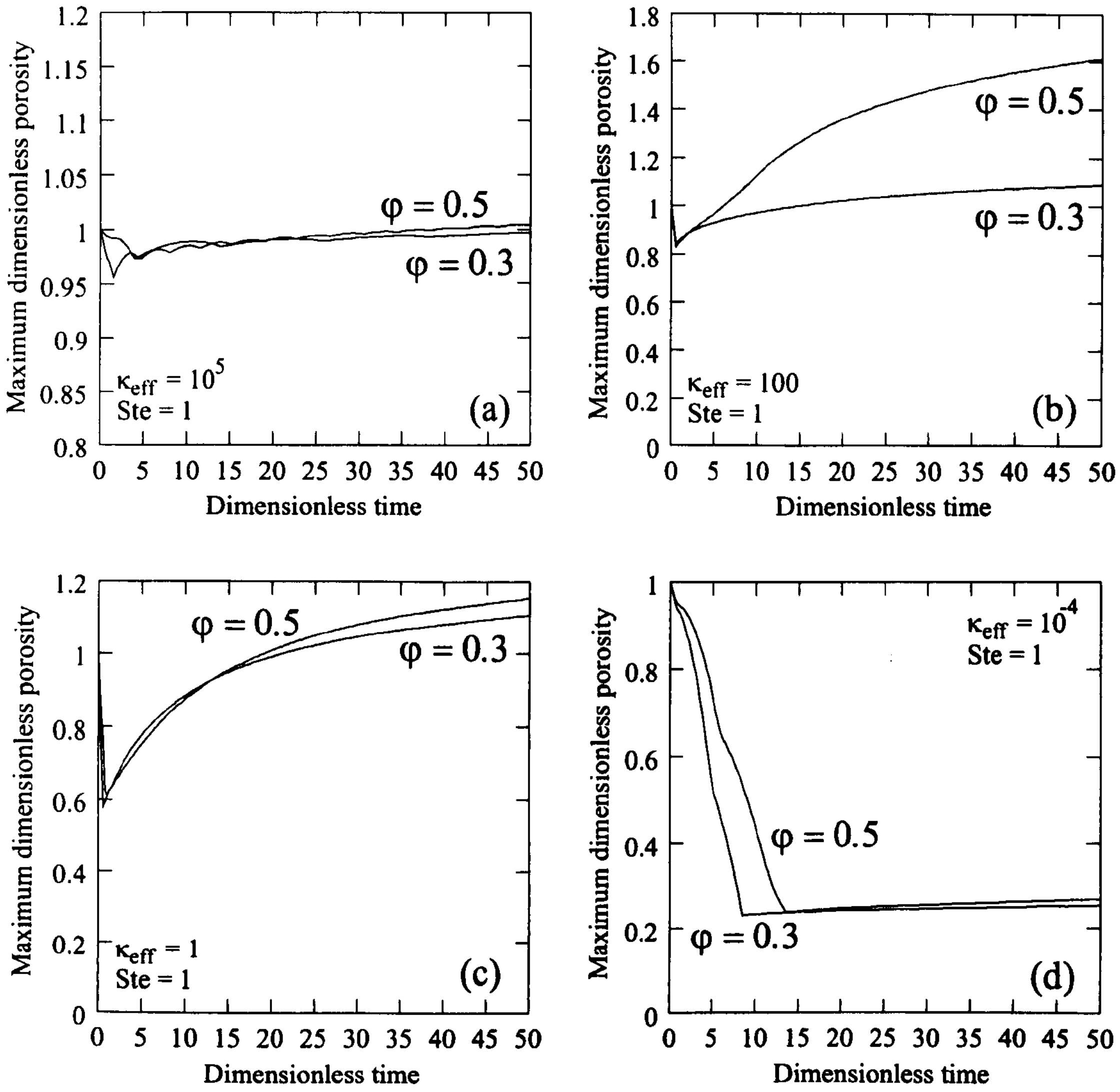

Figure 3.5. Maximum normalised dimensionless porosity as a function of dimensionless time, for the $\varphi = 0.5$ and 0.3 cases, with: (a) $\kappa_{eff} = 10^5$; (b) $\kappa_{eff} = 100$; (c) $\kappa_{eff} = 1$; (d) $\kappa_{eff} = 10^{-4}$. In all cases, Ste = 1. Porosity is normalised to the equilibrium liquid volume fraction at z=0 (φ). Note abscissa axis scale differs between plots.

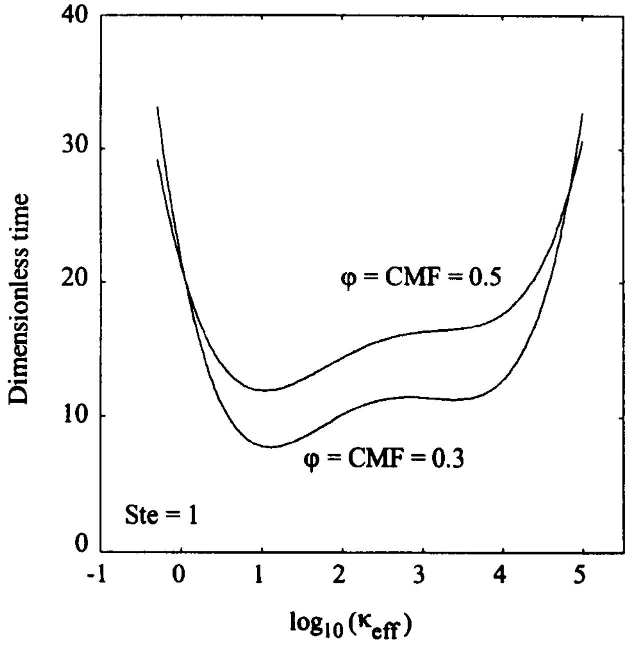

Figure 3.6. Segregation time as a function of κ_{eff}, for φ = CMF = 0.5, and φ = CMF = 0.3. Ste = 1.

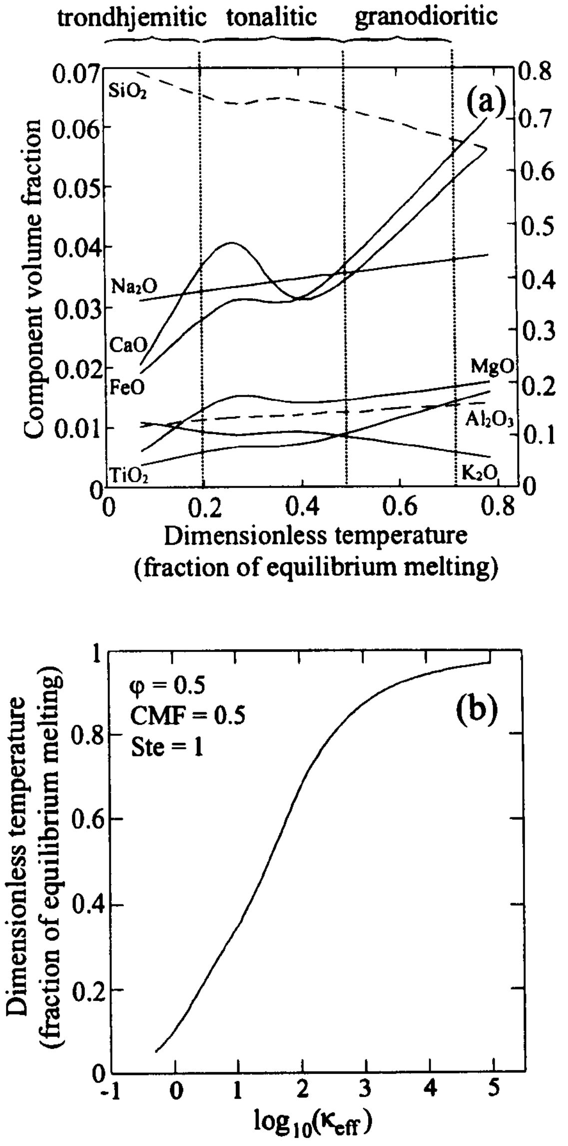

Figure 3.7. (a) Liquid phase composition in terms of component oxide volume fractions, as a function of normalised dimensionless temperature, for an andesitic greenstone. Plain lines plot on the left hand ordinate axis; dashed lines plot on the right hand ordinate axis. Data from Beard and Lofgren (1991). Note that the normalised dimensionless temperature is numerically equivalent to the normalised fraction of equilibrium melting. The temperature is non-dimensionalised assuming T_{sol} = 1163K; T_{liq} = 1443K, and normalised using $\varphi = 0.5$. (b) Normalised dimensionless segregation temperature as a function of κ_{eff}, for φ = CMF = 0.5; Ste = 1.

material during phase change and phase transport. For example, consider the liquid composition at the position of the porosity maximum shown in figure 3.3(b). The porosity maximum is located at a dimensionless position of ~48; the normalised dimensionless temperature at this position is ~0.6. The normalised dimensionless temperature is numerically equivalent to the normalised fraction of equilibrium melting; therefore the liquid at the position of the porosity maximum has a composition which corresponds to a normalised fraction of equilibrium melting of ~0.6. For the rock type shown in figure 3.7(a), its composition would be described as granodioritic. In like fashion, it may be deduced that the composition of the liquid at the position of the porosity maximum in figure 3.3(c) corresponds to a normalised fraction of equilibrium melting of ~0.08; for the rock type shown in figure 3.7(a), its composition would be described as trondhjemitic.

Because the phases are always in local thermodynamic equilibrium, their compositions change in a *predictable* manner in response to spatial and temporal changes in temperature. With increasing distance from the origin, the temperature in the mixed phase region decreases (figure 3.3); consequently, as the liquid phase migrates upwards, its composition changes to correspond to a smaller fraction of equilibrium melting of the solid phase. Physically, this is because it thermodynamically equilibrates with solid phase at progressively lower temperatures; the exchange of components between the phases is described mathematically by the third term on the right hand side of equation (3.36). For a given material, the composition of the liquid phase in a porosity wave therefore depends upon the position of the porosity wave *relative* to the position of the solidus isotherm z_0; for example, the liquid in the leading porosity wave shown in figure 3.3(c) corresponds to a smaller fraction of equilibrium melting than that of the liquid in the leading porosity wave shown in figure 3.3(b), because the liquid in the porosity wave shown in figure 3.3(c) has thermodynamically equilibrated with solid at a lower temperature, closer to the position of the solidus isotherm. With decreasing κ_{eff}, the position of the leading porosity wave moves closer to the position of the solidus isotherm (§3.3.2); consequently, in systems with small values of κ_{eff} ($<10^3$), the liquid phase which accumulates to form the leading porosity wave has a composition which corresponds to only a *small* (<0.8) normalised fraction of equilibrium melting of the solid phase (e.g. figure 3.3(c)).

Empirical data such as that shown in figure 3.7(a) may also be used to deduce the *initial* composition of the liquid part of the slurry which forms if the liquid volume fraction exceeds the CMF (§3.3.3). For a given material, the initial composition of the slurry depends upon the temperature at the position of incipient mush-slurry transition; this temperature is termed the *segregation temperature*. Figure 3.7(b) shows a plot of the normalised dimensionless segregation temperature (fraction of equilibrium melting) as a function of κ_{eff}, for the case φ = CMF = 0.5 (cf. §3.3.3). The segregation temperature increases with increasing κ_{eff}, from ~0.05 to ~0.95. In systems with small κ_{eff}, the position of the porosity maximum, and hence the mush-slurry transition, occurs in the coolest part of the mixed phase region just below the solidus isotherm z_0, so the segregation temperature is low; in systems with larger κ_{eff}, the position of the porosity maximum lags further behind z_0 (§3.3.2), so the mush-slurry transition occurs in hotter parts of the mixed phase region and the segregation temperature increases. Generally, the segregation temperature depends upon the values of φ, κ_{eff}, and the CMF.

For a system with $\kappa_{eff} \sim 3$ and CMF = φ = 0.5, the dimensionless segregation temperature is ~0.2 (figure 3.7(b)); consequently, the composition of the liquid fraction of the slurry corresponds to normalised fraction of equilibrium melting of ~0.2; for the rock type shown in figure 3.7(a), its composition would be described as trondhjemitic. In like fashion, it may be deduced that, for systems with larger κ_{eff}, the composition of the liquid part of the slurry corresponds to a larger normalised fraction of equilibrium melting, and for the rock type shown in figure 3.7(a), its composition would be described as tonalitic or granodioritic. In phase change systems with $\kappa_{eff} < 10^3$, the liquid phase at the position of incipient mush-slurry transition thermodynamically equilibrates with the solid phase at low temperatures near the top of the mixed phase region, so the composition of the liquid fraction of the mobile slurry corresponds to only a *small* normalised fraction (<0.05-0.8) of equilibrium melting of the solid phase, despite having accumulated until it exceeds the normalised CMF.

3.4 Discussion

3.4.1 Heat, mass and momentum transport in a deformable mush

The transport of heat, mass and momentum in a *deformable*, mushy mixed phase region undergoing solid-liquid phase change has, for a simple 1-D system heated from below, been characterised in terms of four externally prescribed dimensionless parameters: the effective thermal diffusivity (κ_{eff}); the Stefan number (Ste); the equilibrium liquid fraction at z = 0 (φ) (which is numerically equivalent to the dimensionless temperature at z = 0); and the exponent in the permeability relation (n).

The dominant mode of heat transport within the mixed phase region depends upon the values of κ_{eff} and Ste, and also upon the net phase velocity ($w_l + w_s$). In systems characterised by large values of Ste, heat transport is dominated by phase transport for a wide range of values of κ_{eff}. Caution must therefore be exercised when describing the transport of heat in a deformable mushy zone; in many systems a conductive only formulation will be inadequate.

The spatial distribution of the liquid volume fraction (porosity) within the mixed phase region depends upon the relative transport rates of heat and liquid, and for given values of φ and Ste, is effectively governed by the magnitude of κ_{eff}. Large values of κ_{eff} result from conditions which promote slow liquid phase transport but rapid conductive heat transport, such as small matrix grain size, high liquid phase viscosity, and high thermal conductivity (equation (3.40)); conversely, small values of κ_{eff} result from conditions which promote rapid liquid phase transport but slow conductive heat transport. Consequently, in systems characterised by large values of κ_{eff} ($\geq 10^5$), the rate of liquid phase transport is slow compared to the rate of heat transport, and the spatial distribution of liquid is similar to that obtained in the *absence* of phase transport. In systems characterised by small values of κ_{eff} ($\leq 10^{-4}$), the rate of liquid phase transport is rapid compared to the rate of heat transport, yet porosities are generally low, and little phase transport occurs. This is because phase change occurs both as a result of conductive heating of the mixed phase region (described by the second term on the right hand side of equation (3.36)), and in response to phase transport coupled with local thermodynamic equilibration (described by the third term on the right hand side of equation (3.36)). In systems characterised by small values of κ_{eff}, phase change due to conductive heating is dominated by phase change due to phase transport, which acts to reduce the porosity because the rate at which the liquid phase migrates upwards into cooler regions and freezes (w_l), is greater than the rate at which the solid phase migrates downwards into hotter regions and melts (w_s) (i.e. $|w_l| > |w_s|$). Consequently, in systems characterised by small values of κ_{eff}, porosities are generally low.

In systems characterised by values of κ_{eff} in the range $10^{-4} < \kappa_{eff} < 10^5$, the liquid phase migrates upwards more rapidly than the position of the solidus isotherm and accumulates below it, leading to the formation of a porosity wave. The amplitude of this wave increases with time, until the contiguity of the solid matrix breaks down, and the rheological description of that part of the mixed phase region changes from mush to slurry. The mush-slurry transition is important, because the liquid fraction of the slurry has effectively segregated from the mush. As the liquid phase migrates through the mixed phase region, its composition continually changes to correspond to a *smaller* fraction of equilibrium melting of the solid phase, because it locally thermodynamically equilibrates with solid at progressively *lower* temperatures. The initial composition of the slurry therefore depends upon both the initial composition of the solid phase, and the position of incipient slurry formation *relative* to the position of the solidus isotherm (i.e. relative to the top of the mixed phase region). The significant result is that, in systems characterised by values of $10^{-4} < \kappa_{eff} < 10^3$, the liquid phase at the position of incipient mush-slurry transition has thermodynamically equilibrated with the solid phase at low temperatures near the top of the mixed phase region, so the composition of the liquid fraction of the mobile slurry corresponds to only a *small* normalised fraction (<0.05-0.8) of equilibrium melting of the solid phase, despite having accumulated until it exceeds the CMF.

3.4.2 The assumptions of the model

In deriving the equations governing conservation of energy and mass, it is assumed that the mixed phase region is always in local thermodynamic equilibrium. This assumption has a significant effect on the dynamics of phase change and phase transport; for example, the compositional evolution of the liquid phase as it migrates through the mixed phase region occurs in response to local equilibration, and results in the segregation of liquid which has a composition which corresponds to only a small fraction of equilibrium melting of the solid. It is therefore important to investigate the conditions for which the assumption of local thermodynamic equilibrium is valid during phase change and phase transport.

Maintenance of local equilibrium requires that the rate at which thermal and chemical equilibrium is attained is rapid compared to the thermodynamic evolution of the mixed phase region. Rates of *thermal* equilibration are rapid in geological systems; the kinetic limit on the rate of *chemical* equilibration is component diffusion in the solid phase. Chemical equilibrium is maintained only if the rate at which components diffuse in the solid is rapid compared to the rate at which components are advected by the liquid. A measure of the relative rates of diffusion and advection is provided by the Peclet number (Pe)

$$\mathrm{Pe} = \frac{4|\mathrm{v}|a^2}{DL} \tag{3.51}$$

where v is the velocity at which components are advected, D is the component diffusivity in the solid phase, and L is the lengthscale over which compositional variations occur. In diffusion-advection systems characterised by values of Pe << 10, the rate of diffusion is rapid compared to the rate of advection, and equilibrium will be maintained; conversely, in systems characterised by values of Pe >> 10, the rate of diffusion is slow compared to the rate of advection, and equilibrium will not be maintained (Bickle and McKenzie, 1987; Kenyon, 1990; Speigelman and Kenyon, 1992).

For the system discussed in this chapter, a suitable estimate of the rate at which components are advected by the liquid phase is provided by the D'Arcy separation velocity

$$\mathrm{v} = \frac{k(\rho_s - \rho_l)g}{\phi\mu_l} \tag{3.52}$$

Assuming *marginal* equilibrium (Pe = 10), substituting equation (3.13) into equation (3.52), substituting equation (3.52) into equation (3.51), simplifying, and re-arranging, yields an expression for the *minimum* diffusivity in the solid phase required for local equilibrium to be maintained

$$D_{\mathrm{eq}} = \frac{2\phi^2 \mathrm{b} a^4 (\rho_s - \rho_l)g}{5\mu_l L} \tag{3.53}$$

In a homogenous, isotropic mixed phase region, the lengthscale L over which compositional variations occur depends only upon the spatial gradient in the fraction of equilibrium melting. If the gradient is steep, then compositional variations occur over a small lengthscale; conversely, if the gradient is shallow, then compositional variations occur over a large lengthscale. In the crust, the mixed phase region (partial melt zone) is typically ~5km thick, and the fraction of equilibrium melting varies from ~0.5 at the base to zero at the top, in which case the spatial gradient in the fraction of equilibrium melting is $\sim 10^{-4}$ km^{-1}. Assuming that a change in the fraction of melting of $\sim 10^{-3}$ (0.2%) causes a negligible variation in the composition of each phase, yields a value of $L \sim$ 10m. For comparison, both Speigelman and Kenyon (1992) and McKenzie (1984) have considered the validity of assuming local thermodynamic equilibration during phase change and phase transport in the mantle, and suggested values for L. Speigelman and Kenyon (1992) set L equal to the total thickness of the mixed phase region ($L \sim$ 50km), which is equivalent to assuming that the spatial gradient in the fraction of equilibrium melting is zero; in contrast, McKenzie (1984) estimated a value of $L \sim$ 300m.

Figure 3.8 shows the minimum diffusivity required to maintain marginal equilibrium, as a function of the matrix grain radius, for the values of μ_l, $(\rho_s - \rho_l)$, and b, which correspond to the *fastest* (curve (a)), *slowest* (curve (c)), and '*average*' (curve (b)) predicted advective transport rates in a lower crustal partial melt zone (§4.2.4), with L ~ 10m and $\phi \sim 0.5$. Also shown on figure 3.8 is the range of estimated component diffusivities in lower crustal minerals (shaded area; data from Freer, 1981). For the *fastest* predicted advective transport rates, and grain sizes >1.4 mm, the *smallest* estimated component diffusivities fall below the curve denoting the minimum diffusivity required to maintain marginal equilibrium (curve (a)); consequently, it is possible that equilibrium will not be maintained. However, for slower advective transport rates (curves (b) and (c)), it is likely that equilibrium will be maintained.

This simple analysis indicates that the assumption of local thermodynamic equilibrium is valid during phase change and phase transport in a lower crustal partial melt zone, except for the *fastest* predicted rates of phase transport and *slowest* estimated component diffusivities. If chemical equilibrium is not maintained, component exchange will still occur between the phases during phase change and phase transport, and it is likely that the composition of the liquid phase will still evolve to correspond to a smaller fraction of melting of the solid phase as it migrates upwards through the mixed phase region. However, the compositions of the phases no longer correspond to their equilibrium values, and cannot be deduced using empirical data derived from equilibrium melting experiments.

In deriving the equation governing conservation of linear momentum (equation (3.11)), it is assumed that the pressures in the solid and liquid phases are equal. The assumption of equal pressures requires that the matrix (solid fraction) has no strength, which is equivalent to assuming that the matrix creep

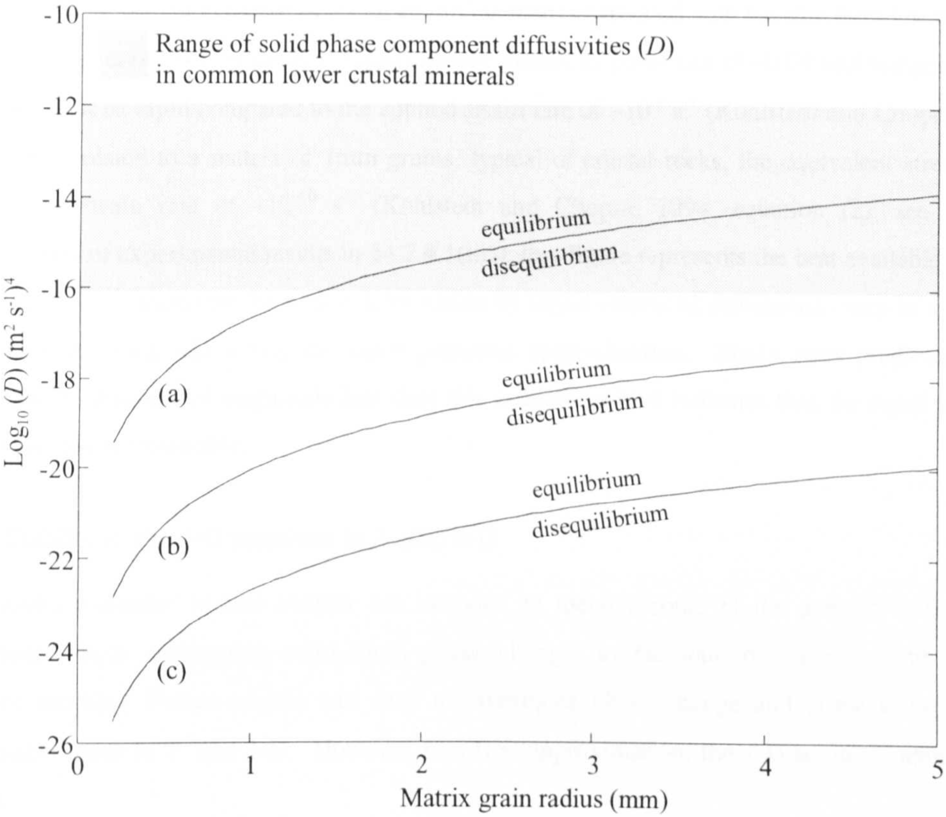

Figure 3.8 Minimum solid phase component diffusivity (*D*) required to maintain marginal chemical equilibrium (Pe = 10), as a function of the matrix grain radius. Curve (a) shows the minimum component diffusivity required to maintain equilibrium for the *fastest* predicted advective transport rates in a lower crustal partial melt zone ($\mu_l = 10^3$ Pa s; b = 1/50; $(\rho_l - \rho_s) = 700$ kg m^{-3}; $\phi = 0.5$); curve (b) shows the minimum component diffusivity required to maintain equilibrium for '*average*' predicted advective transport rates in a lower crustal melt zone ($\mu_l = 10^5$ Pa s; b = 1/1000; $(\rho_l - \rho_s) = 500$ kg m^{-3}; $\phi = 0.5$); curve (c) shows the minimum component diffusivity required to maintain equilibrium for the *slowest* predicted advective transport rates in a lower crustal melt zone ($\mu_l = 10^7$ Pa s; b = 1/2500; $(\rho_l - \rho_s) = 300$ kg m^{-3}; $\phi = 0.5$). See §4.2.4 for the origin of the values of the variables used to calculate advective transport rates. The shaded area shows the estimated range of diffusivities for various components (O, Al, Ca, Ar, Na) in common lower crustal minerals (enstatite, diopside, hornblende, biotite, albite, anorthite, quartz) at temperatures of ~1200 K (data from Freer, 1981).

---

[4] While it should cause no confusion, note that $\log_{10}(D)$ (m^2 s^{-1}) means 'the logarithm to the base ten of the number which represents the solid phase component diffusivity measured in m^2 s^{-1}', as only the logarithm of a pure number has any meaning.

rate is rapid compared to the matrix strain rate. Maximum dimensional matrix strain rates predicted by the model are of the order $1/\tau$, where τ is the characteristic time; values of $1/\tau$ range from 10^{-13} to 10^{-20} s^{-1} for silicate rock phase change systems (equation (3.33); see §4.2.4 for suitable values of the constituent variables). Data on liquid enhanced diffusional creep rates in silicate materials is limited; the results of deformation experiments on an olivine matrix saturated with basaltic liquid indicate that the diffusional creep rate in small (~10μm) olivine grains, at porosities of ~0.08 and temperatures of ~1573K, must be rapid compared to the applied strain rate of ~10^{-4} s^{-1} (Kohlstedt and Chopra, 1994). When extrapolated to a matrix of 1mm grains, typical of crustal rocks, the equivalent stress would result in a strain rate of ~10^{-10} s^{-1} (Kohlstedt and Chopra, 1994, equation (2); see also the extrapolation of experimental results in §4.2.4.1(iii)); this figure represents the best available estimate of the maximum strain rate for which deformation by liquid enhanced diffusional creep in a partially molten silicate rock will satisfy the equal pressures approximation. Strain rates predicted by the model are 3-10 orders of magnitude less than this estimate, which indicates that the equal pressures approximation is reasonable.

3.4.3 Stability of the 1-D solutions in 2- and 3-D

The results presented in this chapter are intended to identify some of the generic features of a deformable mush undergoing solid-liquid phase change, to facilitate the development of more complex models. Future models will need to investigate phase change and phase transport in a deformable mush in 2- and 3-D. However, to a first approximation, the 1-D solutions appear to be robust.

Lowell and Bergantz (1987) suggest that thermal and compositional convection of the liquid phase may cause decoupling of the solid and liquid phase velocities, and convection of the liquid phase in 2- and 3-D. However, in the system discussed here, the liquid is always at its solidus, and so its density is governed *only* by its composition. Heating of the mush from below produces a *stable* compositional density gradient in the liquid for materials in which increasing fractions of equilibrium melting produce liquid of increasing density; this is the case for most silicate rocks (§4.4.5). Hence this simple analysis indicates that convection of the liquid phase is unlikely within partially molten rocks which are heated from below.

Wiggins and Speigelman (1995) have developed solutions in 3-D to the problem of a buoyant liquid migrating through a deformable mush, in the absence of phase change ($\Gamma_l = 0$), and in the limit of small background porosity. Their results indicate that an initially 1-D porosity wave will develop into groups of spherical, 3-D porosity waves. However, they placed no constraint on the vertical distance available for the development of 3-D waves. In the system discussed in this chapter, a 1-D porosity wave forms *only* because the vertical extent of the mixed phase region is constrained by the position of the solidus isotherm, and the upward rate of migration of the leading wave is primarily governed by the upward rate of migration of the solidus isotherm rather than the dynamics of the deformable mush. Furthermore, phase change due to phase transport and local equilibration (described by the third term on the right hand side of equation (3.36)) acts to inhibit the localisation of flow. In any region in which the upwards transport of liquid becomes localised, such as a chimney, the net phase velocity ($w_l + w_s$) increases, so phase change due to phase transport becomes more significant (i.e. the magnitude of the third term on the right hand side of equation (3.36) increases). Phase change due to phase transport acts to *reduce* the porosity; consequently, in any region in which the upward flow of liquid became localised, the permeability would be reduced and liquid transport would be inhibited, pushing the system back to its stable, 1-D configuration.

3.5 Conclusions

The development of the model presented in this chapter was originally motivated by the need to understand better the coupled processes of granitic melt generation and segregation in the continental crust. It was argued in chapter 2 that the production of mobile, granitic magma by partial melting of rocks in the mid- to lower crust presents a paradox. Melt fractions which are granitic in composition correspond to only small fractions of equilibrium melting of the source rock; melt generation and segregation therefore appears to occur at melt fractions which are less than the CMF, yet magma mobilisation can occur only at melt fractions which are greater than the CMF. The results obtained in this chapter are significant because they indicate a possible resolution of the paradox. The results presented in §3.3.2 and §3.3.3 indicate that liquid will segregate from a melting, deformable mush with suitable thermal and physical characteristics, forming a mobile slurry; figure 3.6 allows an estimate of the time required for segregation. The results presented in §3.3.4 indicate that the composition of the segregated liquid will correspond to a *small* fraction of equilibrium melting of the solid.

Chapter 4: The generation, segregation and mobilisation of granitic melt in the continental crust.

"....partial re-melting to a sufficient degree to produce batholithic quantities of magma must normally occur in very deep crustal or mantle environments which are rarely revealed by erosion, so that the processes of segregation and collection of granitoid magmas thus become matters for speculation." **(Pitcher, 1979, p. 643).**

4.1 Introduction

The review presented in chapter 2 argued that the production of mobile, granitic magma by partial melting of rocks in the mid- to lower continental crust presents a paradox. The available evidence indicates that melting occurs under water-absent or water-undersaturated conditions, and is caused by the advection of heat from the mantle to the crust, either by basaltic underplating, asthenospheric upwelling, or a combination of these processes (§2.2.4). During partial melting of the protolith, the unmelted solid fraction (restite) maintains an interconnected matrix, so the partially molten rock forms a *mush*, unless the melt volume fraction reaches the Critical Melt Fraction (CMF). The CMF denotes the melt fraction at which the solid matrix disaggregates and a mobile magma is formed (§2.3.1). In order to form a *granitic* magma, the granitic partial melt fraction *must* separate to some extent from its restite; experimental and field evidence indicates that melt volume fractions which are granitic in composition are less than the CMF, and segregate in the source region from partially molten rock in which the restite maintains an interconnected matrix (§2.3.2). The paradox is that melt generation and segregation appears to occur at melt fractions which are *less* than the CMF, yet magma mobilisation can occur only at melt fractions which are *greater* than the CMF. How then does a small granitic partial melt fraction form a mobile granitic magma?

Most previous models of melt generation and segregation in the continental crust have treated them as separate processes. Models of melt generation consider the thermal conditions required to produce granitic melt, and calculate the static volumes of melt produced if no melt migration occurs (e.g. Clemens and Vielzuf, 1987; Bergantz, 1989; Patiño Douce *et al.*, 1990); conversely, models of melt segregation assume a pre-existing melt distribution, and then model how this melt migrates or becomes mobilised (e.g. Richter and McKenzie, 1984; McKenzie, 1985). However, treating melt generation and segregation in the continental crust as separate processes is not valid; they are complementary, *coupled* processes which occur simultaneously (§2.4). Only Fountain *et al.* (1989) have attempted to present a quantitative, coupled model, and their approach is rather different to that presented in this chapter. Their model is discussed in §4.4.6; a close examination of their formulation and method of solution reveals a number of significant errors, including a failure to correctly formulate the equations governing both conservation of heat and conservation of mass. As yet, no model has successfully resolved the paradox of granitic melt generation, segregation and mobilisation in the continental crust.

A partially molten rock may be described in general terms as a viscously deformable, multicomponent mush; in chapter 3, motivated by the need to understand better the coupled processes of melt generation and segregation in the continental crust, a general, quantitative, coupled model was developed of phase transport in a deformable, multicomponent mush which is melting due to heating from below. The results of this general model indicate a possible resolution of the paradox. They demonstrate that the spatial distribution of the liquid fraction in the mush effectively depends upon the relative upward transport rates of heat and liquid, and that, for a wide range of the dimensionless governing parameters, the liquid fraction accumulates below the solidus isotherm and a porosity wave develops (§3.3.2). The amplitude of this wave increases with time, until the local liquid volume fraction exceeds the CMF, and a slurry forms. The liquid in the slurry has a composition corresponding to a *small* degree of equilibrium melting of the solid, because it has thermodynamically equilibrated with cool matrix near the top of the mushy zone, yet the slurry is mobile, and may migrate away from the mushy zone if a suitable route is made available (§3.3.3).

In this chapter the general model will be applied to a partial melt zone in the lower crust, which is produced by heating from below following the emplacement of hot magma adjacent to the protolith. The aim is to investigate whether, for parameters which are suitable for the lower crust, granitic partial melt fractions will collect and form a mobile magma. The paradox of granitic melt generation, segregation, and mobilisation may then be resolved. Before the general model can be applied to the crust, it must be modified to include a suitable steady state crustal geotherm. The inclusion of a geotherm requires the formulation of a new equation to describe the transport of heat in the solid rock overlying the partial melt zone, and results in the introduction of two new dimensionless governing parameters. In this chapter, as in chapter 3, cooling of the underlying magma heat source is neglected, so as not to obscure the processes which occur in the partially molten rock; a detailed description of the heat source is deferred until chapter 5. Moreover, only the processes which lead to the *formation* of a mobile granitic magma are considered; the consequences of magma formation and the subsequent evolution of the magma are discussed in chapter 6.

4.2 Model Formulation

Consider a region of homogenous, isotropic rock in the lower crust, into which basaltic magma is emplaced. Let the spatial origin of the model (z = 0) denote the position of the magma/rock contact, and the temporal origin (t = 0) denote the time at which the magma is 'instantaneously' emplaced. Before magma emplacement (t < 0), the temperature profile is dictated by a steady-state lower crustal geotherm, the rock is at its solidus (T_{sol}) at z = 0, and there is no melt present (figure 4.1(a)). At t = 0, magma emplacement in the region z < 0 causes the temperature at the contact (z = 0) to be increased from T_{sol} to T_c (figure 4.1(b)), which causes partial melting of the rock in the region z > 0 (figure 4.1(c)). The contact temperature T_c is held constant for t > 0; a valid approach if the timescale of cooling of the magma is long compared to the timescale of melting and melt migration in the overlying rock (see chapter 5). In contrast to the general model presented in chapter 3, the model presented in this chapter can be divided into two distinct regimes: the partially molten rock in the region $0 \le z \le z_{sol}$, and the solid rock in the region $z > z_{sol}$. In the region $0 \le z \le z_{sol}$, the transport of heat, mass and momentum is described by the model presented in chapter 3; i.e. the melt is assumed to be both buoyant, and interconnected along grain edges (§2.3.3); the solid matrix is assumed to viscously deform in response to melt transport (§2.3.4), and both melt and matrix are assumed to be always in local thermodynamic equilibrium (§3.4). In the region $z > z_{sol}$, the transport of heat is described by a conductive formulation; mass and momentum transport are zero because there is no melt present.

4.2.1 Governing Equations

The 1-D conservation equations governing the transport of heat, mass and momentum in the partially molten rock (i.e in the region $0 \le z \le z_{sol}$) may be written as (§3.2.3)

$$k\frac{\partial^2 T}{\partial z^2} = \rho c_p \frac{\partial T}{\partial t} + L\Gamma_m \qquad (4.1)$$

$$\rho\frac{\partial \phi}{\partial t} - \rho\frac{\partial}{\partial z}\left((1-\phi)w_s\right) = \Gamma_m \qquad (4.2)$$

$$\left(\xi_s + \tfrac{4}{3}\mu_s\right)\frac{\partial^2 w_s}{\partial z^2} = (1-\phi)(\rho_s - \rho_m)g - \frac{\mu_m w_s}{k} \qquad (4.3)$$

Also required are the supplementary relations

$$\phi w_m = -(1-\phi)w_s \qquad (4.4)$$

$$\Gamma_m = \rho\frac{\partial v_m}{\partial t} + \rho(w_m + w_s)\frac{\partial v_m}{\partial z} \qquad (4.5)$$

$$k = ba^2\phi^n \qquad (4.6)$$

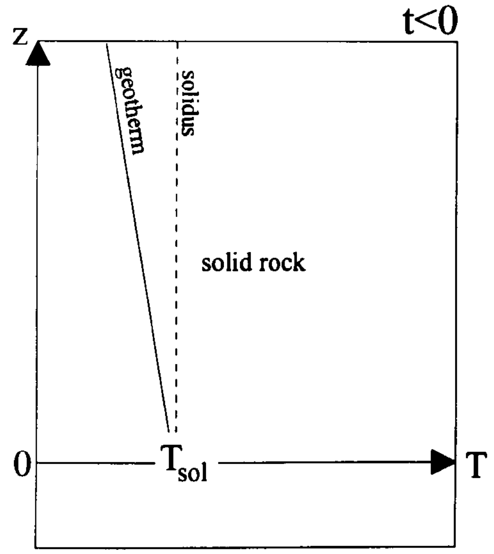

(a) Before magma emplacement ($t<0$), the temperature profile is dictated by a steady state geotherm, the rock is at its solidus (T_{sol}) at $z=0$, and there is no melt present.

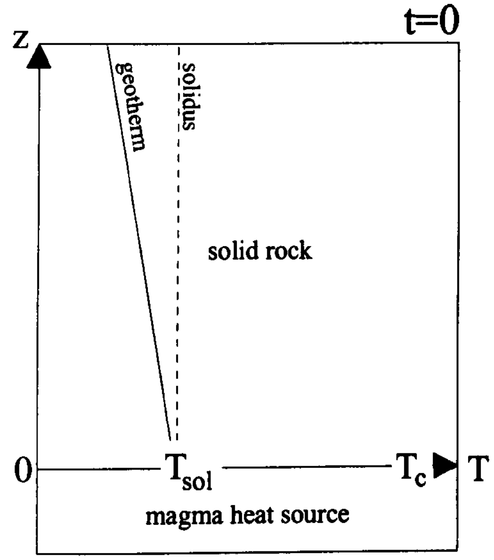

(b) At $t=0$, the instantaneous emplacement of hot magma in the region $z<0$ causes the temperature at the contact ($z=0$) to be increased from T_{sol} to T_c.

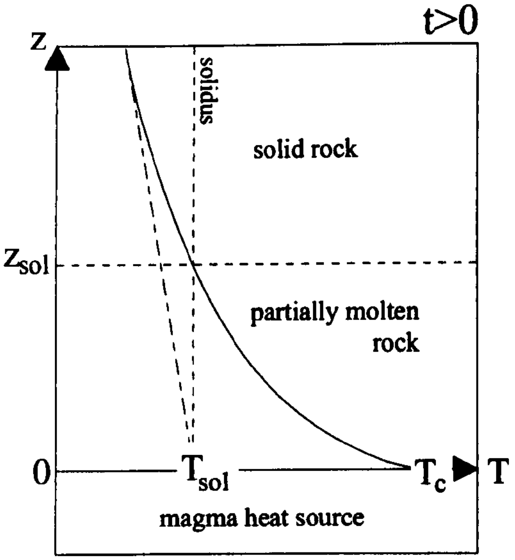

(c) Raising the temperature at the contact ($z=0$) from to T_{sol} to T_c causes partial melting in the overlying rock; T_c is assumed constant for all time. In the region $0<z<z_{sol}$ (i.e. in the partially molten rock), the transport of heat, mass and momentum is described by the model presented in chapter 3. In the region $z>z_{sol}$ (i.e. in the solid rock overlying the partially molten rock), the transport of heat is conductive. With increasing time, the size of the region of partial melting increases, as the position of the solidus isotherm ($z=z_{sol}$) migrates upwards away from the contact ($z=0$).

Figure 4.1. Model formulation for chapter 4: the production of a partial melt zone in the lower crust due to heating from below, following the emplacement of hot magma. Cooling of the magma is neglected, so as not to obscure the processes which occur in the partially molten rock.

(see table 4.1 for an explanation of the nomenclature). Equation (4.1) describes conservation of heat, equation (4.2) describes conservation of mass, equation (4.3) describes conservation of momentum, equation (4.4) relates the melt and matrix velocities, equation (4.5) describes the rate of melt production in terms of the equilibrium melt volume fraction (also termed the 'degree of melting'), and equation (4.6) is a simple expression which relates the permeability of the matrix to the local porosity (melt volume fraction). The 1-D conservation equation governing the conductive transport of heat in the solid rock above the partially molten rock (i.e. in the region $z < z_{sol}$) may be written as

$$k\frac{\partial^2 T}{\partial z^2} = \rho c_p \frac{\partial T}{\partial t} \tag{4.7}$$

Equations (4.1) - (4.6) are valid assuming (i) that the matrix is saturated with melt; (ii) that the thermodynamic properties of the melt and solid matrix are identical and constant; (iii) no internal heat production; (iv) that the pressures in melt and matrix are equal; (v) that both melt and matrix may be treated as Newtonian fluids with constant viscosities; (vi) that the flow of both melt and matrix has a low Reynolds number; (vii) that the Boussinesq approximation is valid; (viii) a constant melt-matrix density contrast, and (ix) that the solid fraction maintains an interconnected network (i.e. that the melt volume fraction does not exceed the CMF). The validity of these assumptions is discussed in §4.4.5.

The initial conditions of the model are

$$T(0,0) = T_{sol} \tag{4.8a}$$

$$\frac{\partial}{\partial z}\big(T(z,0)\big) = T_{geo} \tag{4.8b}$$

$$\phi(z,0) = v_m(z,0) = w_m(z,0) = w_s(z,0) = 0 \tag{4.8c}$$

where T_{geo} is the initial lower crustal geothermal gradient, which is assumed to be linear. The boundary conditions are that both the melt and matrix velocities are zero at the contact ($z = 0$), and zero at the time dependent position of the solidus isotherm ($z = z_{sol}$), that the degree of melting is constant at the contact, and zero at the position of the solidus isotherm, that the contact temperature is constant, and that the temperature gradient tends towards the geothermal gradient as z tends to infinity. They are expressed as

$$T(0,t) = T_c \qquad T(z_{sol},t) = T_{sol} \tag{4.9a}$$

$$\frac{\partial}{\partial z}\big(T(z \to \infty, t)\big) \to T_{geo} \tag{4.9b}$$

$$v_m(0,t) = v_c^m \qquad v_m(z_{sol},t) = 0 \tag{4.9c}$$

$$w_m(0,t) = w_s(0,t) = w_m(z_{sol},t) = w_s(z_{sol},t) = 0 \tag{4.9d}$$

Symbol	Description	Units
a	matrix grain radius	m
b	constant in permeability relationship	None
c_p	specific heat capacity	$J\ kg^{-1}\ K^{-1}$
c_{eff}	effective specific heat capacity	$J\ kg^{-1}\ K^{-1}$
C	dimensionless compaction rate	None
$D\gamma$	effective grain boundary diffusivity	$m^3\ s^{-1}$
g	acceleration due to gravity	$m\ s^{-2}$
k	thermal conductivity	$W\ K^{-1}\ m^{-1}$
k	permeability	m^{-2}
K	characteristic permeability	m^{-2}
k_b	Boltzmann's constant (= 1.381×10^{-23})	$J\ K^{-1}$
L	latent heat	$J\ kg^{-1}$
m	grain size exponent in equation (4.31)	None
n	exponent in permeability relation	None
Q	activation energy for creep	$J\ mol^{-1}$
q	stress exponent in equation (4.31)	None
R	molar gas constant (= 8.314)	$J\ K^{-1}\ mol^{-1}$
Ste	Stefan number	None
t	time	s
t_{seg}	dimensionless segregation time	None
T	temperature	K
T_c	temperature at the contact ($z = 0$)	K
T_{sol}	solidus temperature	K
T_{liq}	liquidus temperature	K
T_{geo}	initial geothermal gradient	$K\ km^{-1}$
w_m	melt velocity	$m\ s^{-1}$
w_s	matrix velocity	$m\ s^{-1}$
z	vertical Cartesian coordinate	m
z_{sol}	position of solidus isotherm	m
z_0	position of dimensionless solidus isotherm ($\theta = 0$)	None
χ	ratio of thermal diffusivities in the partially molten and solid rock	None
δ	characteristic lengthscale (McKenzie's compaction length)	m
$\dot{\varepsilon}$	strain rate	s^{-1}
ϕ	melt volume fraction (porosity)	None
ϕ_c	percolation threshold (equation 4.29)	None
φ	dimensionless temperature (degree of melting) at the contact ($z = 0$)	None
Γ_m	rate of production of melt	$kg\ m^{-3}\ s^{-1}$
κ_{eff}	dimensionless effective thermal diffusivity	None
μ_m	melt shear viscosity	Pa s
μ_s	matrix shear viscosity	Pa s
ν_m	degree of equilibrium melting	None
ν_c^m	degree of equilibrium melting at the contact $z = 0$	None
Ω	atomic or molecular volume of diffusing species	m^3
θ	dimensionless temperature (normalised degree of melting)	None
θ_{seg}	dimensionless segregation temperature	None
ρ	density	$kg\ m^{-3}$
$\rho_s - \rho_m$	matrix - melt density contrast	$kg\ m^{-3}$
ω	characteristic velocity scale	$m\ s^{-1}$
σ	stress	Pa
τ	characteristic timescale	s
ξ_s	matrix bulk viscosity	Pa s
ψ_{geo}	dimensionless initial geothermal gradient	None

Table 4.1. Nomenclature for chapter 4.

4.2.2 The degree of melting and melt/solid compositions

To complete the mathematical description of the partial melt zone, the degree of melting (ν_m), and the compositions of solid and melt, must be described in terms of the local thermodynamic conditions. The assumption of local thermodynamic equilibrium permits the use of empirical data (e.g. Hills *et al.*, 1983; Bennon and Incropera, 1987; Bergantz, 1992), obtained from individual melting experiments in which a rock is brought to complete thermodynamic equilibrium at known conditions, then rapidly quenched and the modal quantities and compositions of solid and glass (quenched melt) recorded. This data has been obtained for a variety of lower crustal rock compositions (Rutter and Wyllie, 1988; Vielzuf and Holloway, 1988; Patiño Douce and Johnston, 1991; Rushmer, 1991; Beard and Lofgren, 1991; Rapp and Watson, 1995).

Melting due to heating in the crust may be expressed as a function of temperature only, because the variation in lithostatic pressure across a typical (~5km) melt zone in the lower crust is negligible (< 2kbar); figure 4.2 shows the degree of melting as a function of temperature, for a variety of common lower crustal rock types. The melting experiments used to produce the curves were performed under water absent or water undersaturated conditions, to reflect conditions in the lower crust (§2.2.1). The curves are of interest only for melt fractions which are less than the CMF, because the momentum equation (4.3) is valid only if the degree of melting (melt volume fraction) at the contact (φ) is less than the CMF (§3.2.1); in §4.2.4.3, the maximum value of the CMF is estimated to be ~0.65. For melt fractions less than ~0.65, both continuous, linear increases in melt fraction with temperature (e.g. plots (a), (b) and (c)), and discontinuous, stepwise increases in melt fraction with temperature (e.g. plots (d) and (e, 16kbar curve)) are observed, depending upon the composition of the melting rock.

Melting under water absent or water undersaturated conditions is governed by the breakdown of hydrous minerals such as micas and amphiboles (Clemens and Vielzuf, 1987; Rutter and Wyllie, 1988; Vielzuf and Holloway, 1988; Patiño Douce and Johnston, 1991; Rushmer, 1991). Compositions which exhibit a continuous, linear increase in melt fraction, such as the meta-pelite, meta-basalt, and tonalite shown in plots 4.2(a)-(c), do so because the hydrous minerals break down gradually over a temperature range; for example, the linear increase in melt fraction exhibited in plot 4.2(a) occurs due to the breakdown of biotite over a temperature range of ~200 K (Patiño Douce and Johnston, 1991). In contrast, compositions which exhibit a discontinuous, stepwise increase in melt fraction, such as the meta-pelite shown in plot 4.2(d), do so because the hydrous minerals break down at specific temperatures; for example, the stepwise increase in melt fraction exhibited in plot 4.2(d) occurs due to the rapid breakdown of biotite followed by hornblende at a temperature of ~1140 K (Vielzuf and Holloway, 1988). Consequently, in order to represent the general melting behaviour of lower crustal rocks, both continuous, linear melting, and discontinuous, stepwise melting, should be incorporated in

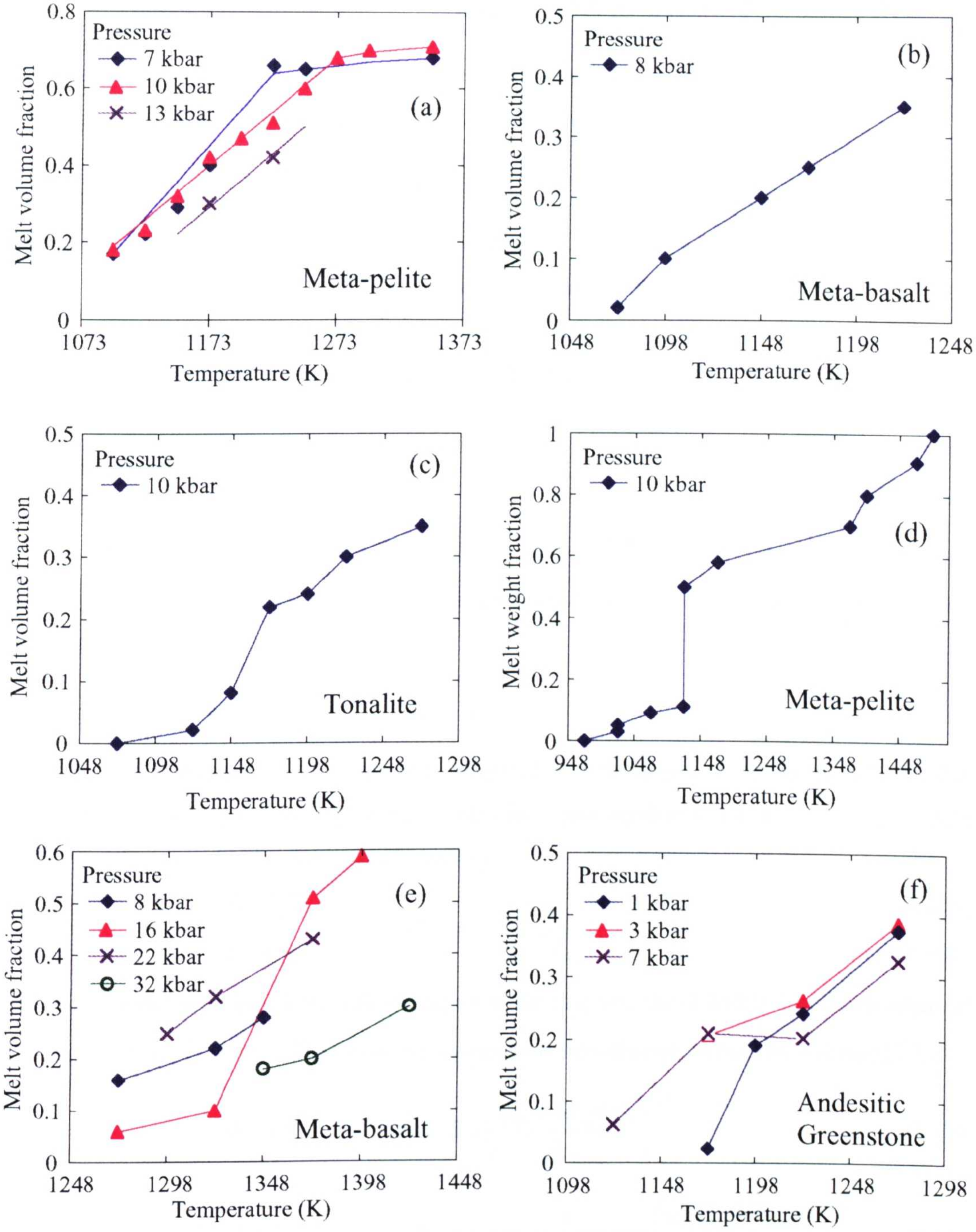

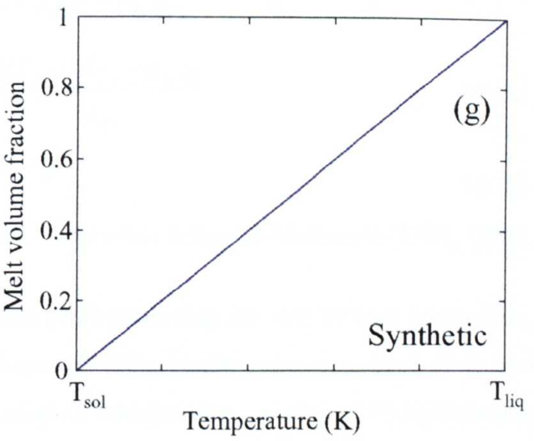

Figure 4.2. Empirically derived degree of melting as a function of temperature, at constant pressure, for a variety of lower crustal rock compositions: (a) Meta-pelite; data from Patino-Douce and Johnston (1991). (b) Meta-basalt; data from Rushmer (1991). (c) Tonalite; data from Rutter and Wyllie (1988). (d) Meta-pelite; data from Vielzuf and Holloway (1988). (e) Meta-basalt; data from Rapp and Watson (1995). (f) Andesitic Greenstone; data from Beard and Lofgren (1991). (g) Synthetic equilibrium melt fraction used in model. All experiments were performed under water-absent or water-undersaturated conditions.

the model; however, following the approach of chapter 3, the degree of melting will be described as a continuous, linear function of temperature for all rock compositions

$$\nu_m = \frac{T - T_{sol}}{T_{liq} - T_{sol}} \tag{4.10}$$

and furthermore, latent heat will be assumed to be absorbed linearly as melting proceeds (Carslaw and Jaeger, 1986). The assumption of linear melting will be made for simplicity, and because it is reasonable for compositions in which the hydrous minerals break down over a temperature range; moreover, although stepwise melting could be incorporated in the model, the number of boundary conditions required in the partially molten zone would increase, and much of the convenience of the continuum formulation would be lost.

4.2.3 Simplification and non-dimensionalisation of the governing equations

The assumption of linear melting leads to a convenient scheme for non-dimensionalising temperature; by writing

$$T' = \frac{T - T_{sol}}{T_{liq} - T_{sol}} \tag{4.11}$$

the dimensionless temperature T' is numerically equivalent to the degree of melting ν_m (§3.2.3). For clarity, both of these quantities will be represented by a new variable θ; i.e. $\theta = T' = \nu_m$. Liquid volume fractions may then be normalised by writing

$$\theta' = \theta/\varphi, \tag{4.12a}$$

$$\text{with } \varphi = \frac{T_c - T_{sol}}{T_{liq} - T_{sol}}$$

$$\phi' = \phi/\varphi, \tag{4.12b}$$

where the scaling factor φ denotes both the degree of melting, and the dimensionless temperature, at the contact; i.e. $\varphi = T_c' = \nu_c^m$. The remaining variables are non-dimensionalised by writing (§3.2.3)

$$z' = z/\delta, \qquad \text{with } \delta = \left(\frac{(\xi_s + 4\mu_s/3)K}{\mu_m}\right)^{1/2} \tag{4.13}$$

$$t' = t/\tau, \qquad \text{with } \tau = \frac{1}{(1-\varphi)(\rho_s - \rho_m)g}\left(\frac{\mu_m(\xi_s + 4\mu_s/3)}{K}\right)^{1/2} \tag{4.14}$$

$$w' = w/\omega, \qquad \text{with } \omega = \frac{K(1-\varphi)(\rho_s - \rho_m)g}{\mu_m} \tag{4.15}$$

$$k' = k/K, \qquad \text{with } K = ba^2\varphi^n \tag{4.16}$$

where the characteristic lengthscale δ is identical to the *compaction length* of McKenzie (1984, 1985).

Substituting for the degree of melting (ν_m) in equation (4.5) governing the rate of melt production, substituting for the rate of melt production in the heat and mass conservation equations (4.1) and (4.2), substituting for the permeability (*k*) in the momentum conservation equation (4.3), substituting the scaled and dimensionless variables (4.12)-(4.16), simplifying, and dropping primes, yields the dimensionless governing equations

$$\frac{\partial \phi}{\partial t}=\frac{1}{\varphi}\frac{\partial}{\partial z}\left((1-\varphi\phi)w_s\right)+\frac{\partial \theta}{\partial t}+\left(w_m+w_s\right)\frac{\partial \theta}{\partial z} \tag{4.17}$$

$$\frac{\partial \theta}{\partial t}=\kappa_{eff}\frac{\partial^2 \theta}{\partial z^2}-Ste\left(w_m+w_s\right)\frac{\partial \theta}{\partial z} \tag{4.18}$$

$$\frac{\partial^2 w_s}{\partial z^2}=\frac{w_s}{\phi^n}+\frac{(1-\varphi\phi)}{(1-\varphi)} \tag{4.19}$$

$$\varphi\phi w_m=-(1-\varphi\phi)w_s \tag{4.20}$$

$$\frac{\partial \theta}{\partial t}=\chi\kappa_{eff}\frac{\partial^2 \theta}{\partial z^2} \tag{4.21}$$

with

$$\kappa_{eff}=\frac{k\tau}{\rho c_{eff}\delta^2} \tag{4.22}$$

$$Ste=\frac{L}{c_{eff}\left(T_{liq}-T_{sol}\right)} \tag{4.23}$$

$$c_{eff}=c_p+\frac{L}{T_{liq}-T_{sol}} \tag{4.24}$$

$$\chi=1+\frac{L}{c_p\left(T_{liq}-T_{sol}\right)} \tag{4.25}$$

The initial conditions become

$$\theta(0,0)=0 \tag{4.26a}$$

$$\frac{\partial}{\partial z}\left(\theta(z,0)\right)=\psi_{geo} \tag{4.26b}$$

$$\phi(z,0)=w_m(z,0)=w_s(z,0)=0 \tag{4.26c}$$

with

$$\psi_{geo}=(\delta/(T_{liq}-T_{sol}))T_{geo} \tag{4.27}$$

The boundary conditions become

$$\theta(0,t)=1 \tag{4.28a}$$

$$w_m(0,t)=w_s(0,t)=w_m(z_0,t)=w_s(z_0,t)=0 \tag{4.28b}$$

$$\theta(z_0,t)=0 \tag{4.28c}$$

$$\frac{\partial}{\partial z}\left(\theta(z\to\infty,t)\right)\to\psi_{geo} \tag{4.28d}$$

where z_0 denotes the dimensionless position of the $\theta = 0$ isotherm.

Simplification and non-dimensionalisation of the governing equations has reduced them to a system of five equations (4.17) - (4.21) governed by six externally prescribed dimensionless parameters: the effective thermal diffusivity in the partial melt zone (κ_{eff}); the Stefan number (Ste); the exponent in the permeability relation (n); the degree of melting at the contact (φ); the ratio of the thermal diffusivity in the solid rock to the effective thermal diffusivity in the partial melt zone (χ); and the initial geothermal gradient (ψ_{geo}). The expression given for χ (equation 4.25) has been simplified, and demonstrates that its value depends only upon the variables L, c_p, T_{liq} and T_{sol}.

4.2.4 Governing parameters

4.2.4.1 Dimensional variables

The values of the dimensionless governing parameters κ_{eff}, Ste, χ and ψ_{geo}, depend upon the dimensional variables which appear in their defining equations (4.22, 4.23, 4.25, 4.27). These variables are listed, along with suitable values for lower crustal rocks, in table 4.2. With the exception of the constant (b) in the permeability-porosity equation (4.6), and the melt and matrix viscosities (μ_m, μ_s, ξ_s), the variables are well constrained. In contrast, the constant in the permeability-porosity equation and the melt and matrix viscosities are poorly constrained, and the choice of suitable values for partially molten crustal rocks warrants further discussion.

4.2.4.1(i) Characterisation of permeability. The simple permeability-porosity equation presented in §3.2.1 and used in this chapter (equation (4.6)), is based upon the semi-empirical Blake-Kozeny-Carman equation, in which the constant b is chosen to fit experimentally derived permeability-porosity data for a given material (Bear, 1972; Dullien, 1979). As yet, no permeability-porosity measurements of partially molten crustal rocks have been made, and so suitable values of b must be deduced from other data.

The relationship between permeability and porosity for any material is defined uniquely by its pore space morphology (Dullien, 1979; Sahimi, 1993). During melting and melt migration, the grains of a partially molten rock must be either completely texturally equilibrated, completely texturally unequilibrated, or at some intermediate stage. If the grains are completely equilibrated, then the pore space morphology is governed only by the solid-solid and solid-liquid interfacial energies at the minimum energy configuration, even if the surface energies of the grains are anisotropic (von Bargen and Waff, 1986; Cheadle, 1989; Waff and Faul, 1992; and see the discussion in §2.3.3); if the grains are completely unequilibrated, then the pore space morphology is governed by individual grain morphologies, and the spatial distribution of the grains within the rock matrix. For a completely equilibrated, fluid saturated, equigranular mush of isotropic grains, the pore space morphology, and hence the relationship between permeability and porosity, may be uniquely characterised;

Symbol	Description	Minimum-maximum values	Units
k	thermal conductivity[1]	1 - 3	$W K^{-1} m^{-1}$
c_p	specific heat capacity[2]	1,020 - 1,220	$J kg^{-1} K^{-1}$
L	latent heat[3]	200,000 - 600,000	$J kg^{-1}$
$T_{liq}-T_{sol}$	liquidus-solidus interval[4]	200 - 600	K
T_{geo}	initial geothermal gradient[5]	5 - 20	$K km^{-1}$
ρ	density[6]	2,700 - 3,100	$kg m^{-3}$
$\rho_s-\rho_m$	matrix-melt density difference[7]	300 - 700	$kg m^{-3}$
a	matrix grain radius[8]	$2.5x10^{-4}$ - $5x10^{-3}$ (0.25-5mm)	m
n	exponent in permeability relation[9]	3	None
b	constant in permeability relation	1/2500 - 1/50	None
μ_m	melt shear viscosity	10^3 - 10^7	Pa s
μ_s	matrix shear viscosity	10^{15} - 10^{20}	Pa s
ξ_s	matrix bulk viscosity	10^{15} - 10^{21}	Pa s
CMF	Critical Melt Fraction	0.3 - 0.65	None
φ	degree of melting at the contact[10]	≤ 0.65	None
κ_{eff}	dimensionless effective thermal diffusivity	10^{-8} - 10^{+8}	None
ψ_{geo}	dimensionless initial geothermal gradient	10^{-6} - 10^{+2}	None
Ste	Stefan number	0.21 - 0.75	None
χ	ratio of thermal diffusivities in the partial melt zone and solid rock	1.27 - 3.94	None

Table 4.2. Summary of the dimensional variables and dimensionless parameters used in the model, with suitable values.

---

[1] Data for common lower crustal rocks from Clauser and Huenges (1995), valid over the temperature range 600 - 1300 K. Thermal conductivities vary by less than 25% over this temperature range. Lower values represent quartz poor rocks (e.g. gabbro, amphibolite); higher values represent quartz rich rocks (e.g. tonalite, granodiorite, meta-pelite). The experimentally determined values presented by Murase and McBirney (1973) for basalt, andesite, and rhyolite melts also lie within this range.

[2] Calculated for common lower crustal rock compositions using data for individual minerals (albite/anorthite, sanidine, diopside, enstatite, quartz, muscovite) from Robie *et al.* (1978), valid over the temperature range 600-1300 K. Specific heat capacities of minerals vary by less than 20% over this temperature range, and by less than 25% between minerals and their melts (Richet and Bottinga, 1986; Neuville *et al.*, 1993).

[3] Calculated for common lower crustal rock compositions using enthalpies of fusion of individual minerals (albite/anorthite, sanidine, diopside, quartz) from Richet and Bottinga (1986). Lower values represent quartz rich rocks; higher values represent quartz poor rocks.

[4] Data from the melting experiments used to derive the equilibrium melt fraction curves shown in figure 4.2. Mica bearing rocks (e.g. meta-pelites) generally have the largest liquidus-solidus interval, because they have lower solidus temperatures than mica free rocks, but similar liquidus temperatures.

[5] Data from Pollack and Chapman (1977). Shallow geothermal gradient represents regions with low surface heat flow (e.g. Baltic Shield); steep geothermal gradient represents regions with high surface heat flow (e.g. Basin and Range Province).

[6] Densities for common lower crustal rock compositions calculated using mineral modal analysis from Rutter and Wyllie (1988), Vielzuf and Holloway (1988), Patiño Douce and Johnston (1991), Rushmer (1991), Beard and Lofgren (1991), and Rapp and Watson (1995), and density data for individual minerals (Deer *et al.*, 1992). The values presented by Turcotte and Schubert (1982) lie within the range of calculated values.

[7] Densities for common lower crustal rock compositions from 6. Densities for granitic melt compositions calculated using the model of Lange and Carmichael (1987), and compositional data from Beard and Lofgren (1991), Rushmer (1991), Rapp and Watson (1995), and analysis of granitic dykes from the Rosses pluton, Co. Donegal, Eire. The experimentally determined values presented by Murase and McBirney (1973) for rhyolite melt lie within the range of calculated values.

[8] Typical grainsize for high grade metamorphic (granulite facies) rocks, many of which are interpreted to be the residues left after the extraction of a granitic partial melt fraction (§2.3.2). Grainsize measurements from Vernon (1968); Spry (1969), Yardley *et al.* (1990), and sections of granulite facies rocks from the Ivrea Zone, north-west Italy.

[9] In the original derivation of the Blake-Kozeny-Carman permeability equation, $n=2$ for a network of randomly oriented tubes of constant cross section, while $n=3$ for a bed of packed spheres (Scott and Stevenson, 1986). The experimental results of Wark and Watson (1997) and Zhang *et al.* (1994), and the theoretical data of Cheadle (1989), indicate that a value of $n=3$ is the most suitable for both texturally equilibrated and unequilibrated rocks (see also figure 4.3).

[10] The degree of melting at the contact depends upon the initial temperature of the crust, the initial temperature of the intruded magma, and the kinetics of heat transfer in the magma. It must be less than the CMF for the model to be valid (§4.2.1). The degree of melting at the contact is discussed in more detail in chapter 5.

permeability-porosity data for such a mush has been derived theoretically by Cheadle (1989), and will be used to obtain a suitable value of b for texturally equilibrated rocks. The data, for a dihedral angle of 50°, is shown in figure 4.3(a); also shown is a best line fit to the data using the permeability-porosity equation (4.6) with b=1/50. The fit is good, except for a slight tendency to overestimate the permeability at high ($\phi > 0.2$) porosity. In contrast, for a completely unequilibrated, fluid saturated mush, the pore space morphology, and hence the relationship between porosity and permeability, cannot be uniquely characterised, because of the potentially 'infinite' number of possible grain morphologies and distributions; however, permeability-porosity data for an unequilibrated, hot pressed calcite aggregate has been obtained experimentally by Zhang *et al.* (1994), and will be used to indicate a suitable value of b for texturally unequilibrated rocks. The data is shown in figure 4.3(b) (*inset*); also shown are best line fits to the data. In contrast to the data for the equilibrated mush (figure 4.3(a)), the fit of equation (4.6) to the data for the unequilibrated calcite aggregate is good only for porosity in the range $\phi > 0.06$, with b = 1/2500. For porosity in the range $0.04 < \phi < 0.06$, a modified form of equation (4.6) is required, with ϕ replaced by $(\phi - \phi_c)$, $\phi_c = 0.04$, and b = 1/100, while for porosity in the range $\phi < 0.04$ (i.e. $\phi < \phi_c$), the aggregate is impermeable (Zhang *et al.*, 1994).

In any natural porous material, the pore space may be divided into *pore bodies*, in which most of the porosity resides, and *pore throats*, which connect the pore bodies (Sahimi, 1993). If all pore bodies are connected by pore throats at all porosities, then the variation in permeability with porosity is due only to the variation in the effective radii of the pore throats (and hence their resistance to flow) with porosity; moreover, the material is permeable at vanishingly small porosities (Bryant *et al.*, 1993). This is the case for a texturally equilibrated mush of isotropic grains, if the dihedral angle is less than 60° (Cheadle, 1989); the permeability decreases smoothly with decreasing porosity (figure 4.3(a)), and equation (4.6) is valid over the entire porosity range. Experimentally determined values of the dihedral angle in partially molten silicate rocks range between 30° and 60° (Cheadle, 1989, and references therein); consequently, a texturally equilibrated, partially molten silicate rock is likely to be permeable at very small porosities (< 0.001), in which case equation (4.6) is valid for equilibrated rocks over the entire porosity range. However, if all pore bodies are not connected by pore throats at all porosities, then the variation in permeability with porosity is due both to the variation in the effective radii of the pore throats, and the variation in the number of connected pore bodies, with porosity; moreover, if at some critical porosity ϕ_c (the percolation threshold) the pore throats no longer form a connected network, then the material becomes impermeable (Bourbie and Zinszner, 1985; Bryant *et al.*, 1993). This is the case for the unequilibrated calcite aggregate investigated by Zhang *et al.* (1994). For porosity in the range $\phi > 0.06$, all pore bodies are interconnected, the permeability decreases smoothly with decreasing porosity, and the permeability-porosity equation (4.6) is valid. For porosity in the range $\phi < 0.06$, an increasing number of pore bodies become disconnected with

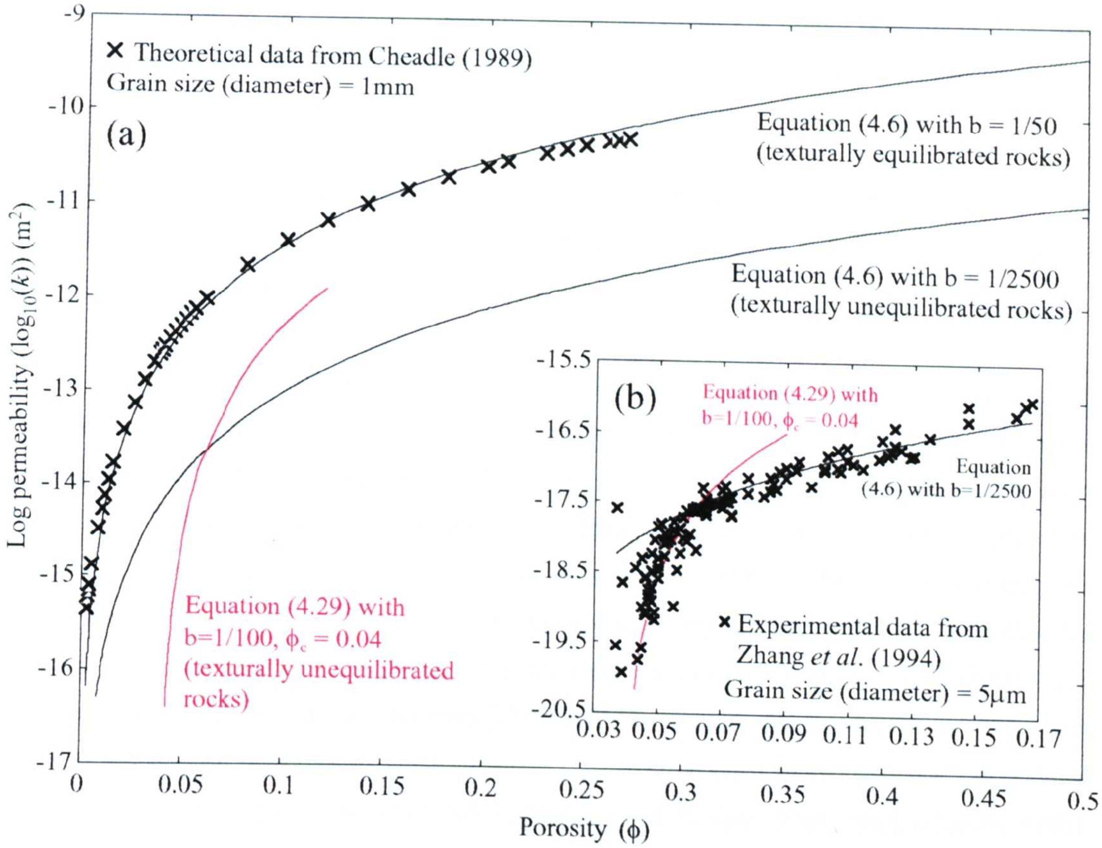

Figure 4.3. (a) Permeability - porosity relations for texturally equilibrated and unequilibrated partially molten rocks with a grain size (diameter) of 1mm. The upper black curve is given by the permeability-porosity equation (4.6) with b = 1/50, and denotes the best fit to the theoretical data of Cheadle (1989), for a texturally equilibrated, monomineralic, fluid saturated mush of isotropic grains with a dihedral angle of 50° and a grain size (diameter) of 1mm. This curve represents the permeability-porosity behaviour of texturally equilibrated rocks. The lower black curve is given by the permeability-porosity equation (4.6) with b=1/2500, and represents the permeability-porosity behaviour of texturally unequilibrated rocks for porosity in the range $\phi > 0.06$. The red curve is given by the modified permeability-porosity equation (4.29) with b = 1/100 and ϕ_c = 0.04, and represents the permeability-porosity behaviour of texturally unequilibrated rocks for porosity in the range $0.04 < \phi < 0.06$. Below the percolation threshold ϕ_c, texturally unequilibrated rocks are impermeable.

(b) (*Inset*) Experimentally determined permeability - porosity relations for a texturally unequilibrated, hot pressed calcite aggregate with a grain size (diameter) of 1-30μm (Zhang *et al.*, 1994), which was used to deduce the permeability -porosity relations for texturally unequilibrated rocks shown in (a). The black curve is given by the permeability-porosity equation (4.6) with b=1/2500, and denotes the best fit to the experimental data of Zhang *et al.* (1994) for porosity in the range $\phi > 0.06$. The red curve is given by the modified permeability-porosity equation (4.29) with b=1/100 and ϕ_c = 0.04, and denotes the best fit to the experimental data of Zhang *et al.* (1994) for porosity in the range $0.04 < \phi < 0.06$. When fitting the curves to the experimental data, the mean grain size of the inequigranular calcite aggregate was assumed to be 5μm, based on the argument that the permeability of inequigranular materials is governed by the small grains, because they reside in channels between large grains (Wark and Watson, 1997). Axis labels are identical to those of plot (a).

decreasing porosity, so the permeability decreases more rapidly, and equation (4.6) is not valid. At $\phi = \phi_c = 0.04$ the pore throats no longer form a connected network, and the aggregate becomes impermeable (Zhang *et al.*, 1994). For porosity in the range $0.04 < \phi < 0.06$; equation (4.6) is valid only if the porosity ϕ is replaced by the *connected* porosity (ϕ - ϕ_c), and equation (4.6) becomes

$$k = \mathrm{ba}^2(\phi - \phi_c)^n \tag{4.29}$$

Consequently, in contrast to texturally equilibrated rocks, unequilibrated rocks are likely to be permeable only at porosities greater than the percolation threshold (ϕ_c), in which case equation (4.6) is not valid for unequilibrated rocks over the entire porosity range.

These arguments yield the permeability-porosity relations for completely texturally equilibrated, and completely texturally unequilibrated, partially molten rocks, shown in figure 4.3(a). The maximum and minimum values of b given in table 4.2 are based upon these permeability-porosity relations, and the range of values includes that proposed by McKenzie (1984) of $b = 1/1000$, based upon permeability-porosity data obtained experimentally by Maaloe and Scheie (1982) for compacted glass beads. However, the data of Cheadle (1989) for an ideal, equilibrated mush overestimates the permeability at high porosities; in equilibrated rocks, there is a maximum porosity for which the solid-liquid interfacial energies are a minimum (~0.19-0.01 for typical dihedral angles of 30° - 60° (Cheadle, 1989)), and at porosities greater than this the melt becomes inhomogeneously distributed and does not all contribute to the permeability (Jurewicz and Watson, 1984, 1985; Cheadle, 1989). Moreover, it must be emphasised that the values of b and ϕ_c (the percolation threshold) obtained for unequilibrated rocks from the data of Zhang *et al.* (1994), do not uniquely define the permeability-porosity relations of all unequilibrated rocks. For example, Wolf and Wyllie (1991) estimate a value of $\phi_c < 0.02$ for an unequilibrated, partially molten, hydrated basalt. The effect of a percolation threshold on solutions of the governing equations is investigated in §4.3.1.2; based on the arguments presented there, *all* the other solutions presented in this chapter are obtained using the permeability-porosity equation (4.6) over the entire porosity range.

4.2.4.1(ii) Melt shear viscosity. The viscosity of a silicate melt depends primarily upon its composition and temperature (Bottinga and Weill, 1972). The variation of viscosity with temperature for granitic (*sensu-lato*) melts of *constant* composition has been investigated experimentally using melted samples of rhyolitic obsidians; measured viscosities vary by over seven orders of magnitude (Shaw, 1963; Murase and McBirney, 1973; Ryan and Blevins, 1987). However, the variation of viscosity with temperature for granitic melts produced during partial melting has not been investigated; during melting, the composition of the melt continuously *changes*. If the composition of the melt is known, its viscosity may be calculated using the empirical model of Shaw (1972); melt compositions during partial melting have been obtained experimentally for a variety of lower crustal rock compositions (Rutter and Wyllie, 1988; Vielzuf and Holloway, 1988; Patiño Douce and Johnston, 1991; Rushmer, 1991; Beard and Lofgren, 1991; Rapp and Watson, 1995). Figure 4.4 shows the calculated variation of viscosity with temperature, for the granitic melt produced during partial melting of hydrated basalts, andesites, and meta-pelites. The water content of the melt is a critical control of its viscosity, and during *dehydration* melting, is governed by the breakdown of hydrous minerals such as amphibole and biotite (Clemens and Vielzuf, 1987; Rushmer, 1991). The 'wet' melt viscosities shown in figure 4.4 were calculated using experimentally determined water contents when available, or alternatively, water contents determined using the model of Clemens and Vielzuf (1987) (see figure 4.5 for details); the 'dry' melt viscosities were calculated assuming anhydrous melt compositions, and are shown for comparison only. The effect of water on viscosity is clear; wet melt viscosities are between 3 and 7 orders of magnitude lower than the corresponding dry viscosities. Moreover, dry melt viscosities decrease by ~0.5 - 5 orders of magnitude with increasing temperature; in contrast, wet melt viscosities decrease by only ~0.1 - 1 orders of magnitude with increasing temperature.

The observed variation in viscosity with temperature is due only to the *compositional* variation of the melt with temperature; the melt is always at its solidus temperature, and as the degree of melting increases, the composition of the melt changes. In general, an increase in the silica content of the melt causes an increase in viscosity; in contrast, an increase in the water content of the melt causes a decrease in viscosity (McBirney and Murase, 1984). To illustrate this, figure 4.5 shows the silica and water content of the melt as a function of temperature. The decrease in the silica content of the melt with increasing temperature (with the exception of the melt from the meta-pelite) causes the large decrease observed in the dry viscosity (figure 4.4). However, the decrease in the water content of the melt with increasing temperature compensates for the decrease in silica; consequently, the decrease observed in the wet melt viscosity with temperature is small (figure 4.4). This viscosity-temperature dependence is different to that observed in melt of *constant* composition, which is due only to the Arrhenius type behaviour of silicate melts, and should not be confused with it. Despite the different compositions of the melting rocks, the wet melt viscosities vary by less than 3 orders of magnitude, between ~450 Pa s and ~1.5×10^5 Pa s. The values of the melt shear viscosity given in table 4.2 are based upon these calculated values, and the selected range includes the values obtained experimentally by Shaw (1963) for hydrous rhyolite.

4.2.4.1(iii) Matrix shear and bulk viscosities. The rheology of a *partially molten* rock is primarily governed by its mineralogy and grain size, and the strain rate regime. The grain size and strain rate govern the deformation mechanism for a particular mineralogy (Ranalli, 1987). Large grain sizes and/or high strain rates favour deformation at the grain scale by dislocation creep, while small grain sizes and/or low strain rates favour deformation at the grain scale by diffusion creep (Dell'Angelo *et*

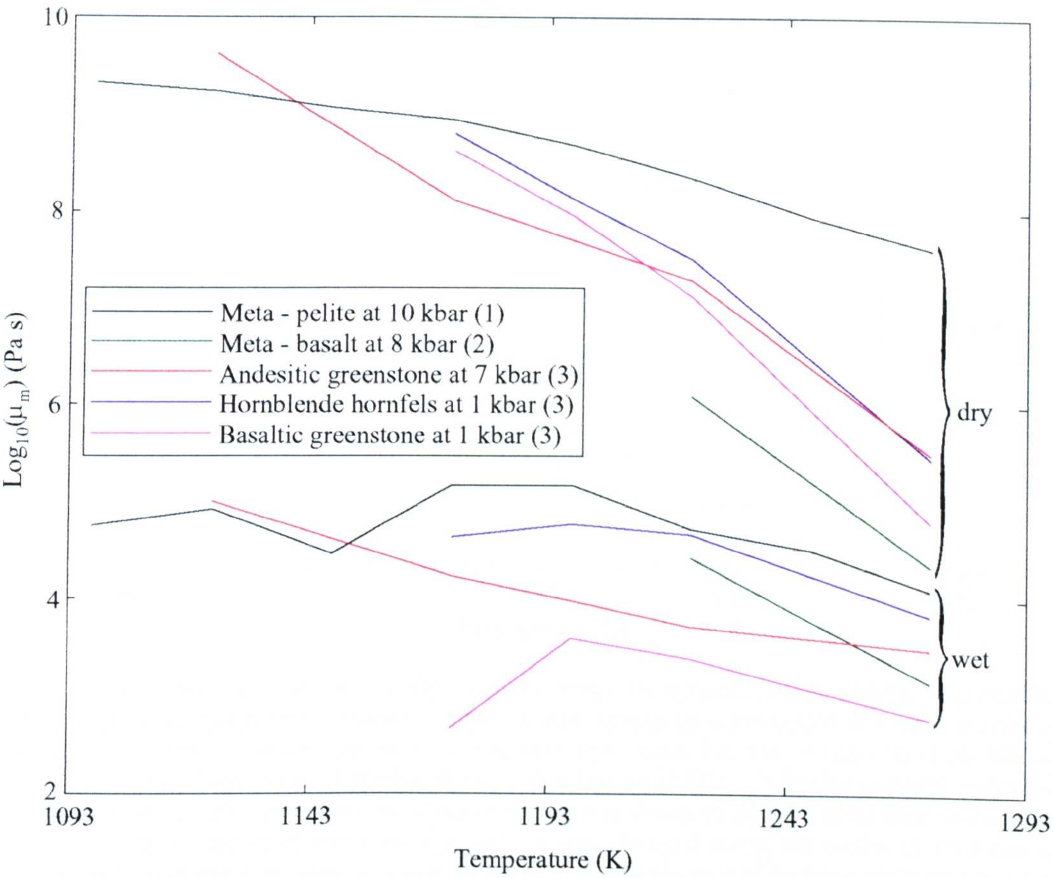

Figure 4.4. Shear viscosity versus temperature of the granitic melt produced during partial melting of hydrated basalts, andesites and meta-pelites, calculated using the empirical model of Shaw (1972). Compositional data from (1) Patiño-Douce and Johnston (1991); (2) Rushmer (1991); (3) Beard and Lofgren (1991). 'Wet' melt viscosities were calculated using the water contents shown in figure 4.5; 'dry' melt viscosities were calculated assuming anhydrous melt compositions, and are shown for comparison only.

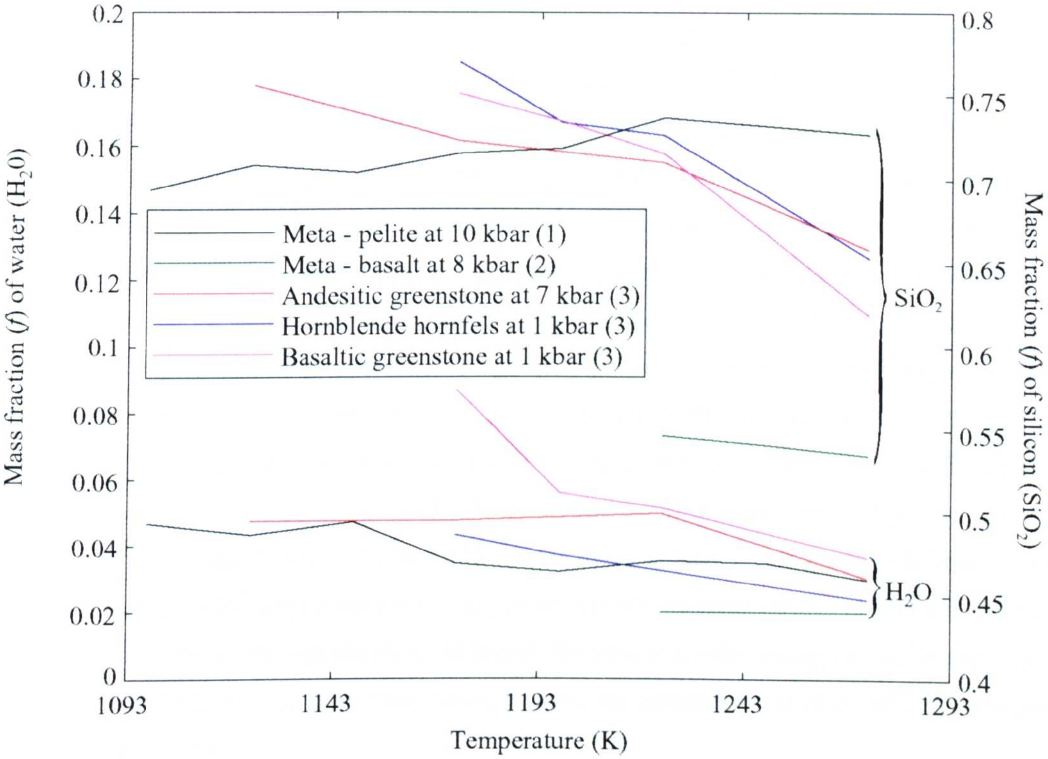

Figure 4.5. The water (H_2O) and silica (SiO_2) content versus temperature, of the granitic melt produced during partial melting of hydrated basalts, andesites, and meta-pelites, expressed as a mass fraction (*f*). Mass fraction of water plots on the left hand ordinate axis; mass fraction of silica plots on the right hand ordinate axis. Data from (1) Patiño-Douce and Johnston (1991); (2) Rushmer (1991); (3) Beard and Lofgren (1991). The mass fraction of water for (1) was obtained directly from their experimental results. The mass fraction of water for (2) and (3) was obtained using the model of Clemens and Vielzuf (1987), following the approach adopted by (2). In the absence of hydrous residual phases, the mass fraction of water in the melt is given by

$$f(H_2O \text{ in melt}) = f(H_2O \text{ in rock before melting}) / f(\text{melt formed}) \qquad (4.30)$$

Clemens and Vielzuf (1987) have proposed that during dehydration melting, the water content of the melt is buffered by the presence of hydrous residual phases, and remains approximately constant while they remain stable. The significant hydrous phase in the basaltic and andesitic rocks investigated by (2) and (3) is amphibole. The stability of amphibole during dehydration melting is poorly understood (Rapp, 1995). (2) found amphibole as a stable residual phase in the presence of melt; in contrast; (3) found that amphibole was unstable and decomposed soon after the onset of melting, leaving an anhydrous residue. For temperature regimes in which amphibole was a stable residual phase, the mass fraction of water in the melt was assumed to be constant, and equal to that when amphibole eventually decomposed (calculated using equation (4.30)). For temperature regimes in which amphibole was not a stable residual phase, the mass fraction of water was calculated using equation (4.30).

al., 1987; Dell'Angelo and Tullis, 1988). Deformation in the *solid* lower crust is thought to occur by dislocation creep (Ranalli, 1987), but deformation in the *partially molten* lower crust is poorly understood. Unless the deformation mechanism is known, the rheology of a rock cannot be specified.

In deformation experiments on sintered, fine grained 'granitic' aggregates, composed of quartz, albite and microcline, Dell'Angelo *et al.* (1987) found that, at a strain rate of ~10^{-6} s^{-1}, confining pressure of 1500 MPa (15 kbar), and temperature of 1173 K, deformation was dominated by *dislocation* creep in melt free aggregates with a grain size (diameter) of ~2-10μm, but that the addition of 3-5% melt induced a transition to deformation dominated by 'melt-enhanced' *diffusion* creep. Melt was produced by adding ~1 wt% water to the samples before sintering. Melt-enhanced diffusion creep is effectively a form of grain boundary (Coble) creep, in which the microscale diffusion rate of components along solid-solid grain boundaries governs the macroscale creep rate (Pharr and Ashby, 1983; Cooper and Kohlstedt, 1984; Ranalli, 1987). In texturally equilibrated rocks, the melt is confined to grain edges, and the presence of melt enhances the creep rate only by shortening the effective (dry) diffusion length of the solid-solid grain boundaries (Cooper and Kohlstedt, 1984). In texturally unequilibrated rocks, the presence of melt is likely to have a similar effect unless the melt completely wets the solid-solid grain boundaries, in which case the creep rate is enhanced by the rapid diffusion of components through the melt. However, the melt in a *compacting*, unequilibrated rock is unlikely to completely wet the grain boundaries, because the compressional stress will act to expel it (Pharr and Ashby, 1983).

In order to estimate the strain rates for which deformation in partially molten crustal rocks will be governed by either dislocation creep, or melt-enhanced diffusion creep, the experimental results of Dell'Angelo *et al.* (1987) for fine grained (a ~ 2.5μm) aggregates must be extrapolated to represent coarse grained (a ~ 0.5mm) crustal rocks. Assuming that the strain rate may be related to grain size and applied stress using a power law of the form (Kohlstedt and Chopra, 1994)

$$\dot{\varepsilon} = A\frac{\sigma^q}{a^m}\exp(-Q/RT) \tag{4.31}$$

then for a given applied stress σ, the strain rate may be scaled to a new grain size using an equation of the form

$$\frac{\dot{\varepsilon}_1}{\dot{\varepsilon}_2} = \left(\frac{a_2}{a_1}\right)^m \tag{4.32}$$

where strain rate $\dot{\varepsilon}_1$ corresponds to grain size a_1, and strain rate $\dot{\varepsilon}_2$ corresponds to grain size a_2. Using a value of m = 3, suitable for grain boundary diffusion creep (Ranalli, 1987; Kohlstedt and Chopra, 1994), the experimental strain rate of ~10^{-6} s^{-1} at which Dell'Angelo *et al.* (1987) found a transition from dislocation to melt-enhanced diffusional creep scales to ~10^{-13} s^{-1} for a typical grain size (diameter) of ~ 1mm. For strain rates equal to or less than this figure, the extrapolated results of

Dell'Angelo *et al.* (1987) indicate that the rheology of a partially molten crustal rock will be governed by melt-enhanced diffusion creep. Maximum strain rates predicted by the model during compaction in the crust are ~10^{-13} - 10^{-20} s^{-1} (§3.4)[1], up to seven orders of magnitude less than the transition estimate; deformation is therefore likely to be governed by melt-enhanced diffusion creep. For comparison, the results of Kohlstedt and Chopra (1994) indicate that melt-enhanced diffusion creep governs the rheology of olivine aggregates containing ~ 9% basaltic melt, at temperatures of ~1573 K, for strain rates of ~10^{-10} s^{-1} and a grain size (diameter) of 1mm (§3.4).

The rheology of an aggregate undergoing steady-state deformation by diffusion creep is Newtonian (Cooper and Kohlstedt, 1984; Ranalli, 1987). For the simplest case of a single component, equigranular aggregate deforming by grain boundary creep, the shear viscosity may be expressed as (Ranalli, 1987)

$$\mu_s = \frac{k_b T a^3}{141 \Omega D\gamma} \tag{4.33}$$

where k_b is Boltzmann's constant (= 1.381×10^{-23} J K^{-1}), Ω is the atomic volume of the material, and $D\gamma$ is the effective grain boundary diffusivity. If the aggregate contains a small fraction (< 0.1) of spherical pores, the bulk viscosity may be expressed as (Arzt *et al.*, 1983)

$$\xi_s = (1-\phi)\frac{\left[3\left(\phi^{2/3}-1\right)+\left(\phi^{2/3}+1\right)\ln(1/\phi)\right]}{1-\phi^{2/3}}\frac{k_b T a^3}{54 \Omega D\gamma} \tag{4.34}$$

Application of these simple expressions to crustal rocks is hampered by the lack of available data for the effective grain boundary diffusivity ($D\gamma$). den Brok (1992) suggests a value of $D\gamma \sim 10^{-21}$ $m^2 s^{-1}$ for oxygen in wet quartz aggregates, at 1200 MPa (12 kbar) and 1073K, based upon the work of Farver and Yund (1991). The value of Ω for quartz is 1.16×10^{-28} m^3 (Lide and Frederiske, 1996). Assuming that the diffusion of oxygen rather than silicon governs creep, assuming a temperature of 1073K, and substituting these values into equation (4.33), yields a maximum shear viscosity of ~10^{20} Pa s for a quartz aggregate with a grain size (radius) of 5 mm, and a minimum shear viscosity of ~10^{16} Pa s for a quartz aggregate with a grain size (radius) of 0.25 mm (table 4.2). Equation (4.34) yields bulk viscosities as a function of porosity shown in figure 4.6. Except at very low porosities ($\phi < 0.001$), equation (4.34) yields a maximum bulk viscosity of ~10^{21} Pa s for a quartz aggregate with a grain size (radius) of 5 mm, and a minimum bulk viscosity of ~10^{16} Pa s for a quartz aggregate with a grain size (radius) of 0.25 mm (table 4.2).

---

[1] Alternatively, an order of magnitude estimate of the strain rate during compaction in the lower crust may be obtained in the following way: assume 10% of the melt is completely extracted from a 'typical' 5 km thick partial melt zone in 500,000 years. The partial melt zone is shortened by 500m in this time, requiring an 'average' strain rate of ~1×10^{-18} s^{-1}. Longer extraction times will lead to smaller 'average' strain rates.

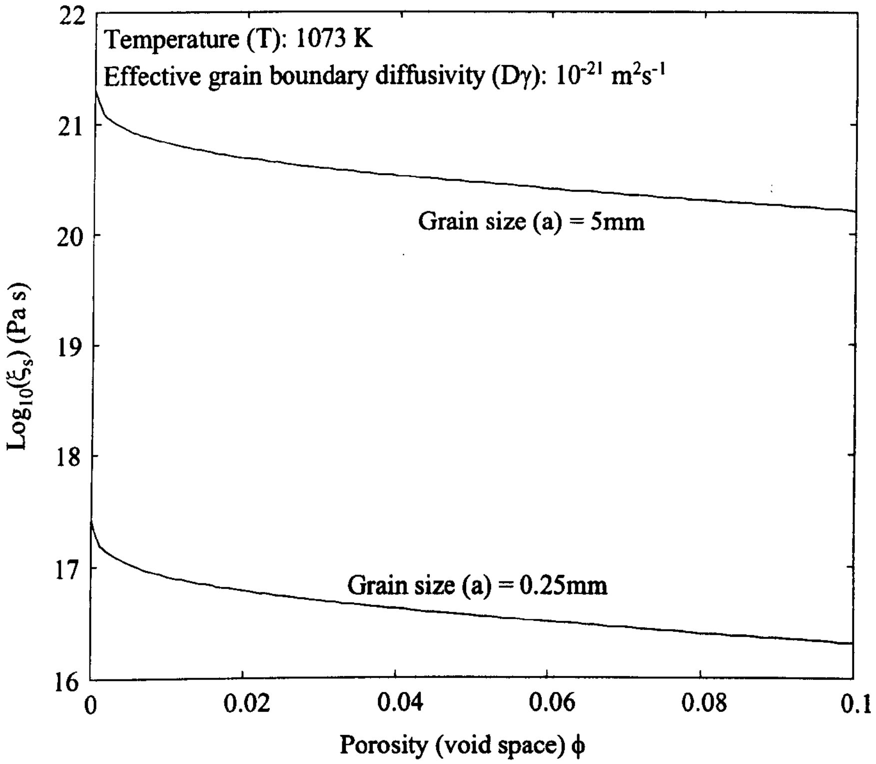

Figure 4.6. Matrix bulk viscosity versus porosity (void space), for a pure quartz aggregate deforming by grain boundary diffusion creep, calculated using equation (4.34).

It is not clear how these estimated viscosities for quartz aggregates relate to the viscosities of partially molten crustal rocks. Most crustal rocks are polymineralic, and the diffusion controlled creep of polymineralic aggregates is poorly understood. Ranalli (1987) states that when more than one diffusing component is present, the slowest moving controls creep, yet Wheeler (1992) argues that components may mix and interact during diffusion, leading to complex behaviour which may significantly enhance diffusional creep rates in polymineralic aggregates when compared to their monomineralic counterparts. Neither of the equations for the shear and bulk viscosity includes the effect of melt in the pore spaces, which should enhance the creep rate (Cooper and Kohlstedt, 1984; Dell'Angelo, *et al.*, 1987), although during compaction the melt must be expelled from the pores and the effect of this on the bulk viscosity is unknown (Dingwell *et al.*, 1993). Moreover, the spherical pores assumed in the derivation of equation (4.34) are not likely to be a good approximation of the interconnected pores of a partially molten rock (McKenzie, 1984). However, in the absence of experimental data for either the bulk and shear viscosities of crustal rocks, or the effective grain boundary diffusivities for crustal minerals other than quartz, the estimated shear and bulk viscosities for quartz aggregates will be used to provide order of magnitude estimates for the shear and bulk viscosities of partially molten crustal rocks. The values of the shear and bulk viscosities given in table 4.2 are based upon these estimates, except that the lower values have been reduced by an order of magnitude; the estimates obtained here are for low porosities, and as the porosity increases, both the shear and bulk viscosities are expected to decrease (Scott and Stevenson, 1986). The selected range includes the values proposed by McKenzie (1984, 1985) and Scott and Stevenson (1986) for partially molten mantle rocks.

4.2.4.2 Dimensionless parameters

Substituting suitable values for the dimensional variables into the defining equations (4.22, 4.23, 4.25, 4.27) yields the values for the dimensionless parameters κ_{eff}, Ste, χ and ψ_{geo}, given in table 4.2. The large variation in the values of κ_{eff} and ψ_{geo} primarily reflects the large variation in the melt and matrix viscosities, which appear in the defining equations for both the characteristic lengthscale (equation (4.13)) and the characteristic timescale (equation (4.14)). In contrast, the variation in values for Ste and χ is small.

4.2.4.3 The Critical Melt Fraction (CMF)

The CMF does not appear directly in the governing equations, or in the equations defining the dimensionless governing parameters, yet is important because it dictates the porosity at which a partially molten rock forms a mobile magma (§2.3.1). If the rock is in textural equilibrium, then the value of the CMF depends only upon the contiguity of the matrix (Miller *et al.*, 1988). Contiguity is a quantitative measure of the solid grain-grain interconnectivity in a fluid saturated mush, and depends upon the fluid volume fraction, the microscopic distribution of fluid throughout the mush, and the solid grain size distribution. The contiguity of an ideal, texturally equilibrated, monomineralic, equigranular mush of isotropic grains as a function of porosity and dihedral angle has been derived theoretically by Cheadle (1989), and for dihedral angles of 30° - 60° (§4.2.4.1(i)), yields values for the CMF of 0.37 - 0.46. These represent *minimum* values, because in equilibrated rocks at porosities greater than the minimum energy porosity the melt becomes inhomogeneously distributed and does not all contribute to reducing the contiguity (§4.2.4.1(i)). For partially molten rocks which are not in textural equilibrium, experimentally and theoretically obtained estimates of the CMF range from 0.2 to 0.7 (e.g. Arzi, 1978; van der Molen and Paterson, 1979; Philpotts and Carroll, 1996). The values of the CMF given in table 4.2 are based upon these estimates for equilibrated and unequilibrated rocks, with the exception of the lowest estimate of 0.2 ± 0.1 presented by Arzi (1978), which was obtained theoretically using simple arguments based upon the Einstein-Roscoe equation for rigid particles suspended in a viscous, Newtonian melt. This is a poor approximation of a partially molten rock. Also, the highest estimate of ~0.7 obtained experimentally by Philpotts and Carroll (1996) for a partially molten tholeiitic basalt has been reduced to 0.65. They performed their experiments at compressive stresses of the order of kPa, yet compressive stresses in the lower crust are of the order of GPa, and it is unlikely that their sample would have maintained its strength at such high melt fractions for stresses of this magnitude.

4.3 Results

The governing equations (4.17) - (4.21) are amenable to solution using standard numerical techniques; they were approximated using explicit finite difference schemes, and solved numerically using FORTRAN codes processed on a Sun SPARC 5 workstation. The implementation and testing of the finite difference schemes is described in Appendix A.

None of the governing dimensionless parameters φ, χ, Ste or ψ_{geo}, are independent of κ_{eff}; substituting for the characteristic time (τ) and length (δ) scales in equation (4.22) reveals that κ_{eff} varies with φ as

$$\kappa_{eff} \sim 1/(1-\varphi)\varphi^{9/2} \qquad (4.35)$$

(§3.3), while κ_{eff}, χ and Ste are governed by the values of the variables L, c_p, T_{liq} and T_{sol} (equations (4.22) - (4.25)). Both κ_{eff} and ψ_{geo} depend upon the value of the characteristic lengthscale δ, which in turn depends upon the variables ξ_s, μ_s, μ_m, b and a (equations (4.13) and (4.16)). However, for fixed values of χ and Ste, κ_{eff} may still vary over effectively its entire range; consequently, χ and Ste are assumed to be independent of κ_{eff} in all numerical experiments. However, χ and Ste cannot be assumed to be independent; inspection of equations (4.23) and (4.25) reveals that Ste varies with χ as Ste = $(\chi-1)/\chi$; i.e. the largest values of χ correspond with the largest values of Ste and *vice-versa*.

More significantly, κ_{eff} and ψ_{geo} cannot be assumed to be independent, and both vary over a wide range of values, the magnitude of which is governed predominantly by the magnitude of the matrix and melt viscosities (ξ_s, μ_s and μ_m), the grain size (a), and the permeability constant (b). Substituting for the characteristic time (τ) and length (δ) scales in equations (4.27) and (4.22) reveals that ψ_{geo} and κ_{eff} vary with ξ_s, μ_s, μ_m, a and b as

$$\psi_{geo} \sim \frac{(\xi_s + 4\mu_s/3)^{1/2} b^{1/2} a}{\mu_m^{1/2}} \tag{4.36}$$

$$\kappa_{eff} \sim \frac{\mu_m^{3/2}}{(\xi_s + 4\mu_s/3)^{1/2} b^{3/2} a^3} \tag{4.37}$$

Inspection of equations (4.36) and (4.37) reveals that the smallest values of κ_{eff} must correspond with the largest values of ψ_{geo}, and vice-versa. Substitution of the values of ξ_s, μ_s, μ_m, a and b given in table 4.2 reveals the range of available values for κ_{eff} and ψ_{geo} shown in table 4.3. For the smallest value of κ_{eff} (10^{-8}), the smallest corresponding value of ψ_{geo} is ~100; for the largest value of κ_{eff} (10^{+8}), the largest corresponding value of ψ_{geo} is ~10^{-6}. Consequently, rather than assuming ψ_{geo} is independent of κ_{eff}, the governing equations were solved only for the values of κ_{eff} and ψ_{geo} shown in table 4.3.

4.3.1 Dimensionless results

4.3.1.1 Form of the spatial porosity distributions

Figure 4.7(i - iii) shows a representative selection of normalised spatial porosity and degree of melting (dimensionless temperature) distributions, for $\varphi = 0.5$, $\chi = 2.5$, and Ste = 0.5, after 30 time units have elapsed. Note that the degree of melting distribution denotes also the distribution of melt in the *absence* of compaction and melt migration. The form of the distributions depends upon κ_{eff} in a similar manner to that found in §3.3.2. In partially molten rocks with large values of κ_{eff} ($\geq 10^4$), there is little difference between the porosity and degree of melting distributions (figure 4.7(iii) (d)). In rocks with values of κ_{eff} between ~10^3 and ~10, the upwardly migrating melt develops a high amplitude 'porosity wave', and trailing porosity waves begin to develop behind the leading wave (figure 4.7(iii) (a-d); figure 4.7(ii) (c-d)). In rocks with κ_{eff} between ~10 and ~10^{-2}, with the exception of the largest (ψ_{geo} = 1) geotherm, the trailing waves are well developed, and display decreasing amplitude with depth (figure 4.7(ii) (a-c); figure 4.7(i) (b-d)). In rocks with small values of κ_{eff} ($\leq 10^{-3}$), the amplitude of the leading porosity wave is small (figure 4.7(i) (a)).

In a partial melt zone with a given value of κ_{eff}, the effect of increasing ψ_{geo} is to maintain or increase the amplitude of the leading porosity wave, and to move the position of the porosity maximum upwards *relative* to the position of the solidus isotherm (z_0); i.e. closer to the top of the partial melt

κ_{eff}	ψ_{geo}								
	10^{-6}	10^{-5}	10^{-4}	10^{-3}	10^{-2}	10^{-1}	10^{0}	10^{+1}	10^{+2}
10^{-8}									●
10^{-7}									●
10^{-6}								●	
10^{-5}								●	
10^{-4}								●	
10^{-3}							●	●	
10^{-2}					●	●	●		
10^{-1}				●	●	●	●		
10^{0}			●	●	●	●	●		
10^{+1}			●	●	●	●	●		
10^{+2}			●	●	●	●			
10^{+3}			●	●	●				
10^{+4}		●	●						
10^{+5}		●							
10^{+6}		●							
10^{+7}		●							
10^{+8}	●								

Table 4.3. The range of available values for the dimensionless initial geotherm ψ_{geo}, and the dimensionless effective diffusivity κ_{eff}, obtained using equations (4.36) and (4.37) and values of the constituent variables (ξ_s, μ_s etc.) from table 4.2. The dimensionless initial geotherm ψ_{geo} and the dimensionless effective diffusivity κ_{eff} are not independent; for a given value of κ_{eff}, the range of available values for ψ_{geo} is restricted. Available values are denoted by a dot. The range of values of ψ_{geo} and κ_{eff} within the red square denotes the range of values for which the formation of a mobile magma is predicted; see text for details.

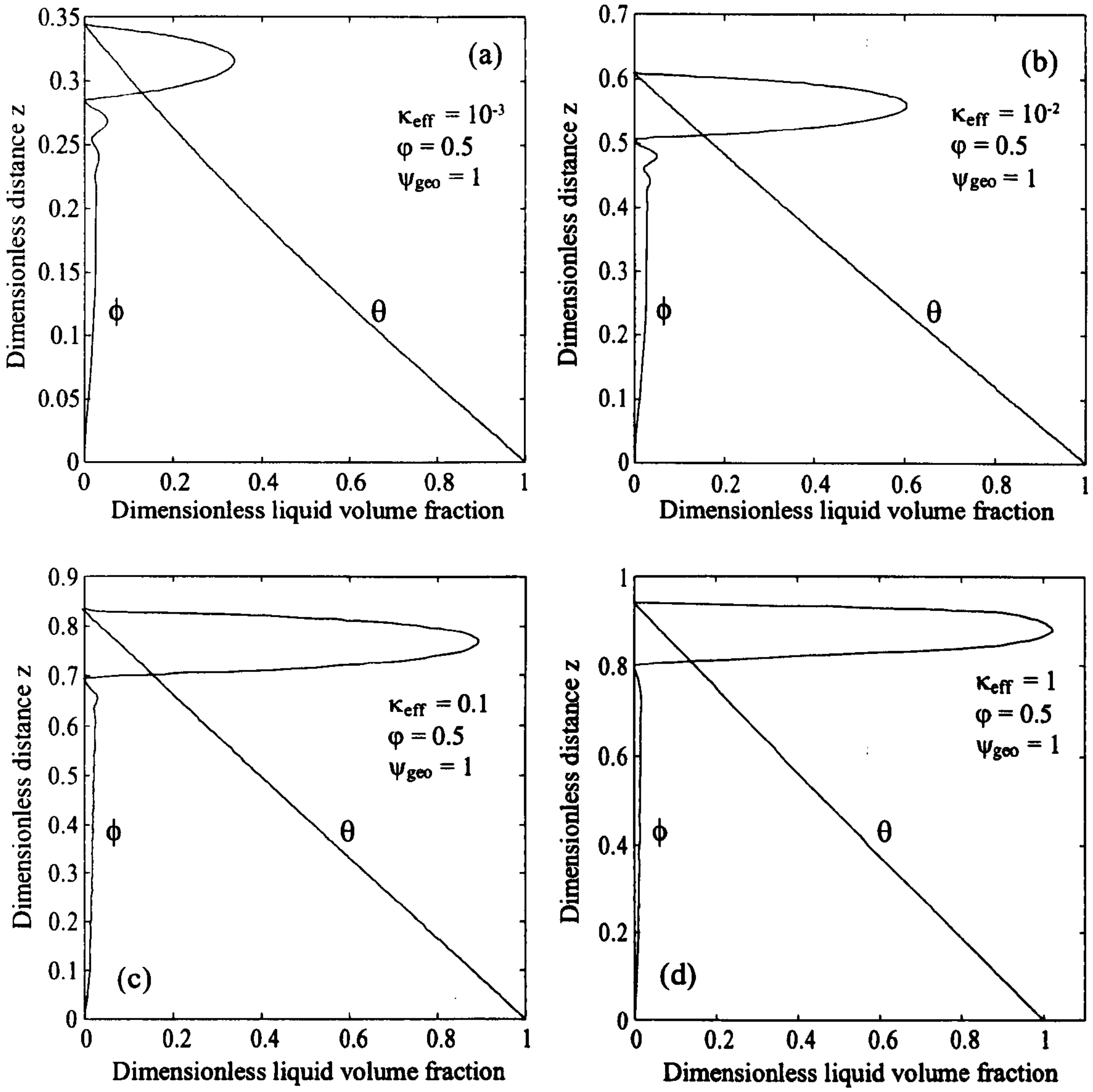

Figure 4.7(i). Normalised dimensionless spatial porosity (ϕ) and degree of melting (θ) distributions, after 30 time units, with: (a) $\kappa_{eff} = 10^{-3}$, $\varphi = 0.5$, $\psi_{geo} = 1$; (b) $\kappa_{eff} = 10^{-2}$, $\varphi = 0.5$, $\psi_{geo} = 1$; (c) $\kappa_{eff} = 0.1$, $\varphi = 0.5$, $\psi_{geo} = 1$; (d) $\kappa_{eff} = 1$, $\varphi = 0.5$, $\psi_{geo} = 1$. In all cases, Ste = 0.5 and $\chi = 2.5$. Liquid volume fractions (porosity and degree of melting) are normalised to the degree of melting at z=0 (φ). Note that both ordinate and abscissa scales differ between plots.

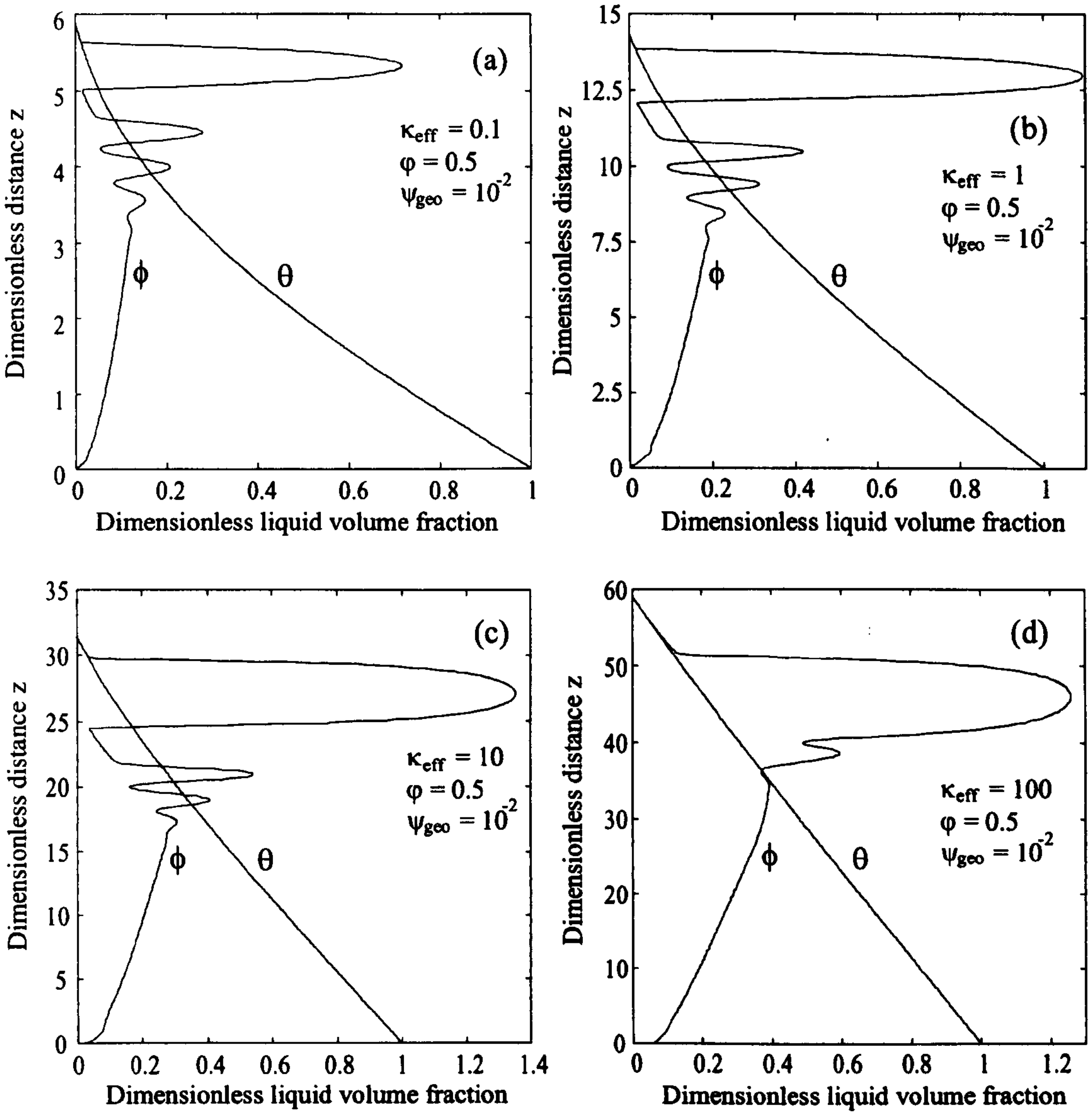

Figure 4.7(ii). Normalised dimensionless spatial porosity (ϕ) and degree of melting (θ) distributions, after 30 time units, with: (a) $\kappa_{eff} = 0.1$, $\varphi = 0.5$, $\psi_{geo} = 10^{-2}$; (b) $\kappa_{eff} = 1$, $\varphi = 0.5$, $\psi_{geo} = 10^{-2}$; (c) $\kappa_{eff} = 10$, $\varphi = 0.5$, $\psi_{geo} = 10^{-2}$; (d) $\kappa_{eff} = 100$, $\varphi = 0.5$, $\psi_{geo} = 10^{-2}$. In all cases, Ste = 0.5 and χ = 2.5. Liquid volume fractions (porosity and degree of melting) are normalised to the degree of melting at z=0 (φ). Note that both ordinate and abscissa scales differ between plots.

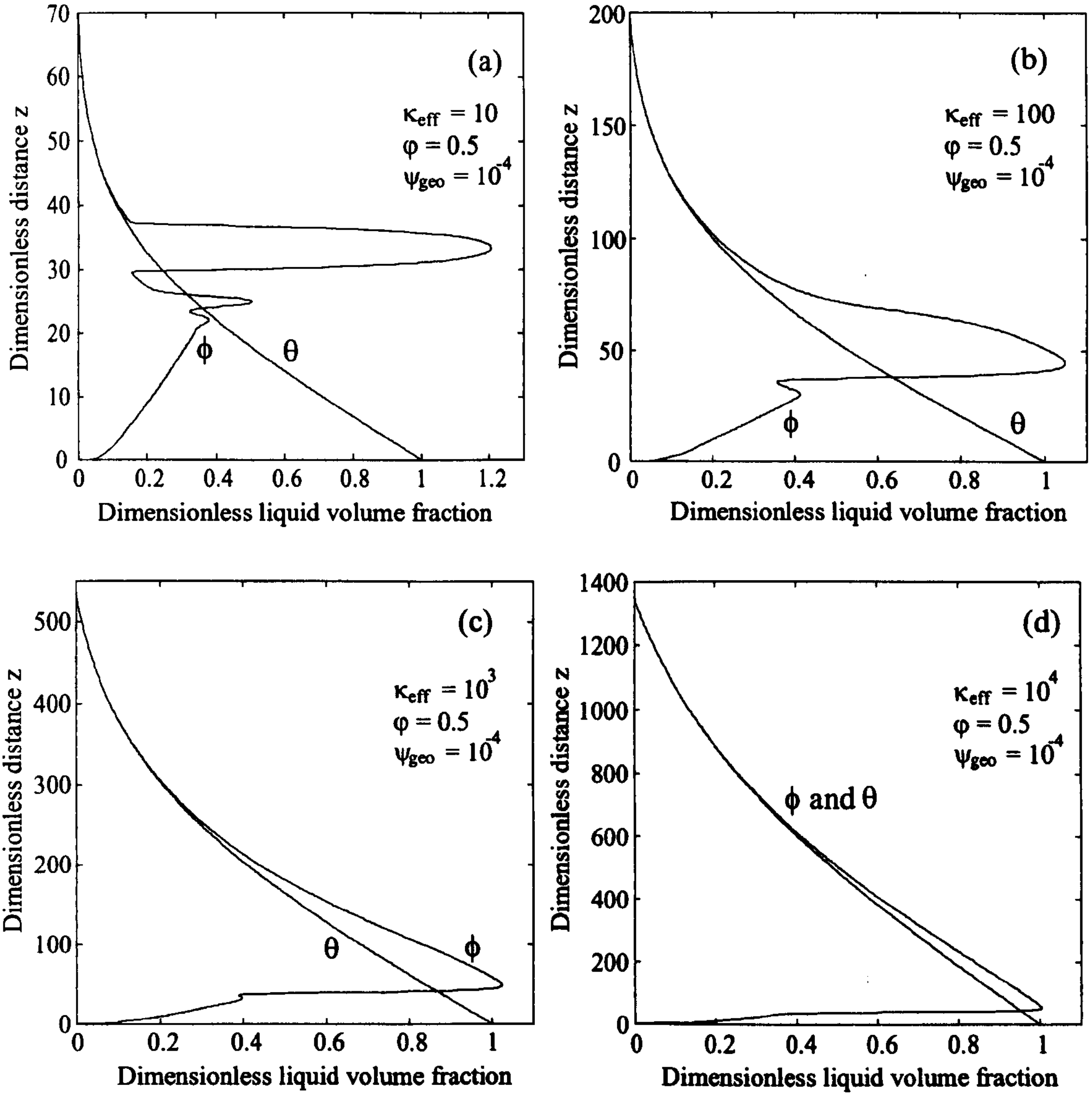

Figure 4.7(iii). Normalised dimensionless spatial porosity (ϕ) and degree of melting (θ) distributions, after 30 time units, with: (a) $\kappa_{eff} = 10$, $\varphi = 0.5$, $\psi_{geo} = 10^{-4}$; (b) $\kappa_{eff} = 100$, $\varphi = 0.5$, $\psi_{geo} = 10^{-4}$; (c) $\kappa_{eff} = 10^3$, $\varphi = 0.5$, $\psi_{geo} = 10^{-4}$; (d) $\kappa_{eff} = 10^4$, $\varphi = 0.5$, $\psi_{geo} = 10^{-4}$. In all cases, Ste = 0.5 and $\chi = 2.5$. Liquid volume fractions (porosity and degree of melting) are normalised to the degree of melting at z=0 (φ). Note that both ordinate and abscissa scales differ between plots.

zone (compare figures 4.7(i) (c) and (d) with figures (4.7)(ii) (a) and (b); also figures 4.7(ii) (c) and (d) with figures (4.7)(iii) (a) and (b)). For the largest value of $\psi_{geo} = 1$, the trailing porosity waves observed for smaller values of ψ_{geo} are suppressed (compare figures 4.7(i) (c) and (d) with figures (4.7)(ii) (a) and (b); also figure 4.7(i) (d) with figure (3.3) (c)).

As discussed in §3.3.2, the spatial porosity distribution in the partial melt zone depends upon the relative rates of upward transport of melt and heat, which for a particular value of φ, and in this case ψ_{geo}, is primarily governed by the magnitude of κ_{eff}. Porosity waves form in melt zones with κ_{eff} in the range $10^{-2} \leq \kappa_{eff} < 10^{4}$, because the rate of melt transport is rapid relative to the rate of heat transport, which results in the melt migrating upwards faster than, and accumulating below, the position of the solidus isotherm (z_0). The effect of increasing the initial geothermal gradient ψ_{geo}, for a given value of κ_{eff}, is to move the position of the solidus isotherm closer to the origin, and hence reduce the spatial extent of the partial melt zone; for example, compare the spatial extent of the partial melt zone in figure 4.7(i) (d) with that in figure 4.7(ii) (b). Increasing the initial geothermal gradient from 10^{-2} (figure 4.7(ii) (b)) to 1 (figure 4.7(i) (d)) has reduced the size of the melt zone from ~14.5 to 0.95 compaction lengths. Consequently, the distance over which the melt must migrate before it reaches the top of the melt zone is reduced, which enhances the accumulation of melt below the solidus isotherm and causes the increase in maximum porosity with increasing ψ_{geo} observed in figure 4.7. Trailing porosity waves are suppressed for the largest value of $\psi_{geo} = 1$, because trailing waves are formed only when the compaction rate in the region immediately below a porosity wave exceeds the melting rate (§3.3.2). The presence of a steep geothermal gradient enhances the rate of heating and hence the rate of melting, so the compaction rate never exceeds the melting rate.

Figure 4.8(a) and (b) shows the effect of varying χ and Ste on the form of the normalised spatial porosity distributions, in a partial melt zone with $\kappa_{eff} = 10$ and $\psi_{geo} = 10^{-2}$, after 30 time units have elapsed, and should be compared with figure 4.7(ii) (c). Figure 4.8(a) corresponds to the *maximum* values of $\chi = 3.94$ and Ste = 0.75; figure 4.8(b) corresponds to the *minimum* values of $\chi = 1.27$ and Ste = 0.21. Comparison of these figures demonstrates that varying χ and Ste between their maximum and minimum values has a negligible effect on the form of the spatial porosity distribution. Consequently, in all subsequent dimensionless numerical experiments, the values of χ and Ste are assumed fixed at $\chi = 2.5$ and Ste = 0.5*[2].

4.3.1.2 The effect of a percolation threshold

The results presented both in this chapter and in chapter 3 are obtained using the permeability-porosity equation (4.6) over the entire porosity range. As discussed in §4.2.4.1(i), partially molten

---

[2] A value of $\chi = 2.5$ corresponds to a value of Ste = 0.6; an oversight led to the value of Ste = 0.5 being used in the numerical experiments. However, this minor discrepancy has a negligible effect on the numerical results.

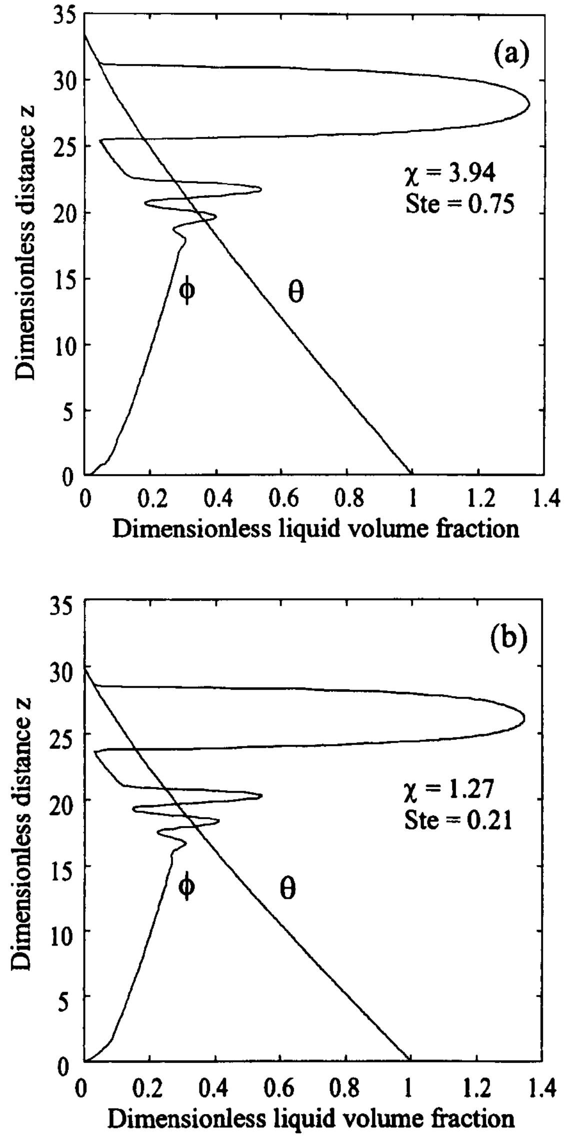

Figure 4.8. Normalised dimensionless spatial porosity (ϕ) and degree of melting (θ) distributions, after 30 time units, with: (a) $\chi = 3.94$ and Ste = 0.75; (b) $\chi = 1.27$ and Ste = 0.21. In both cases, $\kappa_{eff} = 10$, $\varphi = 0.5$, and $\psi_{g\infty} = 10^{-2}$. Liquid volume fractions (porosity and degree of melting) are normalised to the degree of melting at z=0 (φ).

rocks which are texturally equilibrated are likely to be permeable at very small porosities (<0.001), in which case equation (4.6) is valid over the entire porosity range; however, rocks which are texturally unequilibrated may be permeable only at porosities greater than the percolation threshold (ϕ_c), in which case equation (4.6) is not valid over the entire porosity range. The *dimensional* percolation threshold estimated by Zhang *et al.* (1994) for an unequilibrated calcite aggregate is $\phi_c = 0.04$, although this value does not necessarily represent all texturally unequilibrated rocks (§4.2.4.1(i)). Figure 4.9(a - d) shows the effect of a dimensional percolation threshold of $\phi_c = 0.04$ on the form of the normalised spatial porosity distributions, for a partial melt zone with $\kappa_{eff} = 10$ and 100, and $\psi_{geo} = 10^{-2}$ and 10^{-4}, after 30 time units have elapsed. The curves are obtained assuming that the permeability is given by equation (4.6) for dimensional porosity in the range $\phi > 0.04$, and is zero for dimensional porosity in the range $\phi \leq 0.04$. This assumption represents a simplification of the permeability-porosity relations for texturally unequilibrated rocks presented in figure 4.3(a), as strictly, for dimensional porosity in the range $0.04 < \phi < 0.06$, the permeability is given by equation (4.29); however, neglecting equation (4.29) has a negligible effect on the permeability-porosity relations, and obviates the requirement to modify D'Arcy's law to account for the isolated porosity (Ahern and Turcotte, 1979).

Comparison of figure 4.9(a-d) with the corresponding solutions in the absence of a percolation threshold (figure 4.7(ii) (c) and (d); figure 4.7(iii) (a) and (b)) reveals that in partial melt zones with these values of κ_{eff} and ψ_{geo}, the introduction of a percolation threshold has little effect on the form of the spatial porosity distributions. Only for the case $\kappa_{eff} = 10$ and $\psi_{geo} = 10^{-2}$ is there a noticeable difference; the maximum normalised porosity obtained in the presence of a percolation threshold is ~1.48 (figure 4.9(a)), compared to a value of ~1.35 in the absence of a percolation threshold (figure 4.7(ii) (c)). This counter-intuitive result may be explained if the evolution of the spatial porosity distribution through time is considered. Figure 4.10 shows the normalised spatial porosity distribution for the case $\kappa_{eff} = 10$ and $\psi_{geo} = 10^{-2}$, after 5, 10, 15, 20, 25 and 30 time units have elapsed (cf. figure 4.9(a)). Tracing the evolution of the spatial porosity distribution, it is clear that the porosity at the leading edge of the leading porosity wave does not fall to the percolation threshold until t ~ 25, by which time the wave is well developed. Consequently, during the *evolution* of the leading porosity wave, the presence of a percolation threshold is irrelevant to the dynamics of melt migration.

However, the presence of a percolation threshold limits the range of values of κ_{eff} and ψ_{geo} which may be investigated using the model formulation presented in this chapter. The restriction that the permeability is zero in regions where $\phi \leq \phi_c$, strictly requires that the melt and matrix velocities, and the compaction rate C (= $\partial(\phi w_m)/\partial z$; §3.3.2), are also zero. The former requirement ($w_m = w_s = 0$) follows simply from the zero permeability restriction, and may be rigorously implemented when

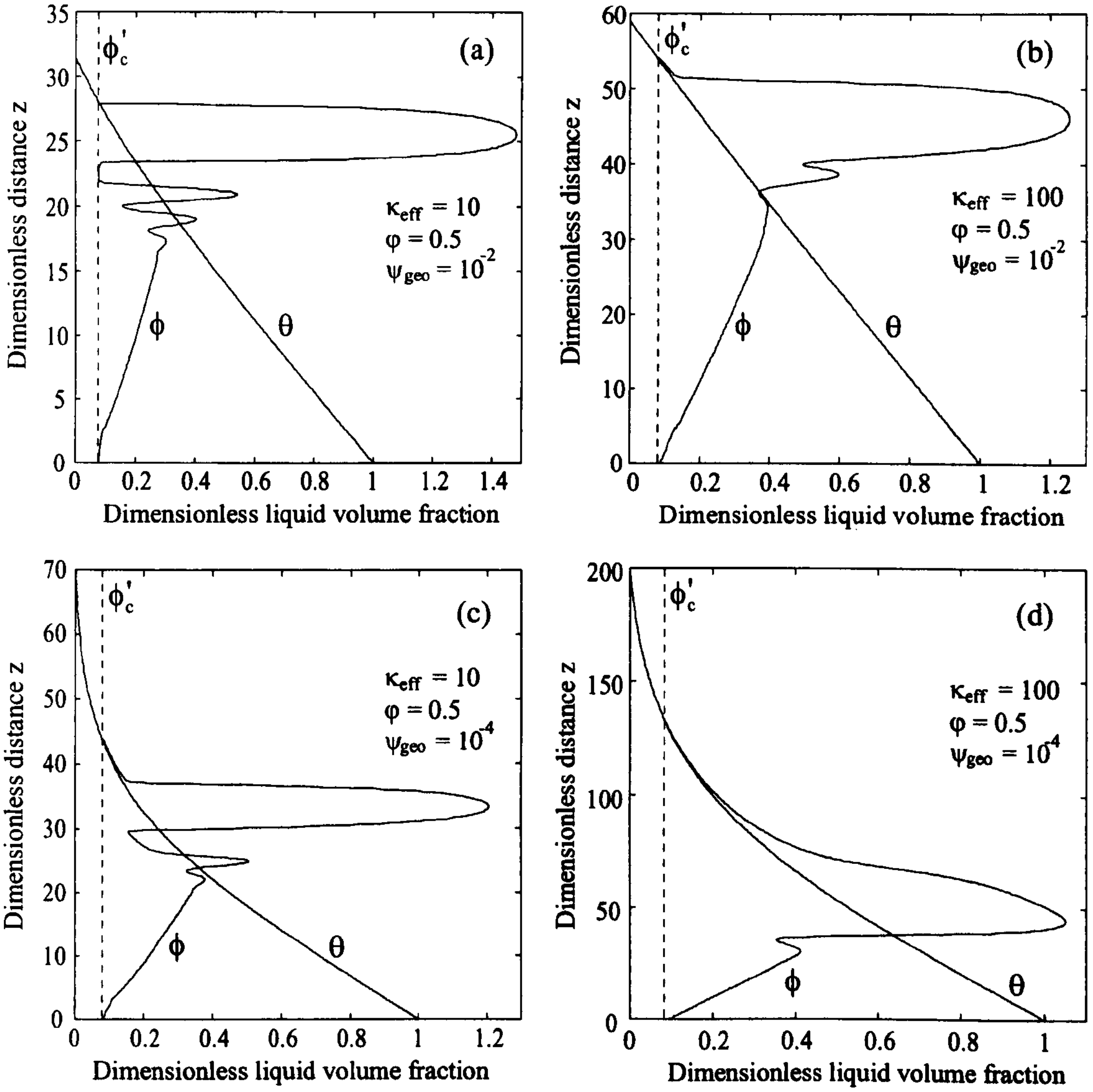

Figure 4.9. Normalised dimensionless spatial porosity (ϕ) and degree of melting (θ) distributions, after 30 time units, for unequilibrated rocks with a dimensionless percolation threshold of $\phi_c' = 0.08$ (which corresponds to a *dimensional* percolation threshold of $\phi_c = 0.04$ if $\varphi = 0.5$; equation (4.12)). The distributions shown are for (a) $\kappa_{eff} = 10$, $\psi_{geo} = 10^{-2}$; (b) $\kappa_{eff} = 100$, $\psi_{geo} = 10^{-2}$; (c) $\kappa_{eff} = 10$, $\psi_{geo} = 10^{-4}$; (d) $\kappa_{eff} = 100$, $\psi_{geo} = 10^{-4}$. In all cases, $\varphi = 0.5$, Ste = 0.5, and $\chi = 2.5$. Liquid volume fractions (porosity and degree of melting) are normalised to the degree of melting at z=0 (φ). Note that both ordinate and abscissa scales differ between plots.

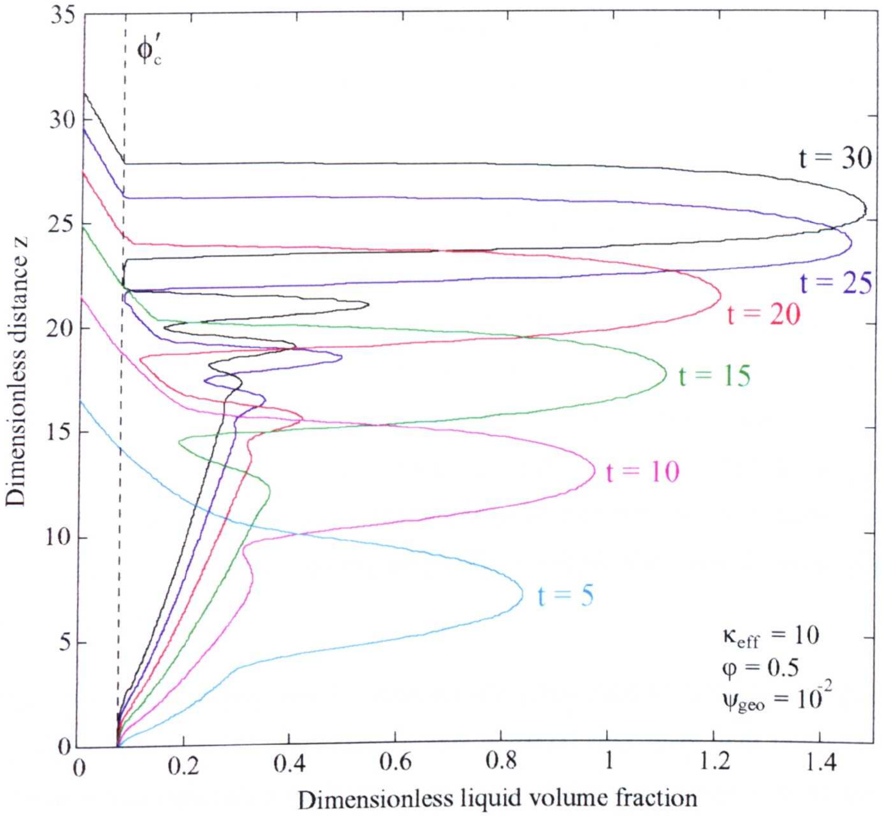

Figure 4.10. Normalised dimensionless spatial porosity (ϕ) and degree of melting (θ) distributions, for an unequilibrated rock with a dimensionless percolation threshold of $\phi'_c = 0.08$ (which corresponds to a *dimensional* percolation threshold of $\phi_c = 0.04$ if $\varphi = 0.5$; equation (4.12)). The distributions are shown after 5, 10, 15, 20, 25 and 30 time units, for $\kappa_{eff} = 10$, $\psi_{geo} = 10^{-2}$, $\varphi = 0.5$, Ste = 0.5, and $\chi = 2.5$. Liquid volume fractions (porosity and degree of melting) are normalised to the degree of melting at z=0 (φ).

solving for conservation of momentum (Appendix A). However, the latter requirement ($C = 0$) follows from the resulting change in the rheology of the partially molten rock; because the melt cannot be 'squeezed' out of the pore space, the bulk viscosity (ξ_s) of the rock is infinite and so it cannot compact. This requirement cannot be rigorously implemented because of the way in which the dimensionless governing equations are formulated. Numerically forcing the compaction rate C to be zero in regions where $\phi \leq \phi_c$ correctly represents the change in the rheology of the matrix (Appendix A), but for values of $\kappa_{eff} \leq 1$ and $\psi_{geo} \geq 1$, the numerical solutions no longer conserve mass. The solutions shown in figure 4.9 are those with the smallest values of κ_{eff} for which mass is satisfactorily conserved (Appendix A); they correspond to those in which the porosity rarely falls below the percolation threshold even in the absence of such a threshold (cf. figure 4.7(ii) (c) and (d) and figure 4.7(iii) (a) and (b)); i.e. to those in which the numerical forcing of the compaction rate C is negligible. Ironically, it is the solutions with $\kappa_{eff} \leq 1$ and $\psi_{geo} \geq 1$ which may be most affected by the presence of a percolation threshold, because it is for these values of κ_{eff} and ψ_{geo} that the porosity in the absence of a percolation threshold falls to its lowest values (figure 4.7(i) (a-d)). However, as in the case of the solution shown in figure 4.10, it is likely that for solutions with these values of κ_{eff} and ψ_{geo}, the porosity at the leading edge of the leading porosity wave will not fall to the percolation threshold until the wave is well developed, and it seems reasonable to assume that the most significant effect of a percolation threshold on the spatial porosity distributions will be to increase the residual porosity left behind the leading wave.

The results of this section indicate that the presence of a percolation threshold has a significant effect on the form of the spatial porosity distributions only in partial melt zones with values of $\kappa_{eff} \leq 1$ and $\psi_{geo} \geq 1$. These values represent a small fraction of the available range (table 4.3); for the majority of values of κ_{eff} and ψ_{geo}, the effect of a percolation threshold is negligible. Consequently, the use of the permeability-porosity equation (4.6) to obtain the results presented in this chapter and in chapter 3 would appear to be justified. Furthermore, the available evidence indicates that partially molten rocks in the lower crust will be at, or near, textural equilibrium, in which case the percolation threshold is likely to be negligibly small (<0.001) and equation (4.6) is valid in all partially molten rocks regardless of the value of κ_{eff} and ψ_{geo} (§4.2.4.1(i)). Cheadle (1989) has estimated the time required for textural equilibrium to be achieved if the rate of equilibration is controlled by diffusion; for a grain size (diameter) of 1mm, equilibrium will be attained within ~10 years. Although this probably represents a minimum value, and is based on the results of experimental studies on olivine-basalt systems which represent the partially molten mantle rather than crust, it is *significantly* less than typical lower crustal melting times of ~0.5-10 M.y. (Hodge, 1974; Fountain *et al.*, 1989), indicating that textural equilibrium will be achieved. Moreover, lower crustal granulites, many of which are interpreted to be residues left after the extraction of a granitic partial melt fraction (§2.3.2), are usually observed to be texturally equilibrated (e.g. Vernon, 1968). However, this observation is based on the use of dihedral angle measurements to identify textural equilibrium, an approach which may not be valid (Elliott *et al.*, 1997); furthermore, the observation that many granulites are texturally equilibrated now does not *necessarily* mean that they were so during partial melting and melt migration.

4.3.1.3 Increase in maximum porosity with time: formation of a magma

If the amplitude of the leading porosity wave continuously increases with time, then the local melt volume fraction may eventually exceed the CMF, in which case the contiguity of the solid grains breaks down and a mobile magma forms (§3.3.3). Figure 4.11(a - c) shows a representative selection of the maximum normalised porosity against dimensionless time curves. In partially molten rocks with small values of κ_{eff} ($\leq 10^{-2}$) the maximum porosity initially falls until the slope abruptly changes and the maximum porosity begins to increase, although the rate of increase is slow (figure 4.11(a)). In rocks with larger values of κ_{eff}, the rate of increase of maximum porosity is rapid (figure 4.11(b - c)). The effect of increasing ψ_{geo} is generally to maintain, or enhance, the rate of increase in the maximum porosity, especially at large dimensionless times (>25), which is in agreement with the results of §4.3.1.1. The minimum requirement for magma formation is that the normalised porosity exceeds 1 (§3.3.3), maximum normalised porosity against time curves obtained for the full range of values of κ_{eff} and ψ_{geo} indicate that magma formation is possible in melt zones with values of κ_{eff} in the range $10^{-2} \leq \kappa_{eff} < 10^{4}$ and ψ_{geo} in the range $10^{-4} \leq \psi_{geo} \leq 1$ (c.f. §3.3.3). These values are enclosed by the red square shown in table 4.3; it is clear that they represent the majority of the available values of κ_{eff} and ψ_{geo}.

4.3.2 Dimensional Results

4.3.2.1 Form of the spatial temperature, porosity, and degree of melting distributions

The dimensionless spatial porosity and degree of melting (dimensionless temperature) distributions obtained from the model may be 'dimensionalised' using the characteristic length, time, velocity, and melt volume fraction scales δ, τ, ω, and φ presented in §4.2.3 (equations (4.11) - (4.16)). However, because of the large number of dimensional governing variables which define these characteristic scales (see table 4.2), the dimensional results are difficult to generalise. In this section, no attempt will be made to exhaustively investigate the dimensional results which may be obtained; rather, 'typical' results will be presented for given values of the dimensional governing variables. The values of the dimensional governing variables used are given in table 4.4.

Figure 4.12 shows the porosity (melt volume fraction), temperature, and degree of melting as a function of vertical distance, after an arbitrary but reasonable time of 2 M.y. (18.4 dimensionless time units), for 'typical' values of the governing variables (table 4.4). Note that the curve labelled 'Temperature T' represents both the temperature (T) if read from the upper abscissa axis, and the

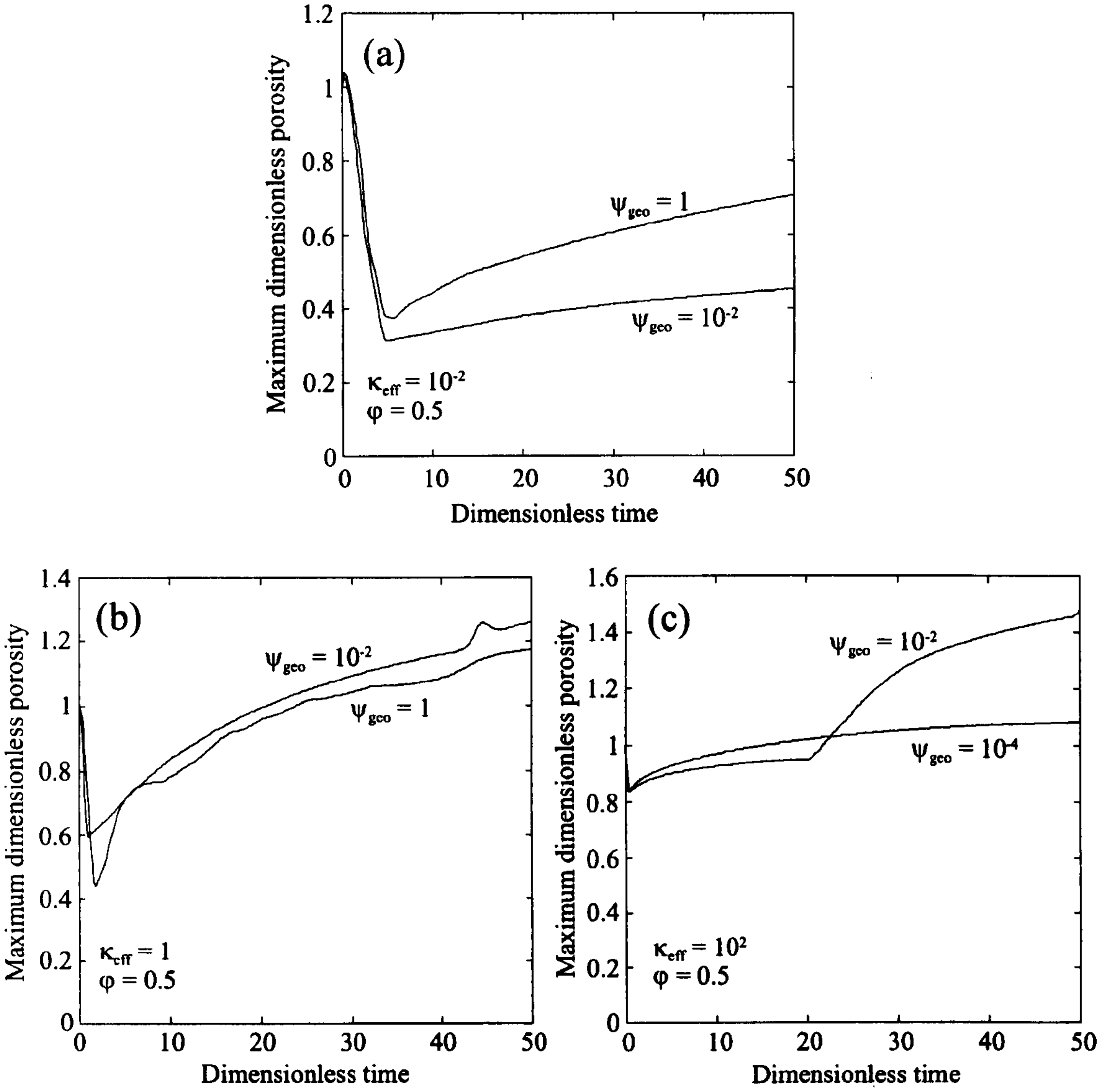

Figure 4.11. Maximum normalised dimensionless porosity as a function of time, for (a) $\kappa_{eff} = 10^{-2}$, $\psi_{geo} = 10^{-2}$ and 1; (b) $\kappa_{eff} = 1$, $\psi_{geo} = 10^{-2}$ and 1; (c) $\kappa_{eff} = 10^{2}$, $\psi_{geo} = 10^{-4}$ and 10^{-2}. In all cases, $\varphi = 0.5$; Ste = 0.5; $\chi = 2.5$.

Symbol	Description	Value	Units
All results			
k	Thermal conductivity	2	W $K^{-1}m^{-1}$
c_p	Specific heat capacity	1,120	J $kg^{-1}K^{-1}$
L	Latent heat	400,000	J kg^{-1}
T_{liq}	Liquidus temperature of source rock	1440	K
T_{sol}	Solidus temperature of source rock	1160	K
$T_{liq}-T_{sol}$	Liquidus-solidus interval	280	K
T_{geo}	Initial geothermal gradient	7	K km^{-1}
ρ	Density	2,900	kg m^{-3}
$\rho_m-\rho_s$	Melt-matrix density difference	550	kg m^{-3}
n	Exponent in permeability relation	3	None
Figure 4.12			
a	Matrix grain radius	$3x10^{-3}$ (3 mm)	m
b	Constant in permeability relation	1/1000	None
μ_m	Melt shear viscosity	10^5	Pa s
μ_s	Matrix shear viscosity	10^{18}	Pa s
ξ_s	Matrix bulk viscosity	10^{18}	Pa s
Figure 4.13(a)			
a	Matrix grain radius	$3x10^{-3}$ (3 mm)	m
b	Constant in permeability relation	1/1000	None
μ_m	Melt shear viscosity	10^3	Pa s
μ_s	Matrix shear viscosity	10^{20}	Pa s
ξ_s	Matrix bulk viscosity	10^{20}	Pa s
Figure 4.13(b)			
a	Matrix grain radius	$3x10^{-3}$ (3 mm)	m
b	Constant in permeability relation	1/1000	None
μ_m	Melt shear viscosity	10^4	Pa s
μ_s	Matrix shear viscosity	10^{19}	Pa s
ξ_s	Matrix bulk viscosity	10^{19}	Pa s
Figure 4.13(c)			
a	Matrix grain radius	$5x10^{-3}$ (5 mm)	m
b	Constant in permeability relation	1/347	None
μ_m	Melt shear viscosity	$4x10^5$	Pa s
μ_s	Matrix shear viscosity	$2x10^{18}$	Pa s
ξ_s	Matrix bulk viscosity	$2x10^{18}$	Pa s

Table 4.4. Values of the dimensional governing variables used to obtain the results shown in figures 4.12 - 4.15.

Symbol	Description	Value	Units
Figure 4.13(d)			
a	Matrix grain radius	$1.5\text{x}10^{-3}$ (1.5 mm)	m
b	Constant in permeability relation	1/1000	None
μ_m	Melt shear viscosity	$1\text{x}10^{5}$	Pa s
μ_s	Matrix shear viscosity	$2.5\text{x}10^{17}$	Pa s
ξ_s	Matrix bulk viscosity	$2.5\text{x}10^{17}$	Pa s
Figure 4.14(a)			
a	Matrix grain radius	$3\text{x}10^{-3}$ (3 mm)	m
b	Constant in permeability relation	1/1000	None
μ_m	Melt shear viscosity	10^{3}	Pa s
μ_s	Matrix shear viscosity	10^{16}	Pa s
ξ_s	Matrix bulk viscosity	10^{16}	Pa s
Figure 4.14(b)			
a	Matrix grain radius	$3\text{x}10^{-3}$ (3 mm)	m
b	Constant in permeability relation	1/1000	None
μ_m	Melt shear viscosity	10^{4}	Pa s
μ_s	Matrix shear viscosity	10^{17}	Pa s
ξ_s	Matrix bulk viscosity	10^{17}	Pa s
Figure 4.14(c)			
a	Matrix grain radius	$1.75\text{x}10^{-3}$ (1.75 mm)	m
b	Constant in permeability relation	1/1000	None
μ_m	Melt shear viscosity	10^{3}	Pa s
μ_s	Matrix shear viscosity	$3\text{x}10^{18}$	Pa s
ξ_s	Matrix bulk viscosity	$3\text{x}10^{18}$	Pa s
Figure 4.14(d)			
a	Matrix grain radius	$3\text{x}10^{-3}$ (3 mm)	m
b	Constant in permeability relation	1/1000	None
μ_m	Melt shear viscosity	10^{6}	Pa s
μ_s	Matrix shear viscosity	10^{19}	Pa s
ξ_s	Matrix bulk viscosity	10^{19}	Pa s
Figure 4.15			
a	Matrix grain radius	$3\text{x}10^{-3}$ (3 mm)	m
b	Constant in permeability relation	1/87.5	None
μ_m	Melt shear viscosity	10^{5}	Pa s
μ_s	Matrix shear viscosity	10^{18}	Pa s
ξ_s	Matrix bulk viscosity	10^{18}	Pa s

Table 4.4 (continued). Values of the dimensional governing variables used to obtain the results shown in figures 4.12 - 4.15.

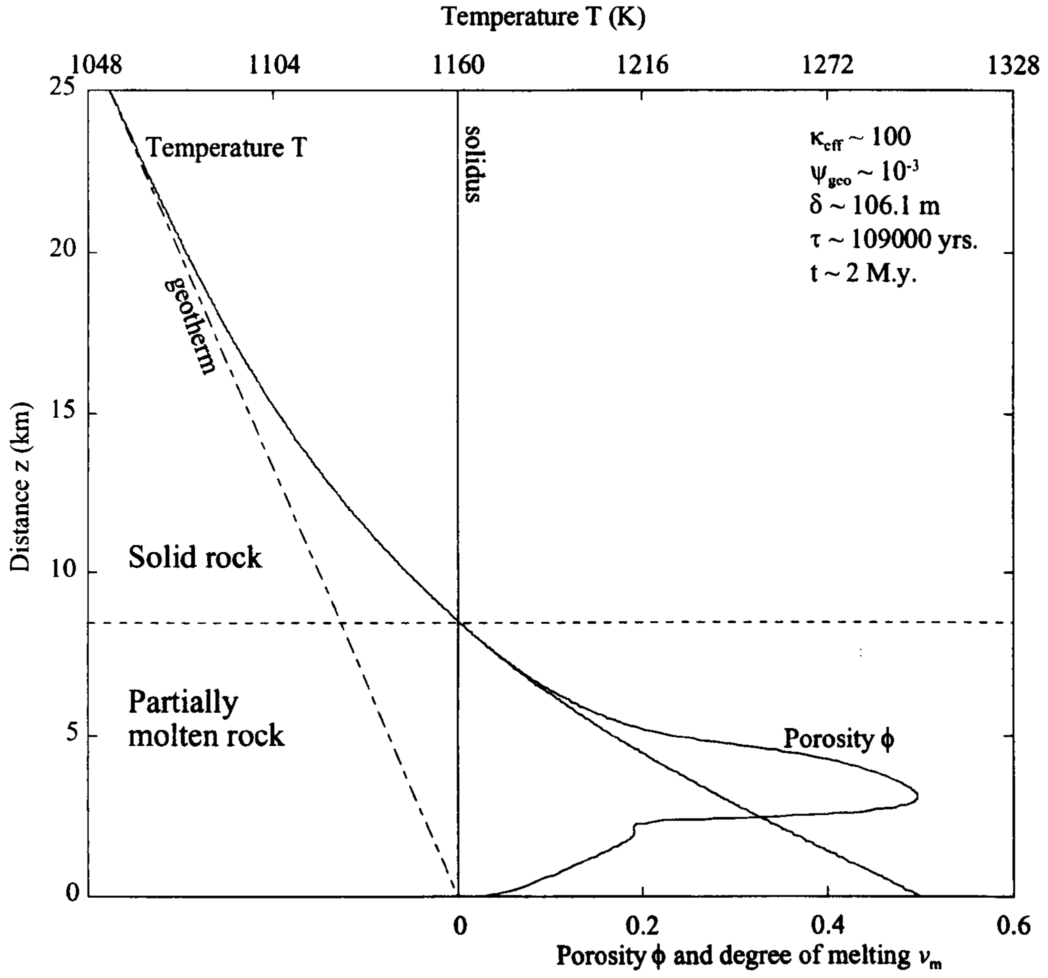

Figure 4.12. Porosity (ϕ) and temperature (T) against vertical distance (z), for $\kappa_{eff} \sim 100$, $\psi_{geo} \sim 10^{-3}$, $\delta \sim 106.1$ m, $\tau \sim 109000$ yrs., t ~ 2 M.y. ($t' \sim 18.4$), $\varphi = 0.5$, Ste ~ 0.5, $\chi \sim 2.5$ See table 4.4 for the values of the governing dimensional variables used. The porosity (ϕ) is plotted against the lower abscissa axis; the temperature (T) is plotted against the upper abscissa axis. The curve which denotes the temperature (T) also denotes the degree of melting (ν_m) if read from the lower abscissa axis. Note that t denotes *dimensional* time; t' denotes *dimensionless* time.

degree of melting (ν_m) if read from the lower abscissa axis. The temperature is dimensionalised assuming that the source rock has a solidus temperature of 1160 K, and a liquidus temperature of 1440 K; these values represent an andesitic greenstone (Beard and Lofgren, 1991; see figure 4.16(a)). After 2 M.y., the thermal perturbation caused by the emplacement of hot magma has propagated ~25 km from the underlying heat source at z=0, and a partial melt zone ~8 km thick has been generated. Melt migration in the partial melt zone has resulted in the formation of a porosity wave, with an amplitude of ~0.5.

Figure 4.13 shows the effect of varying the values of the governing dimensional parameters such that the characteristic timescale (τ) remains (approximately) constant (table 4.4). In all cases, the results are shown after 2 M.y. has elapsed (18.4 dimensionless time units). The curve labelled 'T and ν_m' represents both the temperature (T) if read from the upper abscissa axis, and the degree of melting (ν_m) if read from the lower abscissa axis. After 2 M.y., the partial melt zone is ~9 km thick for all cases except that shown in figure 4.13(c). The amplitude of the leading porosity wave varies between plots from ~0.25 (figure 4.13(a)) to >0.5 (figure 4.13(b) and(c)); in these latter cases, a mobile magma would have formed if the CMF ~ 0.5. Figure 4.14 shows the effect of varying the values of the governing dimensional parameters such that the characteristic lengthscale (δ) remains (approximately) constant (table 4.4). In all cases, the results are shown after 18.4 dimensionless time units have elapsed (except for figure 4.14(a), which is shown after 36.8 time units have elapsed); however, as the characteristic timescale is no longer constant, the *dimensional* time elapsed varies between plots from only ~40000 yrs. (figure 4.14(a)) to ~20 M.y. (figure 4.14(d)). The partial melt zone varies in thickness between plots from ~2 km (figure 4.14(a)) to ~18 km (figure 4.14(d)), and the maximum porosity varies between plots from ~0.48 (figure 4.14(d)) to >0.5 (figure 4.14(b)); again, in this latter case, a mobile magma would have formed if the CMF ~ 0.5.

Figure 4.15 shows the effect of varying the value of the degree of melting at the contact (φ), after 2 M.y. (25.2 dimensionless time units) have elapsed. Note the high frequency of the trailing porosity waves (cf. §3.3.2), and that the maximum porosity attained after 2 M.y. is <0.3, which indicates that the formation of a mobile magma is unlikely for values of $\varphi \leq 0.2$, given that estimated values of the CMF range from 0.3 - 0.65 (table 4.2).

These results give an indication of the *diversity* of the dimensional spatial porosity (melt) distributions which may be obtained using geologically reasonable values of the governing dimensional parameters, and of the dimensional length and timescales over which melting and melt migration are predicted to occur (~2 - 20 km and ~40000 yrs. - 20 M.y. respectively). Note that these length and timescales are geologically reasonable; i.e. the thickness of the partial melt zone does not, for example, exceed the thickness of the crust, and the timescale of melting and melt migration does not exceed the timescale of heating of the crust (Hodge, 1974; Fountain *et al.*, 1989).

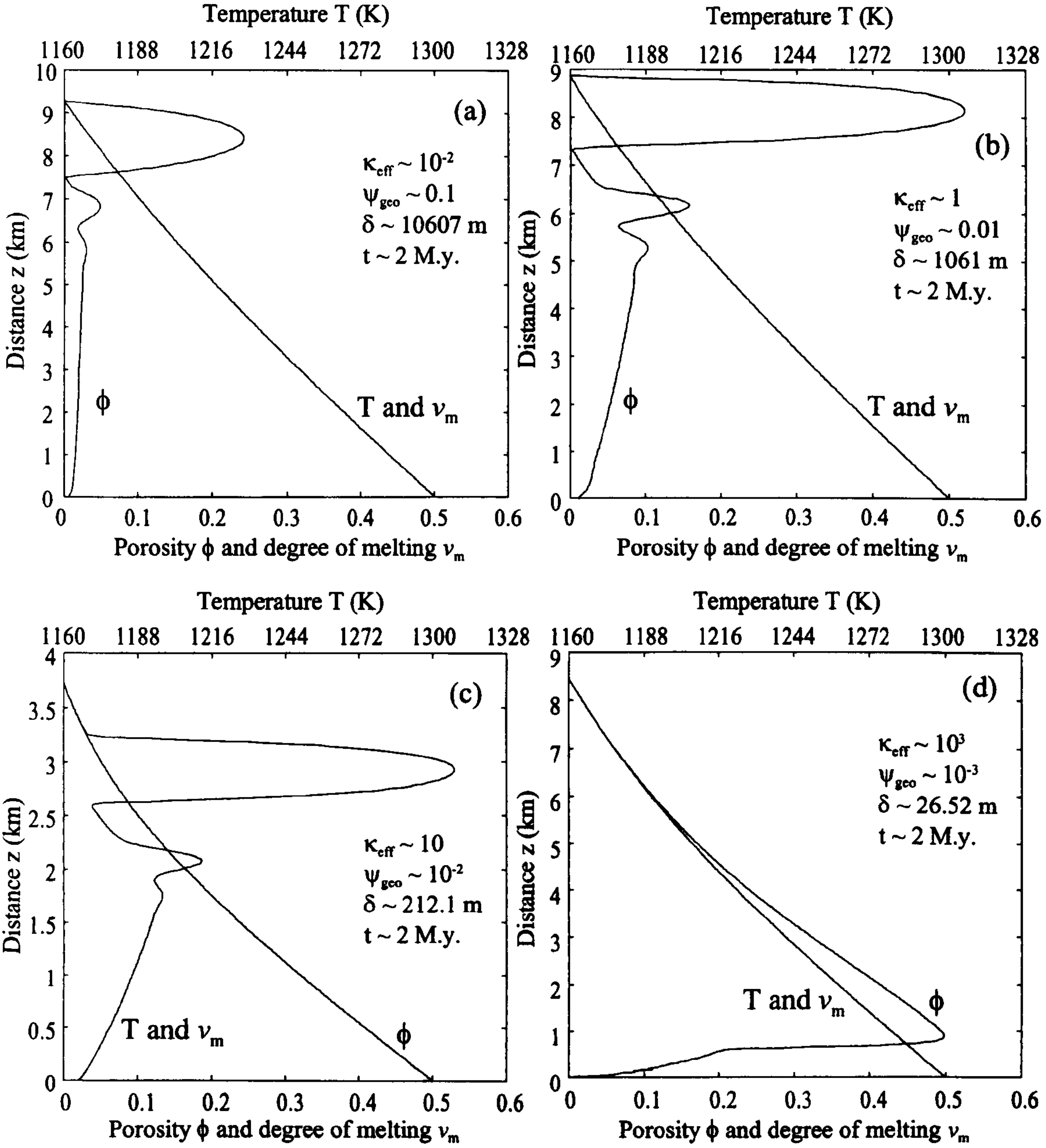

Figure 4.13. Porosity (ϕ) and temperature (T) against vertical distance (z), for t ~ 2 M.y. (t' ~ 18.4), with (a) $\kappa_{eff} \sim 10^{-2}$, $\psi_{geo} \sim 0.1$, $\delta \sim 10607$m; (b) $\kappa_{eff} \sim 1$, $\psi_{geo} \sim 0.01$, $\delta \sim 1061$m; (c) $\kappa_{eff} \sim 10$, $\psi_{geo} \sim 10^{-2}$, $\delta \sim 212.1$m; (d) $\kappa_{eff} \sim 10^3$, $\psi_{geo} \sim 10^{-3}$, $\delta \sim 26.52$m. In all cases, $\tau \sim 109000$ yrs; $\varphi = 0.5$. See table 4.4 for the values of the governing dimensional variables used. The curve labelled "T and v_m" denotes the temperature (T) when read from the upper abscissa axis, and the degree of melting (v_m) when read from the lower abscissa axis. The curve labelled ϕ is read from the lower abscissa axis. Note that t denotes *dimensional* time; t' denotes *dimensionless* time.

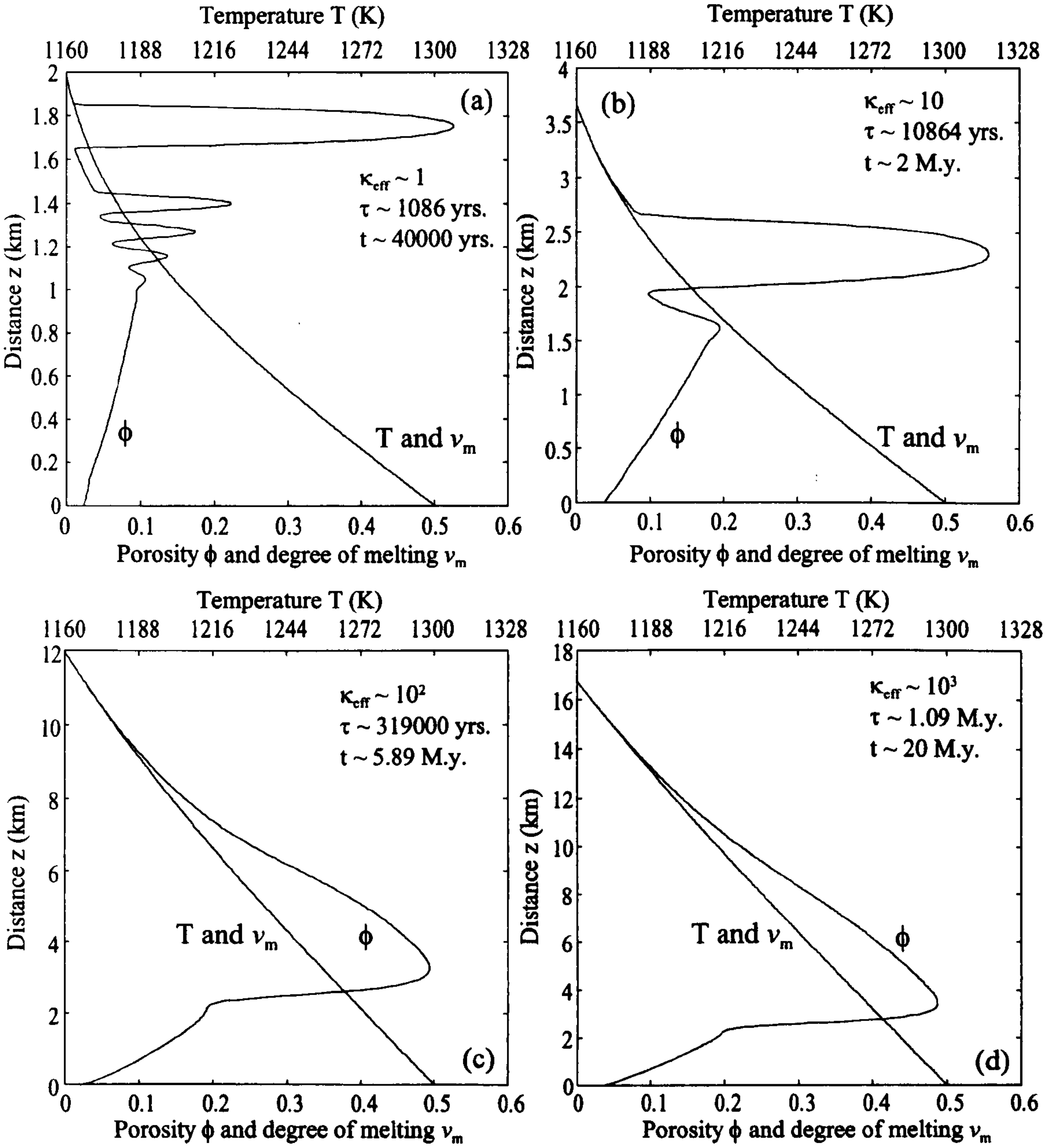

Figure 4.14. Porosity (ϕ) and temperature (T) against vertical distance (z), for (a) $\kappa_{eff} \sim 1$, $\tau \sim 1086$ yrs., t ~ 40000 yrs. (t' ~ 36.8); (b) $\kappa_{eff} \sim 10$, $\tau \sim 10864$ yrs., t ~ 2 M.y. (t' ~ 18.4); (c) $\kappa_{eff} \sim 10^2$, $\tau \sim 319000$ yrs., t ~ 5.89 M.y. (t' ~ 18.4); (d) $\kappa_{eff} \sim 10^3$, $\tau \sim 1.09$ M.y., t ~ 20 M.y. (t' ~ 18.4). In all cases, $\delta \sim 106.1$ m; $\psi_{geo} \sim 10^{-3}$; $\varphi = 0.5$. See table 4.4 for the values of the governing dimensional variables used. The curve labelled "T and ν_m" denotes the temperature (T) when read from the upper abscissa axis, and the degree of melting (ν_m) when read from the lower abscissa axis. The curve labelled ϕ is read from the lower abscissa axis. Note that t denotes *dimensional* time; t' denotes *dimensionless* time.

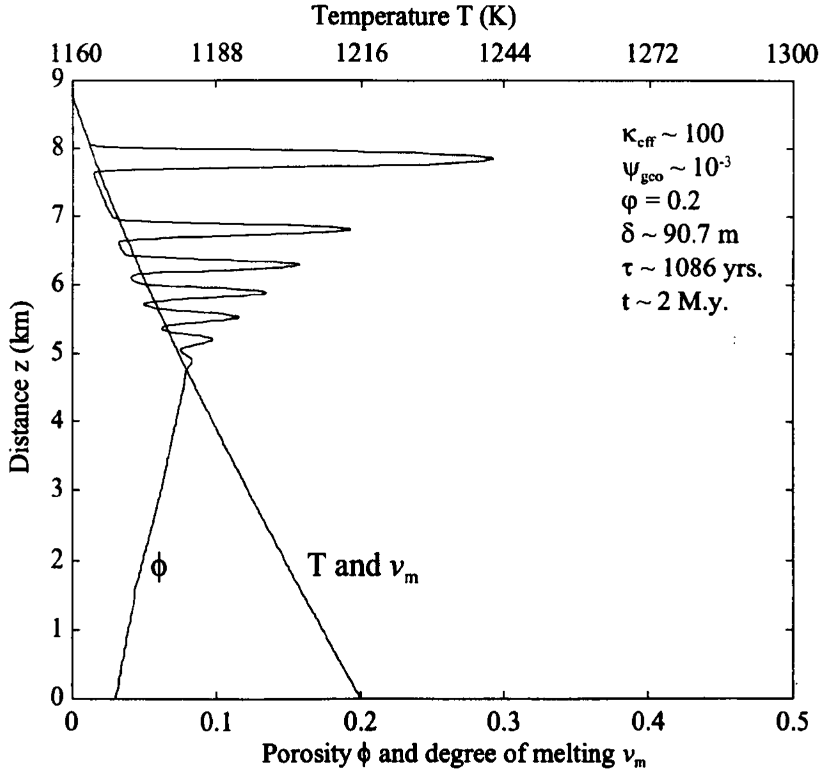

Figure 4.15. Porosity (ϕ) and temperature (T) against vertical distance (z), for $\kappa_{eff} \sim 100$, $\psi_{gco} \sim 10^{-3}$, $\varphi = 0.2$, $\delta \sim 90.7$ m, $\tau \sim 1086$ yrs., $t \sim 2$ M.y., ($t' \sim 25.2$) See table 4.4 for the values of the governing dimensional variables used. The curve labelled "T and ν_m" denotes the temperature (T) when read from the upper abscissa axis, and the degree of melting (ν_m) when read from the lower abscissa axis. The curve labelled ϕ is read from the lower abscissa axis. Note that t denotes *dimensional* time; t' denotes *dimensionless* time.

4.3.2.2 Prediction of melt compositions

Figure 4.16(a-d) shows the empirically derived composition, as a function of the temperature and degree of melting, of the melt obtained during partial melting of a variety of common lower crustal rock types. The composition of the melt is always granitic (*sensu-lato*) for degrees of melting up to ~0.4. However, the composition of the melt produced during partial melting of the meta-igneous rock types shown in figure 4.16(a-c) changes from granitic (*sensu-stricto*) to trondhjemitic, to tonalitic and finally granodioritic as the degree of melting increases to ~0.4 (see figure 4.17 for definitions of these terms); in contrast, the composition of the melt produced during partial melting of the meta-sedimentary rock type shown in figure 4.16(d) is granitic (*sensu-stricto*) for all degrees of melting up to ~0.4.

As discussed in §3.3.4, empirical data such as that shown in figure 4.16 may be used to estimate the melt composition for a given lower crustal source rock during melting and melt segregation. For example, consider the melt composition in the leading porosity wave shown in figure 4.12. The porosity wave is located at a height of ~3km; the composition of the melt at this location corresponds to a degree of melting of ~0.28, and for an andestic greenstone, hornblende hornfels, or meta-basalt source rock, its composition would be described as *tonalitic* (figure 4.16(a) - (c))[3]. For a meta-pelite source rock, its composition would be described as *granitic* (*sensu-stricto*) (figure 4.16(d)). In like fashion, it may be deduced that the melt composition in the leading porosity wave shown in figure 4.13(b) corresponds to a degree of melting of only ~0.04, and would be described as granitic (*sensu-stricto*) to trondhjemitic depending upon the source rock type; in contrast, the melt composition in the leading porosity wave shown in figure 4.14(d) corresponds to a degree of melting of ~0.4, and would be described as granitic (*sensu-stricto*) to granodioritic depending upon the source rock type. Generally, in partial melt zones characterised by smaller values of κ_{eff}, the composition of the melt in the leading porosity wave corresponds to a smaller degree of melting of the source rock (e.g. compare figures 4.13(b) and 4.14(d)).

As the melt migrates upwards through the partial melt zone, its composition *changes* to correspond to a *smaller* degree of melting of the source rock, because it thermodynamically equilibrates with partially molten rock at progressively *lower* temperatures (§3.3.4). For a given source rock composition, the composition of the melt in a porosity wave therefore depends upon the position of the

---

[3] The temperature scale in figures 4.12-4.15 is dimensionalised using the solidus and liquidus temperatures of the andesitic greenstone rock shown in figure 4.16(a) (§4.3.2.1). The hornblende hornfels, meta-basalt, and meta-pelite rocks shown in figure 4.16(b-d) have different solidus and liquidus temperatures; consequently, using the solidus and liquidus temperatures of these rock types to dimensionalise the temperature scale in figures 4.12-4.15 *changes* the temperature scale. However, the shape of the curves, and the porosity/degree of melting scale from which they are read, is *unchanged*, so long as the contact temperature is chosen to yield the externally prescribed value of φ (equation (4.12)). Consequently, although the solidus and liquidus temperatures of the rock types shown in figure 4.16(b-d) are different from those used to dimensionalise the temperature scale in figures 4.12-4.15, the melt composition which corresponds to a given *degree of melting* in figures 4.12-4.15 may nevertheless be estimated for those rock types using figure 4.16(b-d).

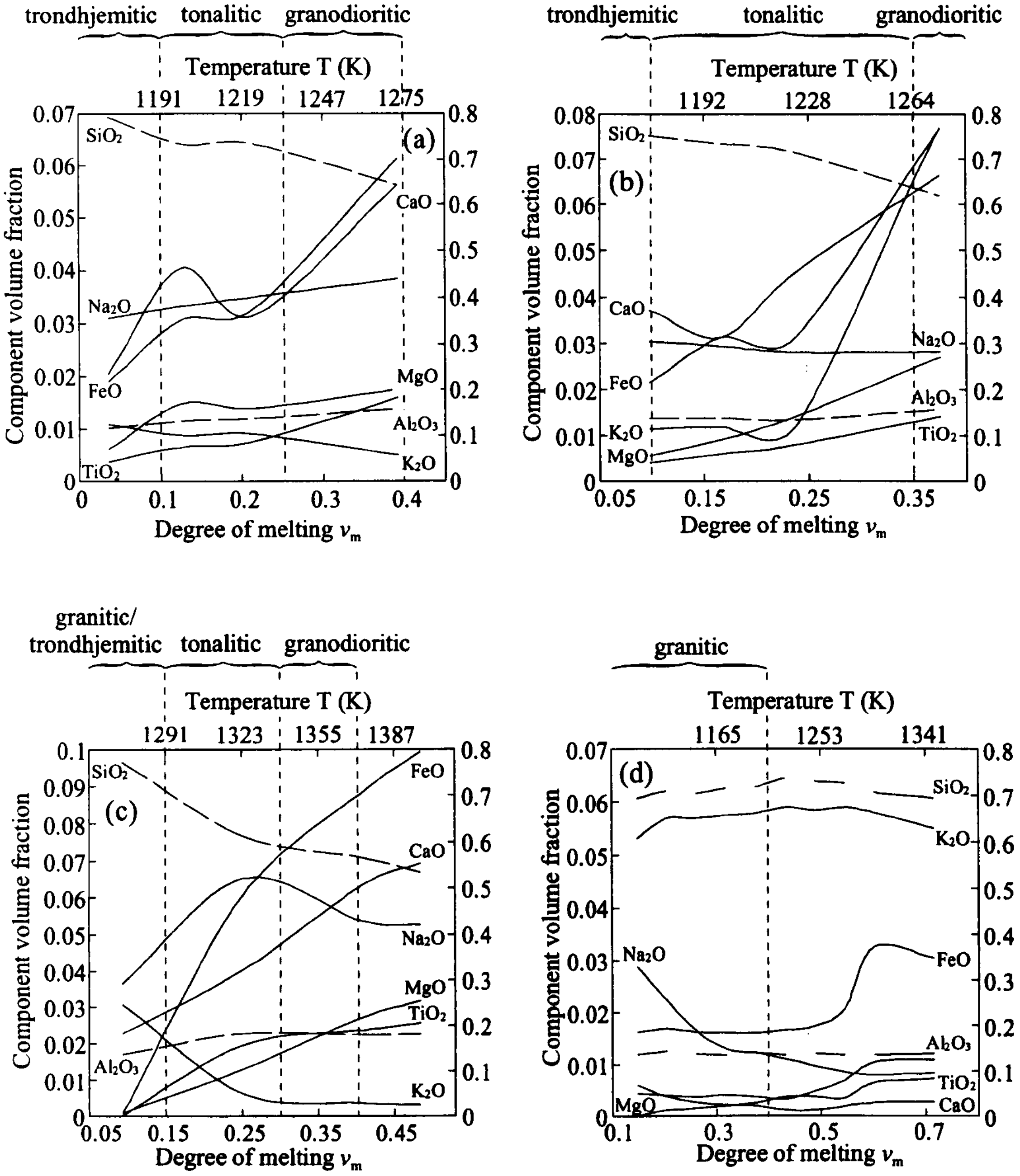

Figure 4.16. Melt composition in terms of component oxide volume fractions, as a function of the degree of melting (v_m) and the temperature (T), during partial melting of a variety of lower crustal rock types: (a) Andesitic greenstone; data from Beard and Lofgren (1991). (b) Horneblende hornfels; data from Beard and Lofgren (1991). (c) Meta-basalt; data from Rapp and Watson (1995). (d) Meta-pelite; data from Patino-Douce and Johnston (1991). In all cases, plain lines plot on the left hand ordinate axis; dashed lines plot on the right hand ordinate axis.

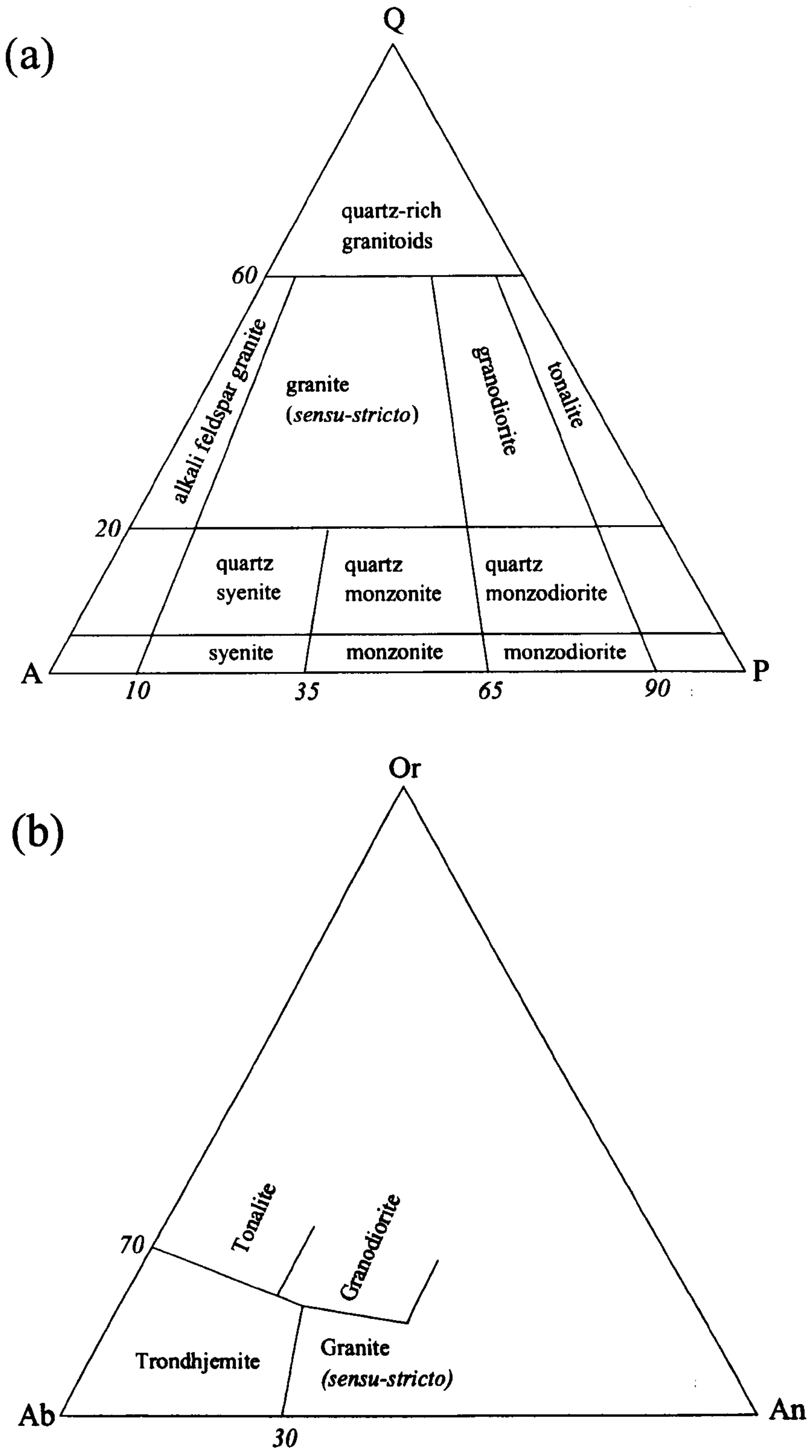

Figure 4.17. Classification of the granitic (*sensu-lato*) rocks. The granodioritic, tonalitic, trondhjemitic and granitic (*sensu-stricto*) melt compositions defined in figure 4.16 are defined as such because their compositions correspond with the compositions of the intrusive rocks defined above. (a) IUGS-Streckeisen classification in terms of the modal abundance of quartz (Q), alkali feldspar (A), and plagioclase feldspar (P) (after Streckeisen, 1976). (b) Classification in terms of normative anorthoclase (An), albite (Ab), and orthoclase (Or). This classification more clearly shows the distinction between trondhjemite and granite (*sensu-stricto*) (after Barker, 1979).

porosity wave *relative* to the position of the solidus isotherm (the top of the partial melt zone); for example, the melt in the leading porosity wave shown in figure 4.13(b) corresponds to a smaller degree of melting than that of the melt in the leading porosity wave shown in figure 4.14(d), because the melt in the porosity wave shown in figure 4.13(b) has thermodynamically equilibrated with partially molten rock at lower temperatures, closer to the position of the solidus isotherm. With decreasing κ_{eff}, the position of the leading porosity wave moves closer to the position of the solidus isotherm (figures 4.7(i-iii) and 4.12-4.14; figure 3.3; see also the discussions in §4.3.1.1 and §3.3.2); consequently, the composition of the melt in the wave corresponds to a smaller degree of melting of the source rock. In partial melt zones characterised by values of $\kappa_{eff} < 10^4$, the melt in the leading porosity wave may occupy a *large* volume fraction (>0.5) of the source rock, yet its composition corresponds to only a *small* (<0.4) degree of melting of the rock.

4.3.3 Segregation times and temperatures: estimates of mobile magma compositions

4.3.3.1 Segregation times and temperatures

The results presented in §4.3.1.3 indicate that the formation of a mobile magma is possible in partial melt zones with values of κ_{eff} in the range $10^{-2} \leq \kappa_{eff} < 10^4$ and ψ_{geo} in the range $10^{-4} \leq \psi_{geo} \leq 1$. For these values of κ_{eff} and ψ_{geo}, the model may be used to determine the dimensionless time required to *initiate* magma formation (the *segregation time* (t_{seg})), by recording the time required for the porosity at any point to reach the CMF (§3.3.3). The model may also be used to determine the *initial* normalised dimensionless temperature of the magma (the *segregation temperature* (θ_{seg})), by recording the temperature at the position of incipient magma formation (§3.3.4). The segregation time is important, because it may be used to estimate whether the time required for magma formation is geologically reasonable (§4.3.3.2); the segregation temperature is important, because it dictates the initial composition of the magma (§4.3.3.2). Figures 4.18-4.20 show examples of the segregation time, and segregation temperature, as a function of κ_{eff}, for several values of ψ_{geo}, φ, and the CMF. In all cases, Ste = 0.5 and $\chi = 2.5$.

Figure 4.18(a, c, e) shows the segregation time as a function of κ_{eff} for $\psi_{geo} = 10^{-4}$, 10^{-2} and 1, with φ = CMF = 0.5 and φ = CMF = 0.3 (c.f. §3.3.3). For $\psi_{geo} = 10^{-4}$ and 10^{-2}, segregation times are shortest ($t_{seg} \sim$ 5-40) in partially molten rocks with values of κ_{eff} in the range 5 to 5×10^3, and increase with both increasing and decreasing values of κ_{eff}; they are shorter for the case φ = CMF = 0.3 than for the case φ = CMF = 0.5 (figure 4.18(a and c)). For $\psi_{geo} = 1$, segregation times are shortest ($t_{seg} \sim$ 25-30) in rocks with values of κ_{eff} in the range 0.25 to 10 (figure 4.18(e)). Figure 4.18(b, d, f) shows the corresponding segregation temperatures as a function of κ_{eff}. For $\psi_{geo} = 10^{-4}$, the segregation temperature for both the cases φ = CMF = 0.5 and φ = CMF = 0.3 increases monotonically with increasing κ_{eff}, from <0.1 to ~0.9 (figure 4.18(b)). In contrast, for $\psi_{geo} = 10^{-2}$, the

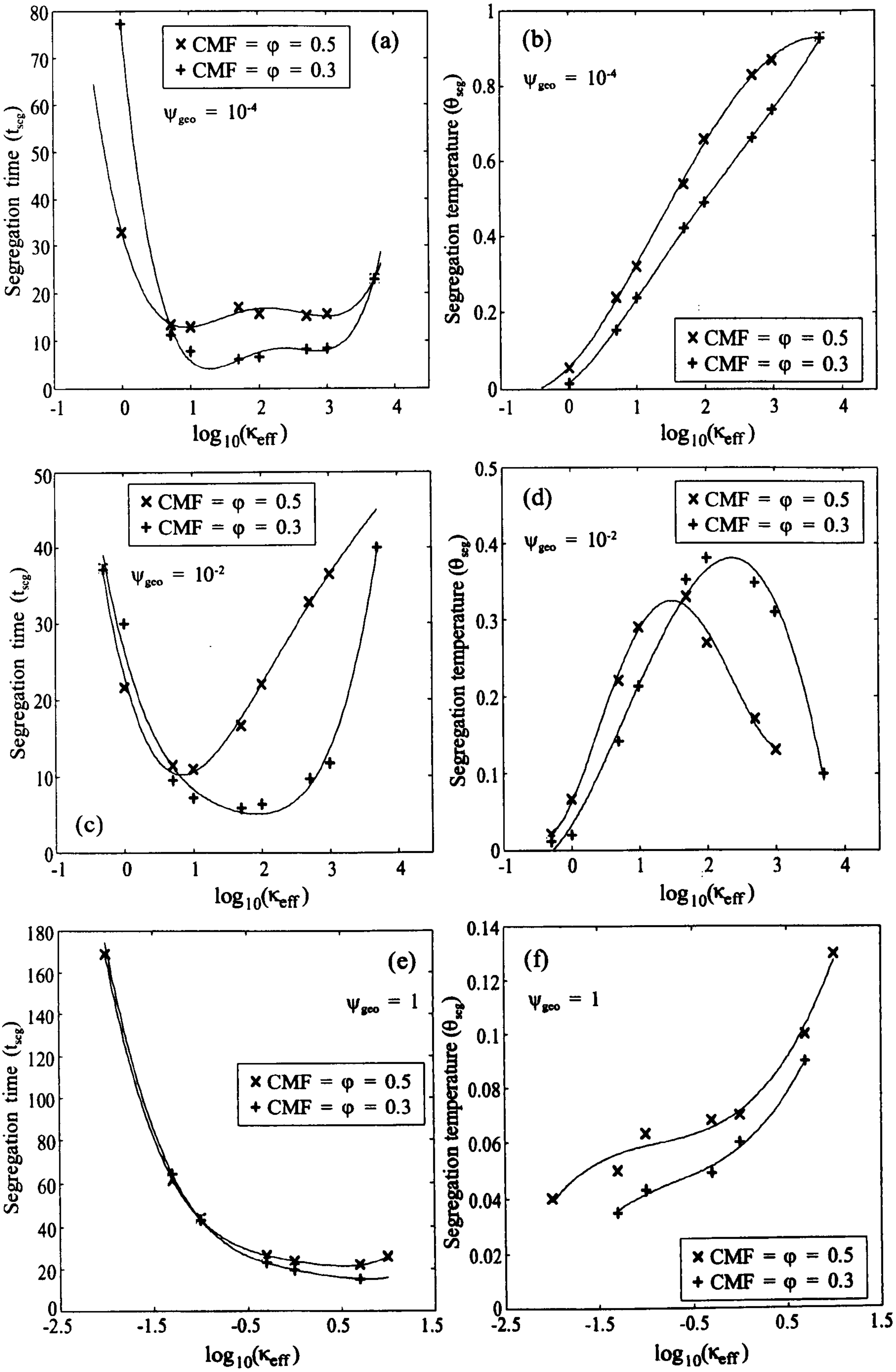

Figure 4.18. Dimensionless segregation time (t_{seg}) and segregation temperature (θ_{seg}) against κ_{eff}, for the cases CMF = φ = 0.5 and CMF = φ = 0.3, with: ((a) & (b)) $\psi_{geo} = 10^{-4}$; ((c) & (d)) $\psi_{geo} = 10^{-2}$; and ((e) & (f)) $\psi_{geo} = 1$. In all cases, Ste = 0.5 and $\chi = 2.5$. Curves denote best fit polynomials.

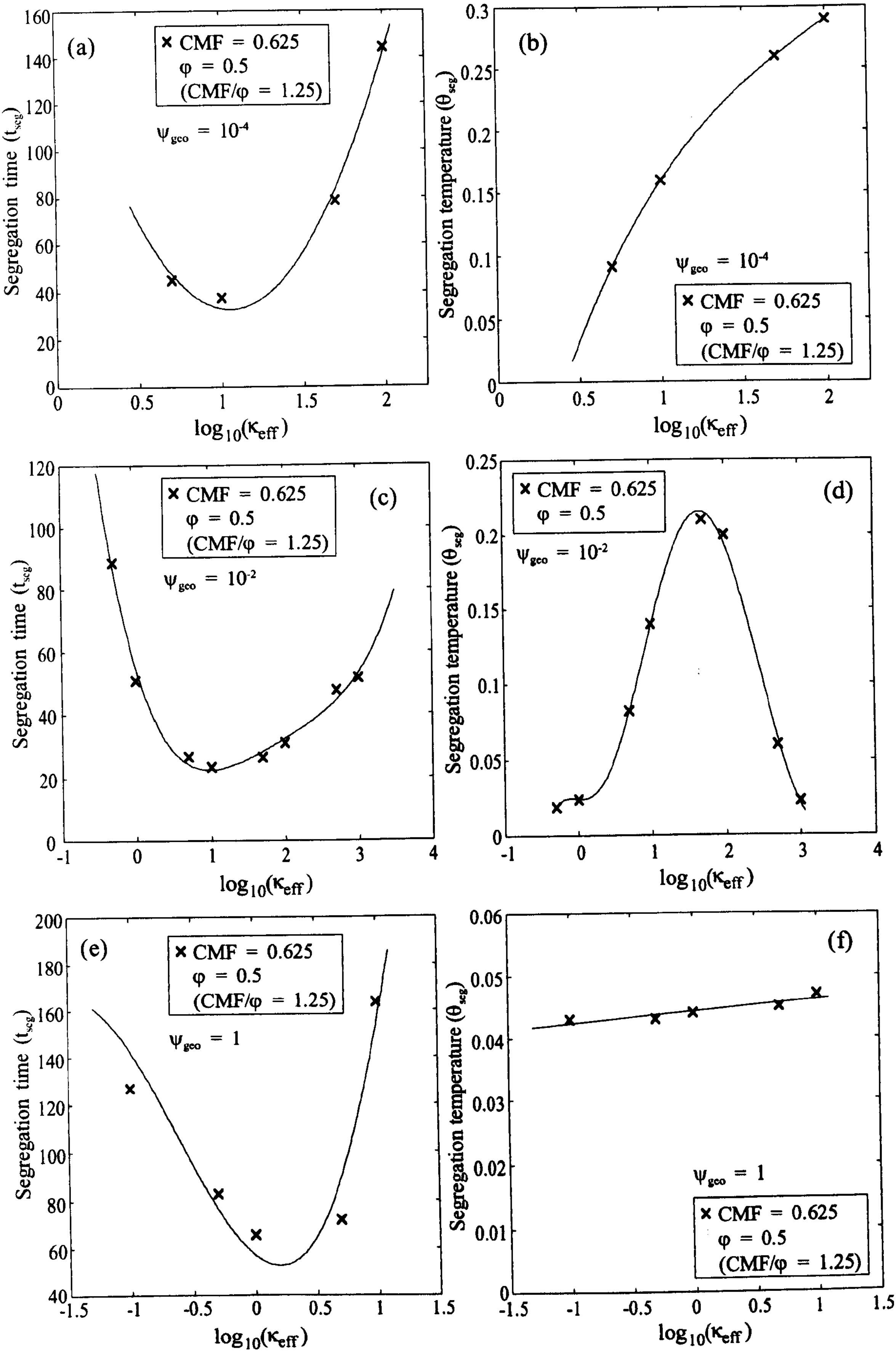

Figure 4.19. Dimensionless segregation time (t_{seg}) and segregation temperature (θ_{seg}) against κ_{eff}, for the case CMF = 0.625, φ = 0.5 (CMF/φ = 1.25), with: ((a) & (b)) $\psi_{geo} = 10^{-4}$; ((c) & (d)) $\psi_{geo} = 10^{-2}$; and ((e) & (f)) $\psi_{geo} = 1$. In all cases, Ste = 0.5 and $\chi = 2.5$. Curves denote best fit polynomials.

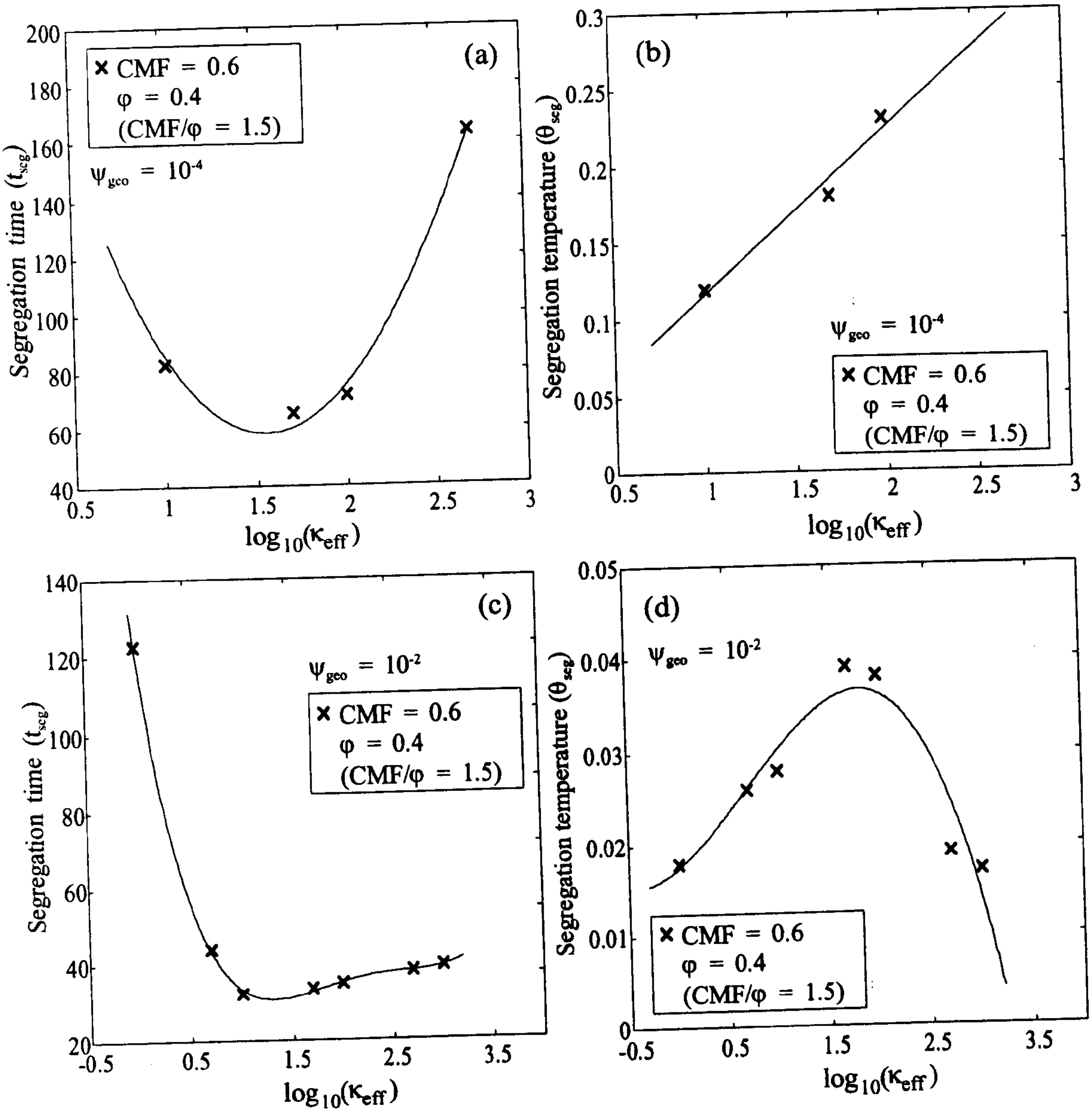

Figure 4.20. Dimensionless segregation time (t_{seg}) and segregation temperature (θ_{seg}) against κ_{eff}, for the case CMF = 0.6, $\varphi = 0.4$ (CMF/φ = 1.5), with: ((a) & (b)) $\psi_{geo} = 10^{-4}$; ((c) & (d)) $\psi_{geo} = 10^{-2}$. In all cases, Ste = 0.5 and $\chi = 2.5$. Curves denote best fit polynomials.

segregation temperature for both the cases φ = CMF = 0.5 and φ = CMF = 0.3 initially increases with increasing κ_{eff}, and then decreases, ranging from <0.1 to ~0.37 (figure 4.18(d)). For ψ_{geo} = 1, the segregation temperature is always low (<0.15) and increases with increasing κ_{eff} (figure 4.18(f)).

Figures 4.19 and 4.20 show the effect of increasing the CMF relative to the degree of melting at the contact (φ). Figure 4.19(a, c, e) shows the segregation time as a function of κ_{eff} for ψ_{geo} = 10^{-4}, 10^{-2} and 1 respectively, with φ = 0.5 and CMF = 0.625 (i.e. CMF/φ = 1.25). For ψ_{geo} = 10^{-4}, the segregation time is shortest (t_{seg} ~ 40) in partially molten rocks with a value of κ_{eff} ~ 10 (figure 4.19(a)). For ψ_{geo} = 10^{-2}, segregation times are shortest (t_{seg} ~ 20-30) in rocks with values of κ_{eff} in the range 5 to 10^2 (figure 4.19(c)); for ψ_{geo} = 1, the segregation time is shortest (t_{seg} ~ 60) in rocks with a value of κ_{eff} ~ 1 (figure 4.19(e)). Figure 4.19(b, d, f) shows the corresponding segregation temperatures as a function of κ_{eff}. For both ψ_{geo} = 10^{-4} and 1, the segregation temperature increases monotonically with increasing κ_{eff}, from <0.05 to ~0.3 for the case ψ_{geo} = 10^{-4}, but from only ~0.04 to 0.05 for the case ψ_{geo} = 1 (figure 4.19(b and f)). In contrast, for ψ_{geo} = 10^{-2}, the segregation temperature initially increases with increasing κ_{eff}, and then decreases, ranging from ~0.05 to ~0.2 (figure 4.19(d)). Figure 4.20 (a and c) shows the segregation time as a function of κ_{eff} for ψ_{geo} = 10^{-4} and 10^{-2} respectively, with φ = 0.4 and CMF = 0.6 (i.e. CMF/φ = 1.5). For ψ_{geo} = 10^{-4}, the segregation time is shortest (t_{seg} ~ 60) in partially molten rocks with a value of κ_{eff} ~ 30 (figure 4.20(a)); for ψ_{geo} = 10^{-2}, segregation times are shortest (t_{seg} ~ 30-40) in rocks with values of κ_{eff} in the range 10 to 10^3 (figure 4.20(c)). Figure 4.20(b and d) shows the corresponding segregation temperatures as a function of κ_{eff}. For ψ_{geo} = 10^{-4}, the segregation temperature increases monotonically with increasing κ_{eff}, from <0.1 to ~0.3 for the case ψ_{geo} = 10^{-4} (figure 4.20(b)); for ψ_{geo} = 10^{-2}, the segregation temperature initially increases with increasing κ_{eff}, and then decreases, ranging from ~0.015 to ~0.04 (figure 4.20(d)).

In general, the segregation *time* (t_{seg}) depends upon the rate of increase of the maximum porosity (e.g. figure 4.11), and the magnitude of the CMF. The segregation time is a minimum in partial melt zones with κ_{eff} in the range 5 to 5x10^3, ψ_{geo} = 10^{-4}, and CMF = φ (figure 4.18(a)), and for a given value of κ_{eff} generally increases with increasing ψ_{geo} and CMF/φ. The segregation *temperature* (θ_{seg}) depends upon the position of incipient magma formation *relative* to the position of the solidus isotherm (§3.3.4); for example, if magma formation occurs in the coolest part of the partial melt zone just below the solidus isotherm, then the segregation temperature is low. The segregation temperature is a minimum (~0.01) in partial melt zones with small κ_{eff}, large ψ_{geo}, and large CMF/φ (e.g. compare figures 4.20(d) and 4.18(b)), and with the exception of the case ψ_{geo} = 10^{-2}, increases with increasing κ_{eff}, decreasing ψ_{geo}, and increasing CMF/φ. The segregation temperature generally increases with increasing κ_{eff}, because in partially molten rocks with small values of κ_{eff}, the position of the porosity maximum, and hence the position of magma formation, occurs in the *coolest* part of the partial melt zone just below the solidus isotherm (i.e. the top of the partial melt zone); with increasing κ_{eff}, the position of the porosity maximum lags further behind the solidus isotherm, so magma formation occurs in *hotter* parts of the partial melt zone (§3.3.4 and §4.3.2.2; see also figures 4.7(i-iii) and 4.12-4.14). Likewise, the segregation temperature increases with decreasing ψ_{geo} and CMF/φ, because the position of the porosity maximum, and hence the position of magma formation, occurs in *cooler* parts of the partial melt zone, closer to the position of the solidus isotherm. The anomalous decrease in the segregation temperature with increasing κ_{eff} (for values >10-100) observed for the case $\psi_{geo} = 10^{-2}$ (figures 4.18(d), 4.19(d) and 4.20(d)) occurs because for these values of κ_{eff}, the leading porosity wave *bifurcates*, and with increasing κ_{eff} the position of the porosity maximum moves *closer* to the position of the solidus isotherm.

4.3.3.2 Predicting magma mobilisation times and compositions

For a given set of dimensional variables, the *dimensional* time required to initiate magma formation, and the *dimensional* temperature (T) (and corresponding degree of melting (ν_m)) at the position of incipient magma formation, may be estimated using the dimensionless segregation time (t_{seg}) and temperature (θ_{seg}) against κ_{eff} plots presented in §4.3.3.1 (figures 4.18-4.20). The procedure is relatively straightforward:

(i) calculate values for the dimensionless effective thermal diffusivity (κ_{eff}) and the dimensionless initial geotherm (ψ_{geo}) using the expressions (simplified from those presented in §4.2.3)

$$\kappa_{eff} = \frac{k}{\rho\left(c_p + \left(L + (T_{liq} - T_{sol})\right)\right)(1-\varphi)(\rho_s - \rho_m)g(\xi_s - (4\mu_s/3)))^{1/2}} \left(\frac{\mu_m}{ba^2\varphi^3}\right)^{3/2} \tag{4.38}$$

and

$$\psi_{geo} = \left(\frac{ba^2\varphi^3(\xi_s + (4\mu_s/3))}{\mu_m(T_{liq} - T_{sol})^2}\right)^{1/2} T_{geo} \tag{4.39}$$

(ii) using a plot (figures (4.18-4.20)) suitable for the values of ψ_{geo}, φ, and the CMF, record the dimensionless segregation *time* (t_{seg}) which corresponds to the calculated value of κ_{eff}.

(iii) convert this to the corresponding dimensional time (t) using the expression (§4.2.3)

$$t = \frac{t_{seg}}{(1-\varphi)(\rho_s - \rho_m)g}\left(\frac{\mu_m(\xi + (4\mu_s/3))}{ba^2\varphi^3}\right)^{1/2} \tag{4.40}$$

(iv) using a plot (figures (4.18-4.20)) suitable for the values of ψ_{geo}, φ, and the CMF, record the dimensionless segregation *temperature* (θ_{seg}) which corresponds to the calculated value of κ_{eff}.

(v) convert this to the corresponding dimensional *degree of melting* (ν_m) using the expression (§4.2.3)

$$\nu_m = \varphi\theta_{seg} \tag{4.41}$$

(vi) convert this to the corresponding dimensional temperature (T) using the expression (§4.2.3)

$$T = (T_{liq} - T_{sol})\nu_m + T_{sol} \quad (4.42)$$

The *dimensional* segregation times and temperatures obtained using equations (4.38)-(4.42) and figures 4.18-4.20 compare favourably with those obtained directly from the numerical solutions. For example, consider the dimensional variables used to obtain the solution shown in figure 4.13(b) (table 4.4). Substituting these values into equations (4.38) and (4.39) yields a value of $\kappa_{eff}' = 0.991$ (~1) and $\psi_{geo} = 0.032$ ($\sim 10^{-2}$). Assuming that $\varphi \sim 0.5$, and that the CMF ~ 0.5, figure 4.18(c) yields a segregation time of $t_{seg} \sim 23$, and figure 4.18(d) yields a segregation temperature of $\theta_{seg} \sim 0.06$. Substituting these values into equations (4.40) - (4.42) yields a dimensional segregation time of ~2.2 M.y., a dimensional degree of melting of ~0.03, and a dimensional segregation temperature of ~1170 K. For comparison, the numerical solution yields a dimensional segregation time of ~2 M.y, a degree of melting of ~0.03, and a segregation temperature of ~1170 K. The slight discrepancy between the dimensional segregation time obtained directly from the numerical solution and that estimated from figure 4.18(c) occurs because the value of ψ_{geo} used to obtain the numerical solution ($\psi_{geo} \sim 0.032$) is slightly different to that used to obtain the segregation times shown in figure 4.18(c) ($\psi_{geo} \sim 0.01$).

Having estimated the dimensional degree of melting (ν_m) at the point of incipient magma formation, the initial *composition* of the melt fraction of the magma may be deduced using empirical data such as that shown in figure 4.16. For example, consider again the partial melt zone shown in figure 4.13(b), in which the degree of melting at the position of incipient magma formation is ~0.03. The initial composition of the melt fraction of the magma therefore corresponds to a degree of melting of ~0.03, and for an andesitic greenstone, hornblende hornfels, or meta-basalt source rock, its composition would be acidic (high SiO_2) granitic (*sensu-stricto*) to trondjhemitic (figure 4.16(a-c)). For a meta-pelite source rock, its composition would be granitic (*sensu-stricto*). Note that the composition of the melt fraction which forms the magma corresponds to a *small* degree of melting of the source rock (~0.03), despite having accumulated until it exceeds the CMF (~0.5).

When the dimensionless segregation temperature shown in figures 4.18-4.20 is dimensionalised to yield the corresponding degree of melting (equation (4.41)), it becomes apparent that the degree of melting at the position of incipient magma formation is *always* small relative to the CMF. For example, if $\varphi = 0.5$, then the degree of melting generally varies from only ~0.01 (figure 4.19(d); note that the CMF = 0.625) to ~0.2 (figure 4.18(d); note that the CMF = 0.5); only in figure 4.18(b), for values of $\kappa_{eff} \geq 10^3$ and $\psi_{geo} = 10^{-4}$, does the degree of melting exceed ~0.4. Consequently, in partial melt zones with values of $\kappa_{eff} < 10^3$ and $\psi_{geo} \geq 10^{-4}$ (i.e. the majority of values of κ_{eff} and ψ_{geo} for which magma formation is predicted), *the composition of the melt fraction which forms the magma* *corresponds to only a small (<0.4) degree of melting of the source rock.* In typical lower crustal source rocks, a degree of melting of <0.4 yields melt which is granitic (*sensu-lato*) in composition (figure 4.16; see also table 2.1); consequently, *the composition of the melt fraction which forms the magma is granitic.*

4.4 Discussion

4.4.1 The mobilisation of granitic melt in the continental crust

A *quantitative*, 1-D physical model of a partial melt zone in the lower crust has been presented, and the dynamics of melt generation, segregation and mobilisation within the zone have been characterised in terms of five externally prescribed dimensionless parameters: the dimensionless effective thermal diffusivity (κ_{eff}); the dimensionless initial geothermal gradient (ψ_{geo}), the degree of melting at the contact between the partially molten rock and the underlying heat source (φ), the Stefan number (Ste), and the ratio of the thermal diffusivities in the partially molten rock and the overlying solid rock (χ).

The spatial distribution of the melt volume fraction (porosity) within the partial melt zone depends upon the relative rates of upward transport of melt and heat, and for given values of ψ_{geo}, φ, Ste and χ, is predominantly governed by the magnitude of κ_{eff}. In melt zones characterised by values of κ_{eff} in the range $10^{-2} \leq \kappa_{eff} < 10^{4}$, the rate of melt transport is rapid compared to the rate of heat transport, so the melt migrates upwards faster than the position of the solidus isotherm. The melt cannot migrate beyond the position of the solidus isotherm, because at that position the porosity and hence permeability falls to zero; effectively, the solidus isotherm acts as a 'lid' on the top of the partial melt zone. Consequently, the melt accumulates below the solidus isotherm, and a porosity wave forms. The amplitude of the leading porosity wave increases with time, and eventually, the local melt volume fraction may exceed the CMF, in which case the solid matrix disaggregates and *a mobile magma forms,* which may migrate away from the partial melt zone if a suitable route is made available; magma formation is predicted unless the CMF is more than 50% greater than the degree of melting at the contact (φ).

With increasing height, the temperature in the partial melt zone decreases; consequently, as the melt migrates upwards, it continually thermodynamically equilibrates with solid phase at progressively lower temperatures, and its composition *changes* to correspond to a *smaller* degree of melting of the source rock. If the melt accumulates to form a porosity wave close to the position of the solidus isotherm where the temperatures is low, then the composition of the melt corresponds to only a *small* degree of melting of the source rock, despite occupying a large volume fraction of the rock.

Moreover, if the amplitude of the porosity wave increases until a mobile magma forms, then the composition of the melt fraction of the magma corresponds to only a *small* (<0.4) degree of melting of the source rock. This result, in conjunction with empirical data, indicates that in partially molten source rocks characterised by κ_{eff} in the range $10^{-2} \leq \kappa_{eff} \leq 10^{3}$, *the composition of the melt fraction of the mobile magma is granitic (sensu-lato).*

4.4.2 Application of the numerical results

Ideally, for a given lower crustal rock type and tectonic setting, the values of the *dimensional* governing variables would be uniquely defined, in which case the values of the *dimensionless* governing parameters κ_{eff}, ψ_{geo}, Ste and χ would also be uniquely defined, and the only 'free' variable would be φ, the degree of melting at the contact between the partially molten rock and the underlying heat source. If this were the case, the model could be used to predict *specific* timescales for magma mobilisation, and in conjunction with empirical data, *specific* magma compositions. Variables such as the latent heat (L), specific heat capacity (c_p), thermal conductivity (k), solidus-liquidus interval (T_{liq}-T_{sol}), and density (ρ) are well constrained for a given rock type (§4.2.4.1), and the melt shear viscosity may be calculated if compositional data is available (e.g. figure 4.4). However, the matrix bulk and shear viscosities (ξ_s, and μ_s), and the permeability constant (b), are poorly constrained; moreover, although values of the grain size (a) are likely to lie within the range given in table 4.2, it is difficult to allocate a *specific* value. Consequently, the magnitude of the *key* dimensionless governing parameter κ_{eff} is poorly constrained even for a given lower crustal rock type and tectonic setting (equation 4.38).

By inspection of equation (4.38), it is possible to gauge the effect of varying the dimensional variables on the magnitude of κ_{eff}, and hence on the dynamics of melt generation, segregation and mobilisation. Low matrix bulk and shear viscosities ($\sim 10^{15}$), high melt viscosities ($\sim 10^{7}$), a small permeability constant (1/2500), and a small grain size (radius ~ 0.25mm), promote *large* values of κ_{eff} ($>10^{3}$), for which magma mobilisation will *not* occur. Conversely, high matrix bulk and shear viscosities ($\sim 10^{21}$), low melt viscosities ($\sim 10^{3}$), a large permeability constant (1/50), and a large grain size (radius ~ 5mm), promote *small* values of κ_{eff} ($<10^{-2}$), for which mobilisation will again *not* occur. This latter result is counter-intuitive; low melt viscosities, a large permeability constant, and a large grain size might be expected to promote efficient melt segregation. However, in partial melt zones characterised by values of $\kappa_{eff} < 10^{-2}$, the melt freezes rapidly as it migrates into cooler regions of the partial melt zone, so the porosity, and hence permeability, is always low; consequently, melt segregation is inhibited (§3.4.1). Melt segregation and magma mobilisation is predicted in partial melt zones with matrix and melt viscosities, permeability constants, and grain sizes in the *mid-range* of those presented in table 4.2, or in partial melt zones where, for example, high melt viscosities are countered by high matrix viscosities, or a large grain size is countered by a small matrix viscosity, to yield a value of κ_{eff} in the range $10^{-2} \leq \kappa_{eff} < 10^{4}$. Within this range of values of κ_{eff}, higher matrix viscosities, larger grain sizes, and smaller melt viscosities yield mobile magma in which the composition of the melt fraction corresponds to a *smaller* degree of melting of the source rock.

The advantage of working with dimensionless equations is that the results obtained are general, and are not invalidated by the use of poorly constrained variables. However, the results are of limited value unless they may be used by other workers. The dimensionless segregation time and temperature curves presented in figures 4.18-4.20 were derived because, in conjunction with equations (4.38)-(4.42), they may be used to estimate the *dimensional* time required for melt segregation, and the degree of melting to which the composition of the segregated melt corresponds (§4.3.3.2). Previous estimates of the time required for melt segregation in the crust have been based on the characteristic compaction time of McKenzie (1985, 1987)

$$t_h = \frac{h\mu_m\phi}{k(1-\phi)^2(\rho_s-\rho_m)g} \tag{4.43}$$

in which the porosity ϕ is equated with the degree of melting of the source rock, and h denotes the source region thickness (see the discussion in §2.3.4.1). Yet equation (4.43) is obtained from a simple model of buoyant fluid flow through a deformable mush which does not adequately reproduce the complexity of a crustal partial melt zone, and generally yields unreasonably high estimates of the time required for melt segregation (§2.3.4.1). For example, consider the time required for melt segregation in a partial melt zone with $\xi_s \sim \mu_s \sim 10^{18}$ Pa s, $\mu_m \sim 10^{5}$ Pa s, a ~ 2.5mm, b ~ 1/1000, $(\rho_s - \rho_m) \sim 500$ kg m^{-3}, $\varphi \sim$ CMF ~ 0.5, and the values of k, c_p, L, $(T_{liq} - T_{sol})$, T_{geo}, and ρ given in table 4.4. Using figures 4.18-4.20 and equations (4.38) - (4.42), yields a geologically 'reasonable' time of ~4 M.y to segregate a granitic melt fraction with a composition corresponding to a degree of melting of ~0.1. In contrast, setting $\phi = 0.1$, assuming a source region thickness of h ~5 km, and substituting for the values of μ_m, a, b, and $(\rho_s - \rho_m)$ in equation (4.43), yields a geologically unreasonable time of ~45 M.y.

4.4.3 Comparison of the model predictions with geological evidence

The geological evidence suggests that granitic (*sensu-lato*) melt must often segregate in the source region, from partially molten rock in which the solid matrix maintains an interconnected matrix (§2.3.2). For example, partial melts of granitic composition represent only small (<CMF) degrees of partial melting of their source rocks; moreover, many exposed lower crustal granulite terrains exhibit geochemical and mineralogical characteristics which indicate that they are residues left after the *in-situ* extraction of a granitic partial melt fraction (e.g. Fyfe, 1973; Clifford *et al.*, 1981; Clemens, 1989, 1990; Pin, 1990; Vielzuf *et al.*, 1990). Of these, some retain mesoscopic layering structures which indicate that the matrix was not disrupted during segregation of the melt (Clemens, 1990). The model

presented in this chapter predicts that in partial melt zones characterised by a wide range of values for the governing variables, melt which corresponds to only a small (<CMF) degree of partial melting of the source rock, and which is granitic (*sensu-lato*) in composition, will segregate and accumulate until it forms a mobile magma. Except in the localised region of magma mobilisation, the solid matrix of the partially molten rock is not disrupted during segregation, and remains in the source region as a 'restitic' residue. The mineralogy of the residue, predicted from empirical data (Vielzuf and Holloway, 1988; Beard and Lofgren, 1991; Patiño Douce and Johnston, 1991; Rushmer, 1991; Rapp and Watson, 1995), corresponds to that of many granulite terrains (anhydrous plagioclase + pyroxene ± quartz, olivine, garnet, magnetite, ilmenite).

Geochemical evidence suggests that many trondjhemite-tonalite-granodiorite (TTG) suites, such as the Cordillera Blanca Batholith in the Peruvian part of the Andes, originate by partial melting of newly underplated basalt (e.g. Atherton and Petford, 1996; Petford and Atherton, 1996). For a basaltic source rock, empirical data is available from which melt compositions may be deduced (figure 4.16), and the dimensional time required for segregation, and the composition of the segregated melt, may be estimated using figures 4.18-4.20 in conjunction with equations (4.38)-(4.42). Table 4.5 shows suitable values for the latent heat (L), specific heat capacity (c_p), thermal conductivity (k), solidus-liquidus interval (T_{liq}-T_{sol}), and density (ρ). The viscosity of the granitic melt produced during partial melting of a basaltic rock is $\sim 10^4$ Pa s (figure 4.4); assuming that the rock is at or close to textural equilibrium, a suitable value for the constant b in the permeability equation is ~1/500 (§4.2.4.1(i)). The remaining variables required are the matrix bulk and shear viscosities (ξ_s and μ_s), the grain size (a), the CMF, and the degree of melting at the contact (φ). If it is assumed that the grain size (diameter) is ~5mm, and that $\varphi \sim$ CMF ~ 0.5, then for matrix viscosities of $\xi_s \sim \mu_s \sim 10^{15}$ Pa s, the time required for melt segregation is ~15,000 yrs, and the composition of the segregated melt is granodioritic-tonalitic. With increasing matrix viscosity, the time required for melt segregation increases, and the composition of the segregated melt becomes tonalitic. For matrix viscosities of $\xi_s \sim \mu_s \sim 10^{20}$ Pa s, the time required for melt segregation is ~10 M.y., and the composition of the segregated melt is trondhjemitic. Note that the the most abundant rock type in the Cordillera Blanca Batholith is trondhjemite (Atherton and Petford, 1996); these results *may* therefore indicate that the bulk and shear viscosities of partially molten basalt are most likely to lie in the range $\sim 10^{17}$ - 10^{20} Pa s.

The model in its current form uses only a simple parameterisation of the 'degree of melting' to predict, semi-quantitatively, melt and matrix compositions during melting and melt segregation. However, until the values of the governing variables, and the compositions and melting relations of the source rocks, are better constrained by experimental and theoretical data, a more sophisticated approach is not warranted. At this stage, it suffices that the model predicts the generation and

Symbol	Description	Values	Units
k	thermal conductivity	2	$W\,K^{-1}m^{-1}$
c_p	specific heat capacity	1,200	$J\,kg^{-1}K^{-1}$
L	latent heat	600,000	$J\,kg^{-1}$
T_{liq}-T_{sol}	liquidus-solidus interval	300	K
ρ	density	3,000	$kg\,m^{-3}$
ρ_s-ρ_m	matrix-melt density difference[1]	600	$kg\,m^{-3}$
μ_m	melt shear viscosity[2]	10^4	Pa s
b	constant in permeability relation[3]	1/500	None
T_{geo}	initial geothermal gradient	7	$K\,km^{-1}$
a	matrix grain radius	2.5×10^{-3} (2.5mm)	m
CMF	Critical Melt Fraction	0.5	None
φ	degree of melting at the contact	0.5	None

Table 4.5. Suitable values of the dimensional variables for a basaltic source rock in the lower crust.

---

[1] Obtained from figure 4.21.

[2] Obtained from figure 4.4.

[3] Assuming the partially molten rock is at, or near, textural equilibrium. The value of 1/50 predicted for texturally equilibrated rocks using the data of Cheadle (1989) was not used, because the data of Cheadle (1989) overestimates the permeability at high porosities (>0.01 - 0.19) (§4.2.4.1(i)).

segregation of granitic (*sensu-lato*) melt within geologically reasonable timescales, and in agreement with the geological evidence.

4.4.4 The effect of fractures in the partial melt zone

The results presented both in this chapter, and in chapter 3, were obtained assuming that melt in the partially molten crust flows *solely* along grain edges until the formation of a mobile magma. In contrast, melt in the partially molten mantle appears to flow along grain edges only until it reaches a network of macroscopic fractures, through which it may rapidly migrate upwards away from the partial melt zone (e.g. Lister and Kerr, 1991; Takada, 1994). If melt flow occurs predominantly along grain edges, then the melt thermodynamically equilibrates with the matrix through which it passes, and its composition corresponds to that predicted by batch (equilibrium) melting (§3.2.2). In contrast, if melt flow occurs predominantly through fractures, then its composition corresponds more closely to that predicted by *fractional* melting (McKenzie and Bickle, 1988; Watson and McKenzie, 1990). The presence of fractures may therefore have a significant effect on the composition of the melt which segregates from the partial melt zone.

Significant quantities of melt will flow through fractures only if they extract melt efficiently from the partial melt zone. The results of Lister and Kerr (1991) indicate that a fracture filled with buoyant melt will spontaneously propagate if its length is of the order of (1-2) hundreds of metres and its width is of the order of millimetres; if such fractures are present in a crustal partial melt zone, they will propagate upwards towards the position of the solidus isotherm. However, the conductive transport of heat from the melt at the tip of the propagating fracture is rapid compared with the advective transport of heat to the tip; consequently, freezing of the melt at the tip halts the fracture soon after it propagates beyond the position of the solidus isotherm into the overlying solid rock (Rubin, 1995). Consequently, it is unlikely that such fractures will transport significant quantities of melt through the partial melt zone. Moreover, the *nucleation* of such fractures is poorly understood. A large positive volume change on melting may generate cracks at the grain scale (Clemens and Mawer, 1992), but the coalescence of these small cracks to form a fracture with the critical size required for propagation has not been considered. Banks (1996) has modelled numerically the nucleation of fractures in the partially molten asthenosphere, and concludes that externally driven horizontal extension at strain rates greater than $\sim 10^{-14}$ s^{-1} generates large vertical fractures near the top of a high porosity region. However, granitic bodies are not found exclusively in extensional regimes (Brown, 1994), which indicates that extension is not required to facilitate granitic melt segregation. In short, it is not clear how fractures are initiated in a crustal melt zone, and in contrast to the mantle, any fractures which do form are unlikely to transport *significant* quantities of melt.

4.4.5 The assumptions of the model

The conservation equations (4.1) - (4.6) governing the model presented in this chapter are valid assuming (i) that the thermodynamic properties of the melt and matrix are identical and constant; (ii) no internal heat production; (iii) that the pressures in melt and matrix are equal; (iv) that both melt and matrix may be treated as Newtonian fluids with constant viscosities; (v) that the flow of both melt and matrix is low Reynolds number; (vi) validity of the Boussinesq approximation; (vii) a constant melt-matrix density contrast (§4.2.1); (viii) local thermodynamic equilibrium, and (ix) that the partially molten rock is homogeneous and isotropic. It is reasonable to question the validity of these assumptions when applied to a partial melt zone in the lower crust.

The assumption that the thermodynamic properties of both melt and matrix are identical and constant is valid; thermal conductivities and specific heat capacities for common lower crustal minerals vary by less than 20-25% over the temperature range 600 - 1300K, and differ by less than 25% between minerals and their melts (Murase and McBirney, 1973; Richet and Bottinga, 1986; Neuville *et al.*, 1993; Clauser and Huenges, 1995). The assumption of no internal heat production in the *lower* crust is also valid, as the available evidence indicates that radiogenic isotopes tend to be concentrated in the *upper* crust (Lachenbruch, 1970; Lachenbruch and Sass, 1978; Pollack and Chapman, 1977). If significant internal heat production did occur, the effect would be to increase the volume of melt generated in the partial melt zone, and consequently enhance the porosity, permeability, and rate of melt migration.

The assumption of equal melt and matrix pressures is discussed in §3.4; it is equivalent to assuming that the matrix creep rate is rapid compared to the matrix strain rate. For the strain rates predicted by the model, the matrix deforms by melt enhanced diffusion creep (§4.2.4.1(iii)), and the assumption of equal melt and matrix pressures is valid (§3.4.2). Likewise, the assumption of a Newtonian rheology for the matrix is valid (§4.2.4.1(iii)), although the assumption of *constant* matrix bulk and shear viscosities may not be. The values of the bulk and shear viscosity depend upon composition, temperature, grain size, and porosity, and the dependence is poorly understood (§4.2.4.1(iii)), although the effect of compositional and temperature variations across the partial melt zone is likely to be negligible compared to the effect of grain size and porosity variations. Assuming a constant *mean* grain size, the key control becomes porosity; the variation in bulk viscosity with porosity (void space) shown in figure 4.6 is less than 1 order of magnitude for porosities in the range $0.005 < \phi < 0.1$. Although this data is derived from equation (4.33), which ignores the effect of melt in the pore spaces, a small (<1 order of magnitude) variation in both the bulk and shear viscosities with melt volume fraction (porosity) is in agreement with the results of deformation experiments (Arzi, 1978; van der Molen and Paterson, 1979), which indicate that the strength of the matrix remains approximately constant until the melt volume fraction approaches the CMF.

Although the rheology of silicate melts at *high* viscosities (> 10^9 Pa s) and strain rates (> 10^{-4} s^{-1}) is non-Newtonian (e.g. Webb and Dingwell, 1990); for the melt shear viscosities predicted in §4.2.4.1(ii), and the strain rates predicted by the model, the assumption of a Newtonian rheology for the melt is valid. The viscosity of granitic (*sensu - lato*) melt of *constant* composition varies by ~4 to 7 orders of magnitude over the temperature range 973 - 1293 K (e.g. Shaw, 1963; Murase and McBirney, 1973; Ryan and Blevins, 1987), an observation which prompted Fountain *et al.* (1989), in their model of melt generation and segregation in the crust, to assume that the melt viscosity varies by ~ 6 orders of magnitude over the temperature range 973 - 1293 K. However, the results of §4.2.4.1(ii) indicate that the viscosity of granitic melt produced *during* partial melting over the temperature range 1093 - 1293 K varies by less than 0.1 - 1 orders of magnitude, because of changes in the silica and water content of the melt during melting. The assumption of constant melt viscosity is therefore reasonable.

The assumption that the flow of both melt and matrix has a low Reynolds number (Re) is valid if

$$\mathrm{Re} = \frac{|\mathrm{v}|L}{\nu} << 1 \qquad (4.44)$$

where v is a characteristic velocity, L is a characteristic lengthscale, and ν is the kinematic viscosity. With v ~ ω and L ~ a (McKenzie 1984), the maximum Reynolds number for the melt is ~10^{-9}, and for the matrix ~10^{-22}; the assumption that the flow of both melt and matrix has a low Reynolds number is therefore valid.

The Boussinesq approximation is commonly invoked in fluid dynamics; essentially, it is equivalent to assuming that volume, rather than mass, is a conserved quantity. The effect of this assumption is to under-estimate the volume of melt produced, although the effect will be negligible unless the volume change on melting is large. For meta-sedimentary rocks with densities of ~2600 - 2800 kg m^{-3}, containing ~10 - 40 wt% biotite, Clemens and Mawer (1992) calculate the volume change on melting to be ~3 - 18 vol%, which does not lead to a significant underestimate of the volume of melt produced.

The density contrast between the melt and matrix (ρ_s - ρ_m) depends upon the densities of the melt (ρ_m) and matrix (ρ_s), which in turn depend upon their compositions. During melting, the compositions of both melt and matrix continually change (cf. 4.2.4.1(ii)). If the composition of the melt is known, its density may be calculated using the empirical model of Lange and Carmichael (1987); if the mineral mode of the matrix is known, then the density of the matrix may be calculated using density data for individual minerals (Deer *et al.*, 1992). Figure 4.21 shows the calculated melt density, matrix density, and melt - matrix density contrast as a function of temperature, during partial melting of hydrated basalts and andesites. As melting proceeds, the denser, more refractory minerals are consumed, and both the melt and matrix densities generally increase with increasing temperature.

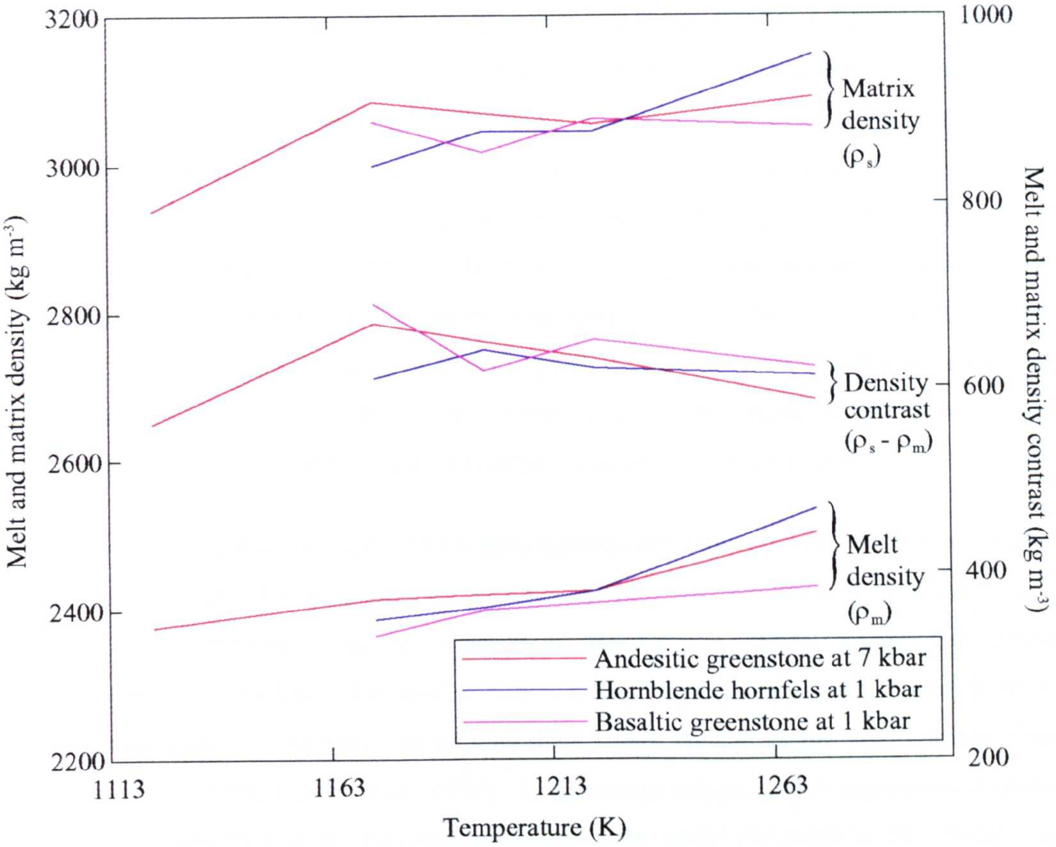

Figure 4.21. Melt density (ρ_m), residual solid matrix density (ρ_s), and melt-matrix density contrast (ρ_m - ρ_s) versus temperature during partial melting of crustal rocks. Melt and matrix densities plot on the left-hand ordinate axis; melt-matrix density contrast plots on the right-hand ordinate axis. Melt densities were calculated using the model of Lange and Carmichael (1987); matrix densities were calculated using data for individual minerals (Deer *et al.*, 1992). Compositional and modal data from Beard and Lofgren (1991).

However, the density contrast remains approximately constant, varying by <10% from its mean value in each case, which indicates that the assumption of a constant density contrast is reasonable. Note that a volume change on melting of ~25% is required to produce the density contrast of ~600 kg m^{-3} observed in figure 4.21, which indicates that in these meta-igneous rocks, which melt primarily by the decomposition of amphibole rather than biotite, the volume change on melting is higher than that estimated by Clemens and Mawer (1992) for meta-sedimentary rocks.

Local thermodynamic equilibration during melting and melt segregation has a significant effect on the compositional evolution of the melt as it migrates through the partial melt zone. Maintenance of equilibrium requires that the rates of thermal and chemical equilibration are rapid compared to the rate of thermodynamic evolution. Rates of *thermal* equilibration are rapid; the kinetic limit on the rate of *chemical* equilibration is component diffusion in the solid phase (§3.4.2). Local thermodynamic equilibrium is maintained only if the rate at which components diffuse in the solid is rapid compared to the rate at which components are advected by the melt. Assuming that melt flow occurs along grain edges, the assumption of local equilibrium during melting and melt segregation in a crustal melt zone is valid except for the *fastest* rates of advective component transport, the *slowest* rates of component diffusion, and a grain size (radius) greater than ~1.4mm (§3.4.2).

Finally, the assumption that the lower crust is homogeneous and isotropic is unlikely to be valid in all lower crustal melt zones. For example, meta-sedimentary protoliths are likely to be layered, and both the composition and rheology of the layers may differ (Brown *et al.*, 1995). Rheological differences between the layers may facilitate *deformation enhanced* melt segregation, in which melt flows along grain edges and collects in dilatant sites such as shear bands, tension gashes, and boudins (Sawyer, 1991, 1994; Brown, 1994; Brown *et al.*, 1995). Deformation enhanced melt segregation operates at the cm-m scale, rather than at the km scale predicted by the model presented in this chapter, and if the segregated melt cannot escape from the source region, results in the formation of migmatites (Brown, 1995). The model presented in this chapter is most likely to be suited to melting of meta-igneous protoliths in the deep crust; for example, in regions such as convergent plate margins where the lower crust is comprised of homogeneous primitive basalt emplaced by repeated underplating (Kono *et al.*, 1989; Rudnick, 1992; Atherton and Petford, 1996; Petford and Atherton, 1996; Petford *et al.*, 1996).

4.4.6 The model of Fountain *et al.* (1989)

The only previous attempt to formulate a *quantitative* model of melt generation and segregation in the continental crust is that of Fountain *et al.* (1989). They correctly observe that the phase change and phase transport aspects of melt generation and segregation are *coupled* processes, and formulate a set of conservation equations governing the transport of heat, mass and momentum which they solve numerically. Their results are qualitatively similar to those obtained from the model presented in this chapter in that they too predict the formation of a mobile magma (their 'melt pool'), yet in all other aspects they are dissimilar. However, the problem they attempt to solve is rather more complex than that considered in this chapter. For example, rather than modelling the partial melt zone only until the incipient formation of a mobile magma ('melt pool'), they attempt to include a description of the subsequent development of the melt pool. Furthermore, they include a description of the underlying magma heat source rather than assuming constant heating, and include a description of variable melt viscosity rather than assuming constant melt viscosity.

However, a close examination of their formulation and method of solution reveals a number of significant errors and ambiguities. For example, the 1-D expressions they present governing both conservation of heat and mass are incorrectly formulated, because they do not include the term $(w_l + w_s - w_m)\partial\rho_l\nu_l/\partial z$ when describing the rate of phase change (or rate of melt production) (cf. equation 3.22). Rather, they describe the rate of phase change as a function of the rate of temperature change only, and do not recognise that phase change occurs both because the temperature field changes temporally, and because the phases migrate through a temperature field which changes spatially (see §3.2.2). The term $(w_l + w_s - w_m)\partial\rho_l\nu_l/\partial z$ is important because it describes component exchange between the melt and matrix during melt migration, which causes the composition of the melt to evolve and results in the segregation of granitic melt. Its neglect means that the model of Fountain *et al.* (1989) fails to describe a crucially important process.

Their method of solution is ambiguous because they do not explain how they solve for the melt and matrix velocities. The purpose of the Boussinesq approximation invoked in chapter 3 is to locate the melt and matrix velocities in the barycentric reference frame, in which the mixture velocity is zero, and in which the melt and matrix velocities are related by $\phi w_m = -(1-\phi)w_s$. The melt velocity may then be eliminated from the equation governing conservation of momentum (equation 3.21), and the equation solved independently for the matrix velocity. No such procedure is described by Fountain *et al.* (1989), yet unless the mixture velocity is specified, the melt and matrix velocities cannot be related to one another (equation 3.15), and the governing equations cannot be solved independently for the melt or matrix velocity. Furthermore, they do not explain how they solve for variable melt viscosities; nor how they non-dimensionalise the governing equations prior to solution. In view of this, and the preceding discussion, the validity of the results presented by Fountain *et al.* (1989) should be treated with caution.

4.5 Conclusions

In chapter 2 it was argued that the production of mobile, granitic magma by partial melting of rocks in the mid- to lower continental crust presents a paradox. Melting occurs under water-absent or water-undersaturated conditions, and is caused by the advection of heat from the mantle to the crust, either by basaltic underplating, asthenospheric upwelling, or a combination of these processes. During partial melting of the protolith, the unmelted solid fraction (restite) maintains an interconnected matrix unless the melt volume fraction reaches the Critical Melt Fraction (CMF). In order to form a *granitic* magma, the granitic partial melt fraction *must* separate to some extent from its restite; experimental and field evidence indicates that melt volume fractions which are granitic in composition are small (<0.4), and segregate in the source region from partially molten rock in which the restite maintains an interconnected matrix. The paradox is that melt generation and segregation appears to occur at melt fractions which are *less* than the CMF, yet magma mobilisation can occur only at melt fractions which are *greater* than the CMF. How then does a small granitic partial melt fraction form a mobile granitic magma?

In this chapter, a *quantitative* physical model has been presented of a crustal partial melt zone which is produced by heating from below. The results obtained indicate that in partial melt zones with suitable thermal and physical characteristics, melt which corresponds to only a small (<0.4) degree of partial melting of the source rock, and which is granitic (*sensu-lato*) in composition, will segregate from the partially molten rock matrix and accumulate until it exceeds the CMF. The resulting granitic magma is mobile, and may migrate away from the partial melt zone if a suitable route is available. Except in the localised region of magma mobilisation, the solid matrix of the partially molten rock is not disrupted, and remains in the source region as a 'restitic' residue; the predicted mineralogy of the residue corresponds to that of many granulite terrains. Thus the paradox is resolved: a small granitic melt fraction has segregated *in the source region*, from partially molten rock in which the restite maintains an interconnected matrix, and has accumulated until it forms a mobile magma.

The values of the variables which govern the dynamics of melting and melt segregation, such as the matrix bulk and shear viscosities, are poorly constrained even for a given rock type and tectonic setting; consequently, the model cannot as yet be used to predict *specific* timescales for segregation or *specific* melt compositions. However, a series of dimensionless curves are presented which may be used to *estimate* the segregation timescale, and in conjunction with empirical data, the composition of the segregated melt. For example, melt is estimated to segregate from a basaltic source rock in ~15,000 yrs. to 10 M.y., depending upon magnitude of the matrix bulk and shear viscosities, and the estimated composition of the segregated melt varies from trondjhemitic to granodioritic. In general, melt segregation and mobilisation is predicted in partial melt zones characterised by values of the variables in the *mid-range* of those estimated for lower crustal rocks, or in partial melt zones where, for example, high melt viscosities are countered by high matrix viscosities, or a large grain size is countered by a small matrix viscosity.

The model presented in this chapter is formulated assuming that heating occurs from below, following the emplacement of hot magma adjacent to the protolith; however, cooling of the underlying magma heat source is neglected, so as not to obscure the processes which occur in the partially molten rock. Moreover, only the model represents only the processes which lead to the *formation* of a mobile granitic magma. In chapter 5, the heat source required for melt generation and magma mobilisation is considered; in chapter 6, the consequences of magma formation and the subsequent evolution of the magma are discussed.

Chapter 5: The heat source for melt generation: conjugate solidification of underplated basalt and melting in the overlying crust.

"....granite emplacement is.....often accompanied by important magmatic activity involving basic magma, largely or entirely derived from the mantle." **(Leake, 1990, p. 580)**

5.1 Introduction

The quantitative model of melt generation and segregation presented in chapter 4 is formulated assuming that melting of the source rock occurs due to heating from below, following the emplacement of hot, mantle derived magma; in the mid- to lower crust, this may be as a result of basaltic underplating, asthenospheric upwelling, or a combination of these processes (§2.2). The results obtained indicate that, for a wide range of the governing parameters, granitic (*sensu - lato*) melt may segregate from its partially molten host rock and form a mobile magma. However, the model does not consider explicitly the transport of heat from the underlying magma to the overlying source rock; rather, a *constant* temperature is assumed at the contact between magma and rock. As discussed by Bergantz (1992), heating of the rock and cooling of the magma are *conjugate* processes which should be modelled simultaneously; in this chapter, a suitable description of heat transport within and from the underlying magma heat source will be coupled with the description of heat, mass and momentum transport in the overlying rock presented in chapter 4. The aim of the chapter is to investigate the viability of basaltic underplating as a heat source for the generation of mobile granitic melt.

Previous models of underplating have considered melt generation in meta-sedimentary source rocks (Bergantz, 1989), and tonalitic-granodioritic source rocks (Huppert and Sparks, 1988; Bergantz, 1989; Fountain *et al.* 1989; Bergantz and Dawes, 1994). However, underplated basalt may itself act as a fertile source of granitic melt; for example, newly underplated basalt concomitant with crustal thickening has been invoked as the source rock of granitic batholiths such as the Cordillera Blanca in the Peruvian part of the Andes (Atherton and Petford, 1996; Petford and Atherton, 1996), and the Chilliwack in the western U.S.A (Tepper *et al.*, 1993). In this chapter, the source rock will be assumed to be basaltic, and the thermal properties and solidus and liquidus temperatures of the source rock and underplated basalt will be assumed to be identical. This leads to a simplification of the governing equations, yet results in the most stringent test of basaltic underplating as a heat source for the generation of mobile granitic melt. Fertile source rocks other than basalt generally have lower solidus temperatures, smaller latent and specific heat capacities, and a larger solidus-liquidus temperature interval; these conditions *promote* melting of the rock, because the underplated basalt can be significantly hotter than the source rock, and the latent heat released during crystallisation of the basalt is greater than that absorbed during melting of the source rock. Consequently, in the model presented in this chapter, the melt volumes which are predicted to be generated by underplating represent *minimum* values.

Melting of the overlying source rock and cooling of the underplated basalt will be considered following the instantaneous emplacement of a single, sub-horizontal sill. Although underplating may result in the emplacement of both dykes and sills, the emplacement of horizontal sills is the most efficient way of generating significant volumes of granitic melt, because horizontal intrusions concentrate their heat at a particular level in the crust, while vertical intrusions dissipate their heat over a wide depth range (Huppert and Sparks, 1988). The transport of heat within and from the cooling sill will be assumed to be by conduction only; the transport of heat by convection of the magma will be neglected. This assumption is based on the work of Marsh (1989), and Bergantz and Dawes (1994). Marsh (1989) argues that crystallisation of the magma during cooling rapidly leads to the formation of a cool, essentially rigid mush at the margin of the sill, within which the transport of heat occurs by conduction. Most of the temperature difference between the sill and the surrounding rock occurs within the mush; consequently, though the magma within the interior of the sill is convecting, the transport of heat from the sill to the rock is governed primarily by conduction within the mush. His arguments are supported by the results of Bergantz and Dawes (1994), who investigated heat transport in a cooling, crystallising, basaltic sill using a sophisticated numerical model, which includes conductive heat transport in the mush and the surrounding rock, convective heat transport in the magma, and the effect of variations in temperature, composition, and crystal content on the viscosity and hence convective vigour of the magma. They found that magma within the interior of the sill convects, yet the transport of heat to the surrounding rock 'is as if the magma were cooling by conduction only,' and concluded that 'calculating the progress of melting following a single episode of underplating can be facilitated by assuming a simple, but still non-linear, conductive cooling model.' Their results are supported by observational data from cooling basaltic lava lakes, which indicates that heat transport from the lava is predominantly conductive (e.g. Helz *et al.*, 1989).

Note that if the magma is superheated, then the mush which initially forms at the margin may be remelted, in which case heat transport from the sill to the surrounding rock is dominated by convection until the magma cools to its liquidus (Huppert and Sparks, 1988). However, the 'well known absence of magmatic superheat' (Marsh, 1989) indicates that this will rarely occur.

5.2 Model Formulation

The formulation presented in this chapter is that presented in chapter 4 (see §4.2 and figure 4.1), modified to include a description of heat transport in the underlying magma heat source. The magma is modelled as a horizontal sill of thickness z_{sill}, which is emplaced at a temperature T_{sill} (figure 5.1(a)). As in chapter 4, the spatial origin of the model ($z = 0$) denotes the position of the sill/rock contact, and the temporal origin ($t = 0$) denotes the time at which the sill is 'instantaneously' emplaced. The transport of heat from the sill in the region $z < 0$ to the rock in the region $z > 0$ causes heating and melting of the rock and conjugate cooling and crystallisation of the sill; in contrast to the formulation presented in chapter 4, the temperature at the contact is governed by the dynamics of heat transport between sill and rock, and is not assumed constant. Moreover, the conjugate model presented in this chapter may be divided into three distinct regions: the solid rock in the region $z > z_{sol}$; the partially molten rock in the region $0 \leq z \leq z_{sol}$, and the sill in the region $z < 0$. In the regions $z > z_{sol}$ and $0 \leq z \leq z_{sol}$, the transport of heat, mass and momentum is described by the model presented in chapter 4; in the region $z < 0$, the transport of heat is described by a conductive formulation, and is assumed to be symmetric about a horizontal plane at the centre of the sill (figure 5.1(b)). This assumption leads to an ***underestimate*** of the heat transported from the sill to the overlying rock; consequently, the melt volumes predicted by the model represent ***minimum*** values.

5.2.1 Governing Equations

The 1-D conservation equation governing the conductive transport of heat in the solid rock above the partially molten rock (i.e. in the region $z > z_{sol}$) may be written as (§4.2.1)

$$k\frac{\partial^2 T}{\partial z^2} = \rho c_p \frac{\partial T}{\partial t} \tag{5.1}$$

The 1-D conservation equations governing the transport of heat, mass and momentum in the partially molten rock (i.e. in the region $0 \leq z \leq z_{sol}$) may be written as (§4.2.1)

$$k\frac{\partial^2 T}{\partial z^2} = \rho c_p \frac{\partial T}{\partial t} + L\Gamma_m \tag{5.2}$$

$$\rho\frac{\partial \phi}{\partial t} - \rho\frac{\partial}{\partial z}\left((1-\phi)w_s\right) = \Gamma_m \tag{5.3}$$

$$\left(\xi_s + \tfrac{4}{3}\mu_s\right)\frac{\partial^2 w_s}{\partial z^2} = (1-\phi)(\rho_s - \rho_m)g - \frac{\mu_m w_s}{k} \tag{5.4}$$

with the supplementary relations

$$\phi w_m = -(1-\phi)w_s \tag{5.5}$$

$$\Gamma_m = \rho\frac{\partial \nu_m}{\partial t} + \rho(w_m + w_s)\frac{\partial \nu_m}{\partial z} \tag{5.6}$$

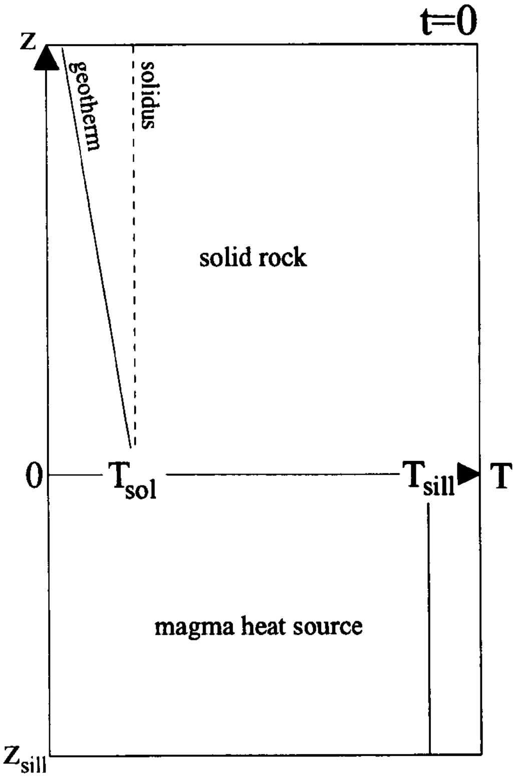

(a) Initially, the temperature in the region z>0 is dictated by a steady state geotherm, the rock is at its solidus (T_{sol}) at z=0, and there is no melt present (cf. figure 4.1(a)). At t=0, a sill of thickness z_{sill}, containing basaltic magma at a uniform temperature T_{sill}, is instantaneously emplaced in the region z<0.

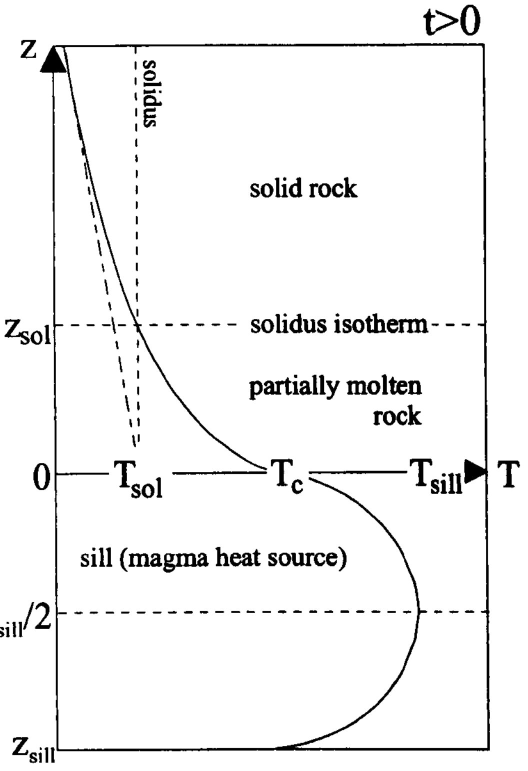

(b) The transport of heat from the magma in the region z<0 to the rock in the region z>0 causes heating and melting of the rock and conjugate cooling and crystallisation of the magma; in contrast to chapter 4 (cf. figure 4.1), the temperature at the contact (T_c) is not assumed constant. In the region z>0 (i.e. in the partially molten rock, and in the overlying solid rock), the transport of heat, mass and momentum is described by the model presented in chapter 4; in the region z<0 (i.e. in the sill), the transport of heat is conductive, and is assumed to be symmetric about a horizontal plane located at z = $-z_{sill}/2$ (the centre of the sill).

Figure 5.1. Model formulation for chapter 5: conjugate melting and solidification of the overlying rock and underlying magma following the emplacement of a single, horizontal basaltic sill of thickness z_{sill}.

$$k = \mathrm{b}a^2\phi^n \tag{5.7}$$

(see table 5.1 for an explanation of the nomenclature).

Given that the thermal properties of the overlying basaltic source rock are assumed to be identical to those of the underlying sill, the 1-D conservation equation governing the conductive transport of heat in the sill (i.e. in the region $z < 0$) may be expressed as (Bergantz, 1992)

$$k\frac{\partial^2 T}{\partial z^2} = \rho c\frac{\partial T}{\partial t} - L\Gamma_c \tag{5.8}$$

where Γ_c denotes the rate of production of crystals (rate of crystallisation). If the degree of melting in the source rock and the degree of crystallisation in the sill are identical functions of temperature, then the rate of crystallisation may be expressed as

$$\Gamma_c = -\rho\frac{\partial \nu_m}{\partial t} \tag{5.9}$$

The initial conditions are given by

$$T(0,0) = T_{sol} \tag{5.10a}$$

$$\frac{\partial}{\partial z}\big(T(z,0)\big) = T_{geo}, \qquad z > 0 \tag{5.10b}$$

$$T(z,0) = T_{sill}, \qquad z < 0 \tag{5.10c}$$

$$\phi(z,0) = \nu_m(z,0) = w_m(z,0) = w_s(z,0) = 0 \tag{5.10d}$$

and the boundary conditions by

$$T(z_{sol},t) = T_{sol} \tag{5.11a}$$

$$\frac{\partial}{\partial z}\big(T(z \to +\infty,t)\big) \to T_{geo} \tag{5.11b}$$

$$\frac{\partial}{\partial z}\big(T(-z_{sill}/2,t)\big) = 0 \tag{5.11c}$$

$$\nu_m(z_{sol},t) = 0 \tag{5.11d}$$

$$w_m(0,t) = w_s(0,t) = w_m(z_{sol},t) = w_s(z_{sol},t) = 0 \tag{5.11e}$$

The boundary condition (5.11e) is valid assuming that there is no transport of mass from the sill to the overlying rock; the boundary condition (5.11c) follows from the assumption that conductive heat transport in the sill is symmetric about a horizontal plane at the centre.

5.2.2 Simplification and non-dimensionalisation of the governing equations

Following the approach of chapter 4, the degree of melting of the rock will be described as a continuous, linear function of temperature (§4.2.2)

$$\nu_m = \frac{T - T_{sol}}{T_{liq} - T_{sol}} \tag{5.12}$$

Symbol	Description	Units
a	matrix grain radius	m
b	constant in permeability relationship	None
c_p	specific heat capacity	$J\ kg^{-1}\ K^{-1}$
c_{eff}	effective specific heat capacity	$J\ kg^{-1}\ K^{-1}$
g	acceleration due to gravity	$m\ s^{-2}$
k	thermal conductivity	$W\ K^{-1}\ m^{-1}$
k	permeability	m^{-2}
K	characteristic permeability	m^{-2}
L	latent heat	$J\ kg^{-1}$
n	exponent in permeability relation	None
Ste	Stefan number	None
t	time	s
t_{seg}	dimensionless segregation time	None
T	temperature	K
T_c	temperature at the contact ($z = 0$)	K
T_{sol}	solidus temperature	K
T_{liq}	liquidus temperature	K
T_{sill}	initial temperature of sill	K
T_{geo}	initial geothermal gradient	$K\ km^{-1}$
w_m	melt velocity	$m\ s^{-1}$
w_s	matrix velocity	$m\ s^{-1}$
z	vertical Cartesian coordinate	m
z_{sol}	position of solidus isotherm	m
z_0	position of dimensionless solidus isotherm ($\theta = 0$)	None
z_{sill}	thickness of sill	m
z_{sill}	dimensionless half thickness of sill	None
z_{min}	dimensionless sill half thickness required for magma mobilisation	None
χ	ratio of thermal diffusivities in the partially molten and solid rock	None
δ	characteristic lengthscale (McKenzie's compaction length)	m
ϕ	melt volume fraction (porosity)	None
φ	*initial* degree of melting at the contact ($z = 0$)	None
Γ_c	rate of production of crystals	$kg\ m^{-3}\ s^{-1}$
Γ_m	rate of production of melt	$kg\ m^{-3}\ s^{-1}$
κ_{eff}	dimensionless effective thermal diffusivity	None
μ_m	melt shear viscosity	Pa s
μ_s	matrix shear viscosity	Pa s
ν_m	degree of equilibrium melting	None
θ	dimensionless temperature (normalised degree of melting)	None
θ_{seg}	dimensionless segregation temperature	None
θ_c	dimensionless contact temperature	None
θ_s	dimensionless temperature at the centre of the sill	None
ρ	density	$kg\ m^{-3}$
$\rho_s - \rho_m$	matrix - melt density contrast	$kg\ m^{-3}$
ω	characteristic velocity scale	$m\ s^{-1}$
τ	characteristic timescale	s
ξ_s	matrix bulk viscosity	Pa s
ψ_{geo}	dimensionless initial geothermal gradient	None

Table 5.1. Nomenclature for chapter 5.

and furthermore, latent heat will be assumed to be absorbed/released linearly as melting/crystallisation proceeds. Following the approach of §3.2.3, the dimensionless temperature may be written as

$$T' = \frac{T - T_{sol}}{T_{liq} - T_{sol}} \tag{5.13}$$

in which case it is numerically equivalent to v_m, and will be represented by a new variable θ; i.e. $\theta = T' = v_m$. The melt volume fraction (ϕ) and dimensionless degree of melting (θ) may then be normalised by writing

$$\theta' = \theta/\varphi, \qquad \text{with} \quad \varphi = \frac{T_{sill} - T_{sol}}{2\left(T_{liq} - T_{sol}\right)} \tag{5.14a}$$

$$\phi' = \phi/\varphi, \tag{5.14b}$$

Note that the scaling factor φ is defined in this chapter as the *initial* degree of melting (and the *initial* dimensionless temperature) at the contact ($z = 0$) immediately after magma emplacement; this definition is different to that used in chapters 3 and 4 because the contact temperature is no longer assumed to be constant (cf. equation (4.12)). Defining φ as the initial degree of melting at the contact is equivalent to defining it as the *maximum* degree of melting.

The remaining variables are non-dimensionalised by writing (§3.2.3)

$$z' = z/\delta, \qquad \text{with} \quad \delta = \left(\frac{(\xi_s + 4\mu_s/3)K}{\mu_m}\right)^{1/2} \tag{5.15}$$

$$t' = t/\tau, \qquad \text{with} \quad \tau = \frac{1}{(1-\varphi)(\rho_s - \rho_m)g}\left(\frac{\mu_m(\xi_s + 4\mu_s/3)}{K}\right)^{1/2} \tag{5.16}$$

$$w' = w/\omega, \qquad \text{with} \quad \omega = \frac{K(1-\varphi)(\rho_s - \rho_m)g}{\mu_m} \tag{5.17}$$

$$k' = k/K, \qquad \text{with} \quad K = ba^2\varphi^n \tag{5.18}$$

Substituting for the degree of melting (v_m) in equations (5.6) and (5.9), substituting for the rate of melt production in equations (5.2) and (5.3), substituting for the rate of crystallisation in equation (5.8), substituting for the permeability (k) in equation (5.4), substituting the scaled and dimensionless variables (5.14)-(5.18), simplifying, and dropping primes, yields the dimensionless governing equations

$$\frac{\partial\theta}{\partial t} = \chi\kappa_{eff}\frac{\partial^2\theta}{\partial z^2}, \qquad z > z_0 \tag{5.19}$$

$$\frac{\partial\phi}{\partial t} = \frac{1}{\varphi}\frac{\partial}{\partial z}\left((1-\varphi\phi)w_s\right) + \frac{\partial\theta}{\partial t} + \left(w_m + w_s\right)\frac{\partial\theta}{\partial z} \tag{5.20}$$

$$\frac{\partial\theta}{\partial t} = \kappa_{eff}\frac{\partial^2\theta}{\partial z^2} - \mathrm{Ste}\left(w_m + w_s\right)\frac{\partial\theta}{\partial z}, \qquad 0 \le z \le z_0 \tag{5.21}$$

$$\frac{\partial^2 w_s}{\partial z^2} = \frac{w_s}{\phi^n} + \frac{(1-\varphi\phi)}{(1-\varphi)} \tag{5.22}$$

$$\varphi\phi w_m = -(1-\varphi\phi)w_s \tag{5.23}$$

$$\frac{\partial \theta}{\partial t} = \kappa_{eff}\frac{\partial^2 \theta}{\partial z^2}, \qquad z < 0 \tag{5.24}$$

with

$$\kappa_{eff} = \frac{k\tau}{\rho c_{eff}\delta^2} \tag{5.25}$$

$$Ste = \frac{L}{c_{eff}\left(T_{liq} - T_{sol}\right)} \tag{5.26}$$

$$c_{eff} = c_p + \frac{L}{T_{liq} - T_{sol}} \tag{5.27}$$

$$\chi = 1 + \frac{L}{c_p\left(T_{liq} - T_{sol}\right)} \tag{5.28}$$

Note that equation (5.24) governing conductive heat transport in the sill is valid only if cooling of the sill is always accompanied by crystallisation (with associated latent heat exchange). Consequently, the emplacement temperature of the sill (T_{sill}) is restricted to be less than or equal to its liquidus; this restriction is in agreement with the observation that magmas are rarely superheated (Marsh, 1989).

The initial conditions become

$$\theta(0,0) = 0 \tag{5.29a}$$

$$\frac{\partial}{\partial z}(\theta(z,0)) = \psi_{geo}, \qquad z > 0 \tag{5.29b}$$

$$\theta(z,0) = 2, \qquad z < 0 \tag{5.29c}$$

$$\phi(z,0) = w_m(z,0) = w_s(z,0) = 0 \tag{5.29d}$$

with

$$\psi_{geo} = (\delta/(T_{liq} - T_{sol}))T_{geo} \tag{5.30}$$

The boundary conditions become

$$\frac{\partial}{\partial z}\left(\theta(-z_{sill}, t)\right) = 0 \tag{5.31a}$$

$$w_m(0,t) = w_s(0,t) = w_m(z_0,t) = w_s(z_0,t) = 0 \tag{5.31b}$$

$$\theta(z_0,t) = 0 \tag{5.31c}$$

$$\frac{\partial}{\partial z}(\theta(z \to +\infty, t)) \to \psi_{geo} \tag{5.31d}$$

where z_0 denotes the dimensionless position of the $\theta = 0$ isotherm, and z_{sill} denotes the dimensionless half thickness of the sill.

Coupling the model formulation presented in chapter 5 with a description of heat transport in the underlying sill has resulted in the addition of a new governing equation to the five presented in chapter 4, (equation (5.24) is the addition; equations (5.19 - 5.23) are those presented in chapter 4). As in chapter 4, the equations are governed by six externally prescribed dimensionless parameters: the effective thermal diffusivity in the partial melt zone and sill (κ_{eff}); the Stefan number (Ste); the exponent in the permeability relation (n); the degree of melting at the contact (φ); the ratio of the thermal diffusivity in the solid rock to the effective thermal diffusivity in the partial melt zone (χ); and the initial geothermal gradient (ψ_{geo}). The formulation presented here represents the simplest which can describe the conjugate processes of solidification in the sill and melting and melt segregation in the overlying rock.

5.3 Results

The governing equations (5.19) - (5.24) were approximated using finite difference schemes and solved numerically using FORTRAN codes processed on a Sun SPARC 5 workstation. The schemes used are identical to those used to solve the governing equations presented in chapter 4; consequently, they are not described again.

As discussed in chapter 4, the values of the dimensionless governing parameters κ_{eff} and ψ_{geo} cannot be assumed to be independent; consequently, the governing equations are solved only for the values shown in table 4.3. However, both χ and Ste can be assumed to be independent of κ_{eff}, and based on the results obtained in §4.3.1.1, their values are fixed at $\chi = 2.5$ and Ste = 0.5. As in chapter 4, values of φ are prescribed externally; however, in the model presented here, the range of available values of φ is dictated by the range of available values of T_{sill}, T_{sol}, and T_{liq} (equation (5.14)). Given that the sill and source rock are assumed to have identical solidus and liquidus temperatures, and that the emplacement temperature (T_{sill}) of the sill is constrained to be less than or equal to its liquidus (T_{liq}), the maximum value of φ is constrained to be 0.5.

5.3.1 Dimensionless results

5.3.1.1 Form of the spatial porosity and normalised temperature distributions

Figure 5.2 shows a representative selection of the normalised spatial porosity and dimensionless temperature distributions, for $\varphi = 0.5$, $\chi = 2.5$, and Ste = 0.5, after 30 time units have elapsed. In all cases, the dimensionless half thickness of the sill is given by $z_{sill} = 2(\kappa_{eff}t)^{1/2}$. Although not marked on the figure, note that the initial dimensionless temperature of the sill is 2 (condition (5.29c)), and that the initial dimensionless contact temperature between the underlying sill and the overlying rock is 1.

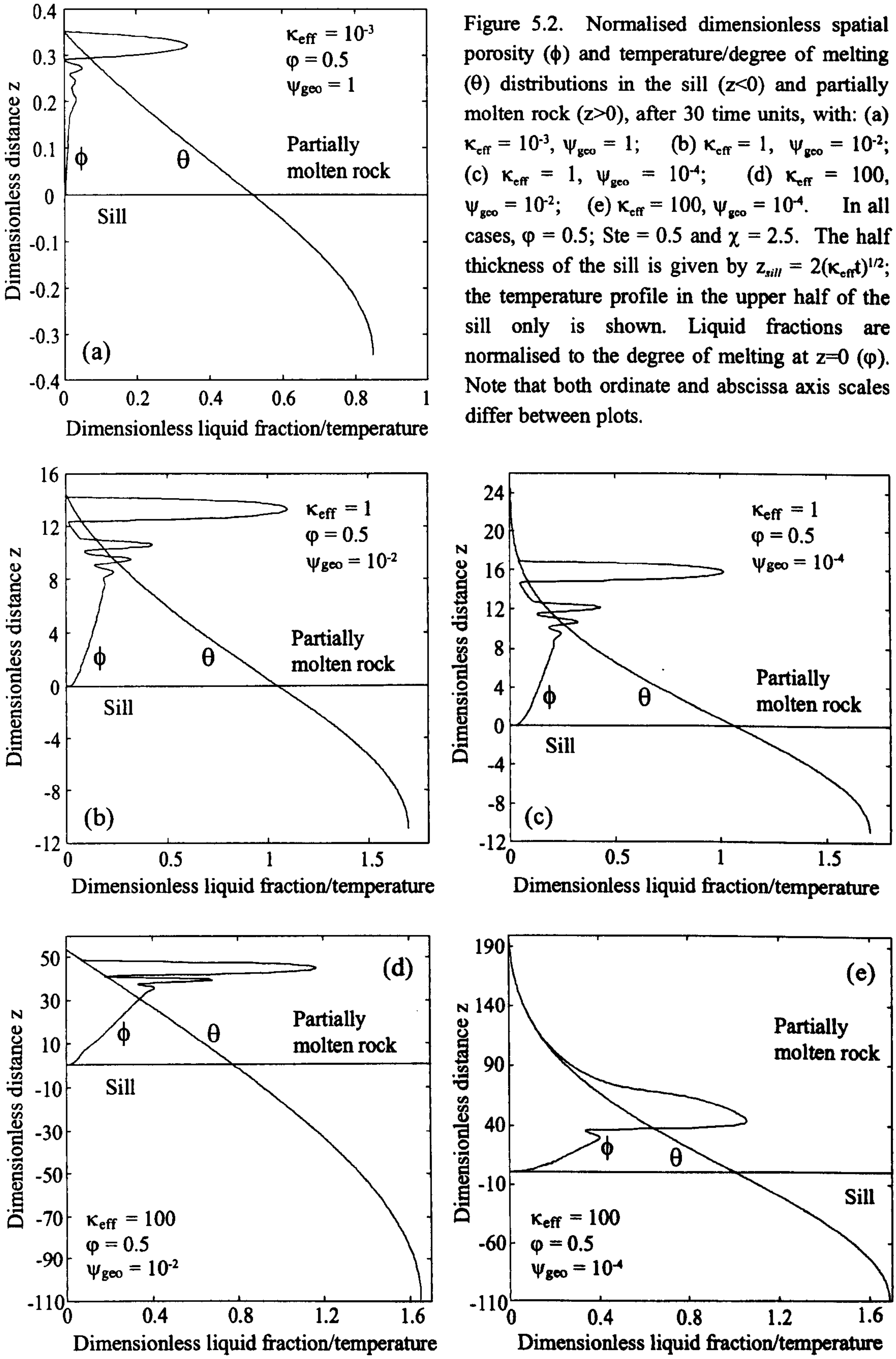

Figure 5.2. Normalised dimensionless spatial porosity (ϕ) and temperature/degree of melting (θ) distributions in the sill ($z<0$) and partially molten rock ($z>0$), after 30 time units, with: (a) $\kappa_{eff} = 10^{-3}$, $\psi_{geo} = 1$; (b) $\kappa_{eff} = 1$, $\psi_{geo} = 10^{-2}$; (c) $\kappa_{eff} = 1$, $\psi_{geo} = 10^{-4}$; (d) $\kappa_{eff} = 100$, $\psi_{geo} = 10^{-2}$; (e) $\kappa_{eff} = 100$, $\psi_{geo} = 10^{-4}$. In all cases, $\varphi = 0.5$; Ste = 0.5 and $\chi = 2.5$. The half thickness of the sill is given by $z_{sill} = 2(\kappa_{eff}t)^{1/2}$; the temperature profile in the upper half of the sill only is shown. Liquid fractions are normalised to the degree of melting at $z=0$ (φ). Note that both ordinate and abscissa axis scales differ between plots.

These dimensionless porosity and temperature distributions may be compared with those obtained assuming a *constant* contact temperature in chapter 4 (figure 4.7(i-iii)). Figure 5.2(a) should be compared with figure 4.7(i)(a); note that although the dimensionless contact temperature in figure 5.2(a) has fallen to ~0.54 (i.e. is ~46% less than its original value), and the temperature at the centre of the sill has fallen to ~0.85 (~58% less than its original value), the amplitude of the leading porosity wave in the source rock is reduced by only ~8% from that shown in figure 4.7(i)(a). Figure 5.2(b) should be compared with figure 4.7(ii)(b); note that although the temperature at the centre of the sill in figure 5.2(b) has fallen by ~15%, the contact temperature is unchanged[1], and the spatial porosity distribution in the source rock is unchanged from that shown in figure 4.7(ii)(b). Figure 5.2(d) should be compared with figure 4.7(ii)(d); again, although the contact temperature in figure 5.2(d) has fallen by ~22%, and the temperature at the centre of the sill has fallen by ~35%, the amplitude of the leading porosity wave is reduced by only ~6% from that shown in figure 4.7(ii)(d). However, in contrast to figure 4.7(ii)(d), the porosity distribution shown in figure 5.2(d) exhibits well developed porosity waves trailing the leading wave.

Because the underlying basalt sill is cooling, the contact temperature between the sill and the source rock must eventually begin to fall. However, unless the contact temperature begins to fall within the timescale of melting and melt segregation in the overlying source rock, the porosity and temperature distributions in the source rock are identical to those obtained assuming a *constant* contact temperature (e.g. figure 5.2(b)). Moreover, even if the contact temperature does begin to fall within the timescale of melting and melt segregation, the effect is minimal if a porosity wave has already developed near the top of the partial melt zone (e.g. figure 5.2(a)), although the reduced melting rate which results from the falling contact temperature may enhance the formation of trailing porosity waves (e.g. figure 5.3(d); see the discussion in §3.3.2).

5.3.1.2 The minimum sill thickness required for granitic magma mobilisation

As discussed in §4.3.1.3 and §3.3.3, if the amplitude of the leading porosity wave in the source rock continually increases with time, then eventually the local melt volume fraction will exceed the CMF, in which case a mobile magma forms (§3.3.3). If the contact temperature remains constant, then magma mobilisation is predicted in partial melt zones characterised by values of κ_{eff} in the range $10^{-2} \leq \kappa_{eff} < 10^{4}$ and ψ_{geo} in the range $10^{-4} \leq \psi_{geo} \leq 1$, (§4.3.1.3). However, if the contact temperature begins to fall before a porosity wave has developed, then the source rock cools too quickly for magma mobilisation to occur. The timescale over which the contact temperature begins to fall is governed by the thickness of the sill, and the values of the dimensionless effective thermal diffusivity κ_{eff} and the

---

[1] Close observation of figure 5.2(b) reveals that the contact temperature is actually slightly higher than its original value. This increase occurs because 'pseudo-advection' acts to inhibit heat transport in the partially molten rock (§3.3.1).

dimensionless initial geotherm ψ_{geo}. For given values of κ_{eff} and ψ_{geo}, the model may be used to estimate the *minimum* dimensionless sill thickness required for magma mobilisation in the overlying source rock, by investigating melt migration in the source rock for progressively thinner sills, and identifying the sill thickness for which cooling causes the maximum porosity to decrease before the CMF is exceeded.

Figure 5.3(a and c) shows the minimum dimensionless sill half thickness (z_{min}) required for magma mobilisation in the overlying source rock, as a function of κ_{eff}, for $\psi_{geo} = 10^{-4}$ and 10^{-2} respectively, and $\varphi = \mathrm{CMF} = 0.5$. In both cases, the minimum half thickness increases with increasing κ_{eff}, from $z_{min} \sim 8$ to $z_{min} \sim 400$ for the case $\psi_{geo} = 10^{-4}$ (figure 5.3(a)), and from $z_{min} \sim 2$ to $z_{min} \sim 55$ for the case $\psi_{geo} = 10^{-2}$. Figure 5.3(b and d) shows the corresponding dimensionless temperatures at the contact (θ_c) and the centre of the sill (θ_s), at the time of magma mobilisation. In both cases, θ_c and θ_s increase with increasing κ_{eff}, from $\theta_c \sim 0.7$ to $\theta_c \sim 1$ and $\theta_s \sim 0.75$ to $\theta_s \sim 1.7$ for the case $\psi_{geo} = 10^{-4}$ (figure 5.3b), and from $\theta_c \sim 0.18$ to $\theta_c \sim 0.6$ and $\theta_s \sim 0.25$ to $\theta_s \sim 0.75$ for the case $\psi_{geo} = 10^{-4}$ (figure 5.3d).

Figure 5.4(a and c) shows the resulting segregation time (the segregation time t_{seg} is defined as the dimensionless time required to initiate magma mobilisation in the source rock (§3.3.3)) which is obtained using the *minimum* sill thickness, as a function of κ_{eff}, for $\psi_{geo} = 10^{-4}$ and 10^{-2} respectively, and $\varphi = \mathrm{CMF} = 0.5$. Also shown is the segregation time which is obtained assuming a *constant* contact temperature (cf. figure 4.18). In both cases, the segregation times are similar, although there is closer agreement for the case $\psi_{geo} = 10^{-4}$ (figure 5.4(a)) than for the case $\psi_{geo} = 10^{-2}$ (figure 5.4(c)), and the times obtained using the minimum sill thickness are generally longer except at small κ_{eff} (<1). Figure 5.4 (b and d) shows the corresponding segregation temperatures (the segregation temperature θ_{seg} is defined as the dimensionless temperature at the point of incipient magma formation (§3.3.4)) as a function of κ_{eff} (cf. figure 4.18). Again, in both cases the segregation temperatures are similar, although there is closer agreement for the case $\psi_{geo} = 10^{-4}$ (figure 5.4(b)) than for the case $\psi_{geo} = 10^{-2}$ (figure 5.4(d)), and the temperatures obtained using the minimum sill thickness are generally smaller.

The generally low dimensionless temperatures in the sill and at the sill/rock contact at the time of magma mobilisation (figure 5.3(b and d)) indicate that, for these minimum sill thicknesses, magma mobilisation in the overlying source rock occurs while the source region as a whole is cooling. The temperatures in the sill and at the contact increase with increasing κ_{eff}, because with increasing κ_{eff} the position of the porosity maximum, and hence of incipient magma formation, moves closer to the sill/rock contact (§4.3.3), in which case the sill must be hotter for magma mobilisation to occur. Because thicker sills cool more slowly, this requirement contributes to the rapid increase observed in the minimum sill thickness required for magma mobilisation with increasing κ_{eff} (figure 5.3(a and c)).

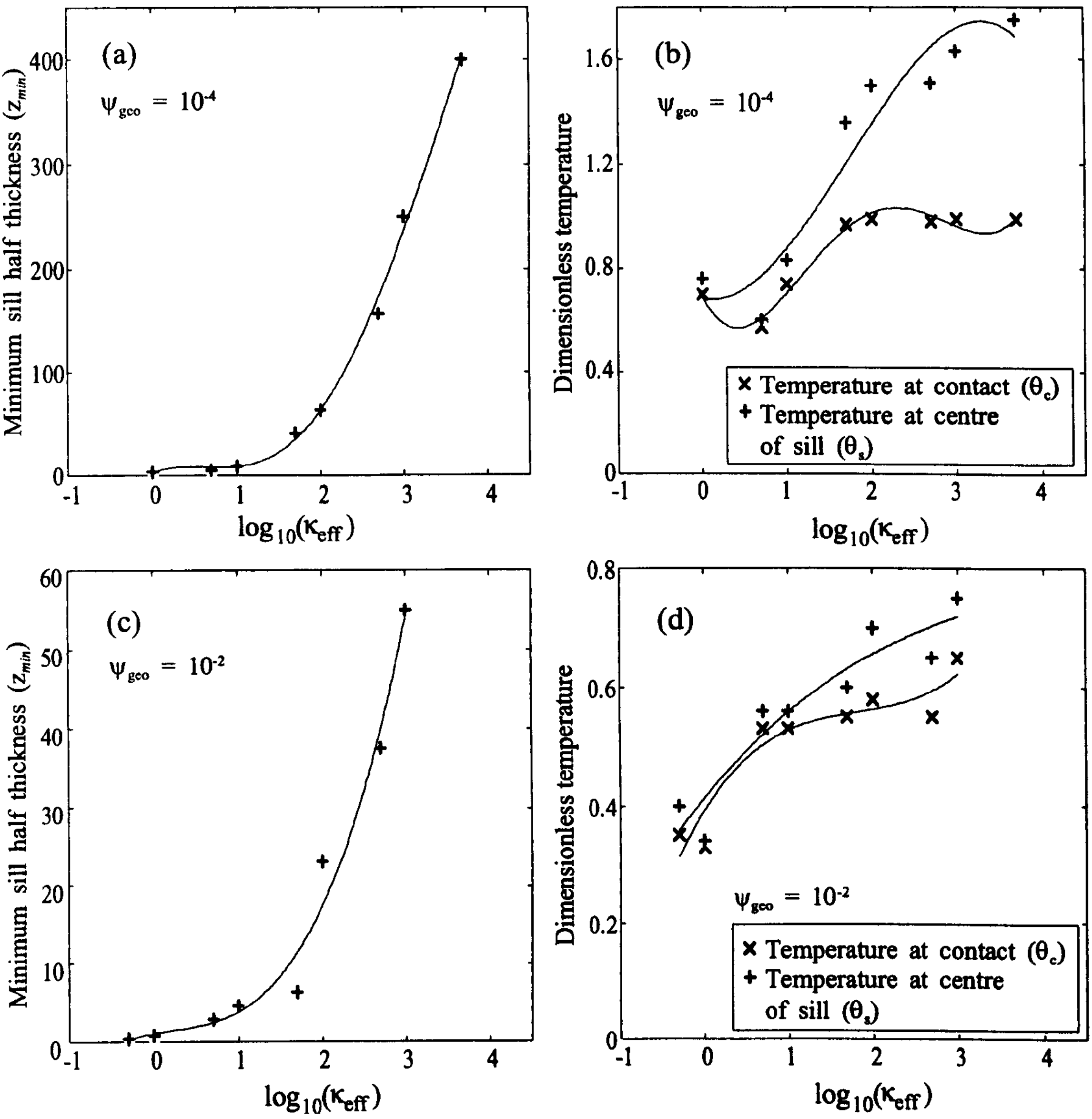

Figure 5.3. Dimensionless minimum sill half thickness (z_{min}) required for magma mobilisation in the overlying rock, and sill temperatures at the time of mobilisation (contact θ_c and centre θ_s) against κ_{eff}, for the case CMF = φ = 0.5 (CMF/φ = 1), with: ((a) & (b)) $\psi_{geo} = 10^{-4}$; ((c) & (d)) $\psi_{geo} = 10^{-2}$. In both cases, Ste = 0.5 and $\chi = 2.5$. Curves denote best fit polynomials.

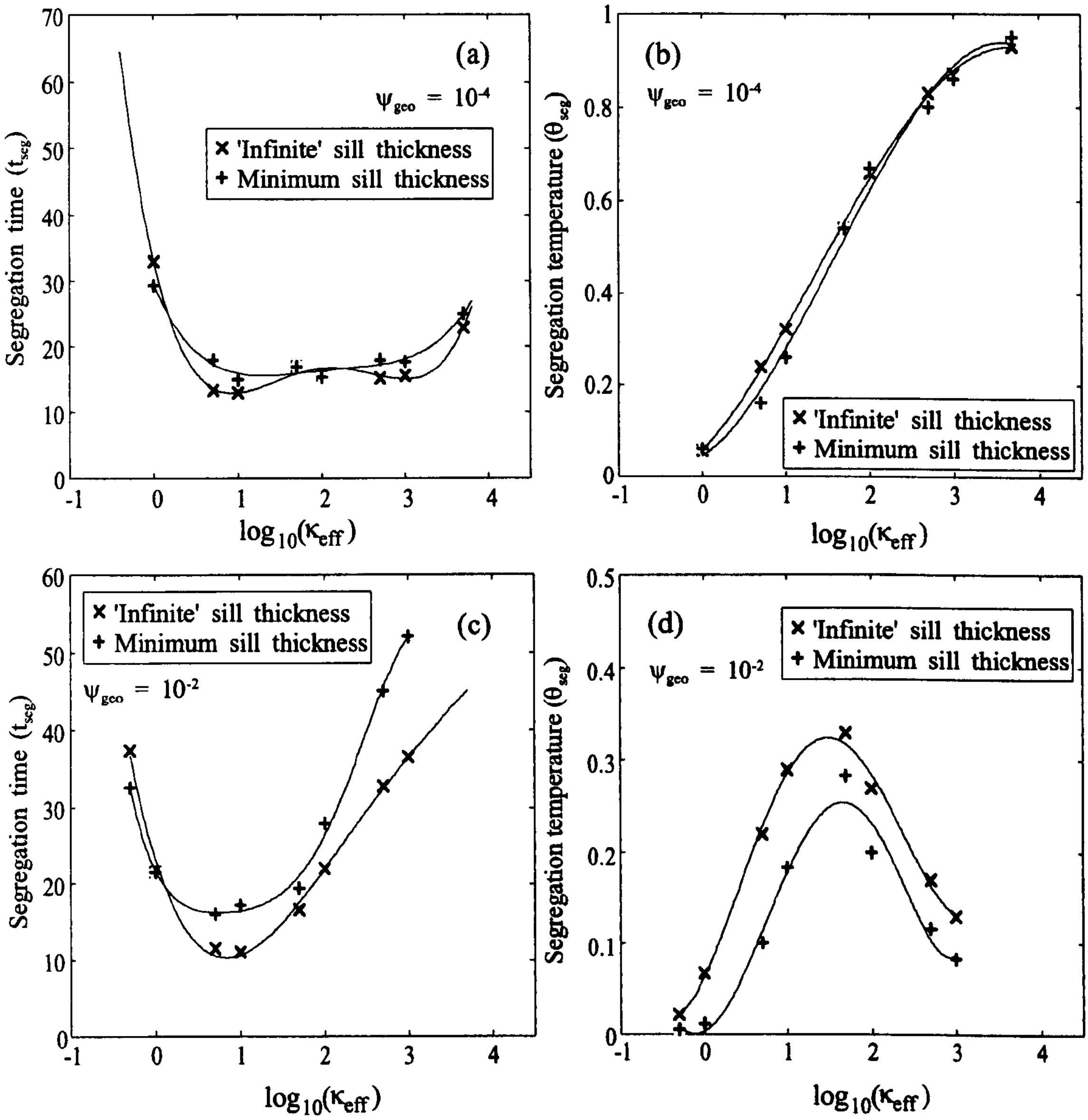

Figure 5.4. Dimensionless segregation time (t_{seg}) and segregation temperature (θ_{seg}) against κ_{eff}, obtained using the minimum sill thicknesses presented in figure 5.3, and an 'infinite' sill thickness (constant contact temperature), for the case CMF = φ = 0.5 (CMF/φ = 1), with: ((a) & (b)) $\psi_{geo} = 10^{-4}$; ((c) & (d)) $\psi_{geo} = 10^{-2}$. In all cases, Ste = 0.5 and χ = 2.5. Curves denote best fit polynomials.

That there should be such a close agreement between the segregation times and temperatures obtained for the minimum sill half thickness (z_{min}), and for an 'infinite' sill thickness (i.e. a constant contact temperature) (figure 5.4) is perhaps surprising, as the range of values obtained for these extreme cases includes *all* the values which would be obtained for sill thicknesses greater than the minimum. However, the similarity of the segregation times and temperatures observed in figure 5.4 indicates that the dimensionless time required for magma mobilisation (t_{seg}), and the dimensionless temperature (θ_{seg}), and hence composition, of the melt which forms the magma, are well approximated by the results obtained in §4.3.3.2, even though they were obtained assuming a constant contact temperature.

5.3.2 Dimensional results

5.3.2.1 Form of the spatial temperature and porosity distributions for a basaltic source rock

The dimensionless spatial porosity and temperature distributions obtained from the model may be 'dimensionalised' using the characteristic length, time, velocity, and melt volume fraction scales δ, τ, ω, and φ presented in §5.2.2 (equations (5.14) - (5.18)). Suitable values of the governing variables for a basaltic source rock and underplate are presented in table 5.2 (see also §4.4.3). With the exception of the shear and bulk viscosities of the partially molten source rock, the variables are reasonably well constrained; estimates of the bulk and shear viscosities vary from 10^{15} Pa s to 10^{21} Pa s (table 4.2; see also §4.2.4.1(iii)).

Figure 5.5 shows the porosity (melt volume fraction) and temperature distributions as a function of vertical distance in a basaltic source rock at the time of incipient magma mobilisation, assuming that melting is caused by the intrusion of a basaltic sill with the ***minimum*** thickness required for mobilisation. Note that the curve labelled 'Temperature T' denotes both the temperature (T) if read from the upper abscissa axis, and the degree of melting of the source rock (ν_m) if read from the lower abscissa axis. The distributions are obtained assuming that the initial degree of melting at the sill/rock contact is $\varphi \sim$ CMF ~ 0.5, and that the bulk and shear viscosities of the source rock are given by: $\xi_s \sim \mu_s \sim 10^{15}$ Pa s (figure 5.5(a)); $\xi_s \sim \mu_s \sim 10^{17}$ Pa s (figure 5.5(b)); $\xi_s \sim \mu_s \sim 10^{19}$ Pa s (figure 5.5(c)); and $\xi_s \sim \mu_s \sim 10^{21}$ Pa s (figure 5.5(d)).

For the lowest source rock bulk and shear viscosities, the emplacement of a sill ~700m thick leads to the formation of a mobile granitic (*sensu-lato*) magma in the overlying source rock after ~15,000 yrs (figure 5.5(a)). The composition of the melt fraction of the magma corresponds to a degree of melting of ~0.15, and from the empirical data presented in figure 4.16, it may be deduced that its composition is tonalitic. For higher bulk and shear viscosities, the sill thickness required for magma mobilisation increases to 900m, 2km, and finally to 25km, and the time required for magma mobilisation increases to 0.2M.y., 1.6M.y., and finally to 25M.y. (figures 5.5b - d respectively). Moreover, the composition of the melt fraction of the magma becomes more acidic and trondhjemitic. Note that in all cases, the

Symbol	Description	Values	Units
k	thermal conductivity	2	$W K^{-1}m^{-1}$
c_p	specific heat capacity	1,200	$J kg^{-1}K^{-1}$
L	latent heat	600,000	$J kg^{-1}$
T_{liq}-T_{sol}	liquidus-solidus interval	300	K
T_{liq}	liquidus temperature	1460	K
T_{sol}	solidus temperature	1160	K
ρ	density	3,000	$kg m^{-3}$
ρ_s-ρ_m	matrix-melt density contrast	600	$kg m^{-3}$
μ_m	melt shear viscosity	10^4	Pa s
μ_s	matrix shear viscosity	10^{15} - 10^{20}	Pa s
ξ_s	matrix bulk viscosity	10^{15} - 10^{21}	Pa s
b	constant in permeability relation	1/500	None
T_{geo}	initial geothermal gradient	7	$K km^{-1}$
a	matrix grain radius	$2.5x10^{-3}$ (2.5mm)	m
CMF	Critical Melt Fraction	0.5	None
φ	degree of melting at the contact	0.5	None

Table 5.2. Suitable values of the dimensional variables for a basaltic source rock and underplate.

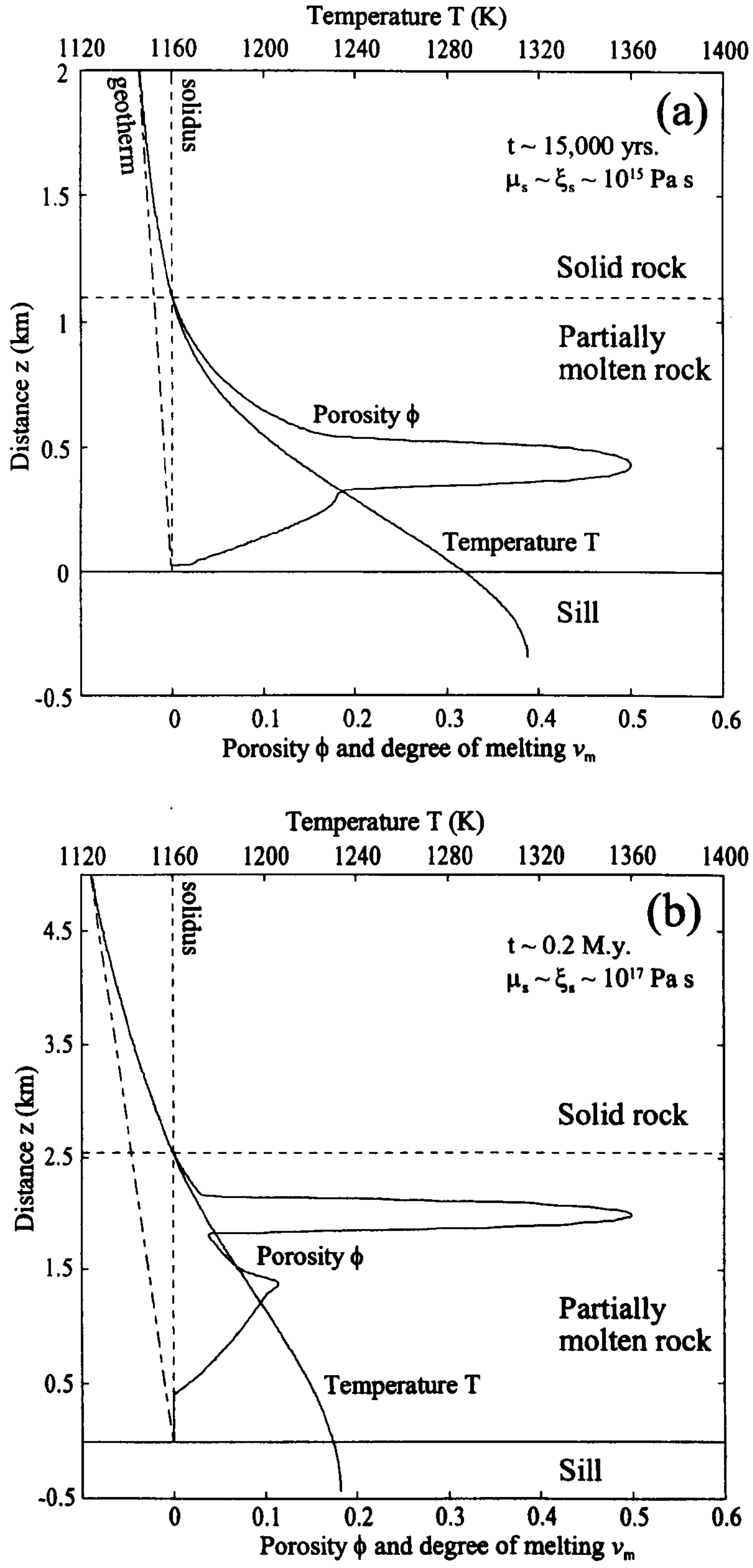

Figure 5.5. Porosity (ϕ) and temperature (T) against vertical distance (z) at the time of incipient magma formation, for (a) $\mu_s \sim \xi_s \sim 10^{15}$ Pa s, and (b) $\mu_s \sim \xi_s \sim 10^{19}$ Pa s. See table 5.2 for the values of the other governing dimensional variables. Porosity (ϕ) is plotted against the lower abscissa axis; temperature (T) is plotted against the upper abscissa axis. The curve which denotes the temperature (T) also denotes the degree of melting (v_m) if read from the lower abscissa axis. The temperature profile in the upper half of the sill only is shown; in both cases CMF ~ φ ~ 0.5.

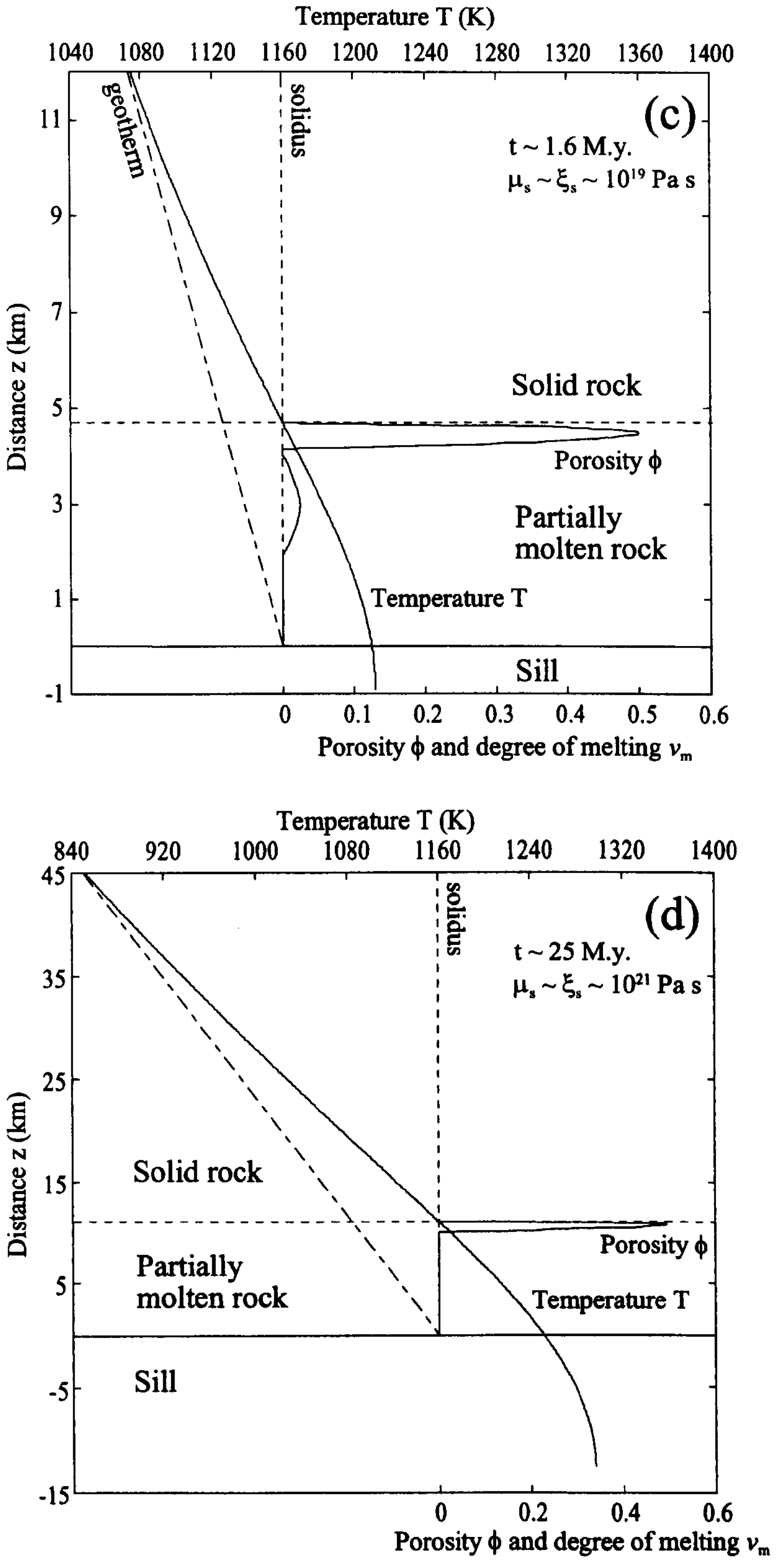

Figure 5.5(continued). Porosity (ϕ) and temperature (T) against vertical distance (z) at the time of incipient magma formation, for (c) $\mu_s \sim \xi_s \sim 10^{19}$ Pa s, and (d) $\mu_s \sim \xi_s \sim 10^{21}$ Pa s. See table 5.2 for the values of the other governing dimensional variables. Porosity (ϕ) is plotted against the lower abscissa axis; temperature (T) is plotted against the upper abscissa axis. The curve which denotes the temperature (T) also denotes the degree of melting (ν_m) if read from the lower abscissa axis. The temperature profile in the upper half of the sill only is shown; in both cases CMF ~ φ ~ 0.5.

temperature of the sill is significantly less than its initial emplacement temperature ($T_{sill} = T_{liq} = 1460K$), and that in figures 5.5(b - d), cooling has resulted in solidification of the source rock close to the sill/rock contact.

These results indicate that the intrusion of small (<1km) basaltic sills may lead to the rapid (15,000 - 200,000 yrs.) mobilisation of granitic magma from a basaltic source rock if the bulk and shear viscosities of the source rock are low (~10^{15} - 10^{17} Pa s). Repeated underplating would lead to the formation of small, distinct batches of mobile granitic magma. If the bulk and shear viscosities of the source rock are higher (~10^{18} - 10^{20} Pa s), then the minimum sill thickness required for magma mobilisation is ~2 - 10km, and the timescale of magma mobilisation is ~1-10 M.y. The minimum sill thickness required is greater than would be expected to be intruded in a single event; however, the repeated intrusion of smaller sills in the region below the source rock results in a similar rate of heat transport from the underplate to the source rock, and would lead to the formation of a large batch of mobile granitic magma. Moreover, the thickness of underplate required and the timescale of mobilisation is not excessive; for example, Petford *et al.* (1996) estimate that the lower 20km of the thickened crust beneath the Cordillera Blanca Batholith is comprised of underplated basalt, while Petford and Atherton (1992) estimate that the batholith itself was emplaced over a timescale of ~10 M.y. However, if the bulk and shear viscosities of the source rock are high (~10^{21} Pa s), then it is unlikely that underplating will lead to the mobilisation of granitic magma, because the thickness of underplate required (~25km) exceeds that which is likely to be emplaced within the crust. Note that the estimated mobilisation times and magma compositions presented in this chapter compare favourably with those presented in §4.4.3, which were obtained assuming a constant contact temperature.

5.3.2.2 Predicting the minimum thickness of basaltic underplate required

For a given set of dimensional variables, the minimum *dimensional* thickness of underplated basalt required for the mobilisation of granitic magma may be estimated using the *dimensionless* minimum sill half thickness (z_{min}) against κ_{eff} plots presented in §5.3.1.2. The procedure is similar to that described in §4.3.3.2:

(i) calculate values for the dimensionless effective thermal diffusivity (κ_{eff}) and the dimensionless initial geotherm (ψ_{geo}) using equations (4.38) and (4.39).

(ii) using a suitable plot (figure 5.3), record the dimensionless sill half thickness (z_{min}) which corresponds to the calculated value of κ_{eff}.

(iii) convert this to the corresponding dimensional sill thickness using the expression (§5.2.2)

$$z = 2z_{min}\left(\frac{(\xi_s + 4\mu_s/3)ba^2\varphi^3}{\mu_m}\right)^{1/2} \tag{5.32}$$

The *dimensional* minimum sill thicknesses obtained using equations (5.32) and figure 5.3 compare favourably with those obtained directly from the numerical solutions. For example, consider the dimensional variables used to obtain the solution shown in figure 5.5(a) (table 5.2). Substituting these values into equations (4.38) and (4.39) yields values of $\kappa_{eff} = 36$ and $\psi_{geo} = 6\times10^{-4}$ ($\sim10^{-4}$). Assuming that $\varphi \sim 0.5$, and that the CMF ~ 0.5, figure 5.3(a) yields a minimum dimensionless sill half thickness of $z_{min} \sim 50$; substituting this value into equation (5.32) yields a dimensional sill thickness of ~650m. For comparison, the numerical solution yields a dimensional sill thickness of ~700m. The slight discrepancy between the dimensional sill thickness obtained directly from the numerical solution and that estimated from figure 5.3 occurs because the value of ψ_{geo} used to obtain the numerical solution is slightly different to that used to obtain figure 5.3(a).

5.4 Discussion

A suitable description of heat transport within and from a basaltic underplate has been coupled with the description of heat, mass and momentum transport in the overlying source rock presented in chapter 4. The formulation represents the simplest which can describe the conjugate processes of solidification in the underplate and melting and melt segregation in the overlying rock, and has been used to investigate the viability of basaltic underplating as a heat source for the generation of mobile granitic magma from a basaltic protolith.

The results obtained indicate that cooling of the underplate does not significantly affect the dynamics of melting and magma mobilisation in the source rock unless the contact temperature begins to fall *before* the leading porosity wave is established. The timescale over which the contact temperature begins to fall is governed by the thickness of the underplate, and the values of κ_{eff} and ψ_{geo}. For given values of κ_{eff} and ψ_{geo}, magma mobilisation occurs only for underplates with thicknesses greater than a minimum value; the model has been used to deduce the *dimensionless* minimum value (z_{min}) as a function of κ_{eff} and ψ_{geo}. Using this *minimum* underplate thickness to deduce dimensionless segregation times and temperatures reveals that they are similar to those obtained in chapter 4 assuming an *infinite* underplate thickness (i.e. a constant contact temperature); consequently, the time required for segregation, and the composition of the segregated melt, are well approximated by the results presented in chapter 4.

Underplating is a viable heat source for the generation of mobile granitic magma from a basaltic source rock unless the bulk and shear viscosities of the partially molten rock are large ($\sim10^{21}$ Pa s). For viscosities less than this, the thickness of underplate required for mobilisation varies from ~700m to ~10km, and the time required for segregation varies from ~20,000 yrs. to ~10 M.y. These underplate thicknesses and mobilisation times are consistent with the geological evidence. Short mobilisation times indicate that repeated underplating may lead to the formation of small, discrete batches of magma, while longer segregation times indicate that repeated underplating may lead to the formation of a single, large batch of granitic magma. A pulsed magma supply is consistent with the internal contacts and compositional zonation observed in many granitic bodies (Pitcher, 1979; 1993); however, until the ascent mechanism of the magma through the crust is considered in more detail, a pulsed supply at the emplacement level should not necessarily be associated with a pulsed supply in the source region.

Chapter 6: Source region processes, ascent mechanisms and a possible origin of chemical diversity.

"...though there may be granites and granites, most of them are of one kind and all of them may likely be of one connected source." **(Read, 1944, p. 90)**

6.1 Source region processes and ascent mechanisms

The results presented in chapter 4 indicate that, in crustal partial melt zones characterised by a wide range of values for the governing variables, melt which corresponds to only a small (<CMF) degree of partial melting of the source rock, and which is granitic (*sensu-lato*) in composition, will segregate and accumulate until it forms a mobile magma. This magma must subsequently ascend from the source region to the emplacement level (see figure 1.1). The ascent mechanism of granitic magmas is still a source of controversy (e.g. Weinberg and Podlachikov, 1994; Petford *et al.*, 1994); the orthodox view is that granitic magmas ascend through the crust as diapirs (e.g. Ramberg, 1970; White and Chappell, 1977, 1990; Chappell, 1984, Weinberg and Podlichakov, 1994), yet magma ascent via diapirism is a slow process limited by the high viscosity of the surrounding crust, and theoretical studies indicate that diapirs cool and crystallise before reaching upper crustal levels (e.g. Marsh, 1982; Mahon *et al.*, 1988). A recently proposed alternative is that granitic magmas ascend through dykes, faults or fractures in a manner analogous to that of basaltic magmas (Clemens and Mawer, 1992; Petford *et al.*, 1993; Petford *et al.*, 1994). In contrast to diapirism, magma ascent via dykes is a rapid process limited only by the viscosity of the magma (Petford *et al.*, 1993; Petford *et al.*, 1994).

The ascent mechanism may ultimately be governed by the rheology and geometry of the mobile magma body which forms in the source region; unfortunately, the results presented in chapter 4 are 1-D, and therefore cannot be used to *quantitatively* predict the 3-D geometry of the magma body. However, in §3.4.3 it was argued that in a *homogeneous*, isotropic mush heated constantly from below, the 1-D results are likely to be robust in 3-D, in which case the magma would form a horizontal, 'sill' like layer. Such a mush is most likely to be produced in the crust by partial melting of regions comprised of primitive basalt emplaced by repeated underplating (§4.4.5), although even in this 'homogeneous' crust, lateral variations in composition and texture are likely to lead to lateral variations in porosity and permeability, and hence to differential melt flow and the formation of instabilities in 3-D. However, it seems reasonable to assume that, given the buoyant melt will generally flow vertically, and given the presence of the 'lid' (the solidus isotherm) at the top of the partial melt zone, a laterally continuous 'sill' of granitic magma is likely to form, although the detailed geometry of the sill may be complex (figure 6.1).

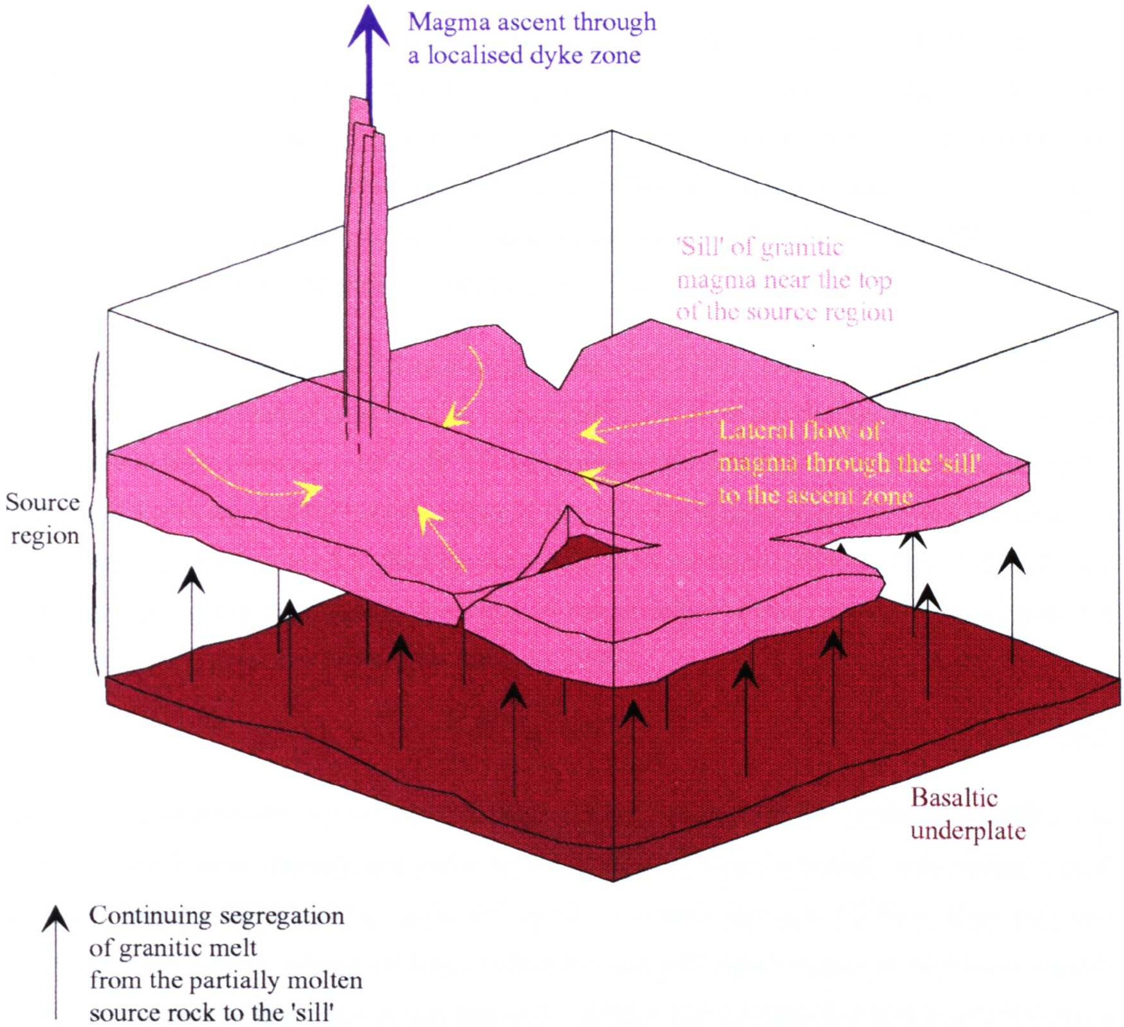

Figure 6.1. Schematic block diagram of a granite source region which is produced by heating from below as a result of basaltic underplating. The 'sill' of mobile granitic magma near the top of the source region which is predicted by the model is shown. Repeated, localised dyking may lead to the formation of a localised ascent zone to which the granitic magma can migrate laterally through the 'sill'. The continued segregation of granitic melt to the 'sill' from the partially molten rock beneath increases the melt content of the 'sill'.

A continuous 'sill' of mobile granitic magma may act as a reservoir from which magma is easily extracted by dykes. The results of Rubin (1995) indicate that *isolated*, granitic magma filled dykes propagating out of a partial melt zone are rapidly halted by freezing of the magma at the tip (see also the discussion in §4.4.4); however, the presence of a magma reservoir facilitates *repeated* dyking which warms the surrounding rock and promotes the propagation of subsequent dykes. Repeated, localised dyking leads to the formation of a localised ascent zone, to which granitic magma could migrate laterally through the 'sill' (figure 6.1). Such an ascent zone is similar to that proposed by Ryan *et al.* (1981) and Ryan (1988) for the ascent of basaltic magma beneath Kilauea Volcano, Hawaii; moreover, granitic plutons are often associated with granitic dyke swarms (Pitcher, 1979, 1993), which may represent the surface manifestation of the ascent zone.

In order to ascend as a diapir rather than through dykes, the viscosity contrast between the magma in the 'sill' and the surrounding crust must be small (Rubin, 1993), in which case the magma must be crystal rich and highly viscous (~10^{14} - 10^{15} Pa s); moreover, the thickness of the sill must exceed the minimum thickness required for buoyant overturn. Initially, the magma is crystal rich; for example, if the Critical Melt Fraction is ~0.5, then the magma initially contains ~50% crystals. However, the crystals can settle out of the magma; an estimate of the (reduced) settling velocity v_r of crystals in a crystal rich liquid is given by (Richardson and Zaki, 1954)

$$v_r = \frac{2(\rho_s - \rho_l)ga^2}{9\mu_l}(1-\phi)^{5.65} \tag{6.1}$$

where $(\rho_s - \rho_l)$ denotes the crystal-liquid density contrast, 'a' denotes the crystal size (radius), μ_l denotes the liquid shear viscosity, and ϕ denotes the volume fraction of crystals. Substituting typical values for a granitic magma of $(\rho_s - \rho_l) = 300$ kg m^{-3}, a = 1mm and $\mu_l = 10^5$ Pa s (table 4.2), and assuming $\phi = 0.5$, yields a settling velocity of ~2cm per year; this figure represents the *lowest* velocity for the given density contrast, crystal size and melt viscosity, yet indicates that within ~20,000 yrs. a 400-500m thick sill would be *entirely* crystal free. Furthermore, the continued segregation of melt from the underlying partially molten rock adds new melt to the sill which effectively decreases its crystal content (figure 6.1). Consequently, the viscosity of the magma in the sill is likely to be too low (~10^5 Pa s) to produce the viscosity contrast required for ascent via diapirism (Rubin, 1993); moreover, the magma is likely to be extracted via dykes before the sill thickness can increase to the minimum required for buoyant overturn. These very simple arguments indicate that the results of the model presented in chapter 4 are more consistent with magma ascent via dykes than via diapirism.

6.2 Source region processes and a possible origin of chemical diversity

Granitic plutons may often be arranged into suites which exhibit *systematic* variations in both mineralogy and chemistry with place and time; individual plutons may also exhibit variations between their centre and margin (e.g. Pitcher, 1979; 1993). Often this petrologic diversity originates in the source region (Tepper *et al.*, 1993; Bergantz and Dawes, 1994; Brown, 1994; Zen, 1995; Petford *et al.*, 1996), and although variations within and between suites and plutons may be produced by melting different source rock compositions, *systematic* variations must be produced by the underlying physical processes of melting, melt segregation and magma mobilisation. The model presented in chapter 4 predicts that different melt compositions segregate from source rocks with identical compositions but different physical characteristics; for example, a basaltic protolith may yield granodioritic-tonalitic melt if the matrix bulk and shear viscosities are low, and trondjhemitic melt if the bulk and shear viscosities are high (§4.4.3). However, *systematic* variations in the composition of the melt extracted from the source region have not been considered.

As discussed in §4.4.3, the Cordillera Blanca Batholith in the Peruvian part of the Andes is a trondhjemite-tonalite-granodiorite (TTG) body, which originated by partial melting of newly underplated basalt (Atherton and Petford, 1996; Petford and Atherton, 1996). The batholith is composed predominantly of trondhjemite, with volumetrically minor tonalite and granodiorite, and the order of intrusion is estimated to be granodiorite-tonalite-trondhjemite (Petford and Atherton, 1996). Yet the melting relations shown in figure 4.16 indicate that during progressive melting of basalt, the *first* melt formed (i.e. the lowest temperature melt) is trondhjemitic, while the *last* melt formed is granodioritic; consequently, if it is assumed that the first melt formed is the first to be extracted from the source region, then the order of intrusion observed in the Cordillera Blanca Batholith is the opposite of that expected.

Figure 6.2 shows the porosity (melt volume fraction), temperature, and degree of melting as a function of vertical distance in a basaltic source rock, after 0.1, 0.2 and 1 M.y. have elapsed. Note that the curve labelled 'T and v_m' denotes both the temperature (T) if read from upper abscissa axis, and the degree of melting (v_m) if read from the lower abscissa axis. The governing variables used to produce the curves are those given in table 5.2; the matrix bulk and shear viscosities are assumed to be $\mu_s \sim \xi_s \sim 10^{17}$ Pa s, and the contact temperature is assumed constant. Figure 6.2 shows that a porosity wave forms in the partially molten basalt, the vertical position and amplitude of which increase with time. After 0.1 M.y., the composition of the melt in the porosity wave corresponds to a degree of melting of ~0.3, and from figure 4.16, its composition is granodioritic. After 0.2 M.y., the composition of the melt in the porosity wave has evolved to tonalitic, while after 1 M.y., the composition of the melt in the wave has evolved to trondhjemitic.

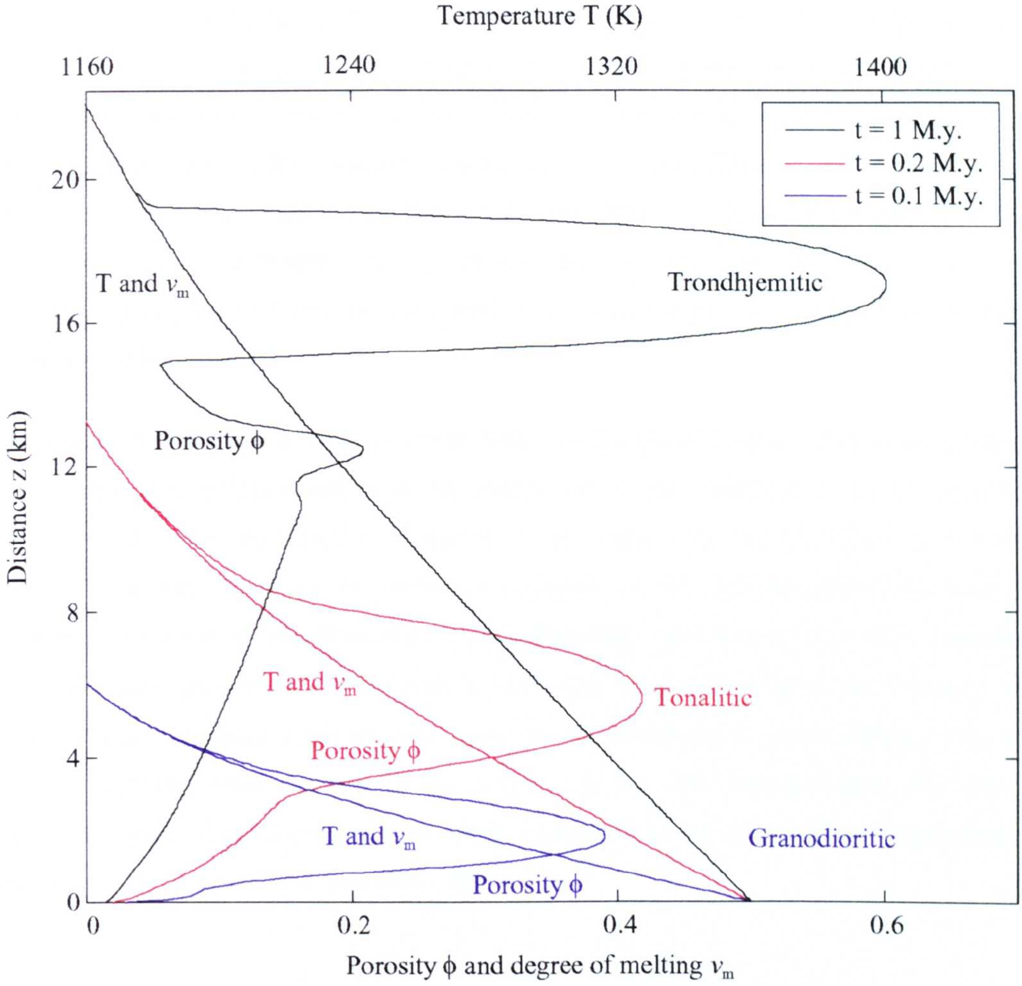

Figure 6.2. Porosity (ϕ) and temperature (T) against vertical distance (z), for a basaltic protolith, after 0.1, 0.2, and 1 M.y. have elapsed. The matrix shear and bulk viscosities are assumed to be $\mu_s \sim \xi_s \sim 10^{17}$ Pa s; see table 5.2 for the values of the other variables. The melt compositions shown correspond to the melt compositions in the porosity waves; note that the melt composition changes from granodioritic to trondhjemitic as the wave migrates upwards through the partial melt region. The porosity (ϕ) is plotted against the lower abscissa axis; the temperature (T) is plotted against the upper abscissa axis. The curve which denotes the temperature (T) also denotes the degree of melting (v_m) if read from the lower abscissa axis.

If the CMF is assumed to be ~0.5-0.6, then a mobile magma will not form until t ~0.9-1 M.y., and if no melt could be extracted from the source region until after magma mobilisation, then the composition of the first melt extracted would be trondhjemitic. However, if the melt in the leading porosity wave migrated *laterally* to a localised ascent zone *before* magma mobilisation, then melt could be extracted from the source region via dykes. The *first* melt extracted by this process would be granodioritic; with increasing time, the composition of the extracted melt would evolve to tonalitic and then to trondhjemitic. The extraction of melt from the leading porosity wave would rapidly reduce the porosity of the wave, in which case further lateral melt migration and extraction would be inhibited until the accumulation of melt below the solidus isotherm caused the porosity of the wave to increase once again. Consequently, only *small* volumes of granodioritic and tonalitic melt would be extracted before magma mobilisation, compared to the large volume of trondhjemitic melt extracted after magma mobilisation.

The process of melt extraction via dykes from zones of high porosity *before* magma mobilisation is a possible origin of chemical diversity in the source region: the composition of the extracted melt depends not only upon the initial composition of the source rock, but also upon *when* extraction occurs. The process explains the order of intrusion of the tonalite-granodiorite-trondhjemite compositions observed in the Cordillera Blanca Batholith, and also *qualitatively* explains their relative volumetric proportions. Moreover, it also explains the observation that in many granitic plutons and suites, the most felsic (granitic *sensu-stricto*) compositions which correspond to the *first* (lowest temperature) melts formed in the source region, were intruded *after* the least felsic (granodiorite, quartz diorite) compositions which correspond to the *last* (highest temperature) melts formed in the source region (Pitcher, 1979, 1993).

Chapter 7: Concluding remarks.

***"In searching for the origin of granites, it is tempting to view them as purely chemical systems"* (Pitcher 1979, p. 90)**

This dissertation presents a new, *quantitative* physical model of a granitic source region in the crust, the development of which was motivated by the need to understand better the *physical* processes which lead to a granitic partial melt fraction in the lower crust eventually forming a granitic pluton in the upper crust. Source region processes are particularly poorly understood, yet they are important because they exert a fundamental control on the composition of the magma which reaches the emplacement level. Key questions which must be answered include: How is partial melting initiated? How efficiently can the granitic melt fraction segregate from the unmelted protolith? By what physical mechanism does this segregation occur? Can the segregation process generate petrological diversity? How long must partial melting be sustained for segregation to occur? Can partial melting be sustained for this length of time?

The results of the model indicate that granitic partial melt may segregate from its protolith by buoyancy driven flow along grain edges, and accumulate in the source region until it forms a mobile magma. The separation process is intrinsically efficient; for a given protolith, the composition of the melt which accumulates to form a magma depends only upon its vertical location in the source region, and *all* the melt of that composition becomes mobilised. Moreover, the results indicate that basaltic underplating can initiate partial melting, and sustain melting for the length of time required for segregation and mobilisation to occur. Petrological diversity may be generated in the source region if the melt is extracted through dykes from regions of high porosity *before* mobilisation. The composition of the melt changes as it migrates upwards through the partial melt zone and thermodynamically equilibrates with cooler matrix; consequently, the composition of the melt depends not only upon the composition of the protolith, but also upon *when* it is extracted.

However, the results of the model are sensitive to the values of the variables which govern the dynamics of melt segregation; in particular, the shear viscosity of the melt, the bulk and shear viscosities of the partially molten protolith, the grain size, and the permeability constant. These variables are poorly constrained for crustal rocks, and the limited experimental and theoretical data has been used to estimate suitable values. The model predicts that magma mobilisation is likely in partial melt zones characterised by values of these variables in the mid-range of the estimated values, or in partial melt zones where, for example, high melt viscosities are countered by high matrix viscosities, or a large grain size is countered by small matrix viscosities. Under these conditions, the model predicts that melt segregation and mobilisation will occur in a basaltic protolith within ~15,000 yrs. to ~10 M.y., that underplate thicknesses of ~700m - 10 km are required to sustain melting for this length of time, and that the composition of the melt which becomes mobilised ranges from granodioritic - trondjhemitic. Until the values of the governing variables are better constrained, it must suffice that the model predicts the segregation and mobilisation of granitic (*sensu-lato*) melt within geologically reasonable timescales, and in agreement with the geological and geochemical evidence.

Clearly, a granitic source region in the lower crust is a complex system, and the model presented in this dissertation represents only the first step in gaining a fuller understanding of the processes which lead to the generation, segregation and mobilisation of granitic melts. The results obtained from the model are only as valid as the assumptions made in deriving the governing equations, and although many of these appear reasonable, future models will need to investigate the significance of the two most fundamental assumptions: that the source rock is homogeneous and isotropic, and that only vertical components of velocity need be considered. However, despite its relatively simple nature, the model presented in this dissertation represents a significant advance on the qualitative and semi-quantitative models of granitic melt generation, segregation and mobilisation which have previously been developed, and some general aspects of the 1-D results obtained are likely to carry through into future models. For example, the spatial distribution of melt in a homogeneous, isotropic mush which is undergoing solid-liquid phase change clearly depends upon the relative rate at which heat and mass are transported, and may be characterised in terms of a single dimensionless parameter: the effective thermal diffusivity (κ_{eff}). This result provides a framework for the systematic investigation of more complex systems.

The development of 2 and 3-D models of *heterogeneous* source rocks will be complex and computationally intensive; a suitable approach might be that used by the water and oil industries when modelling reservoir rocks with heterogeneous permeability distributions. The approach is termed *upscaling*; the rock is subdivided into homogeneous units each of which is allocated a value for the permeability, and the units are then combined and the *effective* permeability of the combined units is calculated using a continuum model. The combined (upscaled) units are then further combined, until a single value for the effective permeability has been deduced for the entire reservoir (e.g. King, 1989; King *et al.*, 1995; McCarthy, 1995). In a heterogeneous source region, the source rocks could be subdivided into homogeneous units and each allocated a value of κ_{eff}. The units could then be upscaled and a single effective value of κ_{eff} deduced for the entire source region, in which case the region is effectively homogeneous. If the source rocks were anisotropic, then κ_{eff} could be recast as a tensor which incorporates the directional and spatial variation of the governing variables. This approach would be particularly suitable if field evidence were available from which the heterogeneities of the source rocks could be characterised.

Finally, the results presented in this dissertation should be placed into the context outlined in chapter 1, of a changing outlook on the rheology of granitic magmas. The traditional view is that they are crystal rich, have high (~10^{15} Pa s) viscosities, and ascend slowly through the crust as diapirs; granitic magmatism in this view is dominated by slow processes hindered by high magma viscosity. The results presented in this dissertation, in conjunction with some simple semi-quantitative arguments, support the alternative view that granitic magmas are crystal poor, have low (~10^5 Pa s) viscosities, and ascend rapidly through the crust in dykes; moreover, the results indicate that granitic magmatism is dominated by rapid processes facilitated by low magma viscosity. For example, predicted segregation times of ~15,000 yrs. indicate that the time which elapses from the inception of melting in the lower crust to the emplacment of magma in the upper crust may be geologically short.

Bibliography

Ahern, J.L. and Turcotte, D.L. Magma migration beneath an ocean ridge, *Earth. Plan. Sci. Lett.* **45**, 115-122 (1979).

Arzi, A.A., Critical phenomena in the rheology of partially melted rocks, *Tectonophysics* **44**, 173-184 (1978).

Arzt, E., Ashby, M.F. and Easterling, K.E., Practical applications of hot-isostatic pressing diagrams: Four case studies, *Metall. Trans.* **14A**, 211-221 (1983).

Atherton, M.P., Granite magmatism, *J. Geol. Soc. Lon.* **150**, 1009-1023 (1993).

Atherton, M.P. and Petford, N., Generation of sodium-rich magmas from newly underplated basaltic crust, *Nature* **362**, 144-146 (1993).

Atherton, M.P. and Petford, N., Plutonism and the growth of Andean crust at 9°S from 100 to 3 Ma., *J. South Am. Earth Sci.* **9**, 1-9 (1996).

Banks, J.M., Nucleation of magma driven cracks in the asthenospheric mantle, Ph.D. Thesis, University of Liverpool, Liverpool, U.K. (1996).

Barcilon, V. and Richter, F.M., Nonlinear waves in compacting media, *J. Fluid Mech.* **164**, 429-448 (1986).

Bateman, R., On the role of diapirism in the segregation, ascent and final emplacement of granitoid magmas, *Tectonophysics* **110**, 211-231 (1984).

Bear, J., *Dynamics of fluids in porous media* (1st Edn), pp. 764, Elsevier, New York (1972).

Beard, J.S. and Lofgren, G.E., Effect of water on the composition of partial melts of greenstone and amphibolite, *Science* **244**, 195-197 (1989).

Beard, J.S. and Lofgren, G.E., Dehydration melting and water-saturated melting of basaltic and andesitic greenstones and amphibolites at 1, 3, and 6.9 kb, *J. Petrol.* **32**, 365-401 (1991).

Beckerman, C. and Viskanta, R., Natural convection solid/liquid phase change in porous media, *Int. J. Heat Mass Transfer* **31**, 35-46 (1988).

Beere, W., A unifying theory of the stability of penetrating liquid phases and sintering pores, *Acta Metall.* **23**, 131-138 (1975).

Bennon, W.D. and Incropera, F.P., A continuum model for the momentum, heat and species transport in binary solid-liquid phase change systems-I. Model formulation, *Int. J. Heat Mass Transfer* **30**, 2161-2170 (1987a).

Bennon, W.D. and Incropera, F.P., A continuum model for the momentum, heat and species transport in binary solid-liquid phase change systems-II. Application to solidification in a rectangular cavity, *Int. J. Heat Mass Transfer* **30**, 2171-2187 (1987b).

Bergantz, G.W., Underplating and partial melting: Implications for melt generation and extraction, *Science* **245**, 1093-1095 (1989).

Bergantz G.W., Conjugate solidification and melting in multicomponent open and closed systems, *Int. J. Heat Mass Transfer* **35**, 35-46 (1992).

Bergantz, G.W. and Dawes, R., Aspects of magma generation and ascent in continental lithosphere. In *Magmatic Systems*, (Edited by M.P. Ryan), Chap. 13. Academic Press (1994).

Bickle, M. and McKenzie, D., The transport of heat and matter by fluids during metamorphism, *Contrib. Mineral. Petrol.* **95**, 384-392 (1987).

Bird, P., Continental delamination and the Colorado Plateau, *J. Geophys. Res.* **84**, 7561-7571 (1979).

Bottinga, Y. and Weill, D., The viscosity of magmatic silicate liquids: A model for calculation, *Am. J. Sci.* **272**, 438-475 (1972).

Bourbie, T. and Zinszner, B., Hydraulic and acoustic properties as a function of porosity in Fontainebleau sandstone, *J. Geophys. Res.* **90**, 11,524-11,532 (1985).

Bowen, N.L., The granite problem and the method of multiple predjudices, *Geol. Soc. Am. Mem.* **28**, 79-90 (1948).

Bowen, N.L. and Tuttle, O.F., The system $NaAlSi_3O_8$ - $KAlSi_3O_8$ - H_2O, *J. Geol.* **58**, 489-511 (1950).

Brown, M., The petrogenesis of some migmatites from the Presqu'ile de Rhuys, southern Brittany, France. In *Migmatites, Melting, and Metamorphism*, (edited by M.P. Atherton and C.D. Gribble), Shiva, Nantwich (1983).

Brown, M., The generation, segregation, ascent and emplacement of granitic magma: The migmatite-to-crustally derived granite connection in thickened orogens, *Earth-Science Rev.*, **36**, 83-130 (1994).

Brown, M., Averkin, Y.A. and McLellan, E.L., Melt segregation in migmatites, *J. Geophys. Res.* **100**, 15,655-15,679 (1995).

Bryant, S., Cade, C. and Mellor, D., Permeability prediction from geologic models, *AAPG Bull.* **77**, 1338-1350 (1993).

Bulau, J.R., Waff, H.S. and Tyburczy, J.A., Mechanical and thermodynamic constraints on fluid distribution in partial melts, *J. Geophys Res.* **84**, 6102-6108 (1979).

Carslaw, H.S. and Jaeger, J.C., *Conduction of heat in solids* (2nd Edn), pp. 510, Clarendon Press, Oxford, U.K. (1986).

Chappell, B.W., Source rocks of I- and S-type granites in the Lachlan Fold Belt, southeastern Australia, *Phil. Trans. R. Soc. Lond. A*, **310**, 693-707 (1984).

Chappell, B.W., White, A.J.R. and Wyborn, D., The importance of residual source material (restite) in granite petrogenesis, *J. Petrol.* **28**, 1111-1138 (1987).

Cheadle, M.J., Properties of texturally equilibrated two phase aggregates, Ph.D. Thesis, University of Cambridge, Cambridge, U.K. (1989).

Christensen, N.I. and Mooney, W.D., Seismic velocity structure and composition of the continental crust: A global view, *J. Geophys. Res.* **100**, 9761-9788 (1995).

Clarke, D.B., *Granitoid Rocks* (1st Edn), pp. 283, Chapman and Hall, London, U.K. (1992).

Clauser, C. and Huenges, E., Thermal conductivity of rocks and minerals. In *Rock Physics and Phase Relations: A Handbook of Physical Constants*, (Edited by T.J. Ahrens), p. 105, AGU Reference Shelf 3 (1995).

Clemens, J.D., Water contents of siliceous to intermediate magmas, *Lithos* **17**, 273-287 (1984).

Clemens, J.D., The importance of residual source material (restite) in granite petrogenesis: A comment, *J. Petrol.* **30**, 1313-1316 (1989).

Clemens, J.D., The Granulite-Granite Connexion. In *Granulites and Crustal Evolution,* (edited by D. Vielzuf and Ph. Vidal), Nato ASI Series C, **311**, Kluwer, Dordrecht, The Netherlands (1990).

Clemens, J.D. and Vielzuf, D., Constraints on melting and magma production in the crust, *Earth Plan. Sci. Lett.* **86**, 287-306 (1987).

Clemens, J.D. and Mawer, C.K., Granitic magma transport by fracture propagation, *Tectonophysics* **204**, 339-360 (1992).

Clifford, T.N., Stumfl, E.F., Burger, A.J., McCarthy, T.S. and Rex, D.C., Mineral-chemical and isotopic studies of Namaqualand granulites, South Africa: A Grenville analogue, *Contrib. Mineral. Petrol.* **77**, 225-250 (1981).

Clyne, T.W., Numerical modelling of directional solidification of metallic alloys, *Metal Science* **16**, 441-450 (1982).

Cooper, R.F. and Kohlstedt, D.L., Solution-precipitation enhanced diffusional creep of partially molten olivine-basalt aggregates during hot pressing, *Tectonophysics* **107**, 207-233 (1984).

Cooper, R.F. and Kohlstedt, D.L., Rheology and structure of Olivine-Basalt Partial Melts, *J. Geophys Res.* **91**, 9315-9323 (1986).

D'Lemos, R.S., Brown, M. and Strachan, R.A., Granite magma generation, asent and emplacement within a transpressional orogen, *J. Geol. Soc. Lon.* **149**, 487-490 (1992).

Davies, J.H. and von Blanckenburg, F., Slab breakoff: A model of lithosphere detachment and its test in the magmatism and deformation of collisional orogens, *Earth Plan. Sci. Lett.* **129**, 85-102 (1995).

Deer, W.A., Howie, R.A. and Zussman, J., *An introduction to the rock forming minerals* (2nd Edn), pp. 696, Longman, Harlow, U.K. (1992).

Dell'Angelo, L.N., Tullis, J. and Yund, R.A., Transition from dislocation creep to melt-enhanced diffusion creep in fine grained granitic aggregates, *Tectonophysics* **139**, 325-332 (1987).

Dell'Angelo, L.N. and Tullis, J., Experimental deformation of partially melted granitic aggregates, *J. Metamorph. Geol.* **6**, 495-516 (1988).

den Brok, B., An experimental investigation into the effect of water on the flow of quartzite, Ph.D. Thesis, University of Utrecht, Utrecht, Netherlands (1992).

Dingwell, D.B., Bagdassarov, N.S., Bussod, G.Y. and Webb, S.L., Magma rheology, *Mineral. Assoc. Canada* **21**, 131-196 (1993).

Drummond, B.J. and Collins, C.D.N., Seismic evidence for underplating of the lower continental crust in Australia, *Earth Plan. Sci. Lett.* **79**, 361-372 (1986).

Dullien, F.A.L., *Porous media, fluid transport and pore structure*, (1st Edn), pp. 396, Academic Press, New York (1979).

Elliott, M.T., Cheadle, M.J. and Jerram, D.A., On the identification of textural equilibrium in rocks using dihedral angle measurements, *Geology* **25**, 355-358 (1997).

Ellis, D.J., Precambrian tectonics and the physicochemical evolution of the continental crust. II. Lithosphere delamination and ensialic orogeny, *Precambrian Res.* **55**, 507-524 (1992).

England, P.C., and Thompson, A. B., Pressure-Temperature-Time paths of regional metamorphism I. Heat transfer during the evolution of regions of thickened continental crust, *J. Petrol.*, **25**, 894-928 (1984).

Farver, J.R. and Yund, R.A., Measurement of oxygen grain boundary diffusion in natural, fine grained, quartz aggregates, *Geochim. et Cosmochim. Acta* **55**, 1597-1607 (1991).

Feeley, T.C. and Grunder, A.L., Mantle contribution to the evolution of middle tertiary silicic magmatism during early stages of extension: The Egan Range volcanic complex, east-central Nevada, *Contrib. Mineral. Petrol.* **106**, 154-169 (1991).

Fountain, J.C., Hodge, D.S. and Shaw, R.P., Melt segregation in anatectic granites: a thermo-mechanical model, *J. Volc. Geotherm. Res.* **39**, 279-296 (1989).

Freer, R., Diffusion in silicate minerals and glasses: a data digest and guide to the literature, *Contrib. Mineral. Petrol.* **76**, 440-454 (1981).

Fyfe, W.S., The granulite facies, partial melting and the Archean crust, *Phil. Trans. R. Soc. Lond. A.* **273**, 457-461 (1973).

Handy, M.R. and Zingg, A. The tectonic and rheological evolution of an attenuated section of the continental crust: Ivrea crustal section, southern Alps, northwestern Italy and southern Switzerland, *Geol. Soc. Am. Bull.* **103**, 236-253 (1991).

Helz, R. T., Kirchenbaum, H. and Marinenko, J.W., Diapiric transfer of melt in Kilauea Iki lava lake, Hawaii: A quick, efficient process of igneous differentiation, *Geol. Soc. Am. Bull.* **101**, 578 (1989).

Hills, R.N., Loper, D.E. and Roberts, P. H., A thermodynamically consistent model of a mushy zone, *Q. J. Mech. Appl. Math.* **36**, 505-539 (1983).

Hills, R.N. and Roberts, P. H., On the formulation of diffusive mixture theories for two phase regions, *J. Engng. Math.* **22**, 93-106 (1988).

Hodge, D.S., Thermal model for origin of granitic batholiths, *Nature* **251**, 297-299 (1974).

Hollister, L.S. and Crawford, M.L., Melt-enhanced deformation; A major tectonic process, *Geology* **14**, 558-561 (1986).

Houseman, G. A., McKenzie, D.P. and Molnar, P., Convective instability of a thickened boundary layer and its relevance for the thermal evolution of continental convergent belts, *J. Geophys. Res.*, **86**, 6115-6132 (1981).

Huppert, H.E. and Sparks, R.S.J., The generation of granitic magmas by intrusion of basalt into continental crust, *J. Petrol.* **29**, 599-624 (1988).

Jones, K.A. and Brown, M., High-temperature 'clockwise' P-T paths and melting in the development of regional migmatites: an example from southern Brittany, France, *J. Metamorph. Geol.* **8**, 551-578 (1990).

Jurewicz, S.R. and Watson, E.B., The distribution of partial melt in a felsic system: The importance of surface energy, *Contrib. Mineral. Petrol.* **85**, 125-129 (1984).

Jurewicz, S.R. and Watson, E.B., The distribution of partial melt in a granitic system: The application of liquid-phase sintering theory, *Geochim. et Cosmochim. Acta* **49**, 1109-1121 (1985).

Karato, S., Paterson, M.S. and FitzGerald, J.D., Rheology of synthetic olivine aggregates: Influence of grain size and water, *J. Geophys. Res.* **91**, 8151-8176 (1986).

Kay, R.W. and Mahlburg-Kay, S., Creation and destruction of lower continental crust, *Geol. Rund.* **80**, 259-278 (1991).

Kenyon, P., Trace element and isotopic effects arising from magma migration beneath mid-ocean ridges and island arcs, *Earth Plan. Sci. Lett.* **101**, 367-378 (1990).

Kerr, R.C. and Lister, J.R., The effects of shape on crystal settling and on the rheology of magmas, *J. Geol.* **99**, 457-467 (1991).

King, P.R., The use of renormalization for calculating effective permeability, *Trans. Porous Media* **4**, 37-58 (1989).

King, M.J., King, P.R., McGill, C.A. and Williams, J.K., Effective properties for flow calculations, *Trans. Porous Media* **20**, 169-196 (1995).

Klemperer, S.L., Hauge, T.A., Hauser, E.C., Oliver, J.E. and Potter, C.J., The Moho in the northern Basin and Range province, Nevada, along the COCORP 40°N seismic reflection transect, *Geol. Soc. Am. Bull.* **97**, 603-618 (1986).

Kohlstedt, D.L. and Chopra, P.N., Influence of Basaltic Melt on the Creep of Polycrystalline Olivine under Hydrous Conditions. In *Magmatic Systems*, (Edited by M.P. Ryan), Chap. 3. Academic Press (1994).

Kono, M., Fukao Y. and Yamamoto, A., Mountain building in the central Andes, *J. Geophys. Res.* **94**, 3,891-3,905 (1989).

Kukowski, H. and Neugebauer, H.J., On the ascent and emplacement of granitoid magma bodies: Dynamic-thermal numerical models, *Geol. Rund.* **79**, 227-239 (1990).

Landau, L.D. and Lifshitz, E.M., *Fluid Mechanics* (2nd Edn), pp. 380, Pergamon Press, Oxford (1987).

Lange, R.A. and Carmichael, I. S. E., Densities of Na_2O-K_2O-CaO-MgO-FeO-Fe_2O_3-Al_2O_3-TiO_2-SiO_2 liquids: New measurements and partial molar properties, *Geochim. et Cosmochim. Acta* **51**, 2931-2946 (1987).

Laporte, D., Wetting behaviour of partial melts during crustal anatexis: The distribution of hydrous silicic melts in polycrystalline aggregates of quartz, *Contrib. Mineral. Petrol.* **116**, 486-499 (1994).

Lauchenbrauch, A.H., Crustal temperature and heat production: Implications of the linear heat-flow relation, *J. Geophys. Res.* **75**, 3291-3300 (1970).

Le Breton, N. and Thompson, A.B., Fluid-absent (dehydration) melting of biotite in metapelites in the early stages of crustal anatexis, *Contrib. Mineral. Petrol.* **99**, 226-237 (1988).

Leake, B.E., Granite magmas: their sources, initiation and consequences of emplacement, *J. Geol. Soc. Lon.* **147**, 579-589 (1990).

Lejeune, A.M. and Richet, P., Rheology of crystal-bearing melts, *J. Geophys. Res.* **100**, 4215-4229 (1995).

Lide, D.R. and Frederiske, H.P.R., *CRC Handbook of Chemistry and Physics* (77th Edn) pp. 695, CRC, Boca Raton (1996).

Lister, J.R. and Kerr, R.C., Fluid-mechanical models of crack propagation and their application to magma transport in dykes, *J. Geophys. Res.* **96**, 10,049-10,077 (1991).

Loper, D.E. and Roberts, P.H., On the motion of an iron-alloy core containing a slurry, *Geophys. Astrophys. Fluid Dynamics* **9**, 298-321 (1978).

Lowell, R.P. and Bergantz, G.W., Melt stability and compaction in a partially molten silicate layer heated from below. In *Structure and Dynamics of Partially Solidified Systems*, (Edited by D.E. Loper), Nato ASI Series E, **125**, Martinus Nijhoff (1987).

Maaloe, S. and Scheie, A., The permeability controlled accumulation of primary magma, *Contrib. Mineral. Petrol.* **81**, 350-357 (1982).

Mahon, K.I., Harrison, T.M. and Drew, D.A., Ascent of a granitoid diapir in a temperature varying medium, *J. Geophys. Res.* **93**, 1174-1188 (1988).

Marsh, B.D., On the crystallinity, probability of occurrence, and rheology of lava and magma, *Contrib. Mineral. Petrol.* **78**, 85-98 (1981).

Marsh, B.D., On the mechanics of igneous diapirism, stoping, and zone melting, *Am. J. Sci.* **282**, 808-855 (1982).

Marsh, B.D., On convective style and vigor in sheet-like magma chambers, *J. Petrol.* **30**, 479-530 (1989).

McBirney, A.R. and Murase, T., Rheological properties of magmas, *Ann. Rev. Earth Planet. Sci.* **12**, 337-357 (1984).

McCarthy, J.F., Comparison of fast algorithms for estimating large scale permeabilities of heterogeneous media, *Trans. Porous Media* **19**, 123-137 (1995).

McKenzie, D.P., The generation and compaction of partially molten rock, *J. Petrol.*, **25**, 713-765 (1984).

McKenzie, D.P., The extraction of magma from the crust and mantle, *Earth Plan. Sci. Lett.* **74**, 81-91 (1985).

McKenzie, D.P., The compaction of igneous and sedimentary rocks, *J. Geol. Soc. Lon.* **144**, 299-307 (1987).

McKenzie, D. and Bickle, M.J., The volume and composition of melt generated by extension of the lithosphere, *J. Petrol.* **29**, 625-679 (1988).

Miller, C.F., Watson, E.B. and Harrison, T.M., Perspectives on the source, segregation and transport of granitiod magmas, *Trans. R. Soc. Edin. Earth Sci.* **79**, 135-156 (1988).

Mitchell, A.R. and Griffiths, D.F., *The finite difference method in partial differential equations* (1st Edn), pp. 350, Wiley, Chichester, U.K. (1980).

Morton, K.F. and Mayers, D.F, *Numerical solution of partial differential equations* (1st Edn), pp. 228, Cambridge University Press, Cambridge, U.K. (1994).

Murase, T. and McBirney, A.R., Properties of Some Common Igneous Rocks and Their Melts at High Temperatures, *Geol. Soc. Am. Bull.* **84**, 3563-3592 (1973).

Nelson, K.D., A unified view of craton evolution motivated by recent deep seismic reflection and refraction results, *Geophys. J. Int.* **105**, 25-35 (1991).

Neuville, D.R., Courtial, P., Dingwell, D.B. and Richet, P., Thermodynamic and rheological properties of rhyolite and andesite melts, *Contrib. Mineral. Petrol.* **113**, 572-581 (1993).

Oldenburg, C.M. and Spera, F.J., Hybrid model for solidification and convection, *Numer. Heat Transfer* **21B**, 217-229 (1992).

Patiño Douce, A.E., Humphreys, E.D. and Johnston, A.D., Anatexis and metamorphism in tectonically thickened continental crust exemplified by the Sevier hinterland, western North America, *Earth Plan. Sci. Lett.* **97**, 290-315 (1990).

Patiño Douce, A.E. and Johnston, A.D., Phase equilibria and melt productivity in the pelitic system: implications for the origin of peraluminous granitoids and aluminous granulites, *Contrib. Mineral. Petrol.* **107**, 202-218 (1991).

Petford, N., Segregation of tonalitic-trondhjemitic melts in the continental crust: The mantle connection, *J. Geophys. Res.* **100**, 15735-15743 (1995).

Petford, N. and Atherton, M. P., Granitoid emplacement and deformation along a major crustal lineament: the Cordillera Blanca, Peru, *Tectonophysics* **205**, 171-185 (1992).

Petford, N., Kerr, R.C. and Lister, J.R., Dike transport of granitiod magmas, *Geology* **21**, 845-848 (1993).

Petford, N., Lister, J.R. and Kerr, R.C., The ascent of felsic magmas in dykes, *Lithos* **32**, 161-168 (1994).

Petford, N. and Atherton, M.P., Na-rich partial melts from newly underplated basaltic crust: The Cordillera Blanca Batholith, Peru, *J. Petrol.* **37**, 1491-1521 (1996).

Petford, N., Atherton, M.P. and Halliday, A.N., Rapid magma production rates, underplating, and remelting in the Andes (9-23°S): Isotopic evidence from N. Peru, *J. South American Earth Sci.* **9**, 69-78 (1996).

Pharr, G.M. and Ashby, M.F., On creep enhanced by a liquid phase, *Acta Metall.* **31**, 129-138 (1983).

Philpotts, A.R. and Carroll, M., Physical properties of partly melted tholeiitic basalt, *Geology* **24**, 1029-1032 (1996).

Pin, C., Evolution of the lower crust in the Ivrea Zone: A model based on isotopic and geochemical data. In *Granulites and Crustal Evolution,* (edited by D. Vielzuf and Ph. Vidal), Nato ASI Series C, **311**, Kluwer, Dordrecht, The Netherlands (1990).

Pitcher, W.S., The nature, ascent and emplacement of granitic magmas, *J. Geol Soc. London*, **136**, 627-662 (1979).

Pitcher, W.S., *The nature and origin of granite* (1st Edn), pp. 321, Blackie, London (1993).

Pollack, H.N. and Chapman, D.S., On the regional variation of heat flow, geotherms, and lithospheric thickness, *Tectonophysics* **38**, 279-296 (1977).

Prescott, P.J., Incropera, F.P. and Bennon, W.D., Modelling of dendritic solidification systems: reassessment of the continuum momentum equation, *Int. J. Heat Mass Transfer* **34**, 2351-2359 (1991).

Press, W.H., Teukolsky, S.A., Vetterling, W.T. and Flannery, B.P., *Numerical Recipes in Fortran* (2nd Edn), pp. 934, Cambridge University Press, Cambridge, U.K. (1992).

Ramberg, H., Model studies in relation to intrusion of plutonic bodies. In *Mechanism of Igneous Intrusion* (edited by G. Newall and N. Rast), Spec. Iss. Geol. J. **2**, Gallery Press, Liverpool, U.K. (1970).

Ranalli, G., *Rheology of the Earth: Deformation and flow processes in geophysics and geodynamics* (2nd Edn), pp. 366, Allen and Unwin, London, U.K. (1987).

Rapp, R.P., Amphibole-out phase boundary in partially melted metabasalt, its control over liquid fraction and composition, and source permeability, *J. Geophys. Res.* **100**, 15,601-15,610 (1995).

Rapp, R.P., Watson, E.B. and Miller, C.F., Partial melting of amphibolite/eclogite and the origin of Archean trondhjemites and tonalites, *Precambrian Res.* **51**, 1-25 (1991).

Rapp, R.P. and Watson, E.B., Dehydration melting of metabasalt at 8-32 kbar: Implications for continental growth and crust-mantle recycling, *J. Petrol.* **36**, 891-931 (1995).

Read, H.H., A commentary on place in plutonism, *Quart. J. Geol. Soc. Lon.* **104**, 155-206 (1948).

Read, H.H., A commentary on time in plutonism, *Quart. J. Geol. Soc. Lon.* **105**, 101-156 (1949).

Read, H.H., *The granite controversy*, pp. 430, Thomas Murby, London (1957).

Ribe, N.M. and Smooke, M.D., A stagnation point flow model for melt extraction from a mantle plume, *J. Geophys. Res.* **92**, 6437-6443 (1987).

Richardson, T.S. and Zaki, Y.W., Sedimentation and fluidisation, *Trans. Inst. Chem. Eng.* **32**, 35-53 (1954).

Richet, P. and Bottinga, Y., Thermochemical properties of silicate glasses and liquids: A review, *Rev. Geophys.* **24**, 1-25 (1986).

Richter, F.M. and McKenzie, D.P., Dynamical models for melt segregation from a deformable matrix, *J. Geol.* **92**, 729-740 (1984).

Robie, R.A., Hemingway, B.S. and Fischer, J.R., Thermodynamic properties of minerals and related substances at 298.15 K and 1 bar (10^5 Pascals) and at higher temperatures, *U.S. Geol. Surv. Bull.* **1452**, (1978).

Rubin, A.M., Dikes vs. diapirs in viscoelastic rock, *Earth Plan. Sci. Lett.*, **119**, 641-659 (1993).

Rubin, A.M., Getting granite dykes out of the source region, *J. Geophys. Res.* **100**, 5,911-5,929 (1995).

Rudnick, R.L., Restites, Eu anomalies, and the lower continental crust, *Geochim. et Cosmochim. Acta* **56**, 963-970 (1992).

Rushmer, T., Partial melting of two amphibolites: Contrasting results under fluid-absent conditions. *Contrib. Mineral. Petrol.* **107**, 41-59 (1991).

Rutter, M.J. and Wyllie, P.J., Melting of vapour-absent tonalite at 10 kbar to simulate dehydration melting in the deep crust, *Nature* **331**, 159-160 (1988).

Ryan, M.P., The mechanics and three-dimensional internal structure of active magmatic systems: Kilauea volcano, Hawaii, *J. Geophys. Res.*, **93**, 4213-4248 (1988).

Ryan, M.P., Koyanagi, R.Y. and Fiske, R.S., Modeling the three-dimensional structure of macroscophic magma transport systems: Application to Kilauea Volcano, Hawaii, *J. Geophys. Res.*, **88**, 7111-7129 (1981).

Ryan, M.P. and Blevins, J.Y.K, The viscosity of synthetic and natural silicate melts and glasses at high temperatures and 1 bar (10^5 Pa s) pressure and at higher pressure, *U.S. Geol. Survey Bull.* **1764**, pp. 563 (1987).

Sahimi, M., Flow phenomena in rocks: from continuum models to fractals, percolation, cellular automata, and simulated annealing, *Rev. Mod. Phys.* **65**, 1393-1534 (1993).

Sawyer, E.W., Disequilibrium melting and the rate of melt-residuum separation during migmatisation of mafic rocks from the Grenville Front, Quebec, *J. Petrol.* **32**, 701-738 (1991).

Sawyer, E.W., Melt segregation in the continental crust, *Geology*, **22**, 1019-1022 (1994).

Scott, D. and Stevenson, D., Magma Solitons, *Geophys. Res. Lett.* **11**, 1161-1164 (1984).

Scott, D. and Stevenson, D., Magma ascent by porous flow, *J. Geophys Res.* **91**, 9283-9296 (1986).

Seber, S., Barazangi, M., Ibenbrahim, A. and Demnati, A., Geophysical evidence for lithospheric delamination beneath the Alboran Sea and Rif-Betic mountains, *Nature* **379**, 785-790 (1996).

Shaw, H.R., Obsidian-H_2O viscosities at 1000 and 2000 bars in the temperature range 700° to 900° C, *J. Geophys. Res.* **68**, 6337-6343 (1963).

Shaw, H.R., Viscosities of magmatic silicate liquids: An empirical method of prediction, *Am. J. Sci.* **272**, 870-893 (1972).

Siemieniuch, J.L. and Gladwell, I., Some explicit finite-difference methods for the solution of a model diffusion-convection equation, *Numerical Analysis Report* **16**, University of Manchester, U.K. (1976).

Siemieniuch, J.L. and Gladwell, I., Analysis of explicit difference methods for a diffusion-convection equation, *Int. J. Num. Meth. Eng.* **12**, 899-916 (1978).

Sleep, N.H., Tapping of melt by veins and dykes, *J. Geophys Res.* **93**, 10,255-10,272 (1988).

Smith, C.S., Grain phases and interfaces: An interpretation of microstructure, *Trans. Am. Inst. Mech. Eng.* **75**, 15-51 (1948).

Smith, C.S., Some elementary principles of polycrystalline microstructure, *Metall. Rev.* **9**, 1-48 (1964).

Sparks, D.W. and Parmentier, E.M., Melt extraction from the mantle beneath spreading centres, *Earth Plan. Sci. Lett.* **105**, 368-377 (1991).

Speer, J.A., McSween, H.Y., and Gates, A.E., Generation, segregation, ascent and emplacement of Alleghanian plutons in the southern Appalachians, *J. Geol.* **102**, 249-267 (1994).

Speigelman, M. and McKenzie, D.P., Simple 2-D models for melt extraction at mid-ocean ridges and island arcs, *Earth Plan. Sci. Lett.* **83**, 137-152 (1987).

Speigelman, M., Melting and melt extraction: the physics of flow in deformable porous media, Ph.D. Thesis, University of Cambridge, Cambridge, U.K. (1989).

Spiegelman, M. and Kenyon, P., The requirements for chemical disequilibrium during magma migration, *Earth Plan. Sci. Lett.* **109**, 611-620 (1992).

Spiegelman, M., Physics of melt extraction: Theory, implications and applications, *Phil. Trans. Roy. Soc. Lond.* **342**, 23-41 (1993).

Spry, A., *Metamorphic Textures* (1st Edn), pp. 343, Pergamon Press, London (1969).

Strong, D.F., and Hanmer, S.K., The leocogranites of southern Brittany: origin by faulting, frictional heating, fluid flux and fractional melting, *Can. Mineral.* **19**, 163-176 (1981).

Tait, S. and Jaupart, C., Compositional convection in a reactive crystalline mush and melt differentiation, *J. Geophys. Res.* **97**, 6735-6756 (1992).

Takada, A., Accumulation of magma in time and space by crack interaction. In *Magmatic Systems*, (Edited by M.P. Ryan), Chap. 11. Academic Press (1994).

Tepper, J.H., Nelson, B.K., Bergantz, G.W. and Irving, A.J., Petrology of the Chilliwack Batholith, North Cascades, Washington: Generation of calc-alkaline granitoids by melting of mafic lower crust with variable water fugacity, *Contrib. Mineral. Petrol.* **113**, 333-351 (1993).

Thompson, A.B., Dehydration melting of pelitic rocks and the generation of H_2O-undersaturated granitic liquids, *Am. J. Sci.* **282**, 1567-1595 (1982).

Thompson, A.B., Heat, fluids, and melting in granulites. In *Granulites and Crustal Evolution*, (edited by D. Vielzuf and Ph. Vidal), Nato ASI Series C, **311**, Kluwer, Dordrecht, The Netherlands (1990).

Turcotte, D.L. and Schubert, G., *Geodynamics: Applications of Continuum Physics to Geological Problems* (1st Edn), pp. 450, Wiley, New York (1982).

Tuttle, O.F. and Bowen, N.L., Origin of granite in the light of experimental studies in the system $NaAlSi_3O_8$-$KAlSi_3O_8$-SiO_2-H_2O, *Geol. Soc. Am. Mem.* **74**, 1-153 (1958).

van den Eeckhout, B., Grocott, J. and Vissers, R., On the role of diapirism in the segregation, ascent and final emplacement of granitoid magmas - Discussion, *Tectonophysics* **127**, 161-169 (1986).

van der Molen, I. and Paterson, M.S., Experimental deformation of partially melted granite, *Contrib. Mineral. Petrol.* **70**, 299-318 (1979).

Vernon, R.H., Microstructures of high grade metamorphic rocks at Broken Hill, Australia, *J. Petrol.* **9**, 1-22 (1968).

Vielzuf, D. and Holloway, J.R., Experimental determination of the fluid-absent melting relations in the pelitic system. Consequences for crustal differentiation, *Contrib. Mineral. Petrol.* **98**, 257-276 (1988).

Vielzuf, D., Clemens, J.D., Pin, C. and Moinet, E., Granites, granulites, and crustal differentiation. In *Granulites and Crustal Evolution,* (edited by D. Vielzuf and Ph. Vidal), Nato ASI Series C, **311**, Kluwer, Dordrecht, The Netherlands (1990).

Viskanta, R., Heat transfer during melting and solidification of metals, *J. Heat Transfer* **110**, 1205-1219 (1988).

Voller, V.R., Brent, A.D. and Prakash, C., The modelling of heat, mass and solute transport in solidification systems, *Int. J. Heat Mass Transfer* **32**, 1719-1731 (1989).

von Bargen, N. and Waff, H.S., Permeabilities, interfacial areas and curvatures of partially molten systems: Results of numerical computations of equilibrium microstructures, *J. Geophys Res.* **91**, 9261-9276 (1986).

von Bargen, N. and Waff, H.S., Wetting of enstatite by basaltic melt at 1350°C and 1.0-2.5 GPa pressure, *J. Geophys Res.* **93**, 1153-1158 (1988).

Voschage, H., Hofmann, A.W., Mazzucchelli, M., Rivalenti, G., Sinigoi, S., Raczek, I. and Demarchi, G., Isotopic evidence from the Ivrea Zone for a hybrid lower crust formed by magmatic underplating, *Nature* **347**, 731-736 (1990).

Waff, H.S. and Bulau, J.R., Equilibrium fluid distribution in an ultramafic partial melt under hydrostatic stress conditions, *J. Geophys. Res.* **84**, 6109-6114 (1979).

Waff, H.S. and Faul, U.H., Effects of crystalline anisotropy on fluid distribution in ultramafic partial melts, *J. Geophys. Res.* **97**, 9003-9014 (1992).

Watson, S. and McKenzie, D., Melt generation by plumes: A study of Hawaiin volcanism, *J. Petrol.* **32**, 501-537 (1991).

Webb, S.L. and Dingwell, D.B., Non-Newtonian rheology of igneous melts at high stresses and strain rates: Experimental results for rhyolite, andesite, basalt, and nephelinite, *J. Geophys. Res.* **95**, 15,695-15,701 (1990).

Weinberg, R.F. and Podladchikov, Y., Diapiric ascent of magmas through power law crust and mantle, *J. Geophys. Res.* **99**, 9543-9559 (1994).

Wheeler, J., Importance of pressure solution and coble creep in the deformation of polymineralic rocks, *J. Geophys. Res.* **97**, 4579-4586 (1992).

White, A.J.R. and Chappell, B.W., Ultrametamorphism and granitiod genesis, *Tectonophysics* **43**, 7-22 (1977).

White, A.J.R. and Chappell, B.W., Per magma ad migma downunder, *Geol. J.* **25**, 221-225 (1990).

Whitney, J.A., The origin of granite: The role and source of water in the evolution of granitic magmas, *Geol. Soc. Am. Bull.* **100**, 1886-1897, (1988).

Wickham, S.M., Crustal anatexis and granite petrogenesis during low pressure regional metamorphism: the Trois Siegneurs Massif, Pyrenees, France, *J. Petrol.* **28**, 127-169 (1987a).

Wickham, S.M., The segregation and emplacement of granitic magmas, *J. Geol. Soc. Lon.* **144**, 281-297 (1987b).

Wiggins, C. and Spiegelman, M., Magma migration and magmatic solitary waves in 3-D, *Geophys. Res. Lett.* **22**, 1289-1292 (1995).

Wilson, M., *Igneous Petrogenesis* (2nd Edn), pp. 466, HarperCollins, London (1989).

Wolf, M.B. and Wyllie, P.J., Dehydration melting of solid amphibolite at 10kbar: Textural development, liquid interconnectivity and applications to the segregation of magmas, *Mineral. Petrol.* **44**, 151-179 (1991).

Wolf, M.B. and Wyllie, P.J., Dehydration melting of amphibolite at 10kbar: The effects of temperature and time, *Contrib. Mineral. Petrol.* **115**, 369-383 (1994).

Wolf, M.B. and Wyllie, P.J., Liquid segregation parameters from amphibolite dehydration melting experiments, *J. Geophys. Res.* **100**, 15,611-15,621 (1995).

Wyllie, P.J., Crustal Anatexis: An Experimental Review, *Tectonophysics* **43**, 41-47 (1977).

Yardley, B.W.D., MacKenzie, W.S. and Guildford, C., *Atlas of metamorphic rocks and their textures* (1st Edn), pp. 120, Longman, Harlow, U.K. (1990).

Yoder, H.S., Heat transfer during partial melting: an experimental study of a simple binary silicate system, *J. Volc. Geotherm. Res.* **43**, 1-36 (1990).

Zen, E., Thermal modelling of stepwise anatexis in a thrust thickened sialic crust, *Trans. R. Soc. Edin. Earth Sci.* **79**, 223-235 (1988).

Zen, E., Crustal magma generation and low-pressure high-temperature regional metamorphism in an extensional environment; possible application to the Lachlan Belt, Australia, *Am. J. Sci.* **295**, 851-874 (1995).

Zhang, S., Paterson, M.S. and Cox, S.F., Porosity and permeability evolution during hot isostatic pressing of calcite aggregates, *J. Geophys. Res.* **99**, 15741-15760 (1994).

Zingg, A., The Ivrea crustal cross-section (northern Italy and southern Switzerland). In *Exposed Cross Sections of the Continental Crust,* (edited by M.H. Salisbury and D.M. Fountain), Kluwer, Dordrecht, The Netherlands (1990).

Appendix A: Numerical Methods.

This appendix describes, and discusses, the numerical methods used to solve the governing conservation equations presented in chapters 3, 4, and 5.

A.1 Numerical methods: chapter 3

The coupled, dimensionless, 1-D equations governing the model presented in chapter 3 are

$$\frac{\partial\theta}{\partial t}=\kappa_{\mathrm{eff}}\frac{\partial^2\theta}{\partial z^2}-\mathrm{Ste}\left(w_l+w_s\right)\frac{\partial\theta}{\partial z} \tag{A.1}$$

$$\frac{\partial\phi}{\partial t}=\frac{1}{\varphi}\frac{\partial}{\partial z}\left((1-\varphi\phi)w_s\right)+\frac{\partial\theta}{\partial t}+\left(w_l+w_s\right)\frac{\partial\theta}{\partial z} \tag{A.2}$$

$$\frac{\partial^2 w_s}{\partial z^2}=\frac{w_s}{\phi^n}+\frac{(1-\varphi\phi)}{(1-\varphi)} \tag{A.3}$$

$$\varphi\phi w_l=-(1-\varphi\phi)w_s \tag{A.4}$$

subject to the initial and boundary conditions

$$\theta(z,0)=\phi(z,0)=w_s(z,0)=0 \tag{A.5a}$$

$$\theta(0,t)=1 \qquad \theta(z_0,t)=0 \tag{A.5b}$$

$$w_s(0,t)=w_l(0,t)=w_s(z_0,t)=w_l(z_0,t)=0. \tag{A.5c}$$

(see table A.1 for a reminder of the nomenclature). Equations (A.1) and (A.2) define an initial value or Cauchy problem, and describe the propagation of θ and ϕ through time; equation (A.3) defines a boundary value problem for w_s. They were solved using suitable explicit finite difference approximations.

A.1.1 Finite difference approximations of the governing equations

The heat conservation equation (A.1) was approximated using a forward-time-centred-space (FTCS) difference scheme, with upstream differencing on the pseudo-advection term for the case $|w_l| > |w_s|$, and downstream differencing on the pseudo-advection term for the case $|w_s| > |w_l|$ (Siemieniuch and Gladwell, 1978; Morton and Mayers, 1994). This scheme is first order accurate in time, second order accurate in space for the diffusive term, and first order accurate in space for the advective term, and yields the explicit difference scheme for propagating θ through time[1]

$$\begin{aligned}\theta_k^{j+1}&=\theta_k^j+\kappa_{\mathrm{eff}}\frac{\theta_{k+1}^j+\theta_{k-1}^j-2\theta_k^j}{\Delta z^2}\Delta t-\mathrm{Ste}\left([w_s]_k^j+[w_l]_k^j\right)\frac{\theta_k^j-\theta_{k-1}^j}{\Delta z}\Delta t, && |w_l|>|w_s|\\ \theta_k^{j+1}&=\theta_k^j+\kappa_{\mathrm{eff}}\frac{\theta_{k+1}^j+\theta_{k-1}^j-2\theta_k^j}{\Delta z^2}\Delta t-\mathrm{Ste}\left([w_s]_k^j+[w_l]_k^j\right)\frac{\theta_{k+1}^j-\theta_k^j}{\Delta z}\Delta t, && |w_s|>|w_l|\end{aligned} \tag{A.6}$$

---

[1] Where there may be ambiguity between variables, subscripts, and the finite difference notation, variables and subscripts are enclosed within square brackets [ ].

Symbol	Description
A	amplitude of porosity wave
A_o	initial amplitude of porosity wave, obtained using the analytic solution
A_{error}	normalised difference between the initial and propagated amplitudes
c	phase velocity of porosity wave
c_o	initial phase velocity of porosity wave, obtained using the analytic solution
c_{error}	normalised difference between the initial and propagated phase velocities
C	compaction rate
E_i	normalised difference between the positions of the *i*th isotherm
n	porosity exponent
Ste	Stefan number
t	time
t_{seg}	segregation time
t^{z}_{diff}	normalised difference between segregation times obtained with Δz and $\Delta z/2$
t^{t}_{diff}	normalised difference between segregation times obtained with Δt and $\Delta t/2$
w_l	liquid velocity
w_m	melt velocity
w_s	solid velocity
z	vertical Cartesian coordinate
z_i	position of the ith isotherm
χ	ratio of thermal diffusivities in the partially molten and solid rock
ϕ	porosity
ϕ_c	percolation threshold
φ	temperature (fraction of equilibrium melting) at $z = 0$
κ_{eff}	effective thermal diffusivity
θ	temperature (fraction of equilibrium melting)
θ_{error}	normalised difference between analytic and numerical solutions (equation (A.19))
θ_{seg}	segregation temperature
θ^{z}_{diff}	normalised difference between segregation temperatures obtained with Δz and $\Delta z/2$
θ^{t}_{diff}	normalised difference between segregation temperatures obtained with Δt and $\Delta t/2$
ψ_{geo}	dimensionless initial geothermal gradient
Finite difference notation	
j	temporal node
k	spatial node
Δt	temporal node spacing
Δz	spatial node spacing

Table A.1. Nomenclature for Appendix A. Note that all quantities are dimensionless.

The upstream/downstream difference scheme used for the advective term has the advantage of removing any limit on the size of the spatial node spacing (Δz) required to achieve stability (Siemieniuch and Gladwell, 1978), and overall the scheme is still 'effectively second order' accurate in space (Price *et al.*, 1966). Stability of the numerical solutions is predicted if the local time step (Δt) is restricted by (Morton and Mayers, 1994)

$$\Delta t \le \frac{\Delta z^2}{2|\kappa_{\mathrm{eff}}| + \Delta z|\mathrm{Ste}(w_l + w_s)|} \tag{A.7}$$

The mass conservation equation (A.2) was approximated using a staggered-leapfrog scheme. This scheme is second order accurate in both time and space (Morton and Mayers, 1994), and yields the explicit difference scheme for propagating ϕ through time

$$\begin{aligned}\phi_k^{j+1} = \phi_k^{j-1} + \frac{\left(\left(1-\varphi\phi_{k+1}^{j}\right)[w_s]_{k+1}^{j}\right) - \left(\left(1-\varphi\phi_{k-1}^{j}\right)[w_s]_{k-1}^{j}\right)}{\Delta z}\Delta t +& \\ \left([w_l]_k^j + [w_s]_k^j\right)\frac{\theta_{k+1}^j - \theta_{k-1}^j}{\Delta z}\Delta t + 2\left(\theta_k^{j+1} - \theta_k^j\right)&\end{aligned} \tag{A.8}$$

The staggered-leapfrog scheme, if correctly implemented, has the advantage of introducing no numerical diffusion (Press *et al.*, 1992). Stability of the numerical solutions is predicted if the local time step Δt is restricted by the Courant-Friedrichs-Lewy (CFL) condition

$$\frac{|v|\Delta t}{\Delta z} \le 1 \tag{A.9}$$

where v is the maximum velocity at which information is locally propagated between spatial nodes (Mitchell and Griffiths, 1980; Press *et al.*, 1992; Morton and Mayers, 1994).

The momentum conservation equation (A.3) was approximated using a centred scheme, which is second order accurate in space

$$\frac{[w_s]_{k+1}^j + [w_s]_{k-1}^j - 2[w_s]_k^j}{\Delta z^2} = \frac{[w_s]_k^j}{[\phi^n]_k^j} + \frac{\left(1-\varphi\phi_k^j\right)}{(1-\varphi)} \tag{A.10}$$

Re-arranging equation (A.10) yields a tridiagonal system of coupled linear equations of the form

$$a_k^j[w_s]_{k-1}^j - b_k^j[w_s]_k^j + c_k^j[w_s]_{k+1}^j = d_k^j \tag{A.11}$$

with

$$a_k^j = \frac{[\phi^3]_k^j}{\Delta z^2} = c_k^j \tag{A.12a}$$

$$b_k^j = \left(\frac{2[\phi^3]_k^j}{\Delta z^2} + 1\right) \tag{A.12b}$$

$$d_k^j = \frac{[\phi^3]_k^j\left(1-\varphi\phi_k^j\right)}{1-\varphi} \tag{A.12c}$$

A.1.2 Method of solution

Given the initial values of θ, ϕ and w_s prescribed by condition (A.5a), the explicit difference equations were solved sequentially (figure A.1). The temperature θ was propagated through one time increment using equation (A.6); the porosity ϕ was then updated using equation (A.8). In order to solve for the matrix velocity w_s, the conditions at both the upper ($z=z_0$) and lower ($z=0$) boundaries are required; the position z_0 of the upper boundary was located at the spatial node k at which $\theta = 0$, and which was also closest to the origin. Finally, the tridiagonal system of coupled linear equations (A.10) was solved for w_s, subject to the boundary conditions (A.5c), by matrix inversion (Press *et al.*, 1992). These steps were repeated for each time increment j until the solutions had been propagated to the required time, using a FORTRAN code executed on a Sun SPARC 5 workstation. Maximum run times were several hours, when investigating systems governed by large values of κ_{eff}.

A.1.3 Accuracy of the numerical solutions

Unless numerical approximations are carefully selected and implemented, the numerical solutions obtained may be inaccurate because of errors introduced and propagated by the approximations. The suitability of a particular numerical scheme, and the likely source of error, depends upon the nature of the equation to be solved. The heat conservation equation (A.1) is a special case of the general 1-D parabolic diffusion-advection equation

$$\frac{\partial u}{\partial t} = a(z)\frac{\partial^2 u}{\partial z^2} + b(z)\frac{\partial u}{\partial z} \qquad \text{(A.13)}$$

Numerical solutions of parabolic diffusion-advection equations can be susceptible to transport errors introduced by the advective term (Siemieniuch and Gladwell, 1978; Press *et al.*, 1992). The mass conservation equation (A.2) is a special case of the general 1-D hyperbolic flux-conservative equation

$$\frac{\partial u}{\partial t} = \frac{\partial}{\partial z} f(u) \qquad \text{(A.14)}$$

where the conserved flux is given by

$$f(\phi) = (1 - \varphi\phi)w_s \qquad \text{(A.15)}$$

and w_s is obtained from the momentum conservation equation (A.3). Numerical solutions of hyperbolic equations can be susceptible to amplitude and phase dissipation due to numerical diffusion (Press *et al.*, 1992; Morton and Mayers, 1994). To ensure accuracy of the numerical solutions obtained for the full set of governing equations (A.1)-(A.4), the numerical schemes used to approximate the parabolic and hyperbolic conservation equations were tested separately for accuracy. Using the insight gained from the individual numerical tests, suitable criterion were deduced to ensure stability and accuracy of the full solutions.

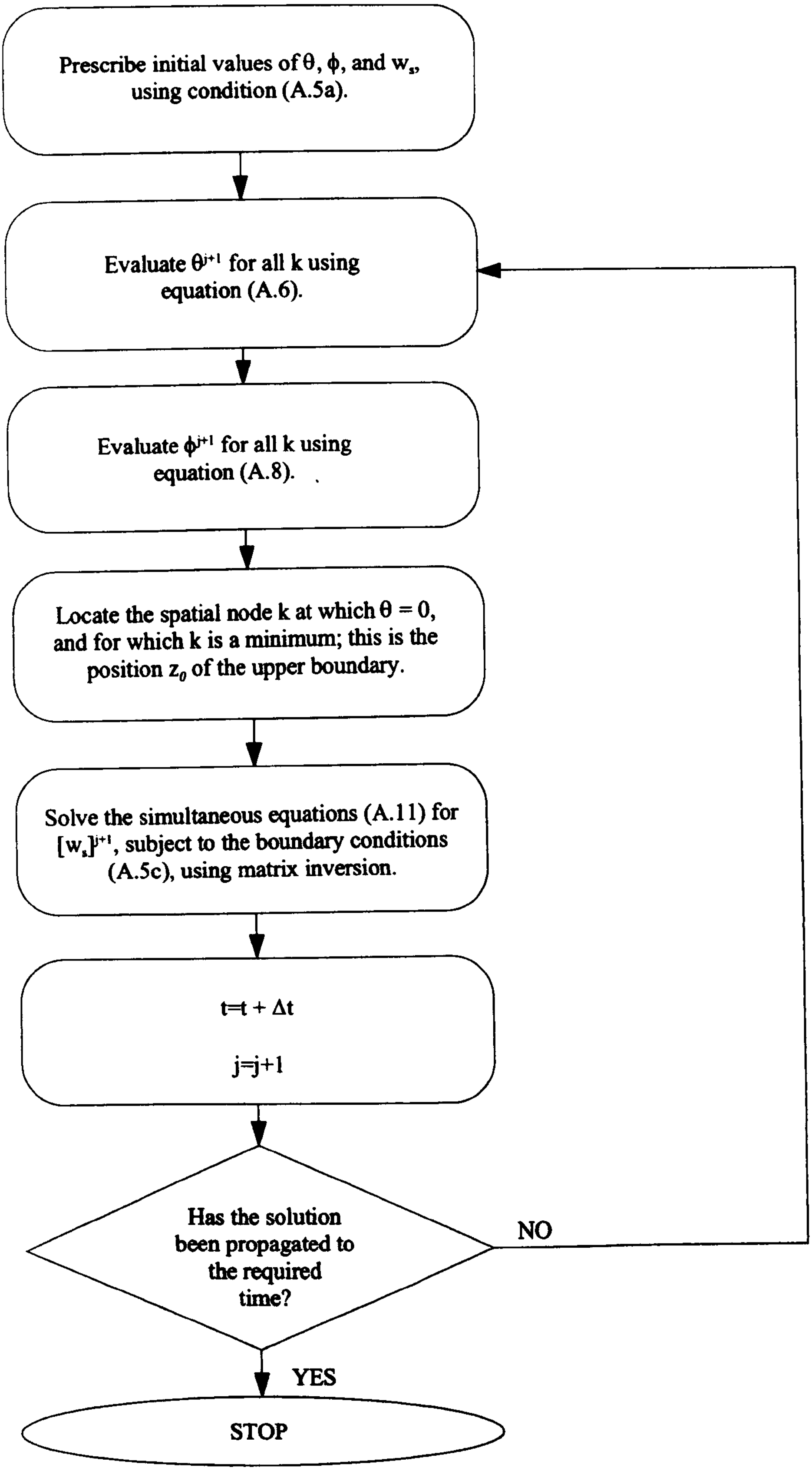

Figure A.1. Flow chart showing the order in which the numerical approximations of the governing equations presented in chapter 3 were evaluated.

A.1.3.1 Heat conservation

Accuracy of the numerical scheme used to approximate the parabolic heat conservation equation (A.1) was investigated using a published analytic approximation to the solution, for the case

$$\kappa_{eff} = 1, \qquad \text{(A.16a)}$$

$$Ste(w_l + w_s) = \lambda, \qquad \text{(A.16b)}$$

where λ is a constant. The approximate analytic solution is given by (Siemieniuch and Gladwell, 1978)[2]

$$\begin{aligned}\theta_{ana}(z,t) = \tfrac{1}{2}\Big\{&\operatorname{erfc}\Big((z-\lambda t)/2\sqrt{t}\Big)+\operatorname{erfc}\Big((z+\lambda t)/2\sqrt{t}\Big)\Big\}\\ &+\exp(-\lambda)\Big\{\Big(1+\tfrac{1}{2}\lambda(2-z+\lambda t)\Big)\operatorname{erfc}\Big((2-z+\lambda t)/2\sqrt{t}\Big)-\lambda\sqrt{(t/\pi)}\exp\Big(-(2-z-\lambda t)^2/4t\Big)\Big\}\end{aligned} \qquad \text{(A.17)}$$

subject to the initial and boundary conditions

$$\theta(z,0) = 0, \qquad 0 < z < 1, \qquad \text{(A.18a)}$$

$$\theta(0,t) = 1, \qquad t > 0, \qquad \text{(A.18b)}$$

$$\frac{\partial\theta}{\partial z}(1,t) = 0, \qquad t > 0 \qquad \text{(A.18c)}$$

(figure A.2). The accuracy with which the FTCS with downstream differencing scheme reproduced the analytic solution was investigated by recording the difference between numerical ($\theta_{num}(z,t)$) and analytic ($\theta_{ana}(z,t)$) solutions, normalised to the analytic solution

$$\theta_{error}(z,t) = \big(\theta_{num}(z,t) - \theta_{ana}(z,t)\big)/\theta_{ana}(z,t) \qquad \text{(A.19)}$$

The normalised difference was recorded as a function of dimensionless time, at three spatial locations z = 0.25, 0.5 and 0.75. Defined in this way, a positive error indicates that the numerical solution is overestimating the analytic solution, and *vice-versa.*

Figure A.3 shows the effect of varying Δz on the accuracy of the numerical solutions, as a function of time, for $\lambda = 1$ and 10. The value of Δt used is constant, and is given by

$$\Delta t = \frac{\Delta z^2}{1.1(2+\lambda\Delta z)} \qquad \text{(A.20)}$$

which is equivalent to equation (A.7), with $\kappa_{eff} = 1$, $Ste(w_l + w_s) = \lambda$, and an *extra* factor of 1.1 in the denominator which is required to ensure stability of the numerical solutions (see following paragraph). In all cases, the error between the numerical and analytic solutions decreases as the solutions are propagated through time; with the exception of the cases $\lambda = 10$ and $z = 0.5$ and 0.75, the decrease is monotonic. The maximum error at $t = 0.5$ is <0.5% (figure A.3(e)). The effect of reducing Δz from 1/100 to 1/400 is always to reduce the magnitude of the error; at $t = 0.5$, the most significant reduction is by <0.25% (figure A.3(e)).

---

[2] The solution presented by Siemieniuch and Gladwell (1978) contains a typographic error, which was eliminated by obtaining the University of Manchester report in which the solution was originally presented (Siemieniuch and Gladwell, 1976).

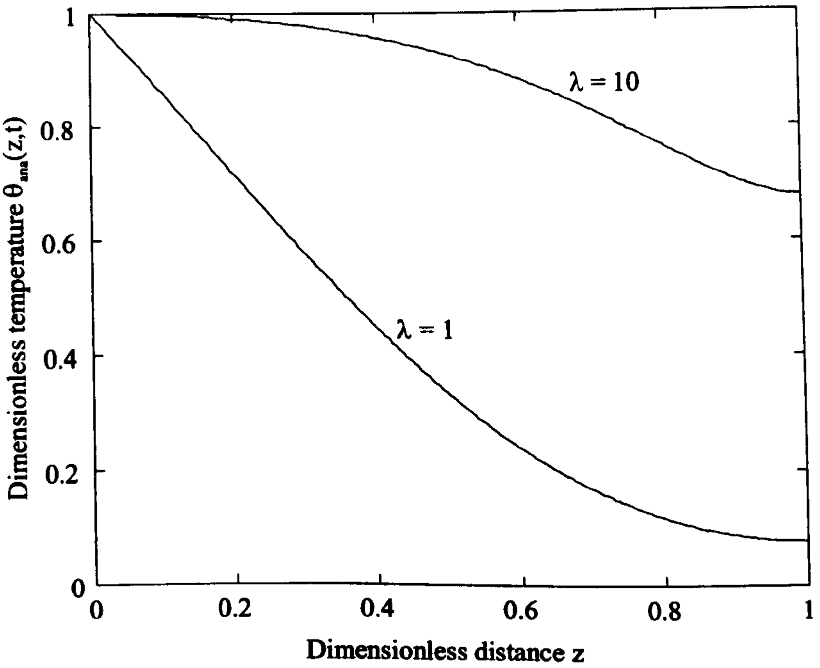

Figure A.2. Approximate analytic solutions to the parabolic heat conservation equation (A.1), obtained using equation (A.17), for the case $\kappa_{eff} = 1$, $Ste(w_l + w_s) = \lambda$. The solutions shown are for $\lambda = 1$ and $\lambda = 10$, after 0.1 time units.

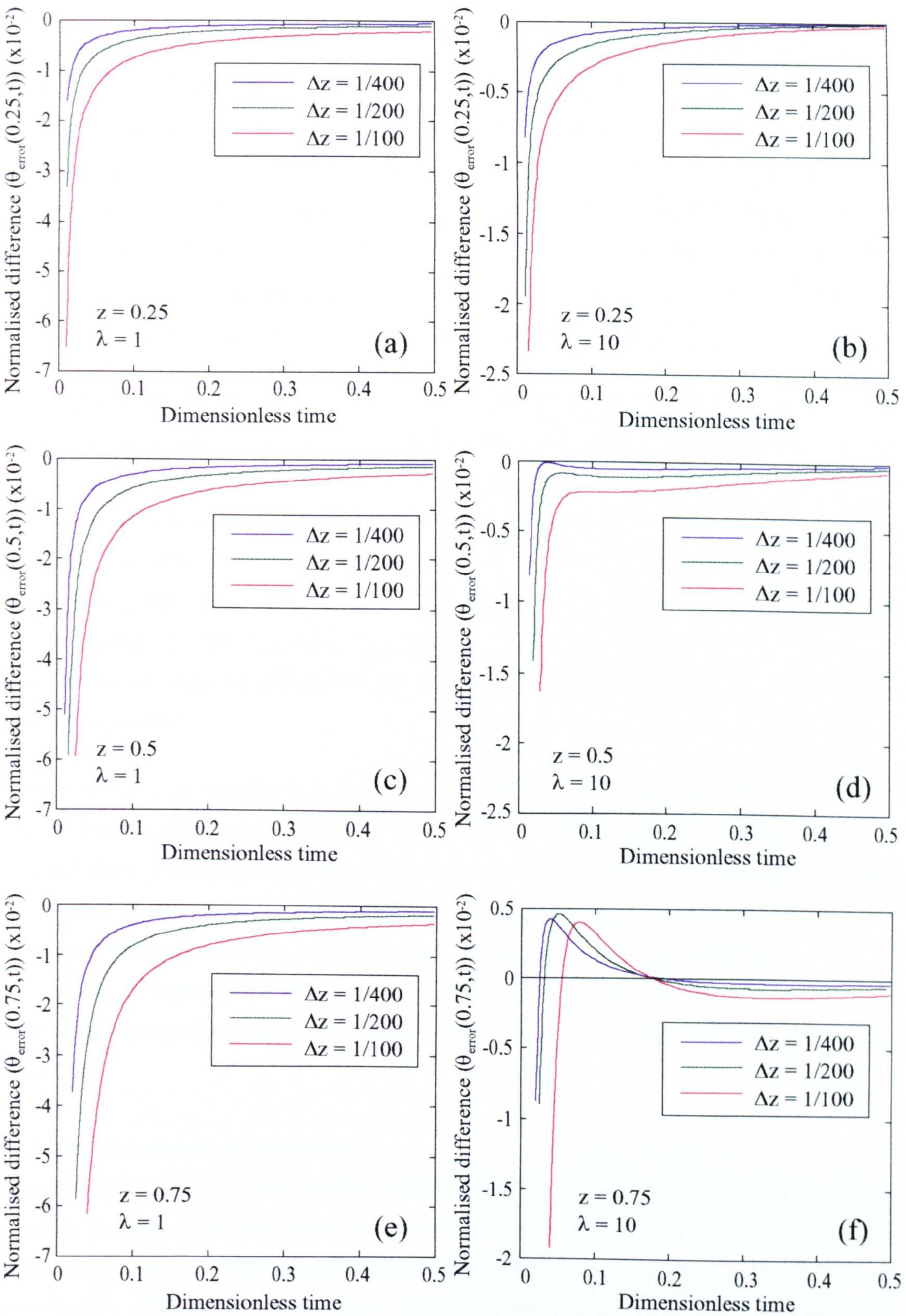

Figure A.3. Effect of varying Δz on the accuracy of the FTCS with downstream differencing scheme when used to approximate the parabolic heat equation (A.1) with $\kappa_{eff} = 1$ and $Ste(w_l + w_s) = \lambda$. Plots show the normalised difference between numerical and analytic solutions $(\theta_{num}(z,t)-\theta_{ana}(z,t))/\theta_{ana}(z,t)$ against dimensionless time for solutions with $\lambda = 1$ and 10, and values of $\Delta z = 1/100$, 1/200 and 1/400. Note that ordinate axis scales vary between left and right hand plots. In all cases, $\Delta t = \Delta z^2/1.1(2+\lambda\Delta z)$.

Figure A.4 shows the effect of varying Δt on the stability and accuracy of the numerical solutions. Plot A.4(a) shows the importance of the factor of 1.1 in the denominator of equation (A.20) on the *stability* of the solutions, for the case $z = 0.25$, $\Delta z = 1/50$, and $\lambda = 10$. Without the factor the solutions are unstable; with the factor the solutions are stable. The factor of 1.1 is the smallest for which the numerical solutions are stable. The large value of $\Delta z = 1/50$ ensures that the instabilities in the solution may be clearly observed. Plots A.4(b) and (c) show the effect of halving Δt on the *accuracy* of the numerical solutions, for the cases $z = 0.25$, $\Delta z = 1/200$, and $\lambda = 1$ and 10. The effect of halving Δt is negligible; the error at $t = 0.5$ is reduced by <0.005% in both cases.

The error between the numerical and analytic solutions shown in figures A.3 and A.4 decreases as the solutions are propagated through time, because the numerical solution initially lags, or underestimates, the analytic solution; as the solutions are propagated they converge. The timescale over which the solutions are investigated ($t = 0.5$) is restricted because the lengthscale of the system is fixed at 1; at large times ($t > 0.5$) the temperature θ tends to 1 for all values of z, and the solutions break down. The full system of equations is propagated for significantly larger times ($t > 10$) than those investigated here (see the results in §3.3.2). The small errors found at $t = 0.5$, and the convergence of the solutions, indicates that at large times the errors introduced by the numerical scheme are negligible.

The results of these numerical tests indicate that the FTCS with upstream/downstream differencing scheme accurately reproduces analytic solutions of the parabolic heat conservation equation (A.1) with $\kappa_{eff} = 1$ and $Ste(w_l + w_s) = \lambda$, when a spatial node spacing of $\Delta z = 1/200$ is used, and Δt is evaluated using equation (A.20), which is equivalent to equation (A.7) with an extra factor of 1.1 in the denominator. Using these values, halving Δz improves the accuracy of the solutions at $t = 0.5$ by <0.1%; halving Δt improves the accuracy of the solutions at $t = 0.5$ by <0.005%. Maximum errors introduced by the numerical scheme at $t = 0.5$ are <0.2%, and have a negligible effect on the accuracy of the solutions.

A.1.3.2 Mass and momentum conservation

Accuracy of the numerical scheme used to approximate the hyperbolic system of coupled mass and momentum equations (A.2) and (A.3), was investigated using a published analytic solution to the equations for the case of a solitary porosity wave propagating with constant amplitude A, and constant phase velocity c. The solution is valid in the absence of phase change, for the case $n = 3$ and in the limit $\varphi << 1$, and may be expressed as (Richter and McKenzie, 1984; Barcilon and Richter, 1986)[3]

---

[3] The solution presented by Barcilon and Richter (1986) is expressed in terms of A rather than φc, and was used here to eliminate typographic errors in the solution presented by Richter and McKenzie (1984). The solution presented by B & R also contains a typographic error; the $(A + 1/2)$ term should read $(A + 1/2)^{1/2}$.

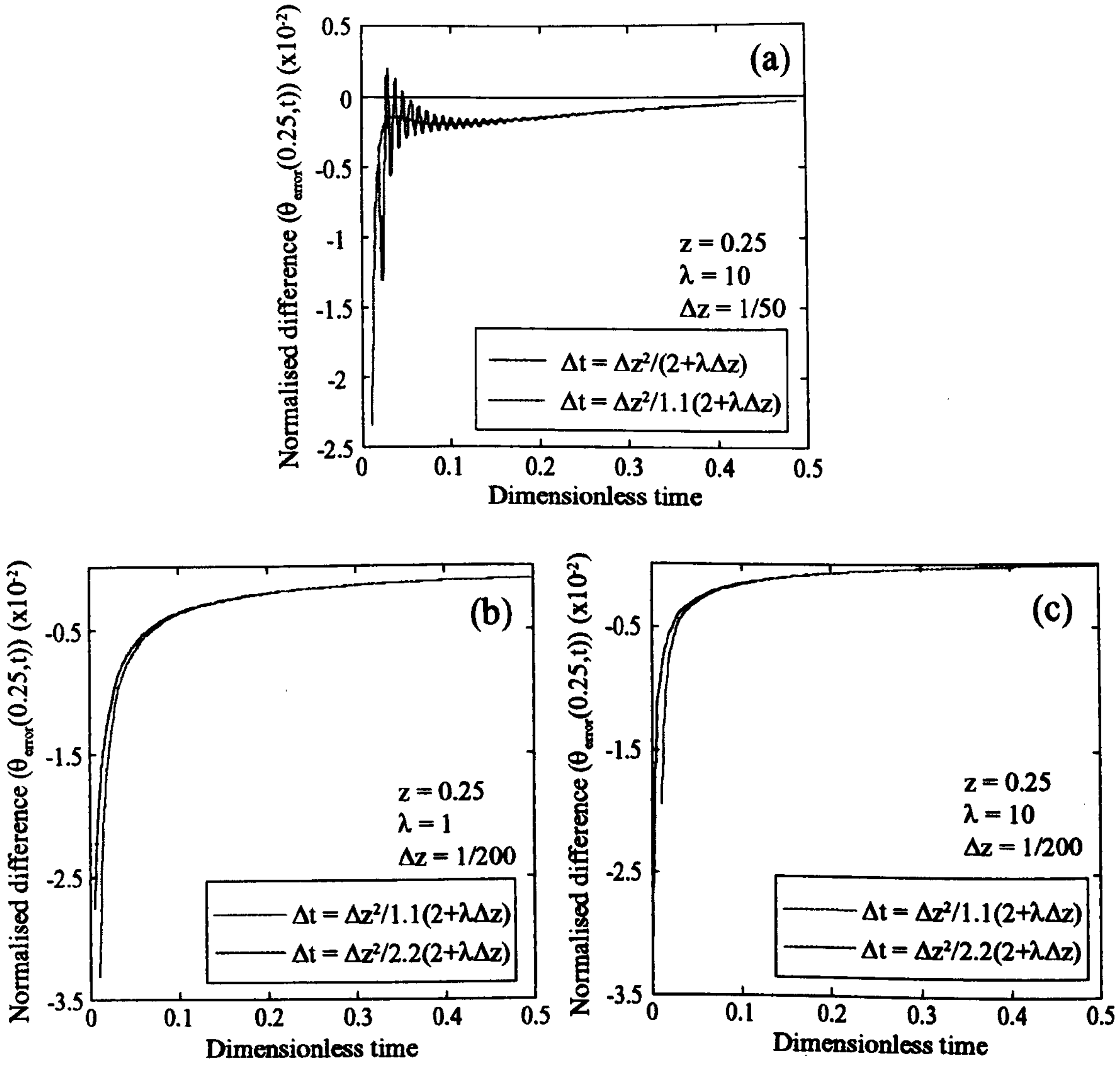

Figure A.4. Effect of varying Δt on the stability and accuracy of the FTCS with upstream differencing scheme when used to approximate the parabolic heat equation (A.1) with $\kappa_{eff} = 1$ and $Ste(w_l + w_s) = \lambda$. Plots show the normalised difference between numerical and analytic solutions $(\theta_{num}(z,t)-\theta_{ana}(z,t))/\theta_{ana}(z,t)$ against dimensionless time for solutions with $\lambda = 1$ and 10. Plot (a) shows the effect of reducing Δt on the stability of the numerical solutions. If $\Delta t < \Delta z^2/(2+\lambda\Delta z)$ then the solutions are stable; if $\Delta t = \Delta z^2/(2+\lambda\Delta z)$ then the solutions are unstable. The large value of $\Delta z = 1/50$ ensures that the instabilities may be clearly observed. Plots (b) and (c) show the effect of halving Δt on the accuracy of the numerical solutions. In both cases $\Delta z = 1/200$.

$$z-ct=\pm\sqrt{\frac{\varphi c}{z}}\left[-2\sqrt{\frac{\varphi c-1}{2}-\phi}+\sqrt{\frac{2}{\varphi c-3}}.\ln\left(\frac{\sqrt{\frac{\varphi c-3}{2}}-\sqrt{\frac{\varphi c-1}{2}-\phi}}{\sqrt{\frac{\varphi c-3}{2}}+\sqrt{\frac{\varphi c-1}{2}-\phi}}\right)\right] \tag{A.21}$$

with

$$A=(\varphi c-1)/2 \tag{A.22}$$

Equation (A.21) was used to provide an initial solitary wave with amplitude A_o and phase velocity c_o, which was then propagated numerically using the staggered-leapfrog scheme, subject to the boundary conditions

$$\phi(z,t)\rightarrow 1, \qquad z\rightarrow\pm\infty \tag{A.23a}$$

$$w_s(z,t)\rightarrow -1, \tag{A.23b}$$

(figure A.5). For the scheme to be accurate, the initial waveform described by equation (A.21) must be propagated with constant amplitude and phase velocity. The accuracy with which the numerical solution maintained constant amplitude was investigated by recording the difference between the propagated amplitude A(t) and the initial amplitude A_o, normalised to the initial value, as a function of dimensionless time

$$A_{error}(t)=\left(A(t)-A_o\right)/A_o \tag{A.24}$$

Likewise, the accuracy with which the numerical solution maintained constant phase velocity was investigated by recording the difference between the propagated phase velocity c(t) and the initial phase velocity c_o, normalised to the initial value, as a function of dimensionless time

$$c_{error}(t)=\left(c(t)-c_o\right)/c_o \tag{A.25}$$

Defined in this way, a positive error represents spurious growth in the amplitude and phase velocity of the propagated wave; a negative error represents spurious amplitude dissipation and phase lag.

Figure A.6(i) shows the effect of varying Δz on the accuracy of the amplitude of the numerically propagated wave, for a variety of values of φ and A_o. The value of Δt used is given by the CFL condition ($\Delta t = \Delta z/c_o$). In all cases, some amplitude dissipation is observed, with a maximum error of ~5% (figure A.6(i)(e)), and a minimum error of ~0.1% (figure A.6(i)(b)). For all values of Δz and A_o, the error is reduced by approximately one order of magnitude when the value of φ used in the numerical solution is reduced by one order of magnitude, a result which is clear when plots A6(i)(a), (c), and (e) are compared with plots A6(i)(b), (d) and (f). The effect of reducing Δz from 1/2 to 1/8 is predominantly to reduce the oscillations in the error; the mean error in each plot is reduced by <0.5%. Increasing A_o leads to an increase in the error, by an order of magnitude in the largest case (compare figures A6(a) & (e)). In all cases, once the numerical solution is established, the magnitude of the mean error subsequently remains constant.

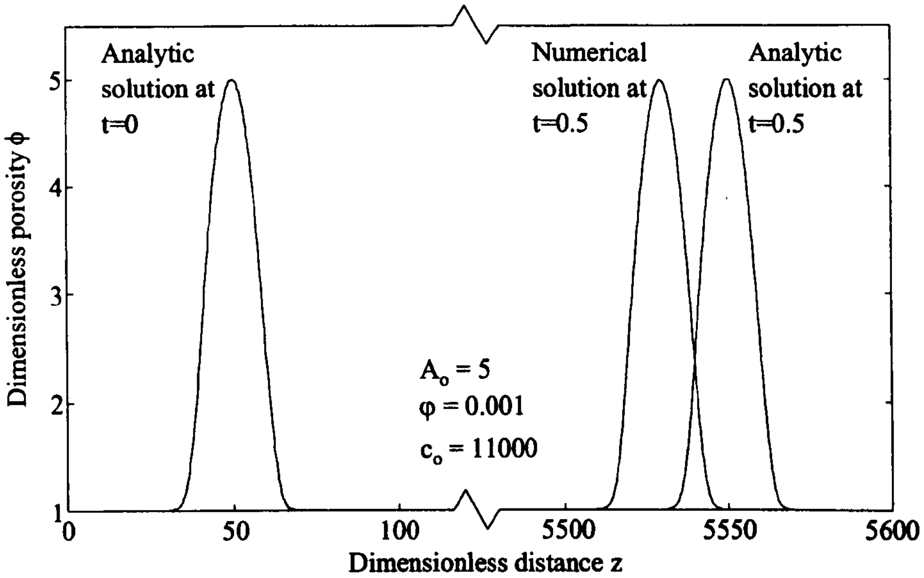

Figure A.5. Examples of the analytic solution for a solitary porosity wave propagating with constant amplitude A_0 and phase velocity c_0, at t=0 and t=0.5. The numerical solution at t=0.5 is shown for comparison. Note the truncated abscissa scale, which was employed in order to show the shape of the porosity wave at t=0 and t=0.5. $A_0 = 5$, $\varphi = 0.001$, and from equation (A.22), $c_0 = 11000$.

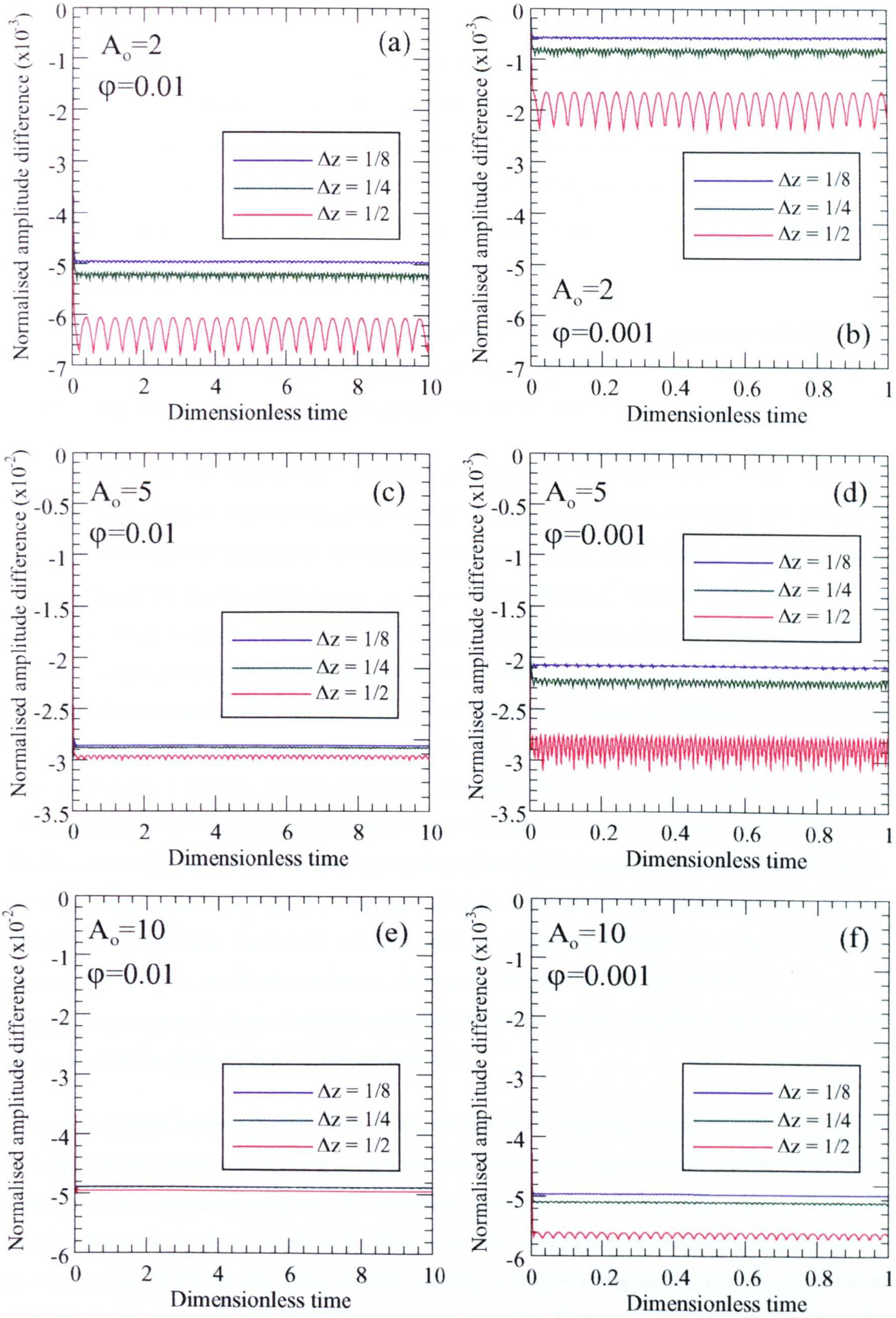

Figure A.6(i). Effect of varying Δz on the accuracy of the staggered-leapfrog differencing scheme when used to propagate the initial analytic solution for a solitary porosity wave. Plots show the normalised difference in amplitude $(A(t)-A_o)/A_o$ against dimensionless time for solitary waves with A_o=2, 5, and 10, and for values of Δz = 0.5, 0.25, and 0.125. Abscissa axis scales vary by one order of magnitude between left and right hand plots; ordinate axis scales differ by one order of magnitude between left and right hand plots, with the exception of (a) and (b). In all cases, $\Delta t = \Delta z/c_o$.

Figure A.6(ii) shows the effect of varying Δz on the accuracy of the phase velocity of the numerically propagated wave, for the same values of φ, A_o and Δt. Some phase lag is observed, with a maximum error of ~9% (figure A.6(ii)(e)), and a minimum error of ~0.3% (figure A.6(ii)(b)). The effects of varying φ, Δz and A_o are similar to those observed in figure (A.6(i)); the exception is that reducing Δz from 1/2 to 1/8 leads to an *increase* in the mean error, although by <1% even for the largest case (figure A.6(ii)(e) and (f)).

Figure A.7 shows the effect of halving Δt on the accuracy of amplitude and phase propagation. The results are for $\Delta z = 1/8$, $A_o = 2$, and the values of φ used in figure A.6. The effect of halving Δt is negligible; both the amplitude and phase errors are reduced by <0.01% in all cases.

For the values of Δz and A_o used, the size of both the amplitude and phase error is most effectively reduced by decreasing φ, which indicates that the errors are predominantly due to the use of a finite value of φ in the numerical solutions, rather than the infinitesimally small value ($\varphi << 1$) assumed in the derivation of the analytic solution (A.21). The *constant* nature of both the mean amplitude and phase errors as the solution is propagated through time therefore indicates that the staggered-leapfrog scheme is being accurately implemented; when the CFL condition is met, the scheme introduces no numerical diffusion, and so no amplitude or phase dissipation is expected (Mitchell and Griffiths, 1980; Press *et al.*, 1992; Morton and Mayers, 1994). The oscillations in the errors are interpreted to be due to the finite mesh size, and the method of calculating the errors. As the numerical solution is propagated, the position of the amplitude maximum is located at the nearest spatial node k; the phase velocity is then calculated by evaluating the number of nodes traversed by the amplitude maximum. For large spatial node spacings (Δz), the nearest node does not always accurately represent the position of the amplitude maximum. At each node, the numerical amplitude maximum leads and then lags the analytic amplitude maximum, causing oscillations in the calculated error. As Δz is reduced, the nearest node more accurately represents the position of the amplitude maximum, and the amplitude of the oscillations in the error is reduced.

The results of these numerical tests indicate that the staggered-leapfrog scheme accurately maintains the amplitude and phase velocity of a solitary porosity wave when a spatial node spacing of $\Delta z = 1/4$ is used, and Δt is evaluated using the CFL condition (equation A.9). Using these values, halving Δz improves the accuracy of the solutions by <0.01% for the amplitude, while reducing the accuracy of the solutions by <0.1% for the phase velocity; halving Δt improves the accuracy of the solutions by <0.005% for the amplitude and <0.01% for the phase velocity. Maximum errors for the smaller value of φ are <0.6% for the amplitude, and <0.8% for the phase velocity; these errors are predominantly due to the finite value of φ used in the numerical solutions, and have a negligible effect on the accuracy of the solutions.

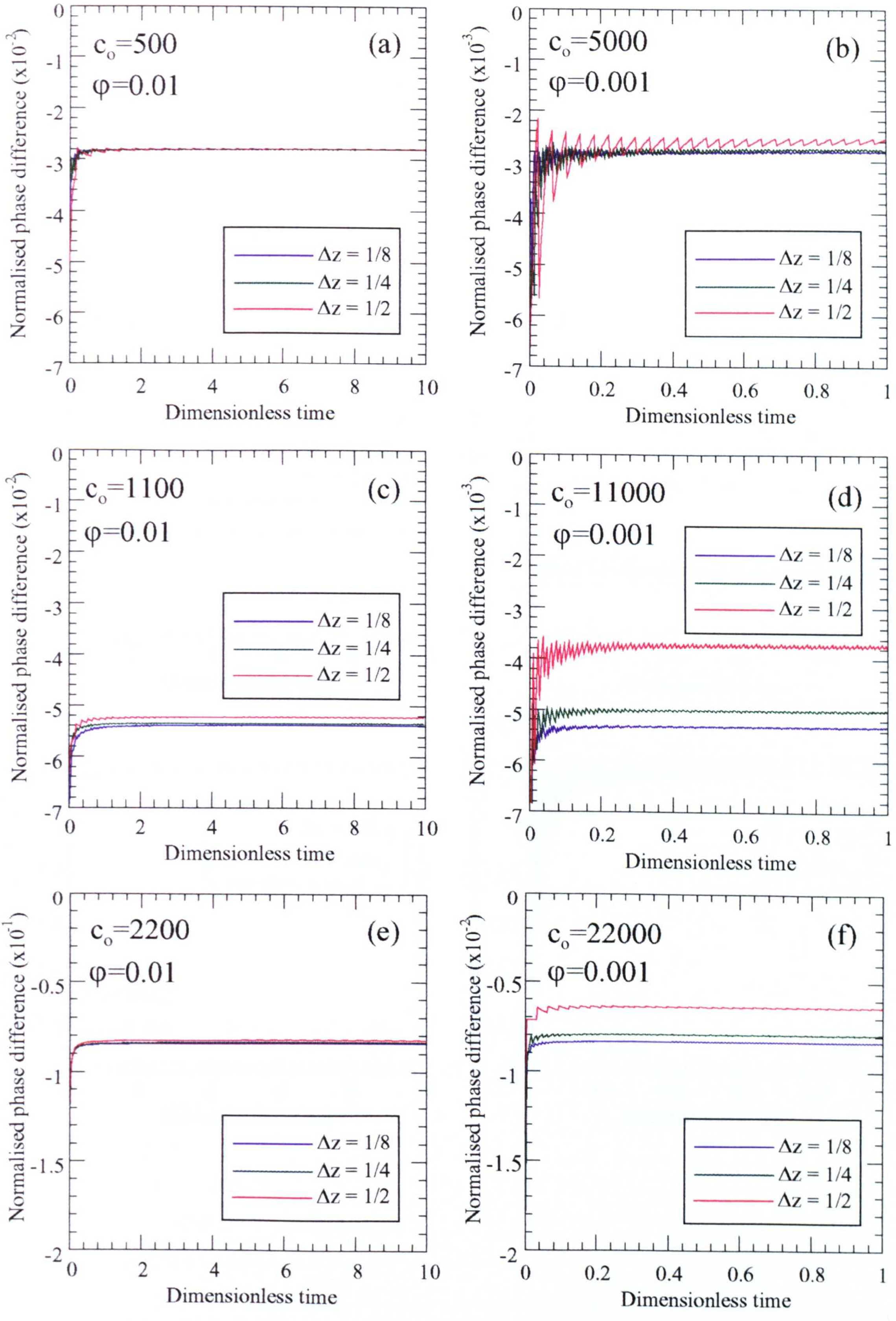

Figure A.6(ii). Effect of varying Δz on the accuracy of the staggered-leapfrog differencing scheme when used to propagate the initial analytic solution for a solitary porosity wave. Plots show the normalised difference in phase velocity $(c(t)-c_o)/c_o$ against dimensionless time for solitary waves with c_o=500, 1100, 2200, 5000, 11000 and 22000, and for values of $\Delta z = 0.5$, 0.25, and 0.125. Both ordinate and abcissa axis scales vary by one order of magnitude between left and right hand plots. In all cases, $\Delta t = \Delta z/c_o$.

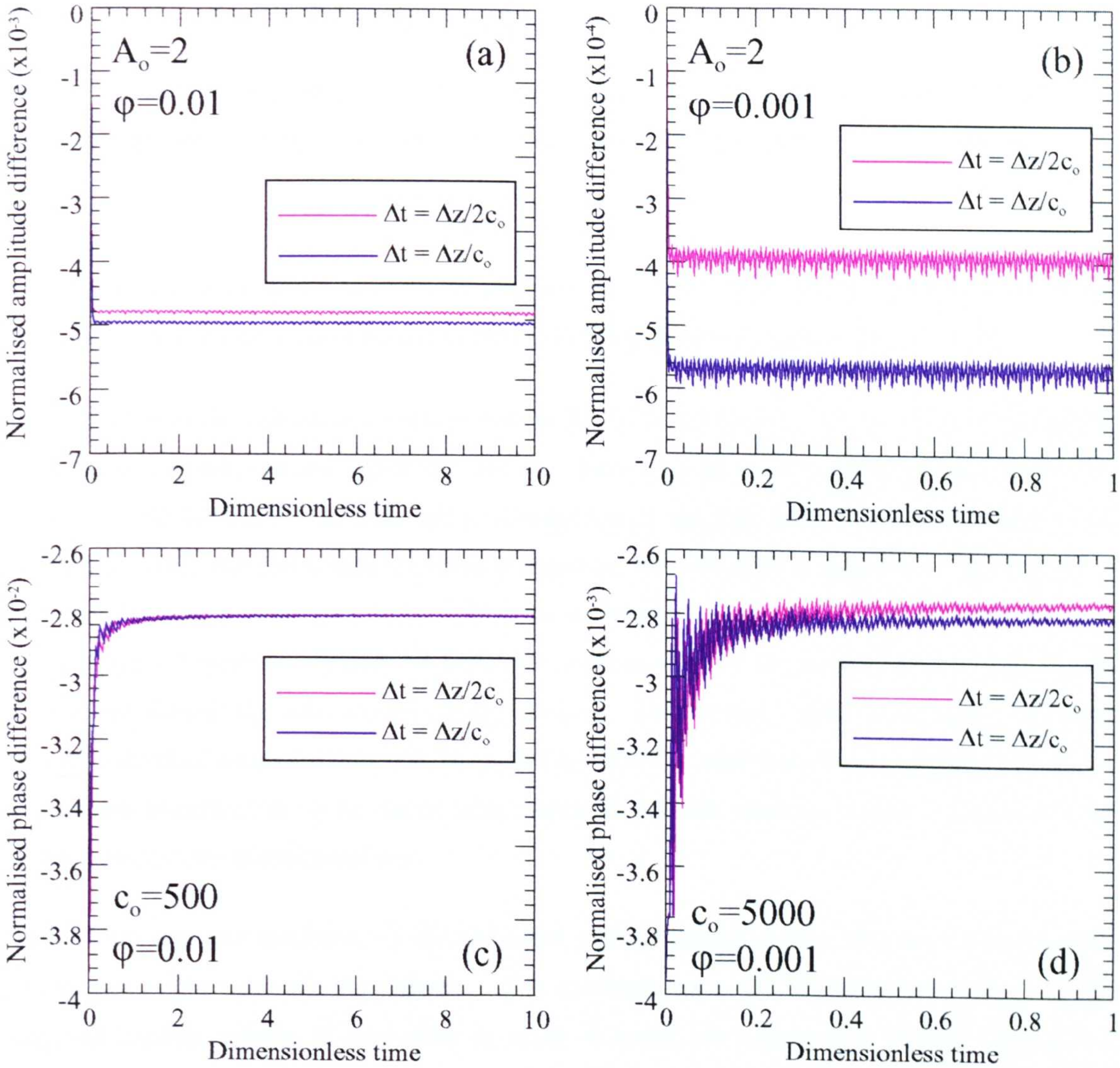

Figure A.7. Effect of halving Δt on the accuracy of the staggered-leapfrog differencing scheme when used to propagate the initial analytic solution for a solitary porosity wave. Plots (a) and (b) show normalised difference in amplitude $(A(t)-A_o)/A_o$ against dimensionless time; plots (c) and (d) show normalised difference in phase velocity $(c(t)-c_o)/c_o$ against dimensionless time. Both ordinate and abcissa axis scales vary by one order of magnitude between left and right hand plots. In all cases, Δz=0.125; A_o=2.

A.1.3.3 The full system of governing equations

The numerical schemes used to approximate the parabolic and hyperbolic governing equations (A.1)-(A.4) are governed by different requirements for stability and accuracy. The FTCS with upstream/downstream differencing scheme used to approximate the parabolic heat conservation equation (A.1) must satisfy the condition

$$\Delta t = \frac{\Delta z^2}{1.1\left(2\left|\kappa_{\text{eff}}\right| + \Delta z\left|\text{Ste}\left(w_l + w_s\right)\right|\right)} \tag{A.26}$$

for stability, and the condition $\Delta z = 1/200$ for accuracy (§A.1.3.1); the staggered leapfrog scheme used to approximate the hyperbolic mass conservation equation (A.2) must satisfy the CFL condition

$$\Delta t = \frac{\Delta z}{\left|\text{Ste}\left(w_l + w_s\right)\right|} \tag{A.27}$$

for stability, and the condition $\Delta z = 1/4$ for accuracy (§A.1.3.2). These conditions must be combined to produce stable, accurate solutions for the full system of governing equations (A.1) - (A.4).

A key result from the individual numerical tests of §A.1.3.1 and §A.1.3.2 is that, with the exception of the phase properties of the hyperbolic solution, decreasing Δz or Δt leads to an increase in the accuracy of the solutions[4], and although over-resolution of the hyperbolic solution does reduce the accuracy at which the phase information is propagated, the reduction is negligible. This result is important, because it means that if the stability or accuracy requirement is more stringent for either the parabolic or hyperbolic solution, the more stringent requirement may be applied to the full system of equations without the other solution losing accuracy. Furthermore, values of Δz and Δt deduced from the individual numerical tests may be applied to the full system of equations, and the accuracy of the solutions tested by halving Δz and Δt, with confidence that this procedure ensures accuracy of *both* the parabolic and hyperbolic solutions.

Although the accuracy conditions for the numerical schemes appear similar, they are not because the lengthscales of the solutions are different. The condition $\Delta z = 1/4$ required for accuracy of the staggered-leapfrog scheme is equivalent to using 4 nodes *per compaction length*, because the compaction length is the characteristic lengthscale of the solutions (§3.2.3). The node spacing Δz defined in this way is lengthscale independent; if the compaction length is changed, the accuracy condition is still given by $\Delta z = 1/4$. In contrast, the condition $\Delta z = 1/200$ required for accuracy of the FTCS with upstream/downstream differencing scheme is valid *only* for solutions with $\kappa_{\text{eff}} = 1$ and a *fixed* lengthscale of 1. If the lengthscale of the problem changes, the accuracy condition is no longer given by $\Delta z = 1/200$. The accuracy condition for the FTCS with upstream/downstream differencing

---

[4] With the possible exception of rounding errors. In an attempt to minimise these, all numerical operations were carried out using double precision. On the Sun SPARC 5 workstation used, this yields a floating point error of $<1\text{x}10^{-18}$.

scheme must be recast in a form which is lengthscale independent. In the absence of advection, the lengthscale of solutions to the heat conservation equation (A.1) is governed by the magnitude of $2\sqrt{\kappa_{eff} t}$ (Carslaw and Jaeger, 1986). The accuracy condition $\Delta z = 1/200$ was obtained for solutions with $t = 0.5$ (§A.3.1.2), in which case the lengthscale is governed by the magnitude of $\sqrt{2\kappa_{eff}}$, and the lengthscale independent accuracy condition

$$\Delta z = \sqrt{2\kappa_{eff}}/200 \tag{A.28}$$

is suggested.

The accuracy conditions for the parabolic ($\Delta z = 1/4$) and hyperbolic (equation (A.28)) solutions are equivalent when

$$\sqrt{2\kappa_{eff}}/200 = 1/4 \tag{A.29}$$

i.e. when $\kappa_{eff} = 1250$. For values of $\kappa_{eff} \geq 1250$, the accuracy condition for the staggered leapfrog scheme is more stringent; for values of $\kappa_{eff} \leq 1250$, the accuracy condition for the FTCS with upstream/downstream differencing scheme is more stringent. A suitable stability condition must now be deduced. The stability conditions (A.26) and (A.27) are the most stringent for large values of $Ste(w_l + w_s)$. Assuming $Ste = 1$ (its maximum value (§3.3)), and $(w_l + w_s) \sim 1$, the stability conditions (A.26) and (A.27) reduce to

$$\Delta t = \frac{\Delta z^2}{1.1\left(2|\kappa_{eff}| + \Delta z\right)} \tag{A.30}$$

$$\Delta t = \Delta z \tag{A.31}$$

and it is clear that condition (A.30) is always the more stringent.

These arguments yield the stability and accuracy conditions for the full set of governing equations

$$\Delta t = \frac{\Delta z^2}{1.1\left(2|\kappa_{eff}| + \Delta z\right)} \tag{A.30}$$

$$\Delta z = \sqrt{2\kappa_{eff}}/200 \qquad \text{for } \kappa_{eff} \leq 1250 \tag{A.32a}$$

$$\Delta z = 1/4 \qquad \text{for } \kappa_{eff} \geq 1250 \tag{A.32b}$$

which were tested by recording the dimensionless segregation time (t_{seg}) (§3.3.3), and the dimensionless segregation temperature (θ_{seg}) (§3.3.4), as a function of the dimensionless effective thermal diffusivity (κ_{eff}), and ensuring that the results remained unchanged when Δz and Δt were halved (typical values of t_{seg} and θ_{seg} are shown as a function of κ_{eff} in figures 3.6 and 3.7a respectively). Solutions for the spatial porosity distribution have a wave like form (§3.3.2), which is a common result of liquid migration through porous, permeable, *deformable* media (e.g. Richter and McKenzie, 1984; Barcilon and Richter, 1986; Scott and Stevenson, 1986); it is important that the numerical solutions accurately reproduce the amplitude and phase information of the porosity waves.

Ensuring that the segregation time and the segregation temperature remain unchanged when Δt and Δz are halved directly tests this. The segregation time is defined as the time required to initiate the mush-slurry transition (i.e. the time required for the porosity to reach the Critical Melt Fraction), and depends upon the *amplitude* of the leading porosity wave (§3.3.3). The segregation temperature is defined as the temperature at the position of incipient slurry formation, and depends upon the position, and hence *phase* velocity, of the leading wave (§3.3.4).

Figure A.8(a) shows the difference between the segregation *times* for solutions obtained using Δz and Δz/2, normalised to those obtained using Δz, as a function of κ_{eff}

$$t^{z}_{\mathrm{diff}}(\kappa_{\mathrm{eff}})=\left(t^{\Delta z/2}_{\mathrm{seg}}(\kappa_{\mathrm{eff}})-t^{\Delta z}_{\mathrm{seg}}(\kappa_{\mathrm{eff}})\right)\Big/t^{\Delta z}_{\mathrm{seg}}(\kappa_{\mathrm{eff}}) \tag{A.33}$$

Similarly, figure A.8(b) shows the difference between the segregation times for solutions obtained using Δt and Δt/2, normalised to those obtained using Δt, as a function of κ_{eff}

$$t^{t}_{\mathrm{diff}}(\kappa_{\mathrm{eff}})=\left(t^{\Delta t/2}_{\mathrm{seg}}(\kappa_{\mathrm{eff}})-t^{\Delta t}_{\mathrm{seg}}(\kappa_{\mathrm{eff}})\right)\Big/t^{\Delta t}_{\mathrm{seg}}(\kappa_{\mathrm{eff}}) \tag{A.34}$$

Figure A.8(c) shows the difference between the segregation *temperatures* for solutions obtained using Δz and Δz/2, normalised to those obtained using Δz, as a function of κ_{eff}

$$\theta^{z}_{\mathrm{diff}}(\kappa_{\mathrm{eff}})=\left(\theta^{\Delta z/2}_{\mathrm{seg}}(\kappa_{\mathrm{eff}})-\theta^{\Delta z}_{\mathrm{seg}}(\kappa_{\mathrm{eff}})\right)\Big/\theta^{\Delta z}_{\mathrm{seg}}(\kappa_{\mathrm{eff}}) \tag{A.35}$$

Similarly, figure A.8(d) shows the difference between the segregation temperatures for solutions obtained using Δt and Δt/2, normalised to those obtained using Δt, as a function of κ_{eff}

$$\theta^{t}_{\mathrm{diff}}(\kappa_{\mathrm{eff}})=\left(\theta^{\Delta t/2}_{\mathrm{seg}}(\kappa_{\mathrm{eff}})-\theta^{\Delta t}_{\mathrm{seg}}(\kappa_{\mathrm{eff}})\right)\Big/\theta^{\Delta t}_{\mathrm{seg}}(\kappa_{\mathrm{eff}}) \tag{A.36}$$

In all cases the solutions were obtained with φ = CMF = 0.5, and Ste = 1. Plots (a) and (b) show that the effect of halving Δz is to *decrease* the segregation time, but by <0.1% for all values of κ_{eff}; likewise, the effect of halving Δt is also to decrease the segregation time, but by <0.02% for all values of κ_{eff}. Plots (c) and (d) show that the effect of halving Δz is to *increase* the segregation temperature, but by <0.2% for all values of κ_{eff}; in contrast, the effect of halving Δt is to decrease the segregation temperature, but by <0.06% for all values of κ_{eff}.

These results indicate that the numerical schemes used to solve the full set of governing equations presented in chapter 3 produce stable, accurate results if the conditions (A.30) and (A.32) are satisfied. Halving Δz and Δt changes the quantitative results by <0.2% in all cases, which has a negligible effect on the values of the segregation time and temperature.

A.1.3.4 Conservation of mass

A final confirmation of the accuracy of the numerical solutions was obtained by comparing the total volume of liquid produced by phase change, with the total porosity, at the end of each run; i.e. by confirming the equality

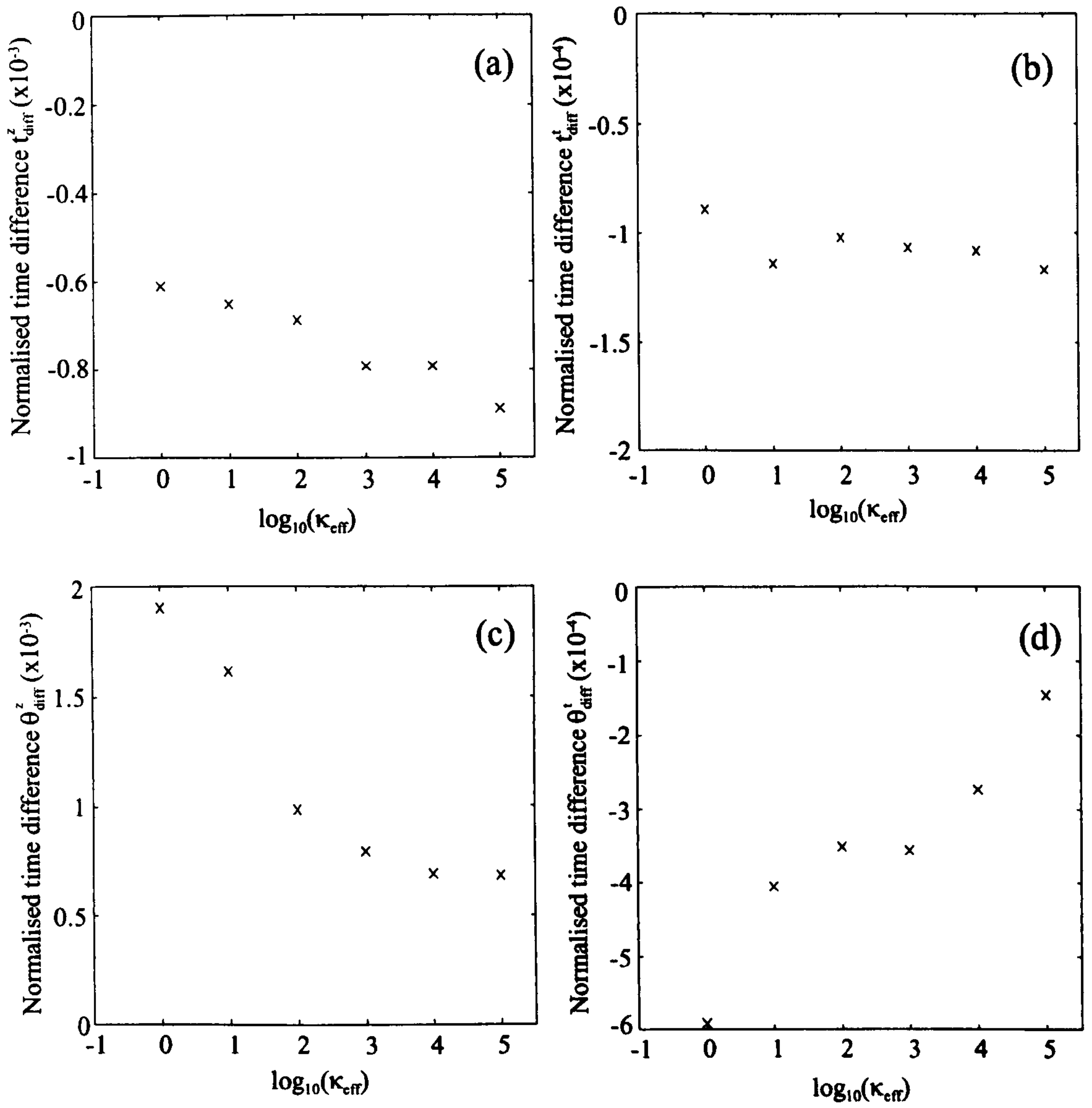

Figure A.8. Effect of halving Δz and Δt on the numerical solutions for the full set of governing conservation equations (A.1) - (A.4). (a) Normalised difference t^z_{diff} between the segregation times for solutions obtained with Δz and $\Delta z/2$, against κ_{eff} (t^z_{diff} given by equation (A.33)). (b) Normalised difference t^t_{diff} between the segregation times for solutions obtained with Δt and $\Delta t/2$, against κ_{eff} (t^t_{diff} given by equation (A.34)). (c) Normalised difference θ^z_{diff} between the segregation temperatures for solutions obtained with Δz and $\Delta z/2$, against κ_{eff} (θ^z_{diff} given by equation (A.35)). (d) Normalised difference θ^t_{diff} between the segregation temperatures for solutions obtained with Δt and $\Delta t/2$ against κ_{eff} (θ^t_{diff} given by equation (A.36)). Δz is given by the condition (A.32); Δt is given by the condition (A.30). In all cases, the solutions were obtained with φ = CMF = 0.5; Ste = 1, and are shown in figures 3.6 and 3.7(a)).

$$\int_0^t \int_0^{z_0} \frac{\partial \phi}{\partial t} \partial z \partial t = \int_0^t \int_0^{z_0} \left(\frac{\partial \theta}{\partial t} + (w_l + w_s) \frac{\partial \theta}{\partial z} \right) \partial z \partial t \tag{A.37}$$

If the numerical solutions have been accurately implemented then this equality must hold, in order to satisfy conservation of mass. Both left and right hand sides were integrated numerically, and if the difference between the values obtained, normalised to the total volume of liquid produced, differed by >0.1%, then the results of that run were discounted, and the source of the error located.

A.2 Numerical methods: chapter 4

The dimensionless, coupled, 1-D equations governing the model presented in chapter 4 are

$$\frac{\partial \phi}{\partial t} = \frac{1}{\varphi} \frac{\partial}{\partial z} \left((1 - \varphi\phi) w_s \right) + \frac{\partial \theta}{\partial t} + (w_m + w_s) \frac{\partial \theta}{\partial z} \tag{A.38}$$

$$\frac{\partial \theta}{\partial t} = \kappa_{\text{eff}} \frac{\partial^2 \theta}{\partial z^2} - \text{Ste}(w_m + w_s) \frac{\partial \theta}{\partial z} \tag{A.39}$$

$$\frac{\partial^2 w_s}{\partial z^2} = \frac{w_s}{\phi^n} + \frac{(1 - \varphi\phi)}{(1 - \varphi)} \tag{A.40}$$

$$\varphi\phi w_m = -(1 - \varphi\phi) w_s \tag{A.41}$$

$$\frac{\partial \theta}{\partial t} = \chi \kappa_{\text{eff}} \frac{\partial^2 \theta}{\partial z^2} \tag{A.42}$$

subject to the initial conditions

$$\theta(0,0) = 0 \tag{A.43a}$$

$$\frac{\partial}{\partial z}(\theta(z,0)) = \psi_{\text{geo}} \tag{A.43b}$$

$$\phi(z,0) = w_m(z,0) = w_s(z,0) = 0 \tag{A.43c}$$

and the boundary conditions

$$\theta(0,t) = 1 \tag{A.44a}$$

$$w_m(0,t) = w_s(0,t) = w_m(z_0,t) = w_s(z_0,t) = 0 \tag{A.44b}$$

$$\theta(z_0,t) = 0 \tag{A.44c}$$

$$\frac{\partial}{\partial z}(\theta(z \to \infty, t)) \to \psi_{\text{geo}} \tag{A.44d}$$

(see table A.1 for a reminder of the nomenclature). The governing equations describe two distinct regions: the partially molten rock in the region ($0 \le z \le z_0$), and the solid rock in the region ($z > z_0$). The equations governing the transport of heat, mass and momentum in the partially molten rock (equations (A.38) - (A.41)) are identical those given in chapter 3, with w_l replaced by w_m (a change in the nomenclature only). The equations governing both regions were solved using suitable explicit finite difference approximations.

A.2.1 Finite difference approximations of the governing equations

The equations governing the transport of heat, mass and momentum in the partially molten rock ($0 \leq z \leq z_0$) (equations (A.38) - (A.41)) were approximated using the schemes described in §A.1.1, which yield the explicit difference equations (A.6) and (A.8) for propagating the dimensionless temperature (θ) and dimensionless porosity (ϕ) through time, and the tridiagonal system of coupled linear equations (A.11) for the matrix velocity (w_s).

The parabolic equation governing the transport of heat in the solid rock ($z > z_0$) (equation (A.42)) was approximated using a simple forward-time-centred-space (FTCS) scheme which is first order accurate in time, second order accurate in space, and yields the explicit difference scheme for propagating θ through time

$$\theta_k^{j+1} = \theta_k^j + \chi \kappa_{eff} \frac{\theta_{k+1}^j + \theta_{k-1}^j - 2\theta_k^j}{\Delta z^2} \Delta t \tag{A.45}$$

A.2.2 Method of solution

The explicit difference equations were solved sequentially in a similar manner to that described in §A.1.2 (figure A.9). The initial values of θ, ϕ and w_s were prescribed by condition (A.43). The temperature θ was propagated through one time increment in both the regions ($0 \leq z \leq z_0$) and ($z > z_0$) using equations (A.6) and (A.45) respectively; the porosity ϕ was then updated using equation (A.8). In order to solve for the matrix velocity w_s, the conditions at both the upper ($z=z_0$) and lower ($z=0$) boundaries of the partially molten rock are required; the position z_0 of the upper boundary was located at the spatial node k at which the modulus of the dimensionless temperature ($|\theta|$) was a minimum. Finally, the tridiagonal system of coupled linear equations (A.11) was solved for w_s, subject to the boundary conditions (A.44b), by matrix inversion (Press *et al.*, 1992). These steps were repeated for each time increment j until the solutions had been propagated to the required time (§A.1.2).

A.2.3 Accuracy of the numerical solutions

As discussed in §A.1, unless numerical approximations are carefully selected and implemented, the numerical solutions obtained may be inaccurate because of errors introduced and propagated by the approximations. To ensure stability and accuracy of the numerical solutions obtained for the full set of governing equations (A.38) - (A.42), the conditions required to ensure stability and accuracy of the numerical schemes used to approximate the governing equations in the regimes ($0 \leq z \leq z_0$) (i.e. in the partially molten rock) and ($z>z_0$) (i.e. in the solid rock) were deduced separately. Using the insight gained, suitable criterion were deduced to ensure stability and accuracy of the full solutions.

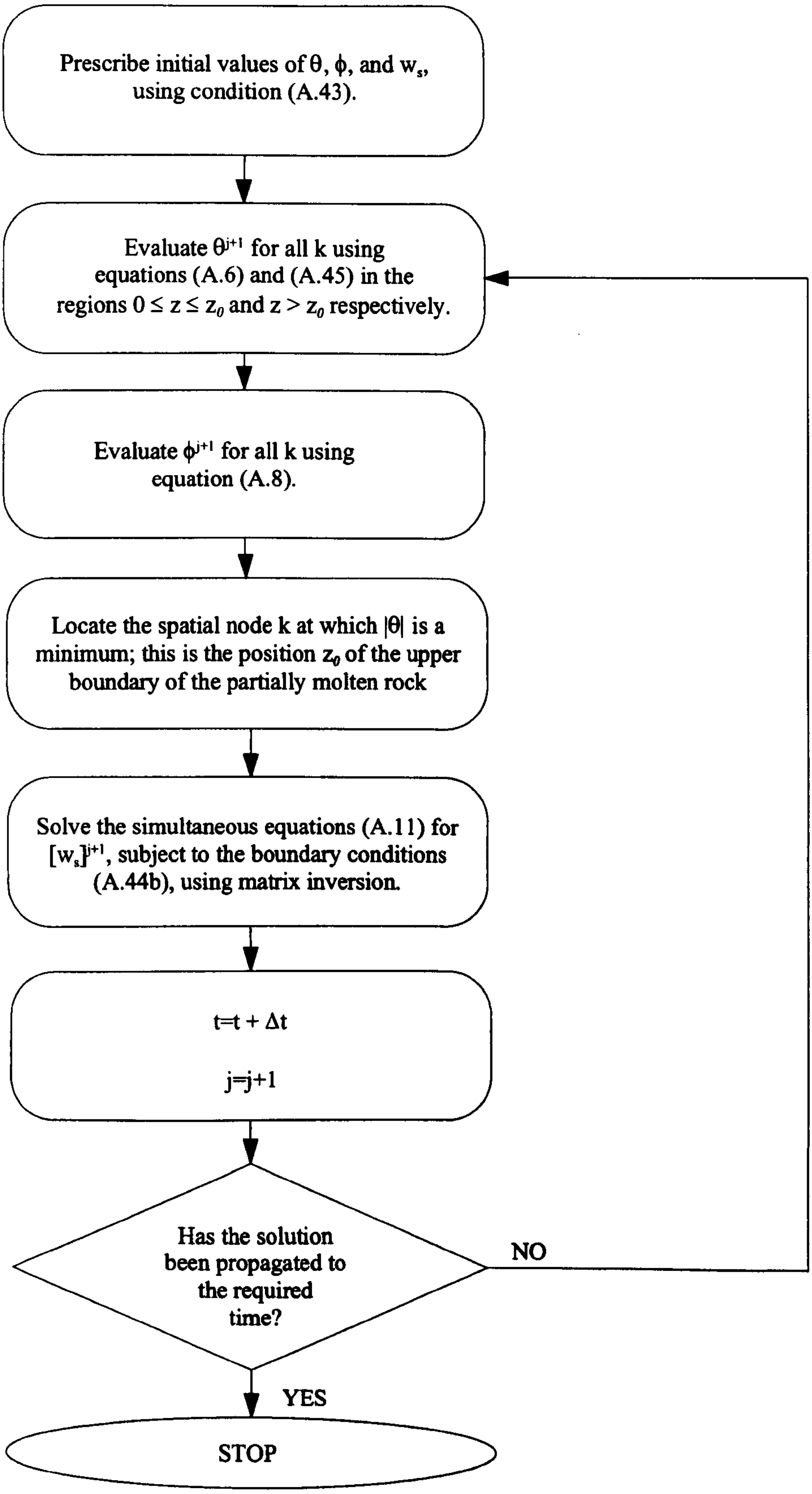

Figure A.9. Flow chart showing the order in which the numerical approximations of the governing equations presented in chapter 5 were evaluated.

A.2.3.1 Heat, mass and momentum conservation in the region ($0 \le z \le z_0$)

The conditions required to ensure stability and accuracy of the numerical schemes used to approximate the equations governing the transport of heat, mass and momentum in the region ($0 \le z \le z_0$) (equations (A.38) - (A.41)) were deduced in §A.1, and are given by equations (A.30) and (A.32).

A.2.3.2 Heat conservation in the region ($z>z_0$)

Stability of the FTCS scheme used to approximate the conservation equation governing the conductive transport of heat in the region ($z>z_0$) (equation (A.45)) is predicted if the local time step (Δt) is restricted by (Morton and Mayers, 1994)

$$\Delta t \le \frac{(\Delta z)^2}{2\chi\kappa_{\mathrm{eff}}} \tag{A.46}$$

Accuracy of the FTCS scheme was investigated using the analytic solution to equation (A.42) for a semi-infinite half space in which the boundary at z=0 is kept at a constant temperature of 1 and the initial temperature is zero. The solution is given by (Carslaw and Jaeger, 1986)

$$\theta_{\mathrm{ana}}(z,t) = \mathrm{erfc}\left(\frac{z}{2\sqrt{\chi\kappa_{\mathrm{eff}}\,t}}\right) \tag{A.47}$$

(figure A.10). The accuracy with which the scheme reproduced the analytic solution was investigated by recording the difference between the positions of selected isotherms (z_i) for the numerical and analytic solutions, normalised to the positions for the analytic solution

$$E_i(t) = \left(z_i^{\mathrm{num}}(t) - z_i^{\mathrm{ana}}(t)\right) / z_i^{\mathrm{ana}}(t) \tag{A.48}$$

where i denotes the selected isotherm. The normalised difference was recorded for the $z_{0.5}$ and z_0 isotherms as a function of dimensionless time. Defined in this way, a positive error indicates that the numerical solution lags the analytic solution, and *vice-versa*.

Figure A.11 shows the effect of halving Δz and Δt on the accuracy of the numerical solutions. As a 'best guess' for the *accuracy* requirement, the value of Δz used is given by condition (A.32); the value of Δt used is given by the *stability* requirement

$$\Delta t = \frac{(\Delta z)^2}{2\chi\kappa_{\mathrm{eff}}} \tag{A.49}$$

Plots A.11(a) - (d) show the effect of halving Δz on the normalised difference between the numerical and analytic solutions obtained for values of $\chi\kappa_{\mathrm{eff}} = 5\times10^{-3}$ and $\chi\kappa_{\mathrm{eff}} = 5\times10^{+3}$. These values were chosen, because for the former Δz is given by condition (A.32a) (plots A.11(a) and (b)), while for the latter Δz is given by condition (A.32b)) (plots A.11(c) and (d)). In all cases, the error between the numerical and analytic solutions decreases monotonically as the solutions are propagated through

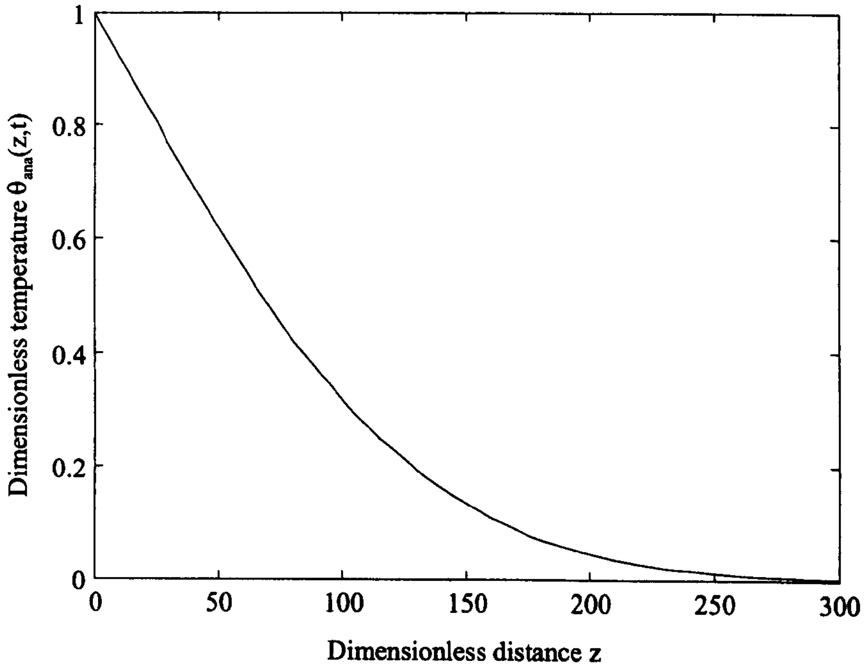

Figure A.10. Analytic solution to the equation governing conductive heat transport in the solid rock, (equation (A.42), obtained using equation (A.47), for a semi-infinite half space in which the boundary at z=0 is kept at a constant temperature of 1 and the initial temperature is 0. The solution shown is for the case $\chi\kappa_{eff} = 100$, after 50 time units.

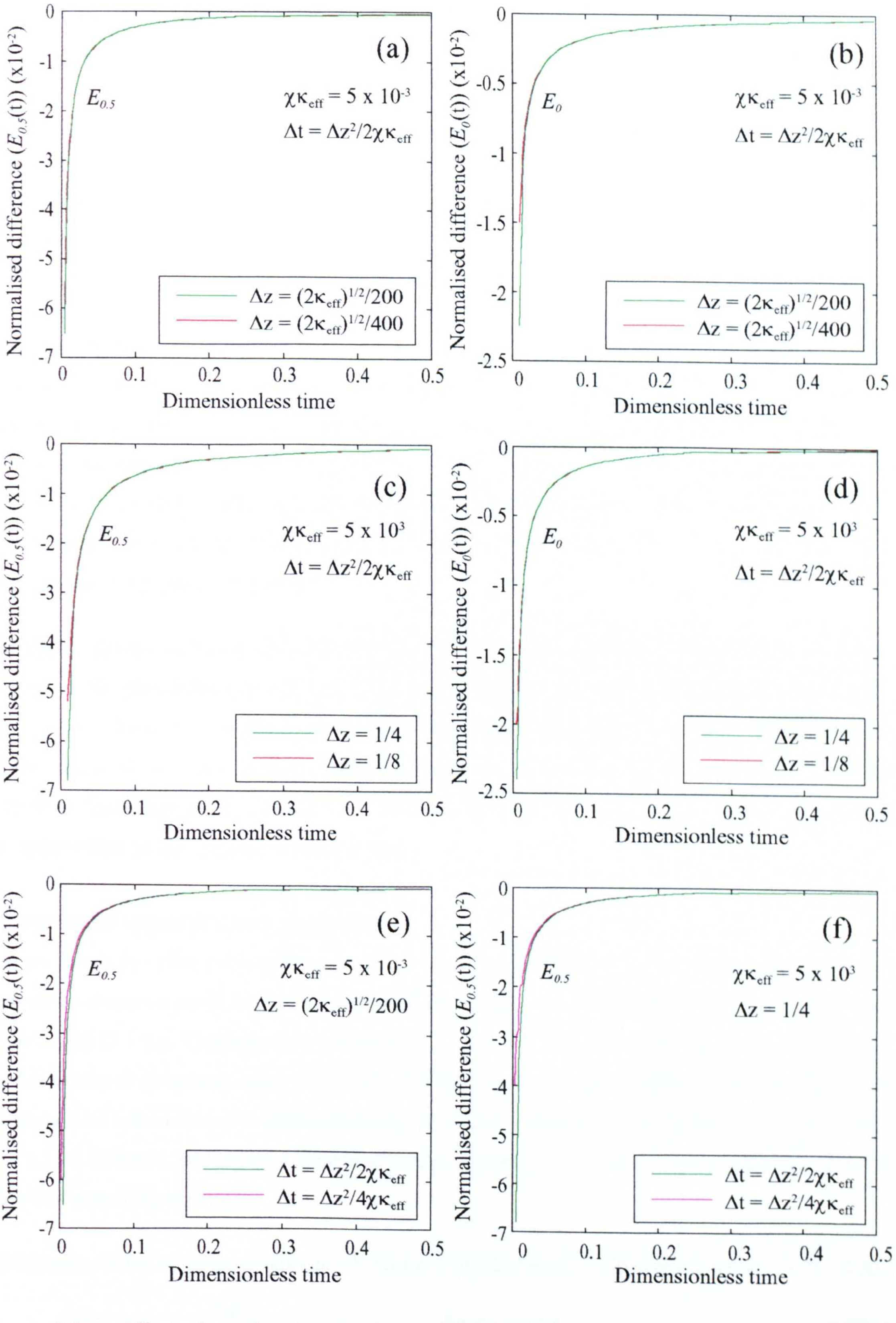

Figure A.11. Effect of varying Δz and Δt on the accuracy of the FTCS scheme when used to approximate the parabolic heat equation (A.42). Plots show the normalised difference E_i between the positions of the isotherms z_i for the numerical and analytic solutions, against dimensionless time. Plots (a-d) show the effect of halving Δz on $E_{0.5}$ and E_0 for solutions with $\chi\kappa_{eff} = 5 \times 10^{-3}$ and 5×10^{3}; plots (e-f) show the effect of halving Δt on $E_{0.5}$ for solutions with $\chi\kappa_{eff} = 5 \times 10^{-3}$ and 5×10^{3}. Note that the ordinate axis scale varies between plots..

time. The maximum error at t = 0.5 is <0.1% (plot A.11b). The effect of halving Δz is negligible; the error at t = 0.5 is reduced by <0.001% in all cases.

Plots A.11(e) and (f) show the effect of halving Δt on the normalised difference between the numerical and analytic solutions obtained for values of $\chi\kappa_{eff} = 5\text{x}10^{-3}$ and $\chi\kappa_{eff} = 5\text{x}10^{+3}$. Again, the error between the numerical and analytic solutions decreases monotonically as the solutions are propagated through time. The maximum error at t = 0.5 is <0.1% (plot A.11f). The effect of halving Δt is negligible; the error at t = 0.5 is reduced by <0.001% in all cases.

The error between the numerical and analytic solutions shown in figure A.11 decreases as the solutions are propagated through time, because the numerical solution initially lags the analytic solution; as the solutions are propagated they converge. The solutions were investigated for dimensionless times up to t = 10; the results are shown in figure 4.11 only for times up to t = 0.5, so that the initial lag of the numerical solution may be observed. The full results obtained demonstrate that for times >0.5, the normalised error asymptotically approaches zero; i.e. the numerical and analytic solutions continue to converge.

The results of these numerical tests indicate that the FTCS scheme accurately reproduces the analytic solution of the heat conservation equation (A.42) for a semi-infinite half space, when the spatial node spacing Δz is given by condition (A.32), and the temporal node spacing Δt is given by equation (A.49). Using these values, halving Δz and Δt improves the accuracy of the solutions at t = 0.5 by <0.001%. Maximum errors introduced by the numerical scheme at t = 0.5 are <0.3%, and have a negligible effect on the accuracy of the solutions.

A.2.3.3 The full system of governing equations

The key result from the numerical test in §A.2.3.2 is that condition (A.32) ensures *accuracy* of the numerical schemes used to approximate the governing equations in both the region $(0 \leq z \leq z_0)$, and in the region $(z > z_0)$. Consequently, condition (A.32) ensures accuracy of the numerical solutions for the *full* system of governing equations (A.38) - (A.42). However, the conditions to ensure *stability* of the numerical schemes used to approximate the governing equations in the regions $(0 \leq z \leq z_0)$ and $(z > z_0)$ are different, and must be combined to ensure stability of the numerical solutions for the full system of governing equations.

Substituting for the accuracy conditions (A.32a) and (A.32b) in the stability requirement (A.30) yields

$$\Delta t = \frac{\kappa_{eff}}{2200\left(2\kappa_{eff} + \left(\sqrt{2\kappa_{eff}}/200\right)\right)} \qquad \text{for } \kappa_{eff} \leq 1250 \qquad \textbf{(A.50a)}$$

and

$$\Delta t = \frac{1}{35.2\kappa_{eff} + 4.4} \qquad \text{for } \kappa_{eff} \geq 1250 \qquad \text{(A.50b)}$$

Likewise, substituting for the accuracy conditions (A.32a) and (A.32b) in the stability requirement (A.49) yields

$$\Delta t = \frac{\sqrt{\kappa_{eff}}}{200\chi\sqrt{2}} \qquad \text{for } \kappa_{eff} \leq 1250 \qquad \text{(A.50c)}$$

and

$$\Delta t = \frac{1}{32\chi\kappa_{eff}} \qquad \text{for } \kappa_{eff} \geq 1250 \qquad \text{(A.50d)}$$

It is not clear whether condition (A.50a) or (A.50c) is the most stringent for $\kappa_{eff} \leq 1250$, or whether condition (A.50b) or (A.50d) is the most stringent for $\kappa_{eff} \geq 1250$. Substituting for the values of κ_{eff} and χ used in chapter 4 (see table 4.2) reveals that no one condition is the most stringent for all values of κ_{eff} and χ; consequently, the numerical code was developed so that the most stringent stability condition would be identified and implemented before each run.

Following the approach of §A.1.3.3, the stability and accuracy conditions (A.50) and (A.32) for the full system of governing equations (A.38) - (A.42) were tested by recording the dimensionless segregation time (t_{seg}) (§4.3.3), and the dimensionless segregation temperature (θ_{seg}) (§4.3.3), as a function of the dimensionless effective thermal diffusivity (κ_{eff}), and ensuring that the results remained unchanged when Δz and Δt were halved (typical values of t_{seg} and θ_{seg} are shown as a function of κ_{eff} in figures 4.19 - 4.20).

Figure A.12(a) shows the difference between the segregation *times* for solutions obtained using Δz and $\Delta z/2$, normalised to those obtained using Δz, as a function of κ_{eff} (equation A.33); figure A.12(b) shows the difference between the segregation times for solutions obtained using Δt and $\Delta t/2$, normalised to those obtained using Δt, as a function of κ_{eff} (equation A.34). Similarly, figure A.12(c) shows the difference between the segregation *temperatures* for solutions obtained using Δz and $\Delta z/2$, normalised to those obtained using Δz, as a function of κ_{eff} (equation A.35); figure A.12(d) shows the difference between the segregation temperatures for solutions obtained using Δt and $\Delta t/2$, normalised to those obtained using Δt, as a function of κ_{eff} (equation A.36). In all cases the solutions were obtained with φ = CMF = 0.5, $\psi_{geo} = 10^{-2}$, Ste = 0.5, and χ = 2.5.

Plots A.12(a) and (b) show that the effect of halving Δz is to *decrease* the segregation time, but by <0.2% for all values of κ_{eff}; likewise, the effect of halving Δt is also to decrease the segregation time, but by <0.025% for all values of κ_{eff}. Plots A.12(c) and (d) show that the effect of halving Δz is to *increase* the segregation temperature, but by <0.25% for all values of κ_{eff}; in contrast, the effect of halving Δt is to decrease the segregation temperature, but by <0.2% for all values of κ_{eff}.

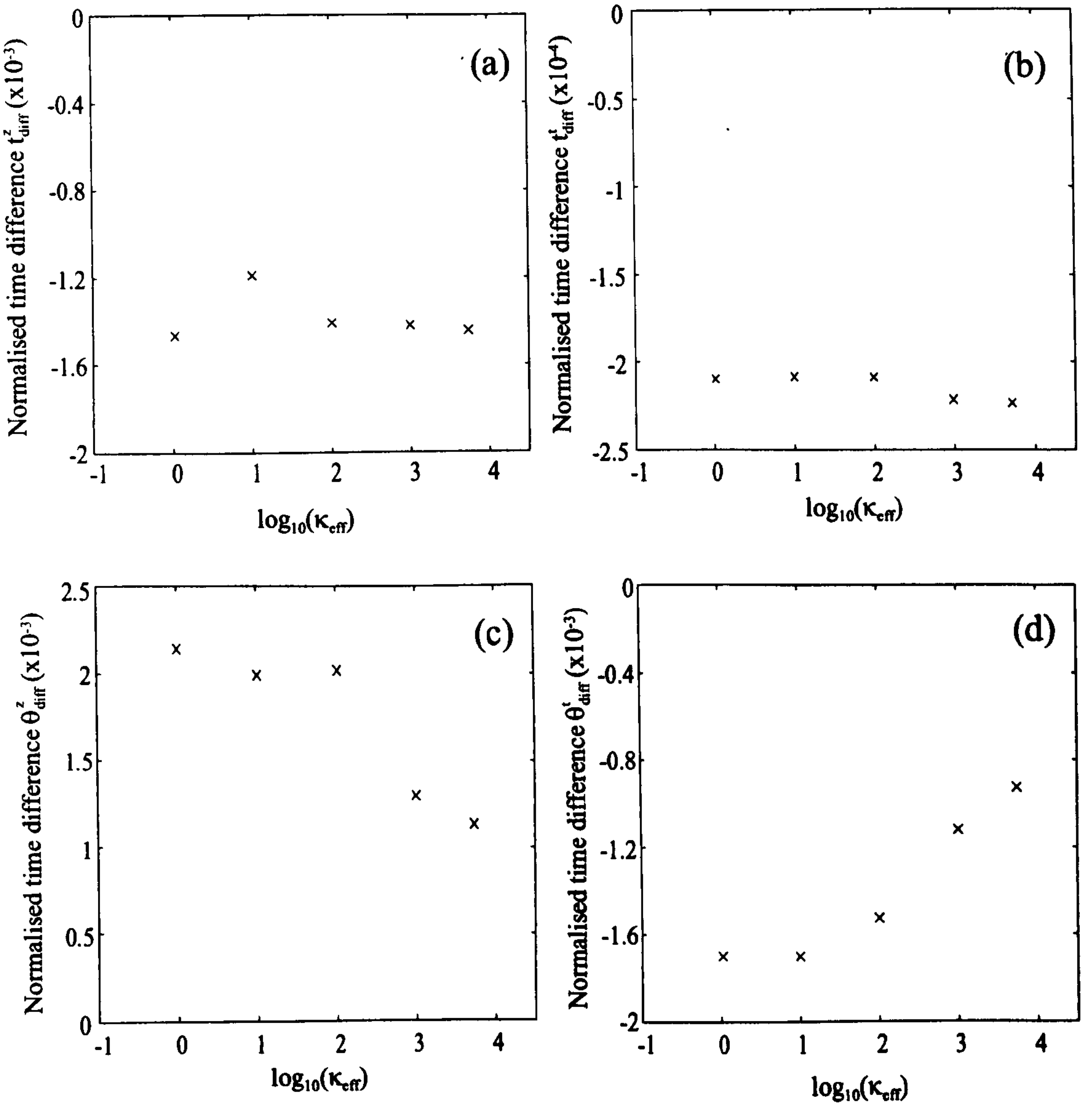

Figure A.12. Effect of halving Δz and Δt on the numerical solutions for the full set of governing conservation equations (A.38) - (A.42). (a) Normalised difference t^z_{diff} between the segregation times for solutions obtained with Δz and $\Delta z/2$, against κ_{eff} (t^z_{diff} given by equation (A.33)). (b) Normalised difference t^t_{diff} between the segregation times for solutions obtained with Δt and $\Delta t/2$, against κ_{eff} (t^t_{diff} given by equation (A.34)). (c) Normalised difference θ^z_{diff} between the segregation temperatures for solutions obtained with Δz and $\Delta z/2$, against κ_{eff} (θ^z_{diff} given by equation (A.35)). (d) Normalised difference θ^t_{diff} between the segregation temperatures for solutions obtained with Δt and $\Delta t/2$ against κ_{eff} (θ^t_{diff} given by equation (A.36)). Δz is given by the condition (A.32); Δt is given by the condition (A.50). In all cases, the solutions were obtained with φ = CMF = 0.5; $\psi_{g\infty} = 10^{-2}$, Ste=0.5, χ = 2.5, and are shown in figure 4.18 (c) and (d).

These results indicate that the numerical schemes used to solve the full set of governing equations presented in chapter 4 produce stable, accurate results if the conditions (A.50) and (A.32) are satisfied. Halving Δz and Δt changes the quantitative results by <0.25% in all cases, which has a negligible effect on the values of the segregation time and temperature.

A.2.3.4. Conservation of mass

A final confirmation of the accuracy of the numerical solutions was obtained by comparing the total volume of melt produced, with the total porosity, at the end of each run; i.e. by confirming the equality (A.37). If the numerical solutions have been accurately implemented, then this equality must hold in order to satisfy conservation of mass. Both left and right hand sides were integrated numerically, and if the difference between the values obtained, normalised to the total volume of melt produced, differed by >0.1%, then the results of that run were discounted, and the source of the error located (cf. §A.1.3.4).

A.2.3.5 The effect of a percolation threshold

In order to obtain the results presented in §4.3.1.2, the numerical schemes were modified to include the effect of a percolation threshold (ϕ_c). The percolation threshold denotes the *minimum* porosity at which the partially molten rock is permeable. In regions with porosities less than the percolation threshold, the permeability is zero; consequently, the melt and matrix velocities, and the compaction rate C ($= \partial(\phi w_m)/\partial z$) are required to be zero. The former requirement ($w_m = w_s = 0$) was rigorously implemented when solving for the matrix velocity (equation (A.11)). The ϕ^3 term in the coefficients (A.12) represents the dimensionless permeability; in regions with $\phi \le \phi_c$ the ϕ^3 term was set to zero, in which case the coefficients reduce to

$$a_k^j = c_k^j = d_k^j = 0 \qquad \text{(A.51a)}$$

$$b_k^j = 1 \qquad \text{(A.51b)}$$

and the matrix velocity $\left[w_s\right]_k^j$ is zero. However, the latter requirement follows from the physical requirement that the bulk viscosity of the partially molten rock become infinite if the permeability is zero (§4.3.1.2), and cannot be rigorously implemented. Rather, in regions with $\phi \le \phi_c$, the compaction term (the second term on the right-hand-side) in equation (A.8)[5] was set to zero, in which case, noting that the melt and matrix velocities are also zero, equation (A.8) reduces to

$$\phi_k^{j+1} = \phi_k^j + 2\left(\theta_k^{j+1} - \theta_k^j\right) \qquad \text{(A.52)}$$

However, although this numerical forcing of the compaction term correctly represents the change in the rheology of the partially molten rock, it was found that for solutions with $\kappa_{eff} \le 1$and $\psi_{geo} \ge 1$, the

---

[5] This term is identical to the compaction rate C, but is expressed in terms of the matrix velocity w_s rather than the melt velocity w_m.

numerical solutions no longer satisfied the equality (A.37); i.e. mass was not conserved. This problem could not be resolved using the numerical techniques outlined. Only the solutions for which mass is satisfactorily conserved are presented in §4.3.1.2.

A.3 Numerical methods: chapter 5

The dimensionless, coupled 1-D equations governing the model presented in chapter 5 are those presented in chapter 4, with the addition of an equation governing conservation of heat in the underlying sill (i.e. in the region $z < 0$)

$$\frac{\partial \theta}{\partial t} = \kappa_{eff} \frac{\partial^2 \theta}{\partial z^2} \qquad (A.53)$$

This equation is identical to that governing conservation of heat in the solid rock (i.e. in the region $z > z_0$), with the exception of the factor χ (see equation A.42).

The equations governing the transport of heat, mass, and momentum in the overlying rock ($z > 0$) were approximated using the schemes described in §A.2.1, while equation (A.53) governing the transport of heat in the underlying sill was approximated using the FTCS scheme described in §A.2.1. Stability of the scheme is ensured if the local time step (Δt) is restricted by

$$\Delta t = \frac{(\Delta z)^2}{2\kappa_{eff}} \qquad (A.54)$$

This condition is similar to condition (A.49), which is required to ensure stability of the scheme when used to approximate the heat conservation equation (A.42) in the region $z > z_0$. Given that the χ term in condition (A.49) is always greater than 1 (table 4.2), it is clear that condition (A.49) is always more stringent than condition (A.54); moreover, it was shown in §A.2.3.2 that the FTCS scheme accurately reproduces the analytic solution of the heat conservation equation when the spatial node spacing (Δz) is restricted by the accuracy condition (A.32). Consequently, the conditions required to ensure stability and accuracy of the governing equations presented in chapter 4 also ensure stability and accuracy of the FTCS scheme when used to approximate equation (A.53), which means that those conditions ((A.32) and (A.50)) ensure stability and accuracy of the full set of governing equations presented in chapter 5.

Following the approach of §A.2.3.3, the stability and accuracy conditions (A.50) and (A.32) were tested by recording the dimensionless segregation time (t_{seg}) (§5.3.1.2), and the dimensionless segregation temperature (θ_{seg}) (§5.3.1.2), as a function of the dimensionless effective thermal diffusivity (κ_{eff}), and ensuring that the results remained unchanged when Δz and Δt were halved (typical values of t_{seg} and θ_{seg} are shown as a function of κ_{eff} in figure 5.4).

Figure A.13(a) shows the difference between the segregation *times* for solutions obtained using Δz and $\Delta z/2$, normalised to those obtained using Δz, as a function of κ_{eff} (equation A.33); figure A.13(b) shows the difference between the segregation times for solutions obtained using Δt and $\Delta t/2$, normalised to those obtained using Δt, as a function of κ_{eff} (equation A.34). Similarly, figure A.13(c) shows the difference between the segregation *temperatures* for solutions obtained using Δz and $\Delta z/2$, normalised to those obtained using Δz, as a function of κ_{eff} (equation A.35); figure A.13(d) shows the difference between the segregation temperatures for solutions obtained using Δt and $\Delta t/2$, normalised to those obtained using Δt, as a function of κ_{eff} (equation A.36). In all cases the solutions were obtained using the minimum sill thickness required for magma mobilisation, with φ = CMF = 0.5, $\psi_{geo} = 10^{-4}$, Ste = 0.5, and $\chi = 2.5$ (§5.3.1.2).

Plots A.13(a) and (b) show that the effect of halving Δz is to *decrease* the segregation time, but by <0.4% for all values of κ_{eff}; likewise, the effect of halving Δt is also to decrease the segregation time, but by <0.03% for all values of κ_{eff}. Plots A.13(c) and (d) show that the effect of halving Δz is to *increase* the segregation temperature, but by <0.3% for all values of κ_{eff}; in contrast, the effect of halving Δt is to decrease the segregation temperature, but by <0.25% for all values of κ_{eff}.

These results indicate that the numerical schemes used to solve the full set of governing equations presented in chapter 5 produce stable, accurate results if the conditions (A.50) and (A.32) are satisfied. Halving Δz and Δt changes the quantitative results by <0.4% in all cases, which has a negligible effect on the values of the segregation time and temperature.

A final confirmation of the accuracy of the numerical solutions was obtained by comparing the total volume of melt produced, with the total porosity, at the end of each run; i.e. by confirming the equality (A.37). If the difference between the values obtained, normalised to the total volume of melt produced, differed by >0.1%, then the results of that run were discounted, and the source of the error located (cf. §A.1.3.4).

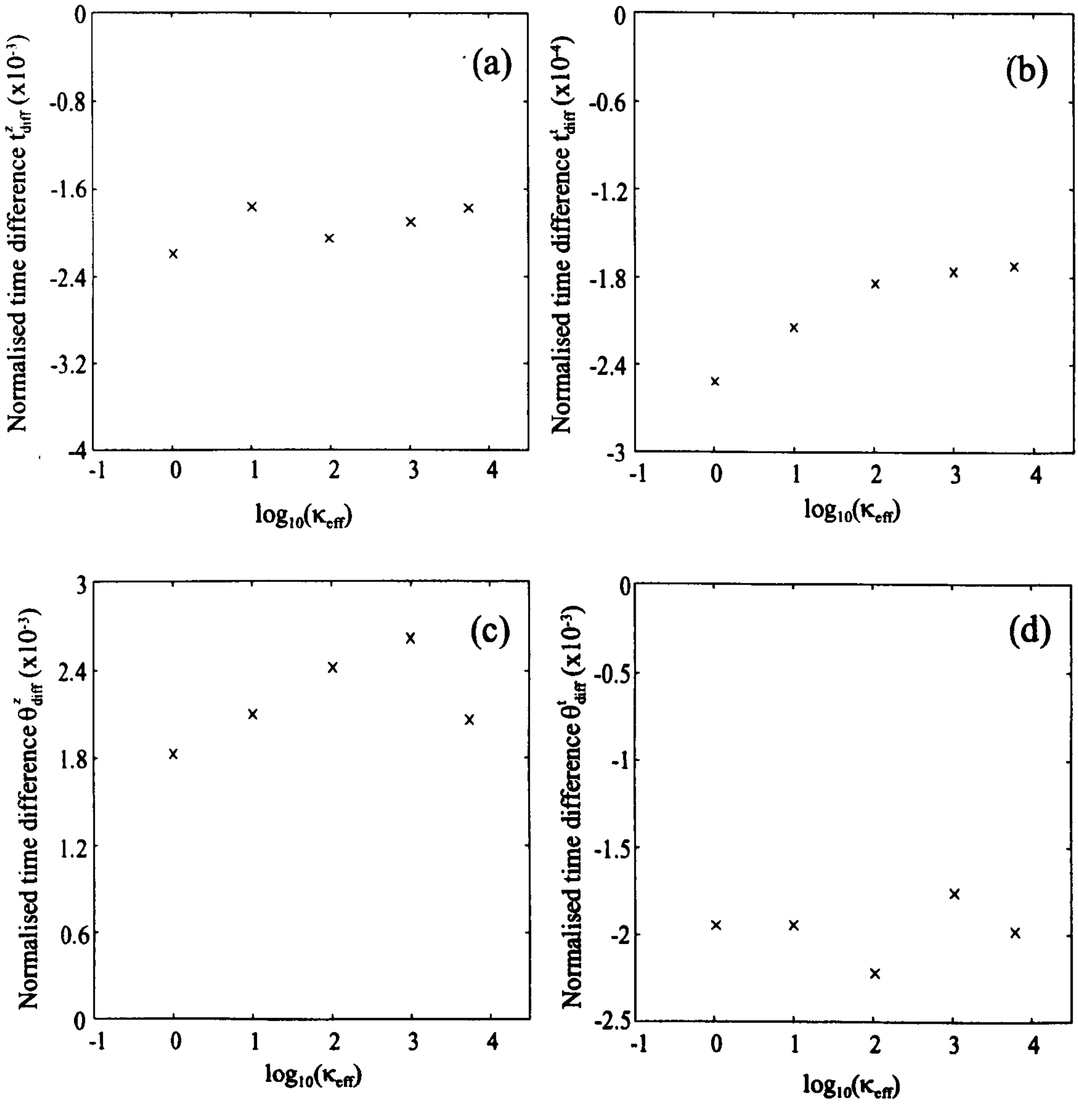

Figure A.13. Effect of halving Δz and Δt on the numerical solutions for chapter 5. (a) Normalised difference t^z_{diff} between the segregation times for solutions obtained with Δz and Δz/2, against κ_{eff} (t^z_{diff} given by equation (A.33)). (b) Normalised difference t^t_{diff} between the segregation times for solutions obtained with Δt and Δt/2, against κ_{eff} (t^t_{diff} given by equation (A.34)). (c) Normalised difference θ^z_{diff} between the segregation temperatures for solutions obtained with Δz and Δz/2, against κ_{eff} (θ^z_{diff} given by equation (A.35)). (d) Normalised difference θ^t_{diff} between the segregation temperatures for solutions obtained with Δt and Δt/2 against κ_{eff} (θ^t_{diff} given by equation (A.36)). Δz is given by the condition (A.32); Δt is given by the condition (A.50). In all cases, the solutions were obtained using the minimum sill thickness required for magma mobilisation, with φ = CMF = 0.5; $\psi_{g\infty} = 10^{-4}$, Ste=0.5 and χ = 2.5, and are shown in figure 5.4(a) and (b).

Appendix B: Publications in support of this dissertation

Jackson, M.D. and Cheadle, M.J. (in press). A continuum model for the transport of heat, mass, and momentum in a deformable, multicomponent mush undergoing solid-liquid phase change. *International Journal of Heat and Mass Transfer.*

Jackson, M.D., Cheadle, M.J. and Atherton, M.P. (1995). A Mechanism for the Segregation and Collection of Crustal Melts. *In*: Brown, M. and Piccoli, P. (eds.) *The Origin of Granites and Related Rocks.* U.S. Geological Survey Circular 1129.